Numerical Study of Semiconductor Optical Amplifiers for Passive Optical Networks

by

Lin Liu

A Thesis

presented to the University of Strathclyde

in fulfilment of the requirements for the degree of Doctor of Philosophy

in

Department of Electronic and Electrical Engineering

Centre for Intelligent Dynamic Communications

May 2013

Declaration

This thesis is the result of the author's original research. It has been composed by the author and has not been previously submitted for examination which has led to the award of a degree.

Lin Liu May 2013

Acknowledgements

First and foremost, I would like to thank my supervisor Dr. Walter Craig Michie for his encouragement, guidance, support and most importantly, patience throughout my PhD study. This work would not have been possible without his ground-breaking work on the adjustable gain-clamped SOA. Over the years, he selflessly sacrificed huge amount of time and efforts for passing on his expertise and keeping my work on the right track. Working under his supervision has proven to be joyful as well as fruitful.

I also would like to express my sincere gratitude to my supervisor Prof. Ivan Andonovic. It's been a great honour for me to be his PhD student and also a member of his CIDCOM family, where I had the opportunity to work with so many talented people. Apart from his greatest insight into telecommunications, his enthusiasm, humour and optimistic character has indeed inspired me in many ways.

The SOA expert – Dr. Anthony E. Kelly from University of Glasgow must surely be thanked for providing SOA parameters, helping with experiment configurations on dynamic gain modulation, reviewing my papers and holding many fruitful discussions.

A good many friends have made my study at Strathclyde University a wonderful time. They are: my labmates Krishna Chytanya Chinnam, Charlie Di Cao, Hammad Yaqoob, Dr. Tsung-Ta Wu, Dr. Kae Hsiang Kwong, Dr. Konstantinos Sasloglou, Hock Guan Goh, Leo Fanyu Meng, Gavin Tsao, Siti Khadijah Binti Idris; my flatmates Dr. Yujie Chen and Dr. Yanfeng Zhang from Institute of Photonics (IoP), and Dr. Hong Li from Accounting and Finance Department. I truly appreciate all their kind help during my PhD in Glasgow.

I am also grateful to my PhD examiners, Prof. Siyuan Yu from University of Bristol and Dr. Michael Lengden at Strathclyde University, who provided insightful and constructive comments. Dr. Robert Atkinson should be thanked for organising and chairing my PhD Viva.

My deepest gratitude also goes to my Master's supervisor: Prof. Zhonghao Shao from Nanjing University of Posts and Telecommunications, China, who introduced me to the optical communications and numerical techniques, which are invaluable to not only my PhD study but also my future career.

I gratefully acknowledge the funds received from Strathclyde University Scholarship and Glasgow Research Partnership in Engineering (GRPE).

I am deeply indebted to my parents, Fugen Liu and Hefen Lu, for their love, understanding and support throughout my entire life. My gratitude also goes to my father-in-law Guizhun Ding, and mother-in-law Xiujuan Yang.

Finally, I dedicate this thesis to my wife Lin Ding for all her sacrifices during my study and writing-up. Without her encouragement and support, nothing would have been happened.

Abstract

The motivation of this thesis is to better understand the characteristics of Semiconductor Optical Amplifiers (SOAs) and their use in the Passive Optical Networks (PON), particularly in packet equalisation.

Following an introduction to physical principles and structure of SOAs the architecture of optical communication system especially PON is explained. The basic characteristics and key applications of SOAs are then discussed.

In this study, the modelling of SOAs has been achieved at both system and device levels. In terms of high efficient system level SOA model, both co-propagation and counter-propagation models are employed to study the cross gain modulation of SOAs. The co-propagation system model has also been used to study the gain compression effect of SOAs. The direct modulation frequency response of a SOA is also investigated numerically. Alternatively, the detailed device level SOA model, which includes a wideband material gain coefficient taking the intraband relaxation effect into account and an efficiency-improved steady state algorithm, is proposed to study the DC characteristics of SOAs.

Based on the detailed device level SOA model, the numerical model for the adjustable gain-clamped SOA (AGC-SOA) has been proposed to investigate both the steady state operation and the case where the gain of the AGC-SOA is dynamically modulated. Through theoretical analysis and experimental investigation, this study demonstrated that the gain of AGC-SOA would be dynamically modulated in response to the changes in packet amplitude in PONs.

Table of Contents

Table of Figures

Table of Abbreviations

ASE	Amplified Spontaneous Emission
CW	Continuous Wave
CAPEX	Capital Expenditure
EDFA	Erbium-Doped Fibre Amplifier
FWM	Four Wave Mixing
FBG	Fibre Bragg Grating
GVD	Group Velocity Dispersion
InGaAsP	Indium Gallium Arsenide Phosphide
InP	Indium Phosphide
MZI	Mach-Zehnder interferometer
MI	Michelson interferometer
MQW	Multiple Quantum Well
NPR	Nonlinear Polarization Rotation
OPEX	Operation Expenditure
OLT	Optical Line Terminal
ONU	Optical Network Unit
PON	Passive Optical Network
QD	Quantum Dot
SOA	Semiconductor Optical Amplifier
TDM	Time Division Multiplexing
WDM	Wavelength Division Multiplexing
XGM	Cross Gain Modulation
XPM	Cross Phase Modulation

Chapter 1 Introduction

1.1 Brief History of Optical Communications

Communication technology has been developing throughout the history of human civilisation. The fundamental thrust is that people have a principal need to communicate with each other [1]. Optical communication has been used as a key method for long distance communication ever since ancient times. The Great Wall of China was built in the fifth century BC. Many signal towers were built along the wall, normally upon hill tops, and used to warn garrisons of enemy movement or call reinforcements through the use of fire beacons. The fire beacons were lit to relay messages from these signal towers to the finally destination. However the on-off fire beacons could provide very limited data rate (about 1 bit/day). This method was improved by French inventor Claude Chappe until 1791 [2]. He proposed the visual (optical) telegraph system which could yield a 196-combination code, transmitting for distances up to 100 km.

In 1861, equations were derived and published by Scottish physicist and mathematician James Clerk Maxwell [3], describing the propagation of electromagnetic waves in free space. Maxwell's equations laid the foundation for electromagnetism and optics. In 1870, English physicist John Tyndall demonstrated that light could be conducted through a curved stream of water, which suggested that light can be confined and guided within a transparent material of high refractive index surrounded by low index material through the phenomenon of total internal reflection (TIR). However this phenomenon was not understood until Hondros and Debye analyzed dielectric waveguides in their studies of the propagation of radio waves in 1910 [4][5]. These early works provided the preliminary understanding of lightwave transmission which is vital for the modern optical communications.

In 1900, German physicist Max Planck introduced the concept of a quantum of energy [6][7], which triggered the study of the statistics of visible and infrared radiation. Without his groundbreaking theory, the laser, which generates a collimated beam of coherent light with sufficient power to work as a signal carrier in communications' system, could not have been invented. However, technological development in the field of optical communications did not show any significant advances until the middle of the twentieth century, when scientists began to utilise the concept of stimulated emission which introduced by physicist Albert Einstein in 1917 [8]. The first operational laser, based on ruby, was demonstrated by Theodore Maiman in 1960 [9]. Subsequently the first semiconductor (Gallium Arsenide, GaAs) laser was realised by Robert N. Hall in 1962 [10]. Soon the technique of modulating the laser's output by varying its driving current in response to a baseband signal was developed which, together with the realisation of the silicon photodiode detector, made the optical transmitter and receiver possible for a typical optical communications system. Later, after Zhores Alferov and Herbert Kroemer introduced the concept of semiconductor heterostructures, the first semiconductor laser operating at room temperature was realised [11]. This made such systems even more practical.

The last and major barrier for building optical communication systems was to find suitable transmission medium for the light. The breakthrough came in 1966 when Charles Kuen Kao and George Alfred Hockham of the Standard Telephone Laboratories (STL) suggested a glassy material fibre with a refractive index higher than its surrounding cladding as a possible practical optical waveguide with potential as a new form of communication medium [12]. They also predicted that a loss of 20 dB/km for the proposed fibre could be achieved provided that the iron-impurity concentration in the basic glass material of fibre was reduced to a sufficiently low level. The fibre attenuation threshold for viable optical communication was set at 20 dB/km, based upon the available laser power and typical detector sensitivity. At that time the lowest loss for an unclad, single component fused silica fibre was larger than 1000 dB/km. In 1970, Felix Kapron, Donald Keck, Robert Maurer of Corning Glass Works successfully produced the first glass fibre with a loss less than 20 dB/km through a chemical method called Chemical Vapor Deposition (CVD) [13]. Later they even achieved fibre loss of 4 dB/km for the optical carrier wavelength at 850 nm. Since then, research activities were focused to realise the first communication system.

The first generation of optical communication system was developed in the late 1970s, this was commercially available in 1980 [14][15]. The GaAs semiconductor laser operating near 850 nm and multimode graded-index fibre were deployed in the system which was capable of transmitting signal at a bit rate of 45 Mb/s with repeater spacing of up to 10 km. The repeater spacing was further improved by operating the optical communication system in the wavelength region around 1310 nm, within which not only the fibre loss could achieve 1 dB/km, but also the fibre dispersion reaches minimum. This prompted the development of the InGaAsP based light sources and photodectors functioning near 1310 nm. Then the second generation of optical communication system operating at 1310 nm was finally available in the early 1980. The research efforts were also made to improve the slow transmitting bit rate of the second generation system by applying single mode fibre in the system instead of multimode ones. This improvement enabled the system transmitting up to 1.7 Gb/s with a repeater spacing of around 50 km commercially available in 1987 [16].

As demonstrated in 1979 [17], the fibre loss could achieve 0.2 dB/km in the wavelength region near 1550 nm. However the dispersion problem within this wavelength region was severe. Until early 1980s, this obstacle was overcome either by deploying dispersion-shifted fibre which was engineered to provide minimum dispersion around 1550 nm or by using single longitudinal mode laser (practically distributed feedback semiconductor lasers, DFB). Thus the third generation of optical communication system was commercially available in 1990s. The system could operate at a bit rate up to 10 Gb/s over distances up to 100 km [18].

The advent of erbium doped optical fibre amplifier (EDFA) [19] and wavelength division multiplexing (WDM) technique [20] bought the optical communication system into the fourth generation, as its repeater spacing and supporting bit rate were increased significantly. The optical fibre amplifier enables in-line amplification in the optical domain instead of using electronic repeaters as in the last generation of system. In 1991, the data transmission distance achieved 21,000 km at 2.4 Gb/s and 14, 300 km at 5 Gb/s in a fibre amplifier system using a circulating loop configuration [21]. On the other hand, the WDM technique was designed to exploit the capacity of the optical fibre by transmitting several optical signals operating at different wavelengths simultaneously over the same fibre. The WDM technique, dispersion management, the use of rare-earth doped optical fibre amplifiers (PDFA, TDFA and EDFA), and Raman amplification lifted the system capacity to a new level. In 2001, an experiment demonstrated the system capacity could reach 10.92 Tb/s (273 WDM channels, each at 40 Gb/s) over 117 km [22]. Thereafter, the research efforts were focused on improving the spectral efficiency of the WDM system using advanced modulation schemes. The spectral efficiency has been increased from below 0.8 b/s/Hz [23][24] for the typical fourth generation system to more than 8 b/s/Hz [25], and the bit rate per channel has been increased from below 40 Gb/s to more than 100 Gb/s [26]. Although the 100 Gb/s per channel optical transmission is at the beginning of commercialisation and deployment stage by now, the network supporting bit rate per channel at a speed of 400 Gb/s or 1 Tb/s has attracted more attentions of research community [27][28]. To achieve fibre capacity higher than 1 Tb/s (per channel), the Kerr nonlinearity of the fibre which limits the optical power level launched, should be reduced [29]. Thus, spatial multiplexing techniques such as multicore fibres (MCF) [30] and multimode fibres (MMF) [31] are proposed to further boost the fibre capacity to 100 Tb/s and beyond.

1.2 Thesis Overview

Chapter 2 introduces the physical principles and structure of semiconductor optical amplifiers. Firstly, the basic two-level system is used to explain the optical amplification process in the laser medium, and demonstrates that population inversion should be obtained in the material in order to achieve optical amplification. Then the p-n junction and heterojunction are studied to show how population inversion is achieved in semiconductor lasers. Secondly, the $In_{1-x}Ga_xAs_yP_{1-y}/InP$ heterojunction system, which is widely used in optical sources, amplifiers and photodetectors in long distance optical communication system, is introduced. An interpolation scheme is also studied to demonstrate that physical properties such as the lattice constant and energy band gap of the active material $In_{1-x}Ga_xAs_yP_{1-y}$ can be engineered by varying the material composition. The four band model is used to further study the photon generation in this III-V direct gap semiconductor. The expressions of quasi-Fermi level, material gain coefficient, and spontaneous emission rate for a SOA are deduced. Finally, the structure of a SOA is discussed through an example of a typical double heterostructure SOA. The impact of facet reflectivity in a SOA and a RSOA are then numerically studied. The techniques which are widely used in reducing the facet reflectivity, such as antireflection coating, angled facet and window facet, are then detailed. The numerous simulation demonstrations of physical coefficients are the main innovation and contribution in this chapter.

Chapter 3 reviews key elements, techniques and architectures of the optical communication system, especially the promising candidate for the future optical access network - passive optical network (PON) systems. Firstly, the point-to-point fibre link is introduced to demonstrate the basic architecture and components in the communication system. Then the characteristics of key elements such as fibre, optical amplifiers, optical sources and detectors are studied. Thirdly, by reviewing the optical networks hierarchy, the first/last mile problem is raised, since the twisted copper pair based traditional access networks can no long meet the end users' bandwidth demand. Thus the typical architecture, advantages and worldwide deployment status of the PON are discussed. PON technologies are divided into Time Division Multiplexing TDM-PON and WDM-PON and discussed separately in this chapter. The channel sharing mechanismspecifications of current commercially available TDM-PONs are introduced, and the design issues regarding the high speed fast response burst mode receiver (BMR) with wide dynamic range are reviewed. The WDM-PON enjoys many advantages compared to the current TDM-PON technologies although it faces many challenges in deployment. Therefore many proposals have been introduced to tackle these problems especially the realisation of the colourless Optical Network Unit (ONU) operation and the hybrid WDM/TDM PON. The last part of the chapter discusses the use of semiconductor optical amplifiers in the PON system. SOA based amplified PONs and reflective SOA based WDM-PONs have been reviewed.

Chapter 4 discusses some basic characteristics and key applications of SOAs. Firstly, through analytical expression deduction, the SOA gain and saturation, noise figure have been discussed. The expressions obtained in this chapter will be used in analyzing SOA and Adjustable Gain Clamped (AGC)-SOA performance in the next two chapters. Secondly, the SOA dynamics is also introduced, specifically the intraband dynamics are reviewed. Finally, the applications of SOAs are divided into linear amplification and optical signal processing which is largely taking advantage of SOA's nonlinearities, i.e. cross gain modulation, cross phase modulation, four-wave mixing and nonlinear polarization rotation effects. In each nonlinear effect, the physical origin is shortly discussed, and its applications in optical signal processing are then briefly introduced. The literature review of the nonlinear polarization rotation effects in SOAs and its applications, is the main innovation in this chapter.

Chapter 5 introduces and discusses two numerical models for studying the characteristics of SOAs, namely system level and device level SOA models. Initially, the classification of SOA theoretical models is presented and two basic equations, the propagation equation and carrier density rate equation, which are employed in both system and device level models, are derived., The propagation equation has been compared with ones in other publications and the underlying consistency has been proved. Based on these equations, the system level model has been introduced and applied into studying all optical wavelength conversion using a SOA. Depending on travelling directions of the pump and probe lights, the system model has been classified into co-propagation and counter-propagation models. Simulated wavelength conversion, achieved by cross gain modulation (XGM) in the SOA, has been performed in both co-propagation and counter-propagation models. The co-propagation system model has also been employed to numerically study the gain compression effect of the SOA. It is clear that the model is demonstrating similar dynamic behaviour to that observed experimentally, which proves the model is capable of studying the characteristics of SOAs. The direct modulation response of a SOA is investigated using a modified system level model. The numerical results show that increasing the length of the active region or unsaturated material gain coefficient would improve the modulation response of the device.

The remainder of the chapter discusses the device level SOA model. It starts with a review of the material gain coefficient for a semiconductor optical device. An improved material gain expression is introduced, which is based on the wideband material gain expression defined from Fermi's Golden rule. It also takes the intraband relaxation effect into consideration. Then the detailed device level model is introduced. The propagation equation for ASE in the SOA, and an efficiency improved steady-state numerical algorithm are discussed. Based on this detailed wideband model, steady-state gain characteristics of SOA is studied, and the output saturation power P_{sat} is discussed. The output ASE spectrum under different bias currents is also simulated.

The main innovations in Chapter 5 are the proposed improved material gain coefficient for bulk SOAs, and the improved high efficiency algorithm employed in the device level SOA model.

In Chapter 6 a theoretical analysis of an AGC-SOA is presented. Both the steady state operation and the case where the gain of the AGC-SOA is dynamically modulated are addressed. The DC parametric behaviour is shown to agree well with experimental measurements. An adaptation of the models has shown that in principle, the gain of the AGC-SOA can be regulated dynamically to respond within the guard band of packet based PON transmissions. Gain settling times within the order of 2 ns are predicted. This analysis was shown to agree well with experimental evaluation of the AGC-SOA behaviour which demonstrated gain modulation and settling within two bit periods of a 1.25 Gbit/s data signal.

A key motivation for this study was to better understand the dynamic behaviour of the AGC-SOA with a view to establishing a means for dynamically modulating the gain of the AGC-SOA in response to changes in packet amplitude. For this to be effective, the gain should be adjusted and stabilised within a timespan of less than 20 ns. Both the theoretical analysis and the experimental investigation indicate that it is possible.

In this chapter, the detailed numerical model for the Adjustable Gain-Clamped SOA (AGC-SOA) has been proposed for the first time, and the dynamic gain modulation performance of AGC-SOA has been studied both numerically and experimentally. These are the main innovations associated with the chapter.

Chapter 7 summarises the thesis, and introduces the future work.

1.3 Summary of Contributions

1. An improved material gain coefficient for bulk SOAs has been proposed;
2. Co-propagation and counter-propagation system level SOA models have been developed to provide high efficiency processing;
3. The small-signal modulation performance of SOA has been theoretically studied;
4. The device level steady-state SOA model has been optimized to achieve higher processing efficiency;
5. The numerical model for the Adjustable Gain-Clamped SOA (AGC-SOA) has been proposed for the first time;
6. The dynamic gain modulation performance of AGC-SOA has been studied both numerically and experimentally.

List of publications related to the thesis:

1. Lin Liu, Craig Michie, Anthony E. Kelly, and Ivan Andonovic, "Detailed theoretical model for adjustable gain-clamped semiconductor optical amplifier," International Journal of Optics, vol. 2012, no. 764084, doi:10.1155/2012/764084, Feb 2012.
2. Lin Liu, Craig Michie, Anthony E. Kelly, and Ivan Andonovic, "The dynamic gain modulation performance of adjustable gain-clamped semiconductor optical amplifiers (AGC-SOA)," Journal of Lightwave Technology, vol. 29, no. 22, pp. 3483-3489, doi:10.1109/JLT.2011.2171669, Nov 2011.

3. Lin Liu, Craig Michie, Anthony E. Kelly, and Ivan Andonovic, “Analysis of packet equalisation in PONs using adjustable gain-clamped semiconductor optical amplifiers (AGC-SOA),” 13th International Conference on Transparent Optical Networks (ICTON), doi: 10.1109/ICTON.2011.5970944, Stockholm, Jun 2011. (Invited).
4. Lin Liu, Craig Michie, Anthony E. Kelly, and Ivan Andonovic, “Packet equalisation in PONs using adjustable gain-clamped semiconductor optical amplifiers (AGC-SOA),” Photonics Global Conference, doi: 10.1109/PGC.2010.5705985, Singapore, Dec 2010.
5. Lin Liu, Craig Michie, Anthony E. Kelly, and Ivan Andonovic, “Numerical analysis of adjustable gain-clamped semiconductor optical amplifiers (AGC-SOA) performance,” 12th International Conference on Transparent Optical Networks (ICTON), doi:10.1109/ICTON.2010.5549318, Munich, Jul 2010.
6. Craig Michie, Anthony E. Kelly, Lin Liu, Ivan Andonovic and Wende Zhong, “Semiconductor optical amplifiers in future passive optical networks,” International Conference on Information, Communications and Signal Processing (ICICS), doi:10.1109/ICICS.2009.5397489, Macau, Dec 2009.

Chapter 2 Introduction to Semiconductor Optical Amplifiers

A semiconductor optical amplifier is a specially designed semiconductor laser operating under its threshold [1]. Most importantly, the optical feedback has been removed from the construction of a semiconductor laser, which enables the SOA to become Travelling Wave (TW) amplifier, which is more practical. Early studies on SOAs date back to 1960's when the first semiconductor laser was invented.

2.1 Basic Principles in Semiconductor

The essential principle of the optical amplification process in semiconductor lasers is the interaction of electromagnetic radiation with semiconductor lasing materials. In order to understand the basic principle of optical amplification in semiconductor optical amplifiers, the simple two-level system is shown in Figure . This basic system is adequate to display the physical processes that take place inside gas, solid state lasers or amplifiers [32].

2.1.1 Optical Amplification Process

InFigure 2.1, the atoms of the material have two discrete energy levels namely E_1 and E_2 ($E_2 > E_1$). N_1 and N_2 are the numbers of atoms per unit volume in these energy states, also known as population densities. When a beam of light travels through this material, the photons may interact with material to exchange energy. There are three ways in which energy exchange can take place: spontaneous emission, absorption and stimulated emission.

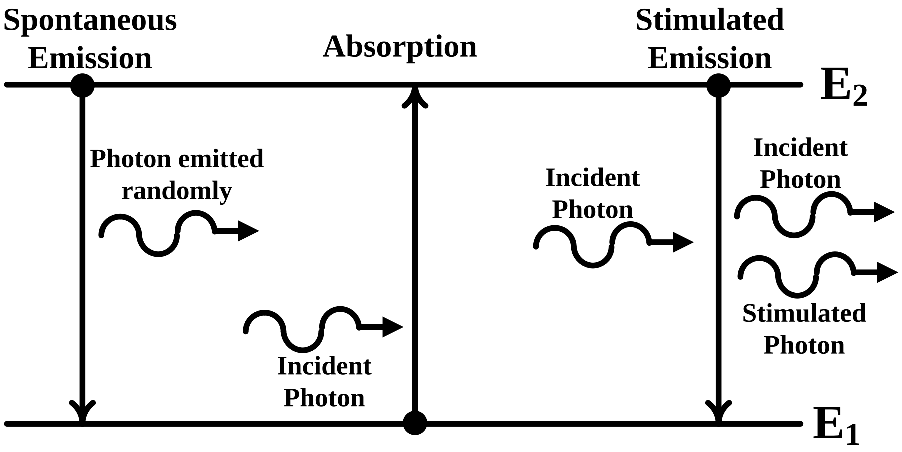

Figure 2.1 Schematic optical processes in a two level system

The spontaneous emission process means an electron within an atom in energy level E_2 makes the transition to energy level E_1 by releasing a photon of energy

$$E_{photon} = E_2 - E_1 = h\nu = h\frac{c}{\lambda} \tag{2.1}$$

where h is Plank's constant, c is the speed of light, ν and λ are the frequency and wavelength of the emitted photon respectively. Spontaneous emission is a random process, which implies that the photon may be emitted in any direction and phase. The rate of photon emission is proportional to the population density in energy level E_2.

$$r_{spon} = A_{21}N_2 \tag{2.2}$$

where A_{21} is the proportionality constant for spontaneous emission.

A photon which is incident on the material may be absorbed by an atom in the energy level E_1, and the absorbed photon energy $E_{photon} = E_2 - E_1$ enables the electron of an atom to be transited to the energy level E_2. The rate of absorption is proportional to the population density in energy level E_1 and the incident photon energy density $\rho(\nu)$ at frequency ν,

$$r_{abs} = B_{12}N_1\rho(\nu) \tag{2.3}$$

where B_{12} is the proportionality constant for absorption

The incident photon of energy $E_{photon} = E_2 - E_1$ may also stimulate an electron of an atom in energy level E_2 to transit to energy level E_1 by emitting a photon with same energy, direction, phase and polarisation as the incident photon. This process is stimulated emission, and its rate is proportional to the population density in energy level E_2 and the incident photon energy density $\rho(\nu)$ at frequency ν:

$$r_{stim} = B_{21} N_2 \rho(\nu) \tag{2.4}$$

where B_{21} is the proportionality constant for stimulated emission

Among these three ways of electron-photon interaction, only stimulated emission will result in optical amplification, i.e. the rate of stimulated emission should be greater than the rate of absorption.

$$r_{stim} > r_{abs} \tag{2.5}$$

Which equals to

$$B_{21} N_2 > B_{12} N_1 \tag{2.6}$$

It can be proved from quantum theory [33], in thermal equilibrium that

$$B_{21} = B_{12} \tag{2.7}$$

thus, $N_2 > N_1$ is the requirement for achieving optical amplification. According to the Boltzmann distribution, in thermal equilibrium, population density in the lower energy level is larger than higher energy level.. Therefore achieving optical amplification is to realise the population inversion in the material.

2.1.2 *p-n* Junctions

In practice, population inversion is achieved in a forward biased *p-n* junction. A semiconductor can be p doped by adding acceptor atoms to increase the number of positive holes, similarly an n-type semiconductor is obtained by adding donor atoms to increase the number of negative electron charge carriers. A *p-n* junction is formed by putting p-type and n-type material together. Forward biasing of a *p-n* junction with positive potential applied to the p side and negative potential to the n side results in a significant reduction of the potential step across the junction compared to unbiased case (thermal equilibrium). This is depicted in Figure 2.2 below.

The light is generated when electrons and holes respectively transit from a donor-doped (i.e., n-type) region and an acceptor-doped (i.e., p-type) region of a semiconductor to the junction depletion region, where the recombination process takes place.

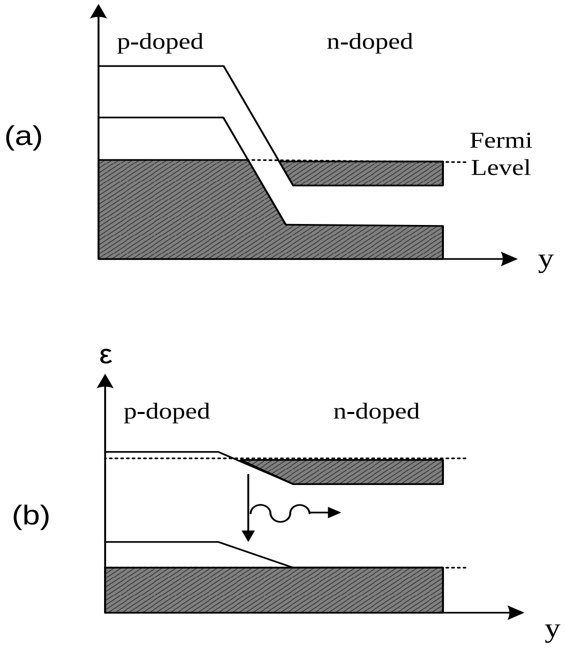

Figure 2.2 Electron energy and occupation perpendicular to the p-n junction plane under the condition of (a) thermal equilibrium and (b) forward biased applied voltage

2.1.3 Heterojunctions

The *p-n* junction is a simple structure to realise photon generation, however this kind of structure is incapable of trapping the carriers in the junction region to increase the probability of electron-hole recombination, so as to improve light generation efficiency. A *p-n* junction is formed between layers of similar materials with different doping, the energy band gap of these materials are the same. This kind of junction is called homojunction. When two semiconductors with different energy gaps are combined, a heterojunction is formed. The conductivity type of the smaller energy gap material is denoted by n or p and the larger energy gap one is denoted by N or P.

Nowadays semiconductor lasers are all fabricated with heterostructures in order to achieve the low thresholds for CW or room temperature operation. And the heterostructure widths can be chosen to produce bulk or quantum-well gain medium [34]. If the heterostructure width is significantly greater than the de Broglie wavelength of carriers, the device is defined as a bulk structure. When the width is one or several orders of the de Broglie wavelength of carriers, the device is a quantum-well structure.

A double heterojunction device is fabricated with a thin layer (active layer) sandwiched between p and n layers. The active layer has a smaller energy gap and consequently a larger refractive index than the adjacent p and n layers. This feature serves to confine both carriers and photons in the active layer, so the photon generation efficiency will be further improved, and the light will be better guided through the device. The typical SOA structure is based on the anti-reflection coated double heterostructure semiconductor laser diode, this will be further discussed in section 2.3.

The active layer can be either doped or undoped, however, its lattice constant must match to that of the surrounding materials. This is usually achieved by using a ternary or quaternary compound semiconductor as the active layer material. According to Vegard’s law, the crystal lattice parameter is linearly dependent on the concentrations of the constituent elements [35]. Therefore, varying alloy composition, i.e. controlling the mole fractions of different atoms in the semiconductor compound makes lattice matching feasible.

2.2 Materials and Structures for SOA

In optical communication systems, the $In_{1-x}Ga_xAs_yP_{1-y}/InP$ heterojunction system can be widely used in light sources, optical amplifiers and photodetectors. For example, the $In_{1-x}Ga_xAs_yP_{1-y}/InP$ double heterojunction lasers emit in the 1.3 – 1.7 µm wavelength range, within which the low attenuation, low dispersion optical fibre is functioning. This feature makes $In_{1-x}Ga_xAs_yP_{1-y}/InP$ laser an ideal light source in long-distance fibre optic communications. Similarly, by varying the composition of the active

$In_{1-x}Ga_xAs_yP_{1-y}$ material, the gain peak of a semiconductor optical amplifier can be chosen from 1.28 μm in the O-band to 1.65 μm in the U-band [1].

2.2.1 Physical Properties for Semiconductor Compounds

As discussed before, in order to form a heterojunction, the lattice constant of the active layer material $In_{1-x}Ga_xAs_yP_{1-y}$ should match that of surrounding material InP. At room temperature (300K), the lattice constant of InP is $a_0 = 5.8688$ Å. And the lattice constant of $In_{1-x}Ga_xAs_yP_{1-y}$ can be obtained using an interpolation scheme based on a general principle of simplicity [36].

$$\begin{aligned} a_0\left(In_{1-x}Ga_xAs_yP_{1-y}\right) \\ &= (1-x)ya_0(InAs) + x(1-y)a_0(GaP) \\ &+ xya_0(GaAs) + (1-x)(1-y)a_0(InP)\ \text{Å} \end{aligned} \tag{2.8}$$

Where the lattice constants for binary compounds $InAs$, GaP, $GaAs$ are 6.0584Å, 5.4512Å, 5.6533Å, respectively [37]. Then the expression can be simplified as

$$\begin{aligned} a_0\left(In_{1-x}Ga_xAs_yP_{1-y}\right) \\ &= 5.8688 - 0.4176x + 0.1896y + 0.0125xy\ \text{Å} \end{aligned} \tag{2.9}$$

The lattice matching requires

$$a_0\left(In_{1-x}Ga_xAs_yP_{1-y}\right) = a_0(InP) = 5.8688\ \text{Å} \tag{2.10}$$

Thus the relation between mole fractions x and y required by lattice matching $In_{1-x}Ga_xAs_yP_{1-y}$ to InP is

$$x = \frac{0.1896y}{0.4176 - 0.0125y} \qquad (0 \le y \le 1) \tag{2.11}$$

This equation can be also approximated as [38]

$$x = 0.47y \qquad (0 \le y \le 1) \tag{2.12}$$

The general interpolation formula for quaternary compound parameters used in Equation 2.8 can be also transformed to obtain the energy band gap expression of the compound.

$$\begin{aligned} E_g\left(In_{1-x}Ga_xAs_yP_{1-y}\right) &= (1-x)yE_g(InAs) + x(1-y)E_g(GaP) \\ &+ xyE_g(GaAs) + (1-x)(1-y)E_g(InP)\ \ eV \end{aligned} \tag{2.13}$$

E_g denotes energy band gap. Using the band gaps of binary compounds $InAs$, GaP, $GaAs$ and InP at room temperature (300K) and the composition fractions relation Equation 2.11, the energy band gap at 300K for $In_{1-x}Ga_xAs_yP_{1-y}/InP$ heterojunction system are found to be [39]

$$E_g(y) = 1.35 - 0.775y + 0.149y^2 \ \ eV \tag{2.14}$$

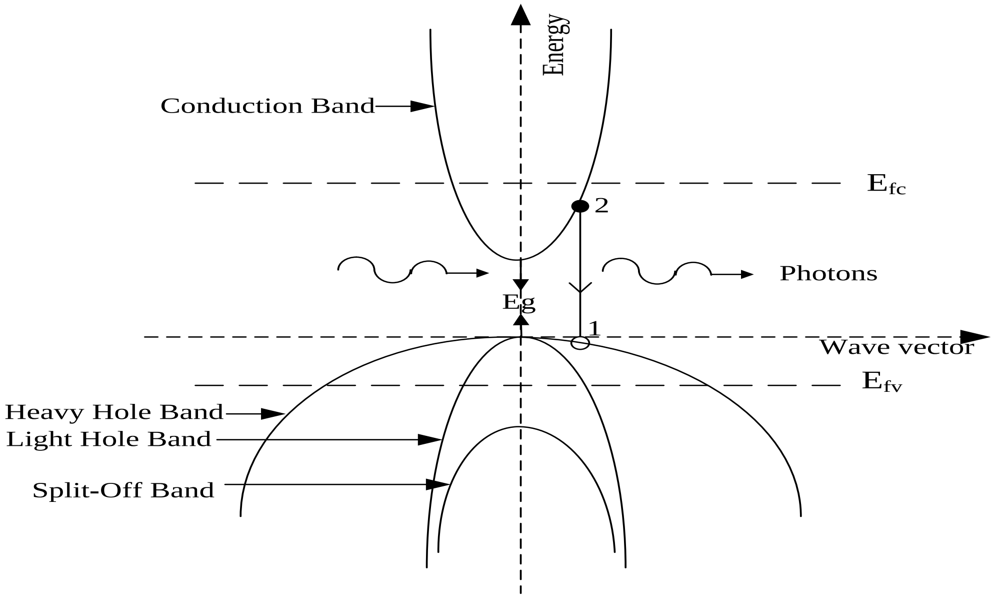

Figure 2.3 Typical four band energy band structure of a direct bandgap semiconductor

2.2.2 Photon Generation

2.2.2.1 The Fermi-Dirac Distribution

Figure 2.3 depicts energy versus wave vector diagram for a direct band gap semiconductor. The horizontal axis of the figure represents the wave vector ($\boldsymbol{k}$) of an electron. And the energy of an electron is depicted in the vertical axis. This four-band model [40] is a realistic band model for a III-V direct gap semiconductor. In this model, there is one conduction (unoccupied) band and three valence (occupied) subbands, the valence band is consist of three subbands: heavy hole (HH) band, light hole (LH) band and split-off (SO) band. The zero of energy is chosen to be the top of valence band. The heavy hole and light hole band is degenerate at $\boldsymbol{k} = 0$. The energy of an electron in the conduction band (E_c) is defined to be positive when measured upward from the zero of energy point, from where the hole energy in the valence band (E_v) is positive when measured downward.

$$E_c = \frac{\hbar^2 k^2}{2m_c} \tag{2.15}$$

$$E_v = \frac{\hbar^2 k^2}{2m_v} \tag{2.16}$$

ħ is reduced Planck constant, which equals to $\frac{h}{2\pi}$, k is the magnitude of the wave vector, m_c is the effective masses of electrons in conduction band and m_v is the effective masses of holes in valence band. As depicted in Figure 2.3, there are two sets of hole subbands in the valence band, since these holes have different effective masses. m_{hh} and m_{lh} is the effective masses of holes in the heavy and light hole subbands, respectively. And m_{hh} is greater than m_{lh}. According to Equation 2.16, the $E - k$ relationship can be treated as parabolic near the band edge. And the curvature of the parabolic band in the $E - k$ diagram is defined as $\frac{d^2E}{dk^2}$, which is given:

$$\frac{d^2E}{dk^2} = \frac{\hbar^2}{m^*} \tag{2.17}$$

where m^* is the associated effective mass. Equation 2.17 shows that, the curvature of the parabola is inversely proportional to the associated effective mass. Therefore, the heavy hole band which has larger effective masses, is wider than the light hole band in the k axis.

The probability of finding an electron at an energy E_c is given by Fermi-Dirac statistics:

$$f_c(E_c) = \frac{1}{1 + \exp\left[(E_c - E_{fc})/k_{\boldsymbol{B}}T\right]} \tag{2.18}$$

E_{fc} is the quasi-Fermi level for the conduction band, $k_{\boldsymbol{B}}$ is Boltzmann constant, T is for temperature. Similarly, the probability of a hole with energy E_v is

$$f_v(E_v) = \frac{1}{1 + \exp\left[(E_v - E_{fv})/k_{\boldsymbol{B}}T\right]} \tag{2.19}$$

E_{fv} is the quasi-Fermi level for the valence band.

The density of states in each band is given by [41], thus the density of states in conduction band $\rho_c(E)$ and valence band $\rho_v(E)$ are

$$\rho_c(E) = \frac{1}{2\pi^2} \cdot \left(\frac{2m_c}{\hbar^2}\right)^{3/2} \cdot E^{1/2} \tag{2.20}$$

$$\rho_v(E) = \frac{1}{2\pi^2} \cdot \left(\frac{2m_v}{\hbar^2}\right)^{3/2} \cdot E^{1/2} \tag{2.21}$$

The number of electrons in the conduction band n

$$n = \int_0^\infty \rho_c(E)\ f_c(E)dE = \frac{1}{2\pi^2} \cdot \left(\frac{2m_c}{\hbar^2}\right)^{\frac{3}{2}} \int_0^\infty \frac{E^{\frac{1}{2}}}{1+\exp\left[\frac{E-E_{fc}}{k_{\boldsymbol{B}}T}\right]} dE \tag{2.22}$$

The number of holes in the valence band p

$$p = \int_0^\infty \rho_v(E)\ f_v(E)dE = \frac{1}{2\pi^2} \cdot \left(\frac{2m_v}{\hbar^2}\right)^{\frac{3}{2}} \int_0^\infty \frac{E^{\frac{1}{2}}}{1+\exp\left[\frac{E-E_{fv}}{k_{\boldsymbol{B}}T}\right]} dE \tag{2.23}$$

The quasi-Fermi level, E_{fc} and E_{fv}, are found from the following empirical expressions [42]:

$$E_{fc} = \ln\left(\frac{n}{n_c}\right) k_{\boldsymbol{B}}T + \frac{\left(\frac{n}{n_c}\right) k_{\boldsymbol{B}}T}{\left[64 + 0.05524\left(\frac{n}{n_c}\right)\left(64 + \sqrt{\frac{n}{n_c}}\right)\right]^{\frac{1}{4}}} \tag{2.24}$$

$$E_{fv} = \ln\left(\frac{p}{n_v}\right) k_{\boldsymbol{B}}T + \frac{(\frac{p}{n_v})k_{\boldsymbol{B}}T}{[64 + 0.05524(\frac{p}{n_v})(64 + \sqrt{\frac{p}{n_v}})]^{\frac{1}{4}}} \tag{2.25}$$

Where n_c and n_v are the effective number of states in the conduction and valence band, which are given:

$$n_c = 2(\frac{m_c k_{\boldsymbol{B}}T}{2\pi\hbar^2})^{\frac{3}{2}} \tag{2.26}$$

$$n_v = 2(\frac{k_{\boldsymbol{B}}T}{2\pi\hbar^2})^{\frac{3}{2}}(m_{hh}^{\frac{3}{2}} + m_{lh}^{\frac{3}{2}}) \tag{2.27}$$

m_{hh} and m_{lh} are the effective masses of heavy hole and light hole in the valence band, respectively. As can be seen, quasi-Fermi levels depend on the carrier densities and the temperature. For a given carrier density, in a bulk InGaAsP material (parameters as shown in Table 1), the quasi-Fermi level can be plotted as a function of carrier density.

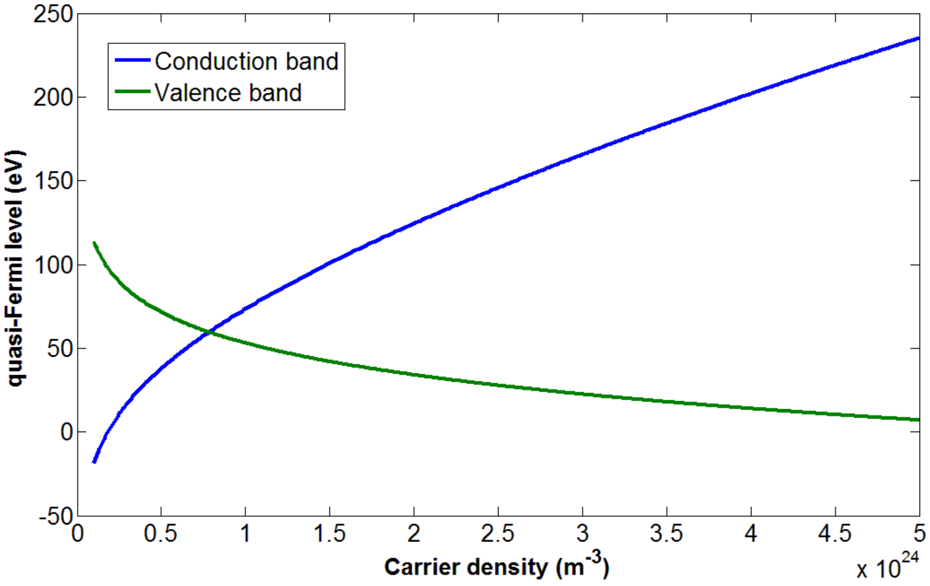

Figure 2.4 quasi-Fermi level as a function of carrier density in conduction band and valence band

2.2.2.2 Optical Gain and Absorption

As depicted in Figure 2.1, an optical beam is incident on the semiconductor material. This beam may induce transitions between an electronic state in conduction band (2) and an electronic state in valence band (1). The transitions consist of downward (2 to 1) and upward (1 to 2) transitions. The downward transition results in optical amplification and the upward leads to absorption as discussed in section 2.1.1. Only if the rate of downward transition exceeds that of upward will bring the net amplification to the incoming optical beam.

The downward transition will happen when the conductive state is occupied and the valence state is empty, that is to say, the downward transition rate is proportional to

$$R_{2\rightarrow 1} \propto \; f_c(E_2)[1 - \; f_v(E_1)] \tag{2.28}$$

Similarly, the upward rate is proportional to

$$R_{1\rightarrow 2} \propto \; f_v(E_1)[1 - \; f_c(E_2)] \tag{2.29}$$

Thus, it can be concluded, as discussed in section 2.1.1, the population inversion density $(N_2 - N_1)$ is proportional to the product of density of states function and the probability of net amplification.

$$\begin{aligned} N_2 - N_1 \rightarrow \; & \rho(E)dE\{f_c(E_2)[1 - \; f_v(E_1)] - \; f_v(E_1)[1 - \; f_c(E_2)]\} \\ = \; & \frac{\rho(k)dk}{V}[f_c(E_2) - \; f_v(E_1)] \end{aligned} \tag{2.30}$$

The conventional laser gain constant [41] can be expressed as

$$g(\omega_0) = \frac{(N_1 - N_2)\lambda_0^2\, T_2}{4\pi^3 t_{spon}[1 + (\omega - \omega_0)^2 T_2^2]} \tag{2.31}$$

This is calculated from the imaginary part of the linear susceptibility. In the expression, T_2 is the mean time for interaction of electrons with a monochromatic field, and t_{spon} is spontaneous lifetime which can be replaced by the radiative carrier recombination lifetime τ (see section 2.2.2.4) for an electron in the conduction band with a hole in the valence band.

After a series of numerical derivations [41], the material gain coefficient is given

$$g_m(\omega_0) = \frac{\lambda_0^2}{8\pi^2 \tau n_1^2} \left(\frac{2m_c m_v}{\hbar(m_c + m_v)} \right)^{\frac{3}{2}} \left(\omega_0 - \frac{E_g}{\hbar} \right) [f_c(\omega_0) - f_v(\omega_0)] \tag{2.32}$$

Where ω_0 is optical angular frequency, λ_0 is optical light wavelength, n_1 is active region refractive index. By using the parameters given by Table 1, for a given carrier density $n = 1.2 \times 10^{24}\ m^{-3}$, the gain coefficient spectrum for SOA can be calculated, as depicted in Figure 2.5.

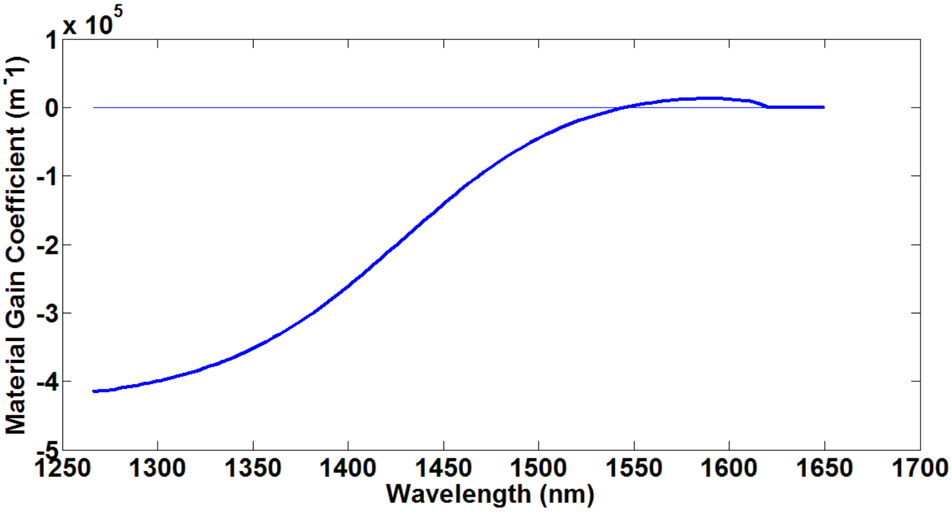

Figure 2.5 Gain coefficient for a typical bulk InGaAsP SOA (the horizontal line y=0 functions as a reference)

2.2.2.3 Spontaneous Emission

As discussed in the last section, the population inversion density $(N_2 - N_1)$ is proportional to the probability of optical gain. However this population inversion would inevitably bring in spontaneous emission, which is the dominant noise in the SOA.

Based on the results of last section, the gain coefficient $g'(\omega_0)$ can be obtained by replacing the factor $f_c(\omega_0) - f_v(\omega_0)$ in Equation 2.31 by $f_c(\omega_0)[1 - f_v(\omega_0)]$, this is related to the stimulated transition from the conduction band to the valence band.

$$g'(\omega_0) = \frac{\lambda_0^2}{8\pi^2\tau n_1^2}\left(\frac{2m_c m_v}{\hbar(m_c+m_v)}\right)^{\frac{3}{2}}\left(\omega_0 - \frac{E_g}{\hbar}\right) f_c(\omega_0)[1-f_v(\omega_0)] \tag{2.33}$$

The spontaneous transitions from the conduction band to the valence band have the same spectral shape as $g'(\omega_0)$.

The spontaneous emission rate $r_{sp}(E)$, or the number of emitted photons per unit volume per second per unit energy interval ($m^{-3}s^{-1}J^{-1}$) is given by [43].

$$r_{sp}(E) = \left(\frac{8\pi n_1^2 E^2}{h^3 c^2}\right) g'(E) \tag{2.34}$$

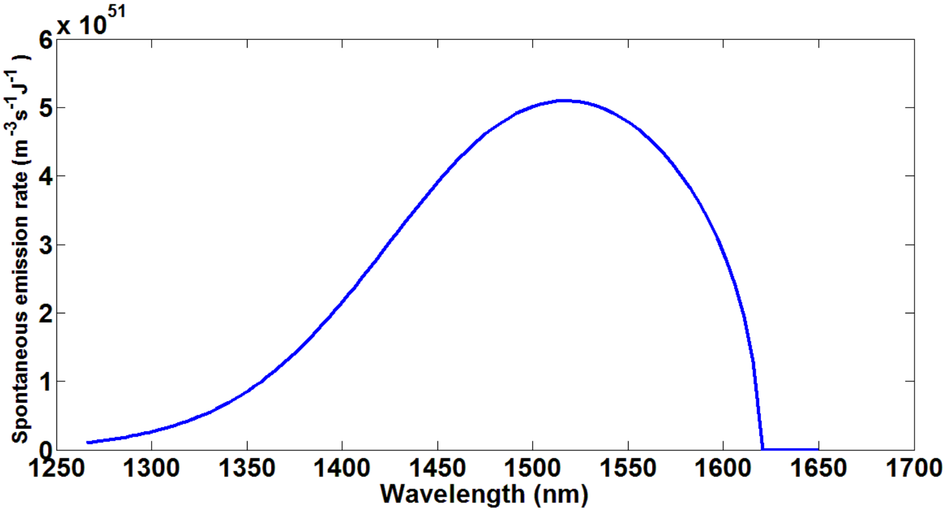

Figure 2.6 Typical plot of the spontaneous emission rate versus wavelength in a bulk InGaAsP SOA (carrier density $\boldsymbol{n = 1.2 \times 10^{24}\ m^{-3}}$*).*

Accordingly, the material gain coefficient in [43] is calculated from the spontaneous emission spectrum, which is quite different from the one discussed in Section 2.2.2.2. Based on these existing expressions discussed in this section, the improved material gain and spontaneous emission rate expressions for bulk semiconductor will been proposed in Chapter 5. And the comparison will also be provided.

2.2.2.4 Carrier Recombination

The processes of spontaneous emission, stimulated emission and absorption are all associated with photon emission during the electron-hole recombination in a direct-bandgap semiconductor. This kind of recombination mechanism is called radiative recombination. On the contrary, nonradiative recombination is characterized by the absence of an emitted photon in the electron-hole recombination process. There are some important nonradiative recombination processes: Auger recombination, surface recombination, and recombination at defects.

The expression for the spontaneous emission rate (Equation 2.34) is useful in calculating the current required to provide a given gain. However, it is too cumbersome for processing. Thus a simple analytical approximation for spontaneous radiative recombination rate using bimolecular recombination expression is given [44].

$$R_{rad} = A_{rad}N + B_{rad}N^2 \tag{2.35}$$

N is the carrier density, A_{rad} and B_{rad} are the linear and bimolecular recombination coefficients. The radiative carrier recombination lifetime τ used in the material gain coefficient expression, can be obtained by:

$$\tau = \frac{N}{R_{rad}} = (A_{rad} + B_{rad}N)^{-1} \tag{2.36}$$

Nonradiative recombination is the dominant recombination mechanisms in an SOA under high drive currents, with Auger recombination being the most dominant nonradiative recombination process, And is significant when the carrier density is high. The rate for Auger recombination is provided, C_{aug} is the Auger recombination coefficient.

$$R_{aug} = C_{aug}N^3 \tag{2.37}$$

The nonradiative recombination rate for defect (traps) and surface effects is described as R_{tr}:

$$R_{tr} = A_{tr}N \tag{2.38}$$

Excluding the recombination rate for stimulated processes, the total carrier recombination rate R is

$$R = R_{rad} + R_{nrad} = (A_{rad}N + B_{rad}N^2) + (A_{tr}N + C_{aug}N^3) \tag{2.39}$$

Depending on the requirement of the modelling accuracy, the nonradiative recombination mechanism caused by carrier leakage can be added to the above equation [45].

The carrier lifetime can be approximated using Equation 2.39 as:

$$\tau_c = (\frac{dR}{dN})^{-1} = \frac{1}{A_{tr} + A_{rad} + 2B_{rad}N + 3C_{aug}N^2} \tag{2.40}$$

Using the coefficients A_{tr}, A_{rad}, B_{rad}, and C_{aug} listed in Table 1, the total carrier recombination rate R (not including stimulated processes) and carrier lifetime τ_c are plotted as a function of carrier density in the active region of a SOA (Figure 2.7). As carrier density increases, for example, increasing the bias current applied on the SOA, the carrier recombination rate is rising and resulting in the shorter carrier lifetime. It also shows the carrier lifetime is varies from hundreds of picoseconds to nanoseconds. The carrier lifetime fall in this range will possibly incur the transient gain variation when the SOA is used to amplify the signal at Gigabit per second data rates. Since the signal speed is too fast to let the SOA provide each data bit with the same gain, the patterning effects will be introduced then the bit error rate (BER) of the traffic after amplification will deteriorate. In SOAs, the carrier lifetime also refers to gain recovery time, and it can be experimentally characterised by a pump-probe measurement [46][47].

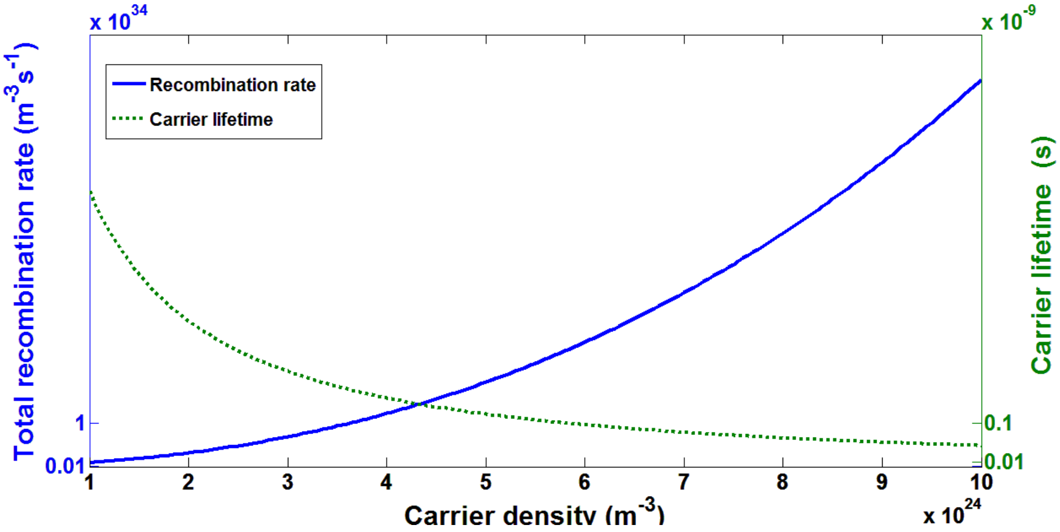

Figure 2.7 Total recombination rate (solid line) and carrier lifetime (dotted line) versus carrier density.

If an external optical light is injected into the SOA, stimulated emission will dominate the carrier recombination. Therefore, the recovery of the carrier density in the active region is governed by the stimulated carrier lifetime τ_s [48], which is inversely proportional to the input optical power. Thus increasing the input signal power level, or adding another control CW light (holding beam [49]) would largely reduce the stimulated carrier lifetime. If the wavelength of the input light is not within the transparent area of the SOA [50], the device would be driven into saturation, which is harmful to linear amplification. However, this phenomenon can be quite useful for the use of a SOA in optical signal processing applications, since the modulation bandwidth is enhanced (this will be discussed in section 4.2.2.1). The effective carrier lifetime combines both the τ_c and the stimulated carrier lifetime τ_s.

$$\frac{1}{\tau_{eff}} = \frac{1}{\tau_c} + \frac{1}{\tau_s} \tag{2.41}$$

2.3 SOA Structures

As discussed above, SOA structure is typically a laser structure without optical feedback. The laser structure can be divided into two categories: gain-guided and index-guided.

Figure 2.8 depicts a typical double heterostructure SOA. The active $InGaAsP$ alloy is sandwiched between the p-InP and n-InP cladding layers, thus two heterostructures will be formed between the active layer and cladding layers. A forward bias voltage is applied to create population inversion within the active region. After the electrons and holes are injected by the electrodes on both sides of the chip, they will be confined in the central active $InGaAsP$ region where the bandgap is smaller than the one of surrounding layers (Figure 2.9). This DH structure is capable of confining both electrons and holes in the same active region, where both carriers have low potential energy.

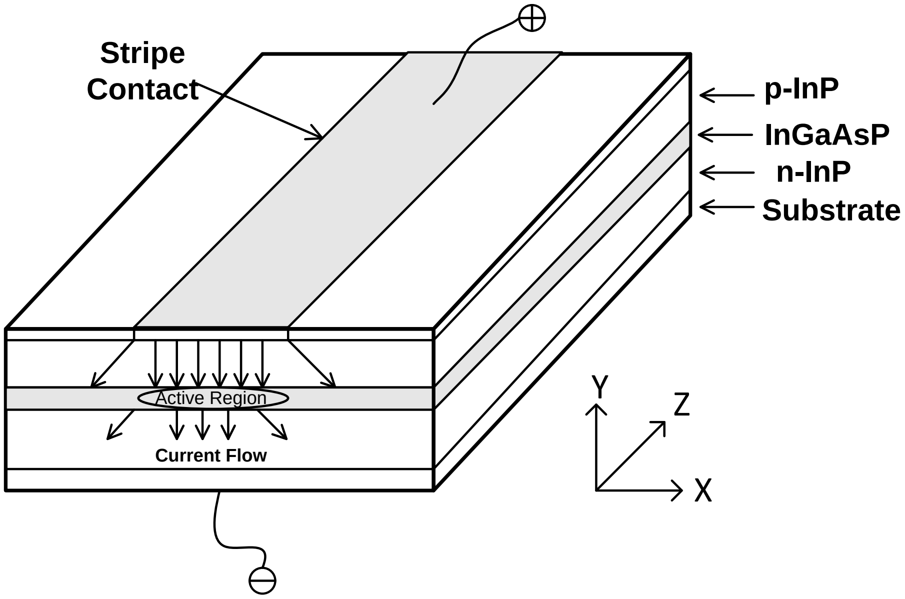

Figure 2.8 Schematic illustration of a typical gain-guide double heterostructure SOA

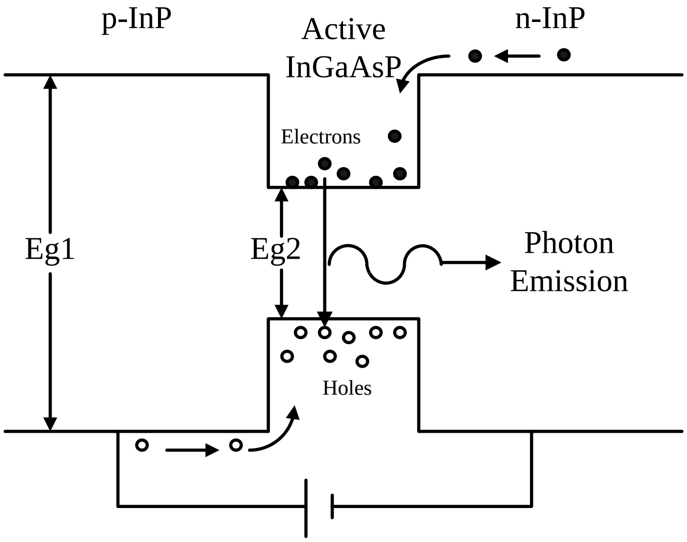

Figure 2.9 Carrier confinement in double heterostructure SOA

As well as carrier confinement, the double heterostructure also demonstrates its capability in optical confinement in the Y direction (perpendicular to the junction plane, Figure 2.8). As shown in Figure 2.10, the refractive index of the central active region is higher than the cladding region. This refractive index step helps confine the optical modes in the active region.

This double confinement of both carriers and photons makes double heterostructure lasers capable of continuous operation at room temperature [51]. In quantum well lasers, the active region is too thin to effectively confine the photons, and another two cladding layers with lower refractive index were added on the original three layers to improve the carrier and optical confinements, this is called Separate Confinement Heterostructure (SCH) [52] design.

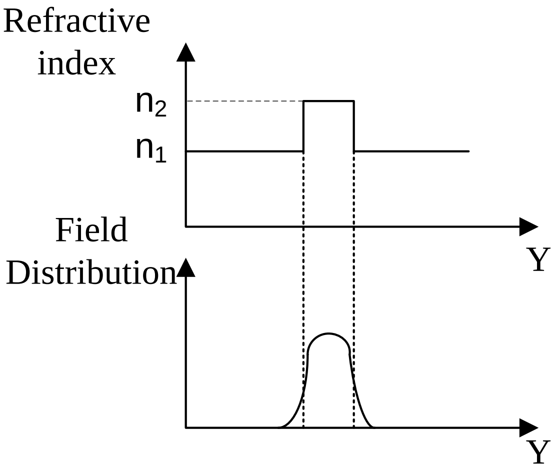

Figure 2.10 Refractive index and field distribution perpendicular to the junction plane, n_2, n_1 denote refractive index of $\boldsymbol{InGaAsP}$ and $\boldsymbol{InP}$, respectively.

The confinement discussed above is in the direction which is perpendicular to the junction plane. The confinement in the lateral (along axis X in Figure 2.8) direction is usually achieved by gain or index guiding. The DH SOA structure depicted in Figure 2.8 is a typical gain-guided laser structure. The current is injected through the stripe contact, and only a narrow part of active layer beneath the stripe provides the optical gain. If the optical mode travels laterally outside this optical gain region (current-pumped region), it will be absorbed by the unexcited active material. Therefore, the optical mode can be confined by the lateral variation of the optical gain in the active layer parallel to the junction plane. Compared to a broad-area laser, which has a lack of current confinement based on the stripe geometry, gain-guided structure lasers would operate with a lower threshold current. However, gain-guided lasers suffer from some undesirable characteristics which will get worse as the laser wavelength increases [45].

The lateral optical confinement efficiency can be improved by using the index-guided structure shown in Figure 2.11. The active $InGaAsP$ layer is surrounded by lower refractive index InP material in both vertical (Y) and lateral (X) directions, i.e. the active material is buried in the lower index layers. Thus this structure is called a buried heterostructure. The fabrication of this structure is complex and requires two epitaxial growths [45]. And the optical mode along the junction plane is confined by the lateral variation of the refractive index, which is normally larger than the carrier induced effects. According to the magnitude of the lateral index step, the index-guided lasers can further be classified as weakly or strongly index guided. The lateral index difference for weakly and strongly index guided lasers is ~0.01 and ~0.2 respectively [45].

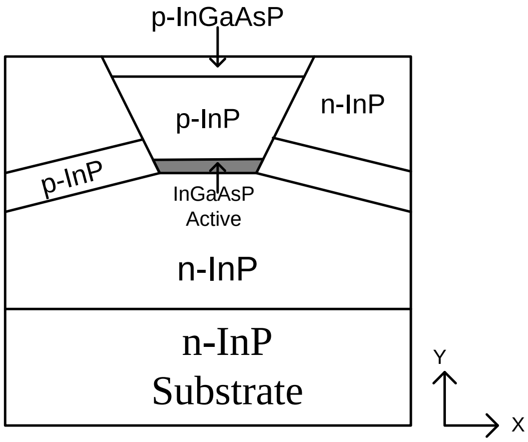

Figure 2.11 Schematic cross section of etched-mesa buried heterostructure laser [45].

2.3.1 Impact of Facet Reflectivity

Depending on the values of facet reflectivity on both sides, the semiconductor laser amplifier can be classified into two categories: the resonant type and the non-resonant type, i.e. the Fabry-Perot amplifier (FPA) and the Travelling-Wave amplifier (TWA) respectively. The FPA is a conventional laser diode functioning under its threshold [53], and it has significant reflections from both facets. The reflections from the facets are usually undesirable because they can severely modulate the amplifier gain and also narrow the amplifier bandwidth. The facet reflectivity of a TWA can be negligible by using techniques such as anti-reflection coating, angled facet and window facet structure, which will be discussed as follows. Compared to the FPA, the TWA enjoys a wider gain bandwidth, larger gain saturation output power, and smaller noise figure [54]. Furthermore, a TWA is less sensitive to the changes in diode temperature, bias current and signal polarisation than a FPA.

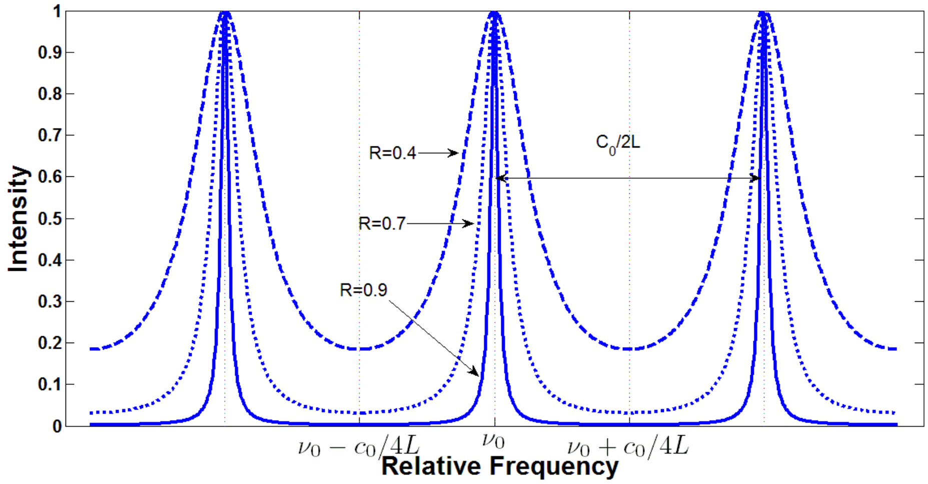

Figure 2.12 The general behaviour of resonant frequencies in a Fabry-Perot cavity for three different values of facet reflectivity.

Although the facet reflectivity in a travelling-wave semiconductor optical amplifier has been reduced significantly, the facets still have some residual reflectivity. Thus, an optical cavity is formed in the amplifier, and the output signal from the amplifier exhibits modulations at longitudinal modes of the cavity.

The signal gain for the amplifier with facet reflectivity R_1, R_2 is of the form [53]:

$$G_C = \frac{1}{\frac{\left(1-\sqrt{R_1 R_2}G_s\right)^2}{(1-R_1)(1-R_2)G_s} + \frac{4\sqrt{R_1 R_2}}{(1-R_1)(1-R_2)} sin^2[\frac{2\pi(\nu-\nu_0)L}{c_0}]} \tag{2.42}$$

where G_s is the single pass gain, ν is the input signal frequency, ν_0 is the cavity resonant mode frequency as depicted in Figure 2.12, L is the cavity length, c_0 is the light velocity in the gain medium, $c_0 = c/n_{eq}$, n_{eq} is the equivalent index of the waveguide . Equation 2.42 was originally deduced for FPA gain. However, it is also valid to calculate the residual gain ripple in the TWA. According to the characteristics of the resonant frequencies in a Fabry-Perot cavity, as shown in Figure 2.12, the intensity maximum and minimum is reached at resonant frequency (e.g. ν_0) and the non-resonant frequency (e.g. $\nu_0 + c_0/4L$) respectively. Similarly, at resonant frequencies, the signal gain G_C will be at a maximum as the sine square term becomes zero, and it will reach minimum at non-resonant frequencies as the sine square term is 1. Thus the peak to valley ratio of the gain ripple V is given [53]:

$$V = \frac{G_c^{max}}{G_c^{min}} = \left[\frac{1+\sqrt{R_1 R_2}G_s}{1-\sqrt{R_1 R_2}G_s}\right]^2 \tag{2.43}$$

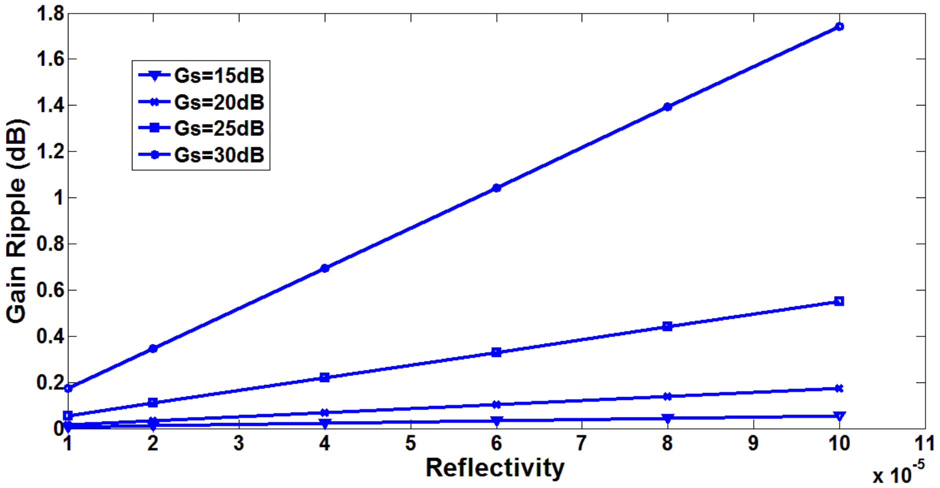

Figure 2.13 Theoretic gain ripple as a function of facet reflectivity ($\boldsymbol{R = \sqrt{R_1 R_2}}$) for different values of the single pass gain.

For a given single pass gain G_s, the gain ripple as a function of facet reflectivity is demonstrated in Figure 2.13. Reducing the facet reflectivity of the amplifier will suppress the gain ripple as predicted. For a $G_s = 25\ dB$, the facet reflectivity should be reduced to less than 1×10^{-4} in order to control the gain ripple below $0.5\ dB$.

The use of reflective semiconductor optical amplifiers (RSOAs) in PONs, especially in the WDM-PON, has attracted more and more research interest in recent years. In theory, the reflective SOA is a double-pass TWA, which was successfully demonstrated by Huang et al for the first time [55]. The structure of a typical RSOA is shown in Figure 2.14. There is only one port in the RSOA serving as the input/output port, thus only one coupling process is required during the fabrication. The facet adjacent to the input/output port is anti-reflection coated, whereas the other (rear) facet is high-reflection coated. Thus the input light can be amplified throughout its roundtrip in the active region. Normally the RSOA is packaged in a transistor outline metal-can (TO-CAN). The RSOA can be directly modulated by applying the data as a bias current. Although the modulation bandwidth of RSOAs is limited to around 3 GHz, its operation speed has been enhanced to 10 Gb/s recently [56][57]. A broadband RSOA was recently reported to cover 100 nm bandwidth over the S, C and L band providing 25 dB path loss capability with – 20 dBm seed power [58].

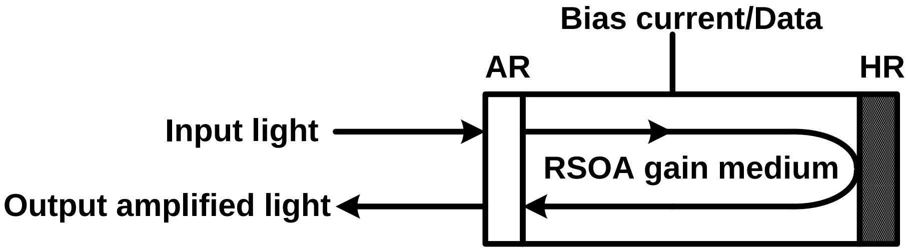

Figure 2.14 Schematic of a reflective SOA structure.

The signal gain for the reflective SOA with facet reflectivity R_1 and R_2, can be analyzed using the modified Equation 2.42. Here we assume the reflectivity of rear facet is equal to 1, which suggests all the input light will be reflected back at the rear facet towards the output port. Thus we replace R_2 and G_s in the Equation 2.42 with R_1 and G_d. G_d is denoted as double pass gain. The Equation 2.42 can be transformed as:

$$G_C{}' = \frac{1}{\frac{(1-R_1G_d)^2}{(1-R_1)^2G_d} + \frac{4R_1}{(1-R_1)^2} sin^2[\frac{4\pi(\nu-\nu_0)L}{c_0}]} \tag{2.44}$$

Then the peak to valley ratio of the gain ripple V' can be derived using the same approach:

$$V' = \frac{G_c'^{max}}{G_c'^{min}} = 1 + \frac{4R_1G_d}{1-R_1G_d} \tag{2.45}$$

For a given double-pass gain G_d, the gain ripple of the RSOA as a function of the front facet reflectivity is shown in Figure 2.15. Similar to Figure 2.13, by reducing the reflectivity of front facet, the gain ripple can be suppressed. And R_1 should be reduced to less than 1×10^{-4} in order to control the gain ripple below $0.5\, dB$, for a double-pass gain 25 dB. In the reference [59], it was proved that the gain ripple of a RSOA is independent of the reflectivity of rear facet, as $G_c'^{max}$ and $G_c'^{min}$ scale together with R_2, keeping V' unchanged.

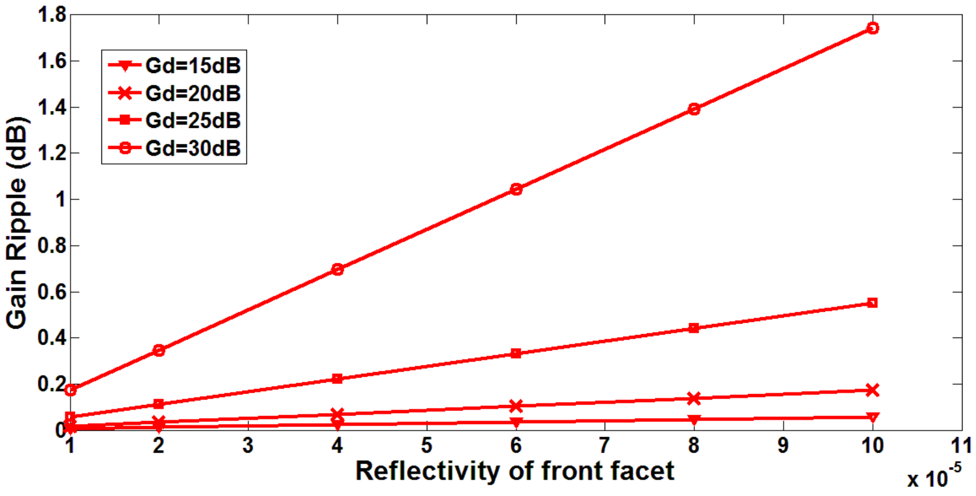

Figure 2.15 Gain ripple of a RSOA as a function of the reflectivity of front facet ($\boldsymbol{R_1}$) at different values of the double-pass gain.

The reduction of facet reflectivity can be achieved by depositing antireflection coating on normal incidence laser facets [53], by tilting the amplifier waveguide with respect to the facet [60], by window facet [61], or by combining AR coating with a tilted waveguide design [62]. All of which are described in Section 2.3.2, 2.3.3 and 2.3.4.

2.3.2 Antireflection Coatings

Conventional AR coating is normally made of a single layer quarter-wave thin film with a refractive index equal to square root of the substrate's refractive index. This kind of design would introduce interference between reflections of the incident plane wave on the upper and lower boundaries of the thin film, thus reduce the reflection. However, the AR coating for semiconductor optical amplifiers is more complicated to design and fabricate as the fundamental mode propagating in a SOA is not a single plane wave [45] thus AR coating supporting a broad bandwidth operation is required. Also, it is difficult to find suitable a thin film material with precise controllability for the semiconductor substrate [63]. Many theoretical works [64] have been done to determine the optimal coating parameters, such as thickness and refractive index, for single or multilayer AR coating designs. General numerical approaches are based on an implicit assumption that a fictitious homogeneous layer with zero width lies between the laser and the AR coating. At the boundary between this *zero thickness fictitious layer* [65] and the laser, the guided mode will experience no reflection or deformation. When the guided mode is arriving in the fictitious layer, it can be decomposed into its angular spectrum using Fourier transform. By applying Fresnel reflection coefficients for each component plane wave incident on the coating interface and summing the reflected angular spectrum, an estimate of the reflected field can be obtained, and the reflection coefficient of the AR coating can be deduced. Hence, the reflectivity of AR coating can be numerically solved and expressed as a function of coating thickness and refractive index. The predicted theoretical results provide a guideline for producing low facet reflectivity by controlling coating thickness and index during the evaporation [64] or sputtering [66] process. Regarding the evaporation method, the coating index is controlled by adjusting the oxygen press in the chamber and evaporation rate, and real-time *in situ* ellipsometry method was proposed to accurately measure both coating index and thickness during the deposition [67]. In practical, the AR coating reflectivity can be measured using modified Hakki-Paoli (HP) method [68][69] which is based on the measurements of modal gain spectrum before and after AR coating [70]. Improved measurement methods are also available [66][71]. Although experiment result demonstrated a facet reflectivity of 5×10^{-6} can be obtained using a single layer AR coating [66], the use of multilayer AR coating could reduce polarization dependence [72] and increase the low reflectivity wavelength range [63] which is vital for the use of SOA in optical communications. As discussed, the AR coating requires stringent process to realize. However, applying angled facet or window facet structure in SOAs could also achieve low facet reflectivity, less polarization dependency and wide bandwidth.

2.3.3 Angled Facet

Another method to suppress the facet reflectivity is to tilt the active region away from the cleaved facet at a certain angle (as depicted in Figure 2.16). This can usually be done before the application of the AR coating.

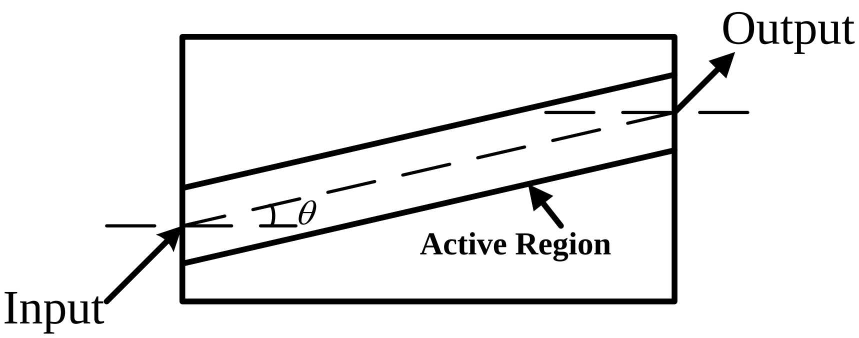

Figure 2.16 Schematic of an angled facet SOA.

As shown in the Figure 2.17 (upper), the SOA waveguide is tilted at an angle θ (alternatively, this can be also understood as the SOA waveguide is terminated by a tilted mirror at an angle θ). The mirror is assumed to be the interface between the waveguide and the air. In order to evaluate the effective reflectivity of the guided mode at an angled facet, the coupling between the incident light and light reflected back into the waveguide should be calculated. The reflected field can be obtained by computing the light transmitted from the SOA waveguide to the virtual waveguide formed by the mirror image [73]. The fundamental mode of the SOA waveguide and its virtual waveguide can be transformed into the angular domain, as shown in Figure 2.17 (lower), which is separated by 2θ. The effective reflectivity is proportional to the overlap integral [74].

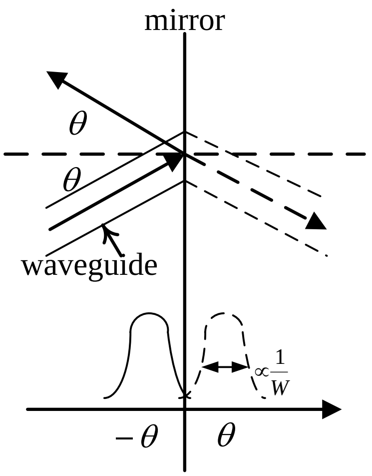

Figure 2.17 (upper) Sketch of an angled facet SOA. Dotted lines: virtual waveguide formed by mirror image. (lower) Optical field in the angular domain [74], solid and dotted line is fundamental mode of waveguide and virtual waveguide respectively.

Assuming the optical distribution is Gaussian, the effective mode reflectivity is given by [75]:

$$R_{eff}(\theta) = R_f(\theta)\exp\left[-\left(\frac{\pi n W\theta}{\lambda_0}\right)^2\right] \tag{2.46}$$

where $R_f(\theta)$ is the reflectivity of the facet, n is the effective refractive index of the waveguide, W is the mode width, θ is the facet angle, λ_0 is the wavelength of incident light.

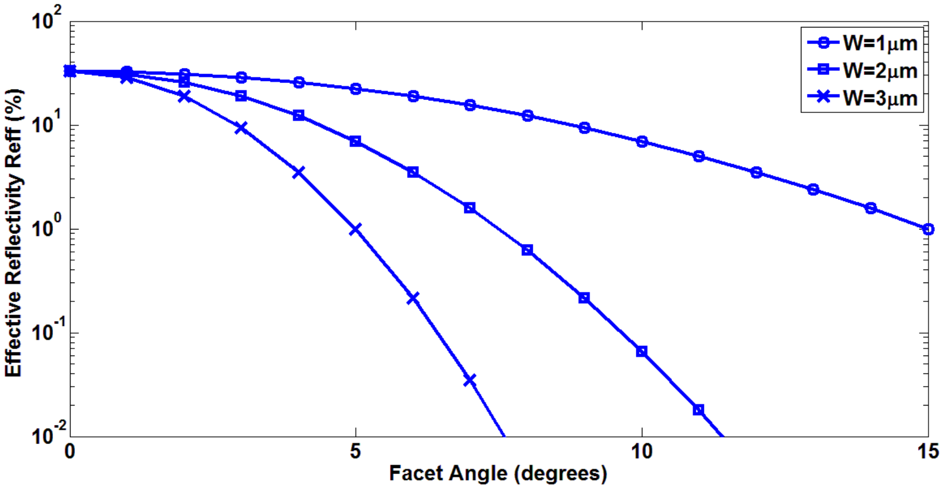

Figure 2.18 Effective reflectivity as a function of the facet angle at different mode sizes (1 μm, 2 μm, and 3μm). The parameters used in the calculation are: Reflection coefficient is 0.33, $\boldsymbol{n = 3.524}$, $\boldsymbol{\lambda_0 = 1.55}$ μ$\boldsymbol{m}$.

Figure 2.18 shows that the effective mode reflectivity decreases as the facet angle and mode size increase, this is straightforward to visualise in the angular domain as shown in Figure 2.17 (lower), as the bigger facet angle θ is, the larger separation will be between two fundamental modes, and the smaller overlap integral will be. Similarly, the bigger mode size W is, the sharp curve will be, the smaller overlap integral will be. As the effective reflectivity is proportional to the overlap integral, the smaller effective reflectivity will be. However increasing the facet angle may induce far-field asymmetry thus degrade the coupling efficiency between SOA and optical fibre, and the AR coating will become more polarization dependent for large incident angle. The optimal facet angles are usually between 7° and 10°. On the other hand, the guided mode size is limited by both the high index active material required to obtain the gain and the requirement that the devices has to remain single moded [76]. This problem can be solved by applying a flared waveguide structure [74].

2.3.4 Window Facet

Window facet, also known as buried facet [45], is another way to reduce facet reflectivity so as to suppress the FP cavity resonance, and to achieve polarisation insensitivity for the device [77]. As showed in Figure 2.19, there are two window regions made of InP material between the both end of active region and the AR coating.

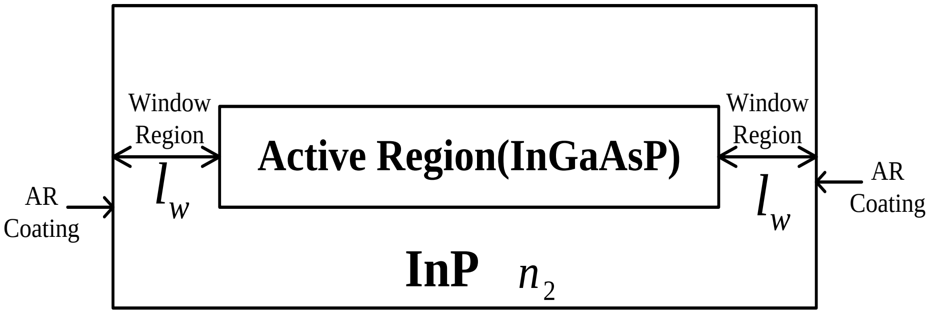

Figure 2.19 Schematic of a SOA with window region.

To study the impact of the window region on the effective mode reflectivity, the expression can be deduced as [78]:

$$R_{eff}(l_w) = R_f \frac{\sqrt{1+\frac{4l_w^2}{k^2W^4}}}{\sqrt{(1+\frac{4l_w^2}{k^2W^4})^2+\frac{4l_w^2}{k^2W^4}}} \tag{2.47}$$

$\mathrm{R_f}$ is the reflectivity of the cleaved facet, l_w is the length of the window region, $k = \frac{2\pi n_2}{\lambda_0}$, W is the mode width. Effective reflectivity as a function of the window region length at different mode sizes is depicted in Figure 2.20. It is clear that the reflectivity decreases as window region length increases and Gaussian mode size decreases. However increasing the window region length may degrade the coupling efficiency between the SOA and optical fibre.

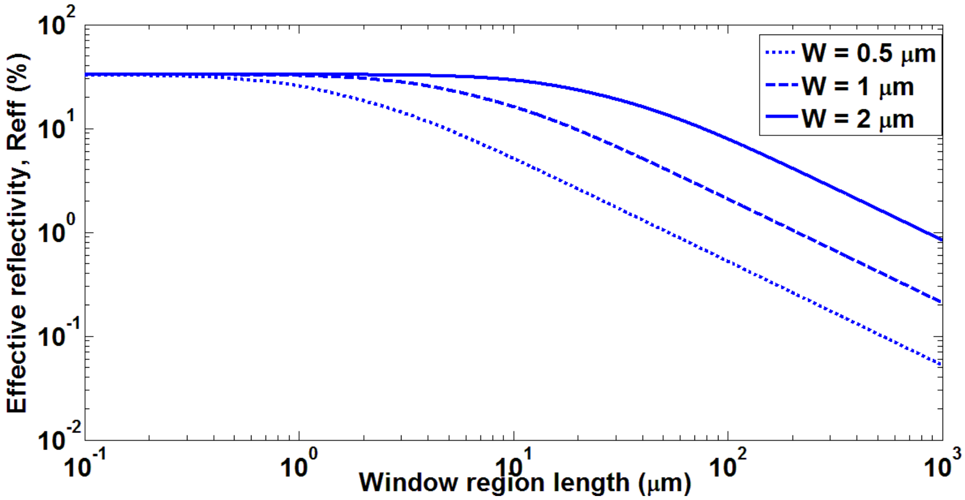

Figure 2.20 Effective reflectivity as a function of the window region length at different mode sizes (0.5 µm, 1 µm, and 2µm). The parameters used in the calculation are: Reflection coefficient is 0.33, $\boldsymbol{n_2 = 3.167}$, $\boldsymbol{\lambda_0 = 1.55}$ $\mu\boldsymbol{m}$.

2.3.5 Polarization Insensitive Structure

Except for some applications based on the nonlinear polarization rotation (NPR) phenomena which will be discussed in Chapter 4, SOAs are required to keep polarization insensitive. The polarization sensitivity effect of SOAs consists of two parts: gain and phase dependence on polarization. In general, reducing the polarization dependent gain (PDG) in a SOA is the major target to achieve polarization insensitive.

The gain of an SOA can be described as:

$$G = \frac{P_{out}}{P_{in}} = \exp\left[(\mathit{\Gamma} g_m - \alpha)l\right] \tag{2.48}$$

Where $\mathit{\Gamma}$ is the confinement factor which represents the fraction of the mode energy contained in the active region [45], g_m is the material gain coefficient, α is the material/internal loss, and l represents the length of the active region. Generally, the confinement factor of Transverse Electric (TE) mode and Transverse Magnetic (TM) mode is different, with $\mathit{\Gamma}_{TE}$ usually being stronger than $\mathit{\Gamma}_{TM}$. This is because the device does not have the same refractive index profile parallel to the epitaxial growth as perpendicular [76]. Furthermore, the material gain coefficient is the same for TE and TM mode. Thus the PDG is induced, and it can be defined as follow [79].

$$PDG = \frac{G_{TE}}{G_{TM}} = \exp\left[(\Gamma_{TE} g_{mTE} - \Gamma_{TM} g_{mTM})l\right] \tag{2.49}$$

In order to minimize the PDG, two approaches can be made. One is to fabricate the SOA with the same confinement factor and material gain coefficient for both TE and TM mode, i.e. $\Gamma_{TE} = \Gamma_{TM}, g_{mTE} = g_{mTM}$. The other is to make the material gain coefficient of TM mode larger than that of the TE mode, so as to compensate the confinement factor difference, i.e. $\Gamma_{TE} > \Gamma_{TM}, g_{mTE} < g_{mTM}$. The first approach is achieved by using a waveguide with near square cross section as the active region [80][81]. However the fabrication process is too difficult for mass production. The latter solution uses strained materials in the active region to increase the material gain coefficient of TM mode relative to that of the TE mode.

As shown in the band diagram (Figure 2.3), the valence band consists of HH, LH and SO subbands. Because of the microscopic selection rules associated with the unit cell wavefunctions [82], the optical transitions from the conduction band to heavy hole subband are forbidden for the TM mode. This implies that the conduction to heavy hole transitions could only contribute to TE gain, and the TM mode will benefit from the conduction to light hole transitions. In the typical band structure as shown in Figure 2.3, the optical transitions from the conduction band to the heavy hole band are more significant than the transition from the conduction band to the light hole band. Therefore, the material gain coefficient of TE mode is larger than that of TM mode in the unstrained material.

In the bulk SOAs, the tensile strain is achieved by growing bulk layers with smaller lattice constant compared to the substrate material, since the bulk layers will grow with small tensile strains [79][83][84]. On the other hand, growing bulk layers with bigger lattice constant compared to the substrate, the compressive strain can be obtained. The introduction of the strain into the active region has many effects on the band structure. Most importantly, in the case of tensile strain, the light hole band is moved to higher energy with respect to the heavy hole band. This suggests that the optical transitions from the conduction band to the light hole band will be increased. Therefore, larger material gain for TM mode can be achieved than TE mode in this tensile strained active region.

In the MQW-SOAs, this can be obtained by carefully tailoring the energy band, i.e. either using barriers and wells of different strain directions (compressive or tensile) [85] or using different number of wells with different strain directions [86][87].

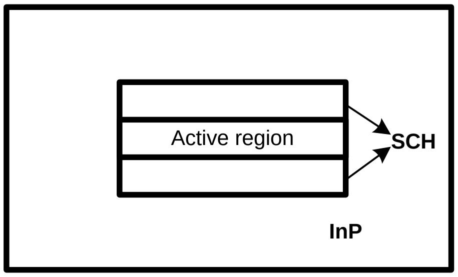

Figure 2.21 Schematic of a bulk SOA with SCH.

In a SOA using a tensile strained bulk active layer, the SCH structure has been also applied into waveguide design to improve the fabrication process tolerance [79][83][88]. As depicted in Figure 2.21, the strained bulk active layer is sandwiched between two thin layers, the refractive index of which is between active layer and substrate. In a SCH structure, adjusting material composition or increasing the thickness of the SCH layer would decrease the optical confinement ratio (Γ_{TE}/Γ_{TM}). Therefore, the strain value required to achieve polarization insensitive could be reduced.

Finally, the active region is tapered linearly in the lateral direction in order to suppress the far-field divergence, so as to improve the coupling efficiency between the SOA and the fibre (Figure 2.22).

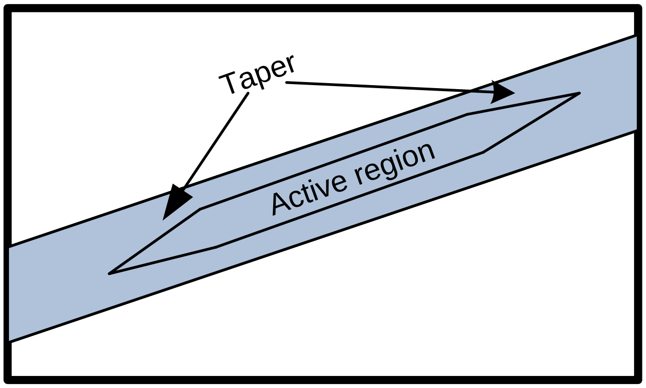

Figure 2.22 Top view of a SOA with tapered active region.

2.4 Summary

This chapter introduces physical principles and structure of semiconductor optical amplifiers. Numerical analysis is employed to demonstrate the characteristics of the device.

Chapter 3 Introduction to Optical Communication Systems

3.1 Optical Communication Systems Overview

The basic optical communication system architecture is a point-to-point link, which consists of an optical transmitter, optical fibre, optical receiver and periodically placed regenerators or optical amplifiers. As depicted in Figure 3.1 , the output of a laser is modulated with electrical data by an optical modulator. The modulation is imposed on the amplitude, phase, frequency or polarization of the light, and this can be achieved by using a directly modulated laser (DML), Mach-Zehnder modulators (MZM) or electro-absorption modulators (EAM) etc. The modulated optical signal is then guided by the fibre towards the receiver. The fiber distance is a few to thousands of kilometers. In long-haul transmission systems, the transmitting signal would experience attenuation and dispersion in the fibre, and this leads to signal degradation. Regenerators or optical amplifiers are employed to solve this problem. At the receiver, the optical signal is converted into an electrical signal using a photodiode. In the following section, the key elements in the system will be discussed.

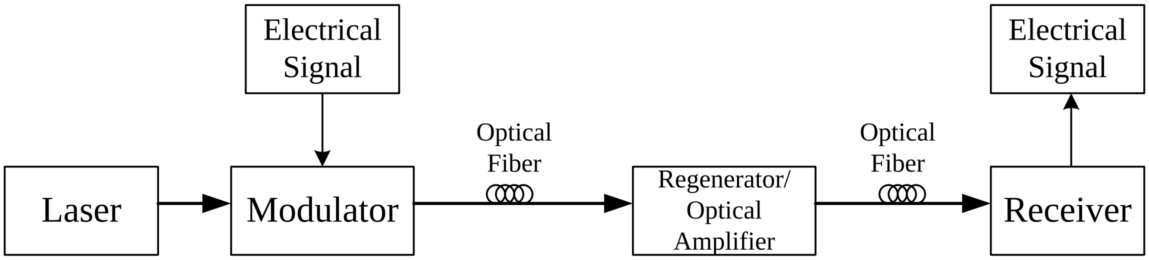

Figure 3.1 Schematic of point-to-point fibre link.

3.2 Key Elements

3.2.1 Fibre

The fundamental element of optical communication system is optical fibre, which extinguishes optical communications from other kinds, such as wireless and copper line based communications. It provides a secure, broadband, most importantly fast channel for modulated lights (signal lights) to pass through. The physical properties of optical fibre have a great influence on the performance of the optical communication system. Especially in long-haul core networks, the limiting factors are fibre attenuation, dispersion, and nonlinearities.

Attenuation is usually caused by absorption and scattering within the material that forms the fibre, and fibre bending losses. The attenuation by absorption can be classified into intrinsic and extrinsic absorption. The intrinsic absorption is caused by the basic material property of the optical fibre i.e. SiO_2 , and it occurs at short wavelengths in the UV region and also at longer wavelengths in the infrared (IR) region of the electromagnetic spectrum. Thus the intrinsic absorption of fibre restricts the extension of the fibre communication towards UV and IR regions. The extrinsic absorption is caused by impurities of the fibre, such as transition metal ions and OH- ions. As depicted in Figure 3.2, the absorption into the OH- ions is responsible for the attenuation peak around 1400 nm. However the OH- ions can be eliminated in fibre through improved manufacturing techniques [89], and such water-free fibre could provide a ~60 THz low-loss bandwidth for supporting optical communication. Scattering loss in the optical fibre results from microscopic variations in the material density and composition. The dominant scattering type is Rayleigh scattering, which is due to microscopic changes in the refractive index of the fibre material. The scattering of light will induce a loss of light intensity. The attenuation coefficient caused by Rayleigh scattering is proportional to the inverse fourth power of wavelength, therefore the attenuation is higher in the short wavelength region. Moreover, bending loss will occur when a fibre is bent smaller than a certain bend radius.

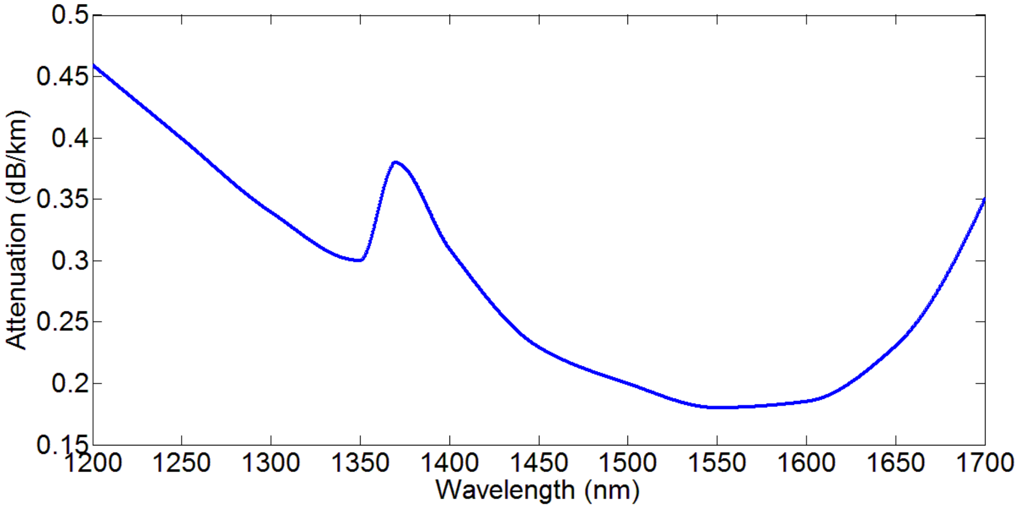

Figure 3.2 Wavelength dependence of the attenuation in a typical low loss optical fibre (SSMF).

Dispersion in a fibre can be classified into material dispersion, waveguide dispersion and modal dispersion. It causes optical pulse spreading and thus leads to intersymbol interference (ISI), which limits the transmission distance. Material dispersion results from variations of the refractive index of the core material as a function of wavelength. This causes a wavelength dependence of the group velocity of a given mode [1]. Waveguide dispersion is caused by the difference in refractive index between the core and cladding. Since not all the light can be confined in the core, and light travels faster in the cladding than in the core as the index is lower in the cladding, dispersion is induced. Assuming the material and waveguide dispersions are additive [90], the total dispersion as a function of optical wavelength for a standard single mode fibre is depicted in Figure 3.3. At 1310 nm, the two dispersion factors cancel to obtain zero total dispersion. As wavelength increases, material dispersion prevails against waveguide dispersion, therefore the total dispersion increases. However, the attenuation minimum of the fibre can be achieved around 1550 nm according to the Figure 3.2. In order to obtain zero dispersion and minimum attenuation at the same wavelength, the core-cladding refractive index profile of the fibre has to be changed to modify both the material and waveguide dispersion factor. By using this technique, zero-dispersion wavelength is shifted around 1550 nm in the dispersion-shifted fibre (DSF) [91]. Modal dispersion in multimode fibres is caused by different group velocities for each mode launched into the fibre. This intermodal time delay leads to pulse spreading in multimode fibre. In high speed long-haul fibre links, polarization-mode dispersion (PMD) is another important origin for signal degradation in single-mode fibre. The two orthogonal polarization states of light launched into the fibre will travel at different velocities due to the non-uniformity of refractive index of fibre.

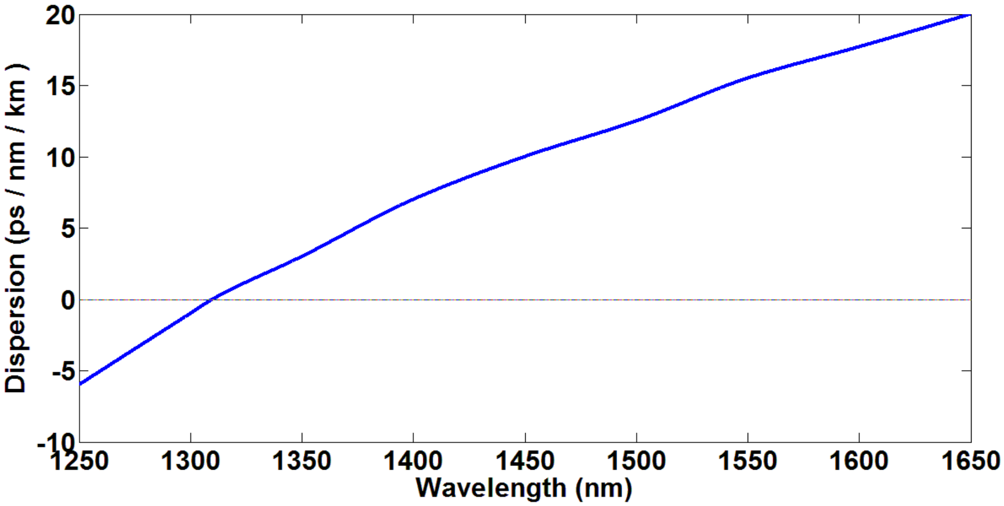

Figure 3.3 Wavelength dependence of the total dispersion in a typical low loss optical fibre (SSMF).

Nonlinear processes in the fibre are caused by high intensity light focusing on the fibre's core. The major nonlinear process is Kerr nonlinearity, including self-phase modulation (SPM), cross phase modulation (XPM), four wave mixing (FWM), and cross polarization modulation (XPolM). The other nonlinear processes are nonlinear phase noise and non-elastic scattering process. The non-elastic scattering process includes stimulated raman scattering (SRS) and stimulated Brillouin scattering (SBS).

3.2.2 Optical Sources and Detectors

Optical sources employed in the fibre optic communications are Light Emitting Diodes (LEDs) and Laser Diodes (LDs). LEDs are often used as the optical source in shorter distance and low data speed systems, while semiconductor LDs are required in long distance and high speed systems. Fundamental semiconductor physics related to optical sources, such as photon generation process, laser structures, and band-gap engineering have been discussed extensively in the Chapter 2. Here the basics of optical detection will be introduced.

Optical detectors employed as a receiver are depicted in Figure 3.1. These devices are used to convert received light signal into an electrical signal. In fibre optic communication, the typical optical detectors are PIN (p-type-intrinsic-n-type) diodes and avalanche photo diodes (APDs). The principles of photodiode detection are based on the photoelectric effect in semiconductors, i.e. injected photons are absorbed in the *p-n* junction, which is designed to have a smaller band-gap energy than the photon energy, and this leads to the generation of electron hole pairs. When a reverse bias is applied to the diode, the electrons and holes form a photocurrent. Since the photocurrent is linear with the injected optical power, by detecting the intensity of the photocurrent the injected optical power can be predicted.

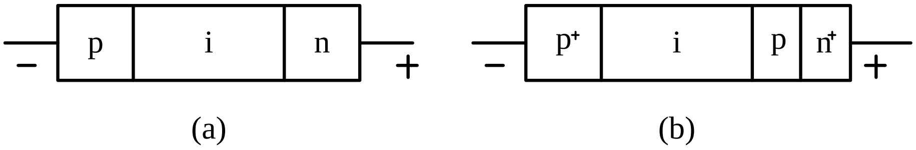

Figure 3.4 Photodiode construction (a) PIN (b) APD.

As shown in Figure 3.4, the name PIN diode refers to the layering of the materials Positive, Intrinsic, Negative. Avalanche photodiodes include an additional p doped layer between the intrinsic and negative material, compared to the PIN diode. This structure will bring an avalanche effect which results in carrier multiplication and photo-current gain. Thus the APD achieves higher sensitivity compared to PIN diode. However, the required operating reverse bias of an APD is very high and the circuitry becomes more complex. Overall, PIN diodes are the main photodetectors used in most optical communication systems.

The optical detector is installed in the receiver, together with the amplifier, and the signal processing circuitry used to sample, recover, and decode the transmitted original signal. In low speed communications, a trans-impedance amplifier is used in the optical receiver. For a high speed system, an optical pre-amplifier should be implemented to improve the bandwidth and gain, as compared to trans-impedance amplifiers.

3.2.3 Optical Amplifiers

Optical amplifiers are implemented to boost optical signal without the need for optoelectronic conversion. In WDM systems, many transmitting signals with different bit rates and data formats can be amplified simultaneously in optical amplifier. Therefore, employing optical amplifiers could not only increase optical system capacity and reach, but also improve the reliability and flexibility of the network operation.

The main optical amplifiers used in optical communications are Semiconductor Optical Amplifiers (SOAs) and Optical Fibre Amplifiers (OFAs). The latter can be classified into Doped Fibre Amplifiers (DFAs) and Raman amplifiers. The optical amplification processes in SOAs and DFAs are achieved by stimulated emission in the gain medium, therefore population inversion is required. The realisation of population inversion is different in SOAs and DFAs. As discussed in Chapter 2, a forward biased semiconductor junction is used to achieve population inversion in a SOA. In DFAs, inversion is achieved by injecting the external pump light which provides energy for raising the atoms from the ground state to higher energy level. The amplification process in Raman amplifiers is based on the stimulated Raman scattering (SRS) effect, which does not rely on population inversion. This nonlinear effect results in transferring the optical power of external pump light at short wavelengths to signal lights at longer wavelengths within the fibre. The gain spectrum of a Raman amplifier is determined by the pump wavelengths, thus Raman amplification can be provided over wide and flexible wavelength regions. Moreover, the Raman gain mechanism can be achieved by using a standard fibre as a gain medium, so all these features make Raman amplifier a promising device. The main drawbacks of Raman amplifiers are twofold: they requires a high power pump light which then poses safety issues; the cost of amplifier is currently expensive.

Semiconductor optical amplifiers were studied nearly ten years before the invention of the Erbium Doped Fibre Amplifier (EDFA) [92]. Since the band-gap energy of a SOA can be engineered by adjusting the composition of the active material, the operation region of a SOA has shown to have great flexibility. The gain peak of a SOA can be chosen from 1280 nm in the O-band to 1650 nm in the U-band [1]. Although the EDFA plays a dominate role in the optical amplification at the 1550 nm transmission window (C-Band), SOAs operating around 1310 nm (O-Band) have attracted considerable interest for use in Passive Optical Networks (PONs) [93]. Especially the wavelength plan for future10 Gbit/s (XG-PON) [94] uses wavelengths from 1260 nm up to 1620 nm and alternative optical amplifier technologies do not function efficiently across this band. The characteristics of SOAs for use in PONs will be further studied in Section 3.4. In addition to their amplification function, SOAs have been used to achieve switching [95] and signal processing [96] functions taking advantage of the fast gain dynamics of SOAs, and SOAs can be integrated easily on an InP-based substrate [97] to build photonic integrated circuits.

Doped Fibre Amplifiers are realised by doping the core material of a fibre with rare earth ions. As depicted in Figure 3.5, DFAs can be operated in the O-, S-, C- and L-Band, depending on the type of rare earth elements and fibre core materials used to construct optical amplifiers. Doping fluoride-based fibres with neodymium (Nd) and praseodymium (Pr) enables DFAs to function in the O-Band. Similarly, Thulium-doped fibre amplifiers (TDFA) operate in the S-Band, Erbium-doped fibre amplifiers (EDFA) operates at the lowest loss transmission window around 1550 nm in the C-Band, both the Er-Doped Tellurite Fibre Amplifiers (ETDFA) and gain-shifted EDFAs function in the L-Band. For use in the long-haul optical communication systems, compared to SOAs, EDFAs could achieve higher gain, lower noise and lower coupling losses. The slow gain dynamics of the EDFA make nonlinearities negligible unlike SOAs, and the EDFA is independent on light polarization.

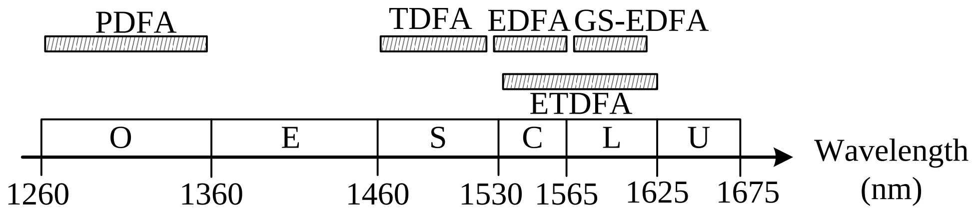

Figure 3.5 Optical band for typical optical fibre amplifiers.

3.3 Optical Network Hierarchy

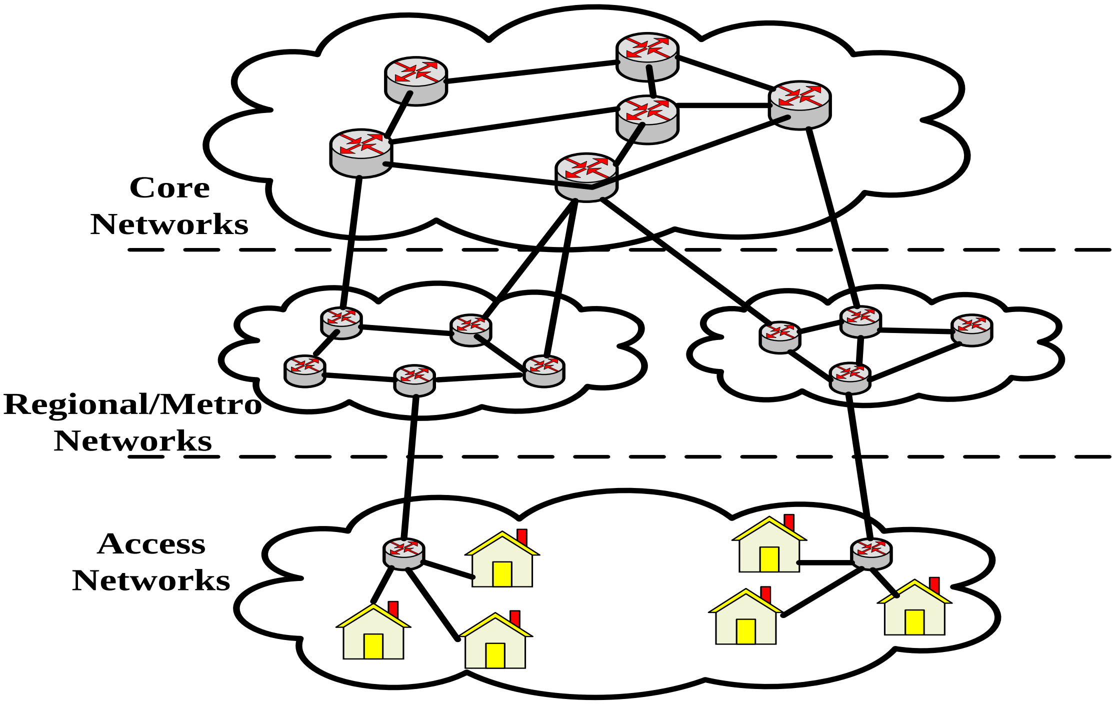

Figure 3.6 Geographic hierarchy of optical networks

Figure 3.6 illustrates a simple model of an optical network hierarchy which consists of long-haul core networks, regional/metropolitan networks, and the “first/last mile” access networks. The access network is closest to the end users, so it is used for distributing and also collecting traffic directly to/from users, and typically spans up to 100 kilometers. The current most popular access technology is digital subscriber line (DSL), mainly because of the existing cooper based access network infrastructure. Although DSL technology is commercially mature, developments are ongoing to push the speed limit over copper wiring to 700 Mb/s [98]. An optical fibre based access network has a huge advantage over copper network as it could provide much higher speed and longer span [99]. Since the beginning of this century, network operators have invested heavily in the deployment of optical access networks. The regional/metro networks are used to not only aggregate traffic from access networks but also distribute the traffic from the core networks. They usually interconnect several telecommunication central offices and span up to 1000 kilometers [100]. Moving up the hierarchy, multiple regional/metro networks are interconnected by the core (backbone) networks. WDM technology is employed in core networks to support high capacity data traffic over long-haul transmission distance. Compared to core networks, WDM technology used in regional or access networks support less wavelengths with lower capacity per fibre. Moving towards the end users' side, the economic issue becomes more sensitive and should be taken account into network planning and deployment [101].

3.4 Passive Optical Networks

3.4.1 Introduction

The traditional access networks are based on twisted copper pairs, initially developed for analogue voice services, or residential coaxial cables used to provide TV services. The first twisted copper based access network is the plain old telephone service (POTS) network which was deployed by telephone companies connecting homes and businesses to local exchanges. It normally covers up to several tens of kilometres, provides analogue voice service and low speed data services up to 56 kb/s. In the 1980s, the integrated services digital network (ISDN) was developed to provide two 64 kb/s channels for voice and data and one optional 16 kb/s digital channel. Compared to the POTS system, the ISDN enjoyed more bandwidth and improved quality. As the bandwidth demand continued to grow, digital subscriber line (DSL) technologies were invented for broadband access networks based on twisted copper pairs. In the DSL system, a DSL modem placed at the user's premises is connected by twisted copper wires to the DSL access multiplexer (DSLAM) at a central office (CO) or remote node. The data transmission service is then carried by this channel. DSL technologies use a lower frequency range (0~4 kHz) on the twisted pair for voice services and a higher frequency range (typically 25~160 kHz for the upstream from user to CO, 240 kHz~1.5 MHz for the downstream from CO to user) for data transmission. There are many types of DSL available such as the Asymmetric DSL (ADSL), High-bit-rate DSL (HDSL), Very-high-bit-rate DSL (VDSL). The popularity of ADSL is due to the fact that more bandwidth is required for downloading than uploading in Internet applications. Therefore ADSL provides up to 8 Mb/s bit rate for downstream and up to 800 kb/s for upstream over a maximum distance of 5.5 km [102]. However, DSL technologies suffer from high attenuation at higher frequencies on the twisted copper pairs, and this limits the coverage of the DSL based access network. For example, the VDSL can support downstream either at a speed of 13 Mb/s over a distance of 1.5 km or at 52 Mb/s over up to 300 m. Thus the bit rate-length product (BL) of the DSL network is limited.

Alternatively, access networks can be carried on residential coaxial cables namely community antenna television (CATV) networks. Originally, the TV signals were transmitted from service provider's headend (HE) offices (like central office in telecommunications) to remote fibre nodes where they were converted back to the radio frequency domain and transmitted over coaxial cables to the end users. The traditional cable network is a one-way broadcast system. However, with the introduction of bidirectional RF amplifiers and return optical links in the 1990s, the cable network is now capable of providing a bidirectional data service [102]. The Data Over Cable Service Interface Specification (DOCSIS) developed by CableLabs provides operational specification for data service over the cable networks. In a DOCSIS architecture, a cable modem placed at the user's premise is connected to the cable modem termination system (CMTS) at the headend office. According to the latest DOCSIS 3.0, the maximum data rate in the cable access system reaches 343 Mb/s for downstream and 122 Mb/s for upstream. The cable network is also called hybrid fibre-coaxial (HFC) network according to the network infrastructure.

The global bandwidth demand has been increasing for more than two decades because of the significant development of the internet. Realistic predictions estimate annual traffic growth is about 34% to 50% [103], and residential access bandwidth demand is increasing accordingly. Email and the World Wide Web were the first and second major driving forces for the bandwidth growth in the history of the Internet [102]. After that, many internet based applications such as cloud computing, peer-to-peer networking, online gaming began to emerge, especially video on demand (VOD) is becoming an important part of people's lives. The current standard TV, with a resolution of 720×480, requires transmission bit rates up to 10 Mb/s after using Moving Pictures Experts Group's MPEG2 compression. The requirement of transmission bit rate for high definition TV with a resolution of 1920×1080 reaches to 24 Mb/s. And the next generation of high definition TV proposed by the Japanese TV broadcast company NHK, is Ultra high definition TV (UHDTV) with a resolution of 7680×4320 and 24 channels of audio. Some of the programs in London Olympics games 2012 were live broadcasting in UHDTV format via internet by British Broadcasting Corporation. The targeted transmission bit rate for the UHDTV is 200 Mb/s after compression [104]. Moreover the 3D version of the UHDTV will require up to 1.8 times of the transmission bit rate compared to 2D version. Therefore the dated copper based access network is under huge pressure to meet the exponential demand on bandwidth.

A passive optical network (PON) is usually a point-to-multipoint (P2MP) optical fibre based access network architecture in which passive/unpowered optical splitters are deployed. As depicted in Figure 3.7, the basic architecture of PON consists of three main parts. The Optical Line Termination (OLT) lies in the central office (CO) and represents the interface between the regional/metro network and the access network. The Remote Node/Terminal (RN or RT) which contains the passive optical splitters, and is connected to the OLT by an optical fibre. The passive optical splitters are mainly optical power splitters and WDM couplers, which are able to split the incoming optical signal into a number of separate transmission channels which feed different Optical Network Units (ONUs) next to the subscribers' equipments. The passive power splitters are usually employed in the RNs of Time Division Multiplexing (TDM)-PONs in which signals are multiplexed and de-multiplexed in the time domain, while the WDM couplers are used in the RNs of WDM-PONs to distribute the signals to different ONUs at different assigned wavelengths [105].

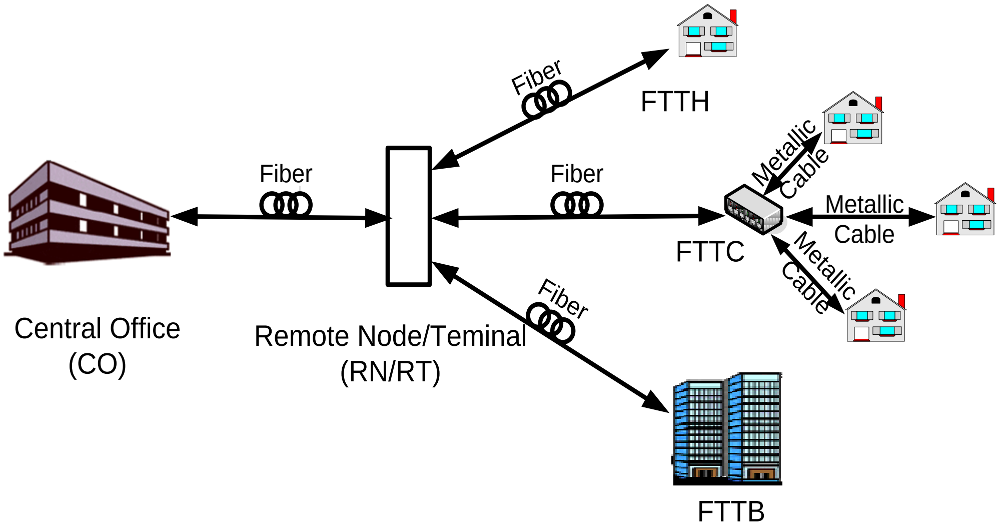

Figure 3.7 Architecture of Passive Optical Network (PON).

Depending on the location of the ONU, the system can be classified into Fibre-to-the-Home (FTTH), Fibre-to-the-Curb (FTTC), Fibre-to-the-Building (FTTB) or Fibre-to-the-Cabinet (FTTCab). The big advantage of this architecture is that the expensive optoelectronic equipment in the CO are shared amongst many users which make PONs a viable solution for broadband access.

Recently, more and more network providers have selected PON technology as the best solution for solving the last mile problem, as it has many advantages compared to other broadband access solutions such as xDSL, HFC or WiMAX. First of all, PON employs fibre as the transmission medium in the last mile, compared to metallic lines or microwave. The fibre could therefore provide a larger bit rate-length product (BL) which enables PON to operate at higher transmission speed over longer distance. Secondly, PON eliminates the active components in the Optical Distribution Network (ODN), which reduces both the capital expenditures (CAPEX) and operational expenditures (OPEX). And this also makes system maintenance and future upgrade/migration easy. Furthermore, the matured PON technology (TDM-PON) is suitable for providing broadcasting service, which is an important part of the network provider’s triple play strategy.

Some state-led FTTH projects were deployed very early in Asian countries like Japan and South Korea. According to a report conducted by IDATE [106], until mid 2011, Japan was still the leading FTTH/B market in the world. In Asia, it is followed by South Korea and Hong Kong. However the FTTH/B deployment in China has been growing rapidly since 2009 [107], and the market is expected to overtake Japan in the future. The total FTTH/B subscribers reach 67 million worldwide in 2011, with 75% of the subscribers in the Asia-Pacific region. In Europe, the total number of subscribers rose to 5.1 million at the end of 2011[106].

3.4.2 TDM-PON

As discussed above, optical power splitters are used at the remote nodes in TDM-PON architectures. Current PON technologies, such as ATM-PON/Broadband-PON (APON/BPON), Gigabit-PON (GPON) and Ethernet-PON (EPON), are all TDM-PONs. The A/BPON, GPON and next generation XGPON (10G PON) are standardized by the telecommunication standardization sector of the International Telecommunication Union (ITU-T), whereas the EPON (as well as GE-PON and 10G EPON) standards are produced by the Institute of Electrical and Electronics Engineers (IEEE). GPON and GEPON take up the major portion in the current FTTH/B market share.

The downstream traffic in a typical TDM-PON is demonstrated in Figure 3.8(a), i.e. from OLT to ONUs, the signals are broadcasted to the ONUs. Each ONU receives the same signal. Then ONUs select their own data through the address labels embedded in the downstream packets. Thus a shared time domain multiplexing (TDM) channel is used in the downstream traffic. This feature enables TDM-PON to provide the broadcast service to the subscribers easily, however it also requires an encryption scheme to be employed in the TDM-PON, otherwise information security will be an issue. The BPON (ITU-T G.983.1 section 8. 3. 5. 6) has addressed this problem by using a *churning* mechanism.

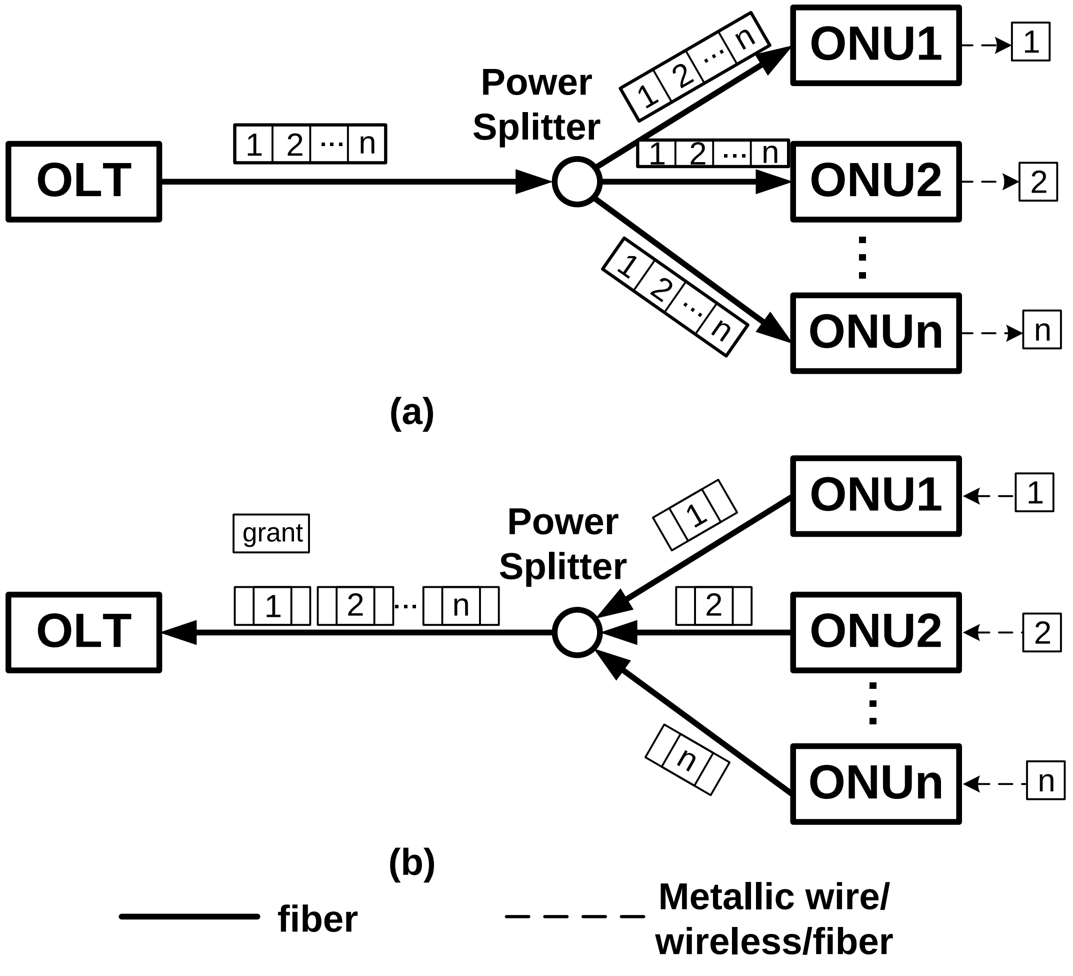

Figure 3.8 Schematic of traffic in a typical TDM-PON (a) downstream, (b) upstream.

The upstream traffic control in a TDM-PON is governed by the OLT. Since the architecture of the upstream in TDM-PON is a multipoint to point configuration, if each ONU send packets to the OLT at random times, collision is inevitable. Thus, time division multiple access (TDMA) as a media access mechanism is employed in the OLT to synchronize the ONUs and to use the upstream channel efficiently. Before transmission, the *ranging* process is established to make the OLT aware of the transmission delays between itself and each ONU. With the help of the TDMA mechanism, each ONU is assigned a specific timeslot (so called *grant* in PON) to transmit its data. Within its time slot, the ONU can transmit the data gathered from the user to the OLT, and it then needs to keep gathering and buffering data and wait for the next period. If the ONU does not have any data to transmit, then it has to turn off its transmitter to avoid interfering with other ONUs' upstream signals as the laser transmitter will generate amplified spontaneous emission (ASE) when idle. This is quite different from the conventional transmission system, which also brings in burst mode transmission in the upstream traffic of PON. The size of the timeslot assigned for each ONU and the transport frame structure are determined by the scheme employed by the PON system (such as APON, GPON). In order to efficiently use the available bandwidth of the channel, dynamic bandwidth allocation (DBA) is employed in TDM-PONs to adjust the timeslot dynamically.

There are two ways to separate TDM-PON downstream traffic from upstream traffic: the two-fibre and one-fibre approach [102]. The first approach requires a pair of fibres to be deployed in order to carry bidirectional signals on separate fibre at the same time, therefore an extra power splitter is needed. This is a straightforward solution, however, the CAPEX is higher for the network operator. The latter solution can be divided into three categories: one-fibre single-wavelength full duplex, time division duplex and wavelength division duplex. The first one places a directional coupler at the OLT and ONU to separate the bidirectional signals, however it suffers from near end cross talk in the couplers. The cross talk is eliminated by using the time division duplex scheme on the one-fibre single-wavelength full duplex approach, but the channel efficiency is quite low. The wavelength division duplex method is chosen to be employed widely in the current commercially available PON systems. In a standard PON (G. 983.3), the wavelength ranges for downstream and upstream traffic are 1490 (±10) nm and 1310 (±50) nm band respectively. The WDM couplers are placed at the OLT and ONU to separate two wavelengths. The reasons for choosing 1310 nm band as the upstream transmission carrier are twofold: the low cost FP laser emitting around 1310 nm is commercially matured, it can be installed at ONUs where deployment cost is sensitive. Furthermore, the dispersion of a standard single-mode fibre around 1310 nm is near zero. This feature is very suitable for transmitting optical light generated by a FP laser, since FP lasers have a larger linewidth compared to more expensive distributed feedback (DFB) laser, which makes the light liable to suffer from increased dispersion during transmission. The 1550 nm band is reserved for sharing the PON fibre with a HFC network to provide CATV services. According to the latest PON specification, the next generation XG-PON uses 1260-1280 nm band for upstream and 1575-1580 nm band for downstream (G.987).

The original BPON standard (G. 983.1) defined the 155.52 Mb/s data rate for both downstream and upstream, and the transmission rate was amended to 1244.16 Mb/s for downstream and 622.08/155.52 Mb/s for upstream in the new version published in 2005. The reach of BPON called for 20 km with 32 to 64 ONUs. The bit rates defined for GPON (G. 984) are 1244.16/2488.32 Mb/s for downstream and 155.52/622.08/1244.16/2488.32 Mb/s for upstream. The GPON allows 64 to 128 splits and its coverage is usually 20 km. GPON is also recommended a low-cost 10 km reach which employed FP lasers in ONUs as optical sources, and a 60 km physical reach with a 20 km differential reach, which stands for distance between nearest and fastest ONUs. The next generation XG-PON (G.987) will allow higher transmission rate (9.95328 Gb/s for downstream and 2.48832 Gb/s for upstream). With the transmission speed and split ratio increasing, and differential reaches becoming variable, the transceiver issue is becoming more and more critical in PONs. This requires: optical transmitters to achieve higher data rates, higher optical transmitter output power and shorter warm up and stabilizing/locking time; accordingly optical receivers need to operate at higher speed and sensitivity. Furthermore, due to the bursty nature of the PON’s upstream traffic, the transceivers should be optimized to operate in burst mode. Especially the high performance burst mode receiver (BMR) installed at the OLT, which requires high sensitivity, wide dynamic range and short response time. A high sensitivity PIN or APD together with low noise preamplifier IC and limiting amplifier IC are key components to improve the optical sensitivity and dynamic range of a burst mode receiver. Depending on the methodology of the design, the burst mode receiver can be classified into two types: DC-coupled and AC-coupled BM receivers. The DC-coupled BM receivers usually achieve faster response time than AC-coupled, due to the charging and discharging time of the capacitors used in the AC-coupled signal path limiting the response to the amplitude change at incoming signals. Therefore, the DC-coupled BMRs are suitable for deploying in BPON or GPON, which requires shorter settling time. For example, the guard time and preamble time defined in the PON specifications are for laser turning on and off, gain control and recovery. The guard time for 1244.16 Mb/s upstream in GPON is 32 bits which equals to 25.6 ns, and the guard time in XG-PON for

2.48832 Gb/s upstream traffic increases to 64 bits which is also equates to 25.6 ns. The preamble time is 44 bits (35.4 ns) and 160 bits (64 ns) for GPON and XG-PON respectively. Whereas AC-coupled devices are normally deployed in EPON, as the standard settling time for receivers in EPON has been defined below 400 ns, and 800 ns for the 10G-EPON (IEEE 802. 3av) [108].

As the transmission speed and PON reach increases, the dynamic range becomes wider and the design of the BMR becomes more and more complicated, cost increases significantly. In Chapter 6, the dynamic gain modulation performance of an adjustable gain clamped SOA (AGC-SOA) will be studied, the numerical simulation and preliminary experimental results demonstrated the proposed device is capable of dynamically regulating optical power difference between packets without loss of linearity, which will largely alleviate the issue regarding the BMR in OLT.

3.4.3 WDM-PON

As discussed in the last section, the GPON and GE-PON standards dominate the current FTTH/B deployment worldwide. With the surge of bandwidth consuming Internet applications, the need for higher bit rate PON is set to grow again. The ITU-T and IEEE suggest the next generation PON as 10 Gb/s scale. However the opto-electronic transceivers located at both OLT and ONUs are struggling to meet the technical requirements, and of course the cost of these components will rise accordingly. Moreover, the number of ONUs is limited by the current splitter size and PON reach. Therefore, the TDM-PON is not a scalable solution in the long term as the transmission speed and PON subscriber increase.

The WDM-PON is a promising solution in addition to the current PON technologies. Its specification is currently in progress in ITU-T SG15. As shown in Figure 3.9, in a typical WDM-PON architecture, a passive WDM coupler or arrayed waveguide grating (AWG) based wavelength router is located at the remote node and connects each ONU to the OLT. Unlike passive power splitters in the TDM-PON, the WDM coupler does not induce power splitting loss in the signal path. Each ONU is assigned a specific wavelength channel, thus in WDM-PON, the point-to-point connection between ONU and OLT is realized in the wavelength domain. Therefore, there is no need for the ONU to share the communication channels as in TDM-PON, protocols like ranging and DBA are not required in the media access control (MAC) layer. Furthermore, individual wavelength channels can operate at different speeds and under different protocols. This makes the management of networks more flexible. Furthermore, since the WDM coupler at the RN also works as a wavelength router, the information security is enhanced as compared to the TDM-PON.

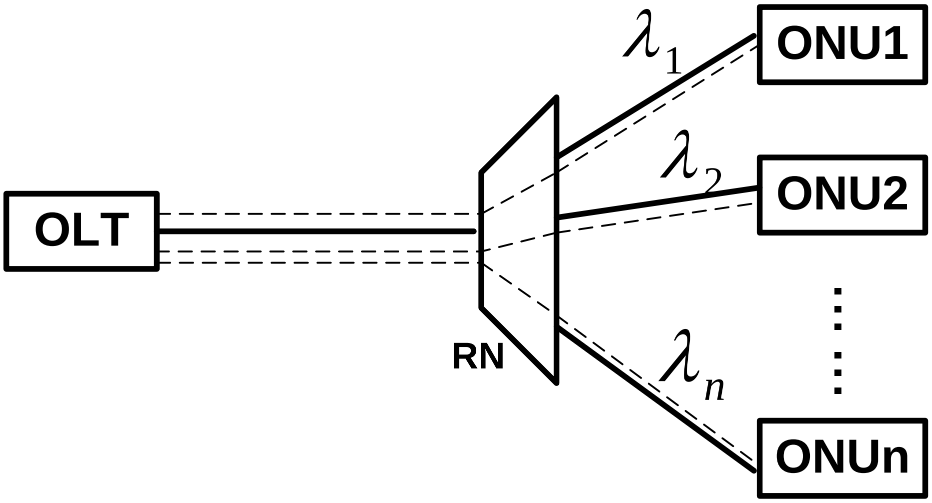

Figure 3.9 Architecture of a WDM-PON.

However, the deployment of the WDM-PON also faces many challenges. For example, the WDM components such as tuneable light sources and AWGs are currently more expensive than the TDMA equipment, and the performance of WDM components is influenced by environmental temperature changes. Most importantly, *colourless* ONU operation is essential. In terms of equipment cost, the equipment used in OLT can be shared by the all subscribers in the network. Thus the ONU, which is normally placed at the user's premise or near a few users' premises, is cost sensitive. Therefore, the colourless ONU operation must be cost effective. Many methods have been proposed to address the challenge. Generally, depending on the location of the upstream light source, these proposals can be classified into two categories: central seeding and self seeding. Central seeding means the colourless upstream light is provided by the optical source placed in the CO. There are many ways to achieve that, economical approaches are proposed such as the centralized spectral slicing technique and downstream wavelength reuse scheme. The centralized spectral slicing technique deploys a broadband light source

(BLS) such as a LED [109], superluminescent LED (SLED) [110], FP-LD [111] at the CO. The emitted broadband signal together with the downstream signals which are generated by multiple distributed feed back laser diodes (DFB-LDs) at CO, are transmitted over the same fibre. Then the broadband signal is spectrally sliced by the AWG at the RN, thus separated signals are routed to each ONU as the upstream signal carriers. However the downstream wavelength reuse scheme has attracted more interest, especially the re-modulation scheme based on a Reflective SOA. In this scheme, a RSOA is placed at the ONT or ONU, the downstream light is injected into the saturated RSOA where the modulated downstream signal is flattened out, reflected at the rear facet of the RSOA, and then re-modulated with the upstream signal [112].

The self seeding ONU means a colourless light source is placed at the ONT or ONU. This can be achieved by using the distributed spectral slicing technique and injection-locking techniques. Regarding the distributed spectral slicing technique, similar to centralized spectral slicing technique, the BLS placed at each ONU is modulated with upstream data. Then the broadband upstream signal is spectrally sliced by the AWG, only required wavelengths carrying upstream data could pass through to the OLT. However, the modulation speed of distributed spectral slicing technique is limited by the inherent noise. The injection-locking technique can improve these fundamental limitations. Here, light is injected into a broadband laser source, if the wavelength of injected light is aligned to one of the BLS's multiple modes, the BLS can be transformed to a single mode laser by emitting a light at the same wavelength of the injected light. Depending on the source of the injected light, this scheme can be divided into external injection-locking and internal injection-locking. In the external injection-locking scheme, a BLS such as a FP-LD [113] or a RSOA [114] is placed at the ONT, the injection source (usually another BLS) is located at the CO or RN. External injection-locked FP (IL-FP) has been successfully implemented into WDM-PON in a field test by the Korea Telecom [115]. However, it requires high injection optical power to turn the FP-LD at the ONT into the injection-locked mode. In the internal injection-locking scheme, the injection light is generated by the BLS (FP-LD or RSOA) located at the ONT/ONU which is reflected back at the remote node to injection lock itself. The reflection at RN can be achieved by employing a fibre Bragg grating (FBG) [116][117] or a circulator with a band-pass filter (BPF) [118].

The WDM-PON enjoys high transmission speed, protocol transparency, improved security and guaranteed Quanlity of Service (QoS) [119], however the CAPEX is high due to the expensive WDM components. The WDM-PON could offer a 1.25 Gb/s per wavelength bandwidth which exceeds most general subscriber's needs under the current service environment [115]. As a future access network solution, the deployment of WDM-PON should take the current PON infrastructure into account to make the migration more cost effective. Therefore, the hybrid WDM/TDM PON has been studied extensively [120]. In a typical WDM/TDM PON (as shown in Figure 3.10), optical power splitters are connected to an AWG wavelength router in the remote node of the PON. Then each wavelength transmitted over the PON system can be shared by using the TDMA mechanism to serve more subscribers. As the number of subscribers (viz. PON splits) increases, the equipment cost per subscriber reduces. If the bandwidth demand of the subscriber is increases in future, the number of PON splits will be reduced. In a field trial in South Korea, WDM-PON and EPON have been successfully combined together (WE-PON) to serve 1024 end users using 32 downstream wavelengths and 32 splits [119].

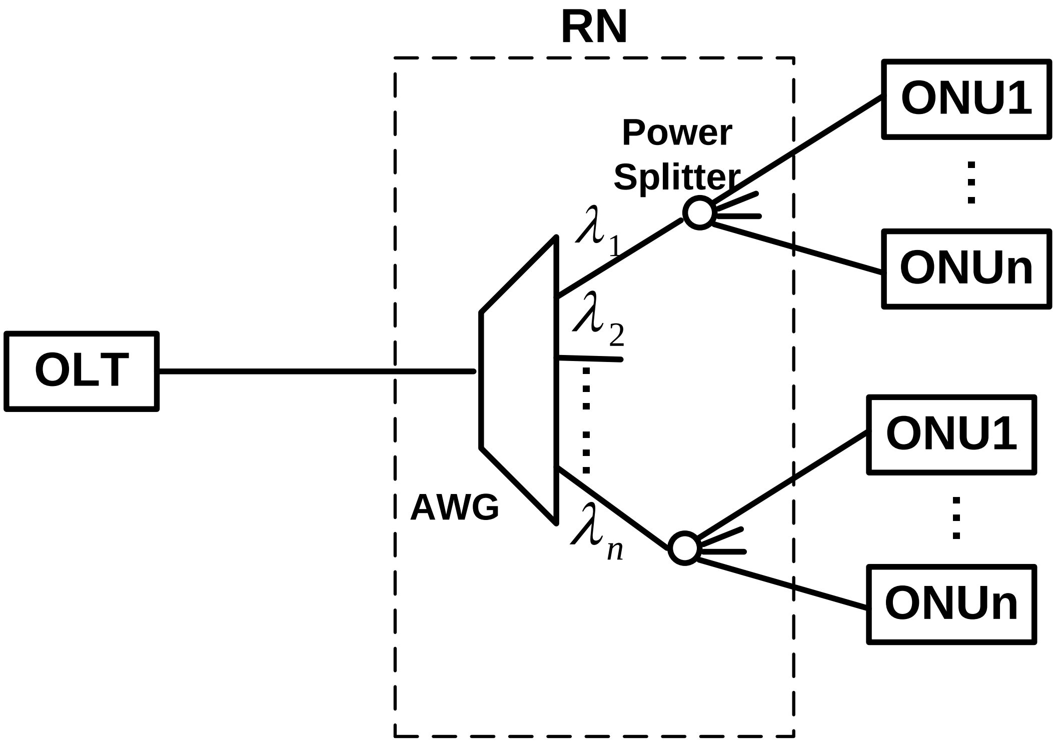

Figure 3.10 Architecture of a hybrid WDM/TDM-PON.

3.4.4 SOAs in PONs

Semiconductor optical amplifiers have been used in the standard PON to extend the optical link budget and achieve a longer reach with more splits [121][122]. In a standard GPON, the typical reach is 20 km and split ratio is 1:32. An amplified PON could provide a better coverage and accommodate more subscribers, thus leading to a CAPEX and OPEX saving [93]. The downstream and upstream wavelength defined in GPON is 1490 nm and 1310 nm respectively. The traditional EDFA does not function within this range. Moreover, the next generation XG-PON uses 1260-1280 nm band for upstream and 1575-1580 nm band for downstream (G.987). The SOA has a key role in this context, as it can amplify signals from the O-band to the U-band (1260 nm ~ 1675 nm) by adjusting the composition of its active material.

The optimum position for an amplifier in a PON is a trade-off between split loss and trunk fibre loss; the amplifier can perform as a booster, a mid-span amplifier or a pre-amplifier immediately before a receiver. In most cases the amplifier is optimally placed before the splitter but this may not always be possible depending upon the availability of power sources at this point [58].

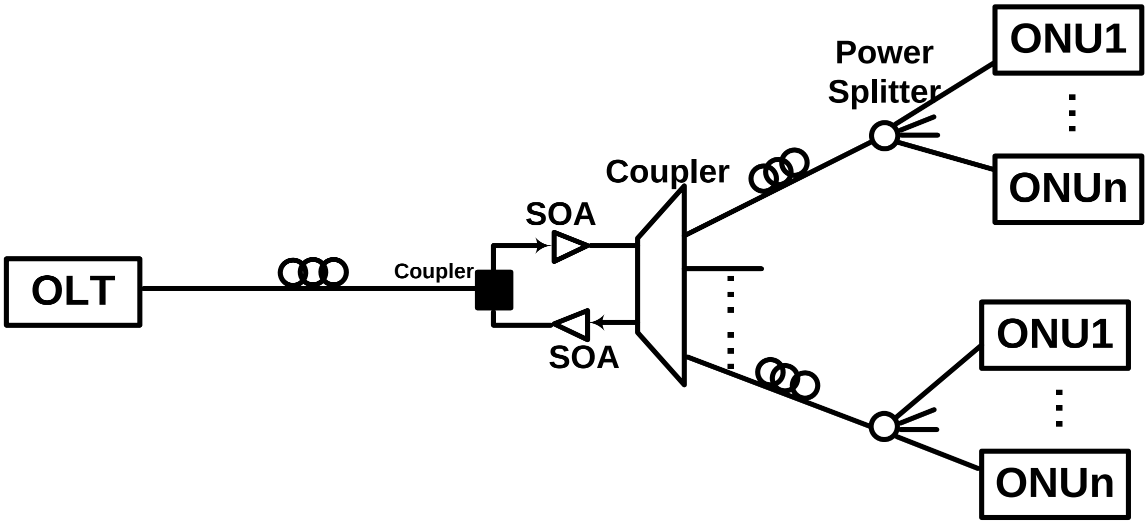

Figure 3.11 Schematic of a typical amplified PON system using SOA.

RSOAs used in PONs are usually located in ONUs responsible for upstream signal light generation, amplification or modulation. The upstream light can be generated either in the CO (central seeding) or by the RSOA itself (self seeding). The latter one is usually achieved by using the internal injection-locking scheme [117][118]as discussed in section 3.4.3. However, the central seeding scheme attracted more research interest. In this scheme, the seed light for upstream traffic is generated in the CO either by a BLS or TLS. The seed light together with downstream signals are transmitted to ONUs, and separated by the WDM couplers. Then the seed light is amplified and modulated with upstream data in the RSOA and sent back to the CO, as depicted in Figure 3.12 (a). As dedicated upstream signals are provided by the CO, colourless ONU operation is achieved. However the CAPEX of this approach is high due to the introduction of extra light sources. This issue is addressed by the re-modulation technique shown in Figure 3.12 (b). The downstream signals can be re-modulated with upstream signals in the RSOA then reflected back to the CO by taking advantage of the gain saturation characteristic of the RSOA. This is demonstrated in Figure 3.13, when the input downstream signal power is within the saturation region of a RSOA, the extinction ratio of output downstream signal is significantly reduced (the saturation characteristic of SOAs will be discussed in the next chapter), which implies the downstream data can be almost removed from the lightwave. Then the optical carrier can be re-modulated by directly modulating the RSOA with the upstream data. However, this technique is not very practical as the optical power of downstream signal light should be high enough to drive the RSOA into gain saturation. This problem can be alleviated by using different modulation schemes on the downstream signals [123].

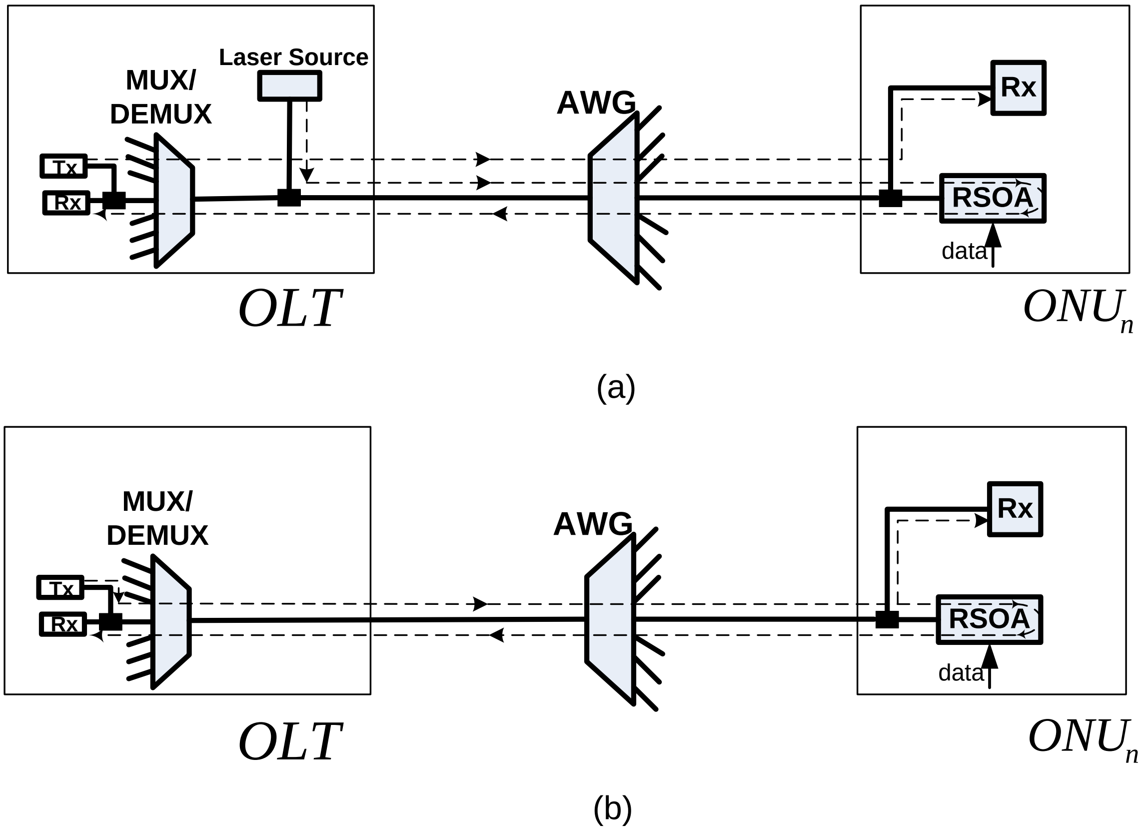

Figure 3.12 Schematic of central feeding WDM-PON based on RSOA (a) upstream light is provided by a BLS or TLS in the CO, (b) downstream light is re-modulated as upstream light by RSOA.

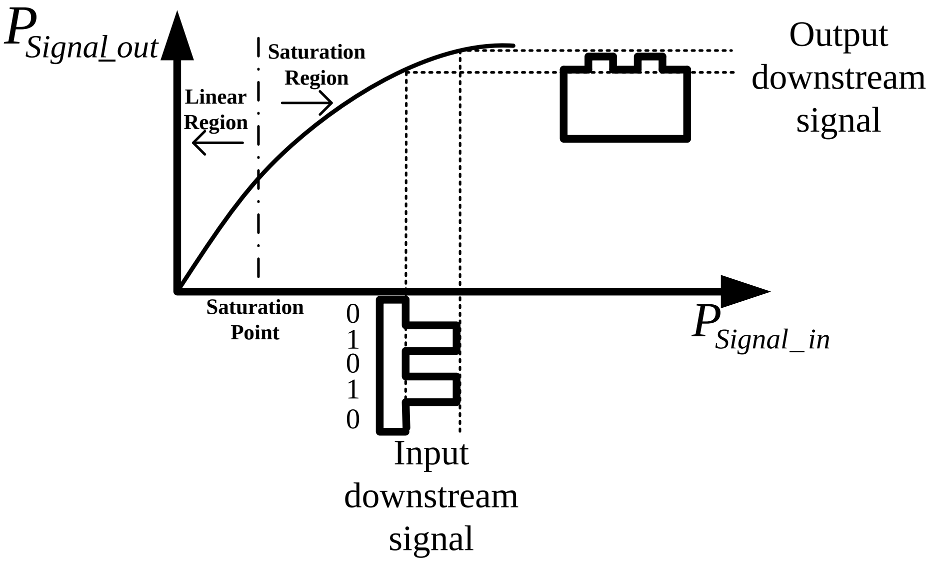

Figure 3.13 Demonstration of the amplitude squeeze technique using a saturated RSOA.

The system performance of the central feeding WDM-PON can be degraded by the external reflection caused by the fibre connector, splices, etc. Since the same wavelength is used in the downstream and upstream traffic on a single fibre, the back-reflected light will interfere with the light with the same wavelength in the same transmission direction, result in optical beat interference (OBI) noise. The issue can be found in both configurations of the central feeding system depicted in Figure 3.12. Effective measures are also studied and proposed to tackle this problem [124]. In the WDM-PON architecture where continuous-wave (CW) light is generated in the CO as the seed light, techniques such as broadening the linewidth of the laser diode [125], using a low coherent light source [126] and optimizing the ONU gain [127] have been proposed. While in the WDM-PON architecture which employs a downstream wavelength re-modulation technique, the system performance can be improved by broadening the optical spectrum of the downstream signal, for example, using Manchester coding for the downstream signal modulation [128].

3.5 Summary

This chapter reviews key elements, techniques and architectures of the optical communication system, especially the promising candidate for the future optical access network - passive optical network (PON) system has been thoroughly discussed. Firstly, the basic point-to-point fibre link is introduced to demonstrate the basic architecture and components in the communication system. Then the characteristics of key elements such as fibre, optical amplifiers, optical sources and detectors are generally studied. Secondly, by reviewing the optical networks hierarchy, the first/last mile problem is raised, since the twisted copper pairs based traditional access networks can no long meet the end users' bandwidth demand. Thus the typical architecture, advantages and worldwide deployment status of the PON are discussed. The PON technologies is divided into TDM-PON and WDM-PON and discussed separately. The channel sharing mechanism, specifications of current commercially available TDM-PONs are introduced, and the design issues regarding the high speed fast response burst mode receiver with wide dynamic range are reviewed. The WDM-PON enjoys many advantages compared to the current TDM-PON technologies although it faces many challenges in the deployment. Therefore many proposals have been introduced to tackle these problems especially the realisation of the colourless ONU operation and the hybrid WDM/TDM PON. In the end, the use of semiconductor optical amplifiers in the PON system has been reviewed.

Chapter 4 Characteristics and applications of SOAs

4.1 Basic Characteristics

4.1.1 Signal Gain and Saturation

The optical material gain coefficient in a semiconductor can be calculated using two approaches. The first is based on the physical analysis of interband transitions, i.e. the rate of stimulated emission and absorption in semiconductors as introduced in section 2.2.2.2. The other is a phenomenological approach, which is based on the observation that the material gain coefficient is carrier-concentration and wavelength dependent. Many empirical expressions for material gain coefficient, such as Lorentzian shape [16], inverse quadratic function [129], and cubic formula [130], have been proposed to achieve fast processing speed, which is essential for modelling the SOA in the system level. Comparisons of these approaches will be further discussed in the Chapter 5.

Here the material gain coefficient g_m is taken to be directly proportional to the carrier density N.

$$g_m = a_d(N - N_0) \tag{4.1}$$

where a_d is the differential of g_m relative to N. N_0 is the carrier density at transparency point where is the onset of the population inversion [45]. Although this approximation is not as accurate as other expressions, it is useful to deduce the analytical solutions for steady-state gain characteristics of SOAs.

In a SOA, a forward bias current injection is applied to create population inversion providing optical amplification, similarly to laser diodes. Thus, the carrier-density rate equation used in the numerical analysis of semiconductor lasers [131] has been adopted to describe the SOA carrier density variation in the excited state (conduction band).

$$\frac{dN}{dt} = \frac{J}{ed} - \frac{N}{\tau} - a_d(N - N_0)\frac{I}{h\nu} \tag{4.2}$$

From left to right, the first term on the right hand side (RHS) of the Equation 4.2 stands for the addition of carriers from external injection. J is injection current density, e is the electronic charge, d is active layer thickness. The second and third term on the RHS of Equation 4.2 represents the recombination rates due to spontaneous emission and stimulated emission. τ is the radiative carrier recombination lifetime, discussed in Chapter 2, h is the Planck's constant, ν is the input signal frequency, I is input signal intensity, which is governed by the travelling-wave equation inside the active region of SOA (the detailed derivations will be discussed in Chapter 5)

$$\frac{dI}{dz} = [\Gamma g_m - \alpha]I \qquad (4.3)$$

where α is the internal loss coefficient of the waveguide, z denotes the position of input light propagation along the amplifying cavity, and t in (4.2) denotes time.

Under steady state condition (i.e.$\frac{dN}{dt} = 0$), the Equation 4.2 can be rearranged as:

$$N = \frac{\frac{\tau J}{ed}}{1 + \frac{a_d \tau}{h\nu} I} + \frac{n_0 I}{I + \frac{h\nu}{a_d \tau}} \qquad (4.4)$$

and the saturation light intensity I_{sat} is defined as the intensity at which the gain has been halved:

$$I_{sat} = \frac{h\nu}{a_d \tau} \qquad (4.5)$$

Equations 4.4 and 4.5 can be substituted into 4.3, then obtaining:

$$\frac{dI}{dz} = (\frac{\Gamma g_0}{1 + \frac{I}{I_{sat}}} - \alpha)I \qquad (4.6)$$

where g_0 is unsaturated material gain coefficient:

$$g_0 = a_d(\frac{\tau J}{ed} - N_0) \qquad (4.7)$$

By integrating Equation 4.6 from $z = 0$ to $z = L$ (L denotes the active region length) we obtain the amplifier gain G expression:

$$G = \frac{P_{out}}{P_{in}} = \frac{I_{out}}{I_{in}} = \exp\left[(\Gamma g_0 - \alpha)L\right] \tag{4.8}$$

P_{out} and P_{in} is output and input optical power, respectively. $P = A_{cross} I / \Gamma,\ A_{cross}$ is the cross section area of active region.

If the internal loss α is neglected in Equation 4.6, then the solution gives:

$$G = G_0 \exp\left(-\frac{G-1}{G} \cdot \frac{I_{out}}{I_{sat}}\right) \tag{4.9}$$

where $G_0 = \exp\left(\Gamma g_0 L\right)$ is the unsaturated amplifier gain.

P_{3dB} (or P_{sat})is saturation output power defined as a point where the amplifier gain is reduced by 3dB (halved) from its unsaturated value.

$$P_{3dB} = \frac{A_{cross} I_{3dB}}{\Gamma} = \frac{A_{cross}}{\Gamma} \frac{G_0 \ln 2}{G_0 - 2} I_{sat} \tag{4.10}$$

4.1.2 Noise Figure

The nature of the optical amplification process inside a SOA indicates that spontaneous emission will be added onto the output amplified signal, thus spontaneous emission is a major noise source in a SOA. Moreover, there are other noise components associated with the amplification processes. The total noise power of an output amplified signal, which is measured after detection, can be described as [132]:

$$\sigma_{tot}^2 = \sigma_T^2 + \sigma_S^2 + \sigma_{sp}^2 + \sigma_{S-sp}^2 + \sigma_{sp-sp}^2 \tag{4.11}$$

The terms on the RHS of the Equation 4.11, from left to right, are the thermal noise, signal, induced shot noise, spontaneous shot noise, beat noise between the signal and the spontaneous emission, and spontaneous-spontaneous beat noise respectively. The origin of last two terms can be explained as follows. As the photodetectors are square law detectors, the output of which is proportional to the square of the input field. We assume the input field has both signal and noise components. After detection, we will get (signal + noise)^2 = (signal)^2 + 2(signal • noise) + (noise)^2. The first term on the RHS of the equation is the wanted signal, the second term is so-called signal-spontaneous beat noise, and the last term is the spontaneous-spontaneous beat noise. In the presence of a narrowband optical filter before the photon detection, only signal dependent noises, i.e. signal shot noise and signal-spontaneous beat noise, will exist [133]. Then the total noise power equation can be rewritten as:

$$\sigma_{tot}^2 = \sigma_S^2 + \sigma_{S-sp}^2 = 2eR\alpha GP_sB_e + 4R^2G\alpha^2P_sB_e\rho_{ASE} \qquad (4.12)$$

where $\sigma_S^2 = 2eR\alpha GP_sB_e$, $\sigma_{S-sp}^2 = 4R^2G\alpha^2P_sB_e\rho_{ASE}$. e is the electron charge, R is the photodetector responsivity given by $R = \frac{\eta e}{h\nu}$, η is the detector quantum efficiency,α is the post amplification loss (loss between the amplifier and the receiver), G is the amplifier gain, P_s is the received signal power, B_e is the receiver bandwidth, ρ_{ASE} is the spectral density of ASE induced noise [45] (pp. 492).

$$\rho_{ASE} = (G-1)n_{sp}h\nu \qquad (4.13)$$

n_{sp} is spontaneous emission factor or population inversion factor [54], for a two level system:

$$n_{sp} = \frac{N_2}{N_2 - N_1} \qquad (4.14)$$

where N_1 and N_2 are the numbers of atoms per unit volume in two energy states (see section 2.1.1).

The noise figure (NF) of a SOA has been defined as same as for electronic amplifiers: it is the ratio of the signal/noise ratios (SNRs) before and after the optical amplification.

$$NF = \frac{SNR_{in}}{SNR_{out}} \qquad (4.15)$$

where

$$SNR = \frac{average\ signal\ power}{noise\ power} = \frac{R^2P^2}{\sigma_{tot}^2} \tag{4.16}$$

The SNR before the amplification is:

$$SNR_{in} = \frac{R^2P_s^2}{2eR\alpha GP_sB_e} \tag{4.17}$$

And the output SNR is:

$$SNR_{out} = \frac{R^2(GP_s)^2}{2eR\alpha GP_sB_e + 4R^2G\alpha^2P_sB_e\rho_{ASE}} \tag{4.18}$$

Assuming the quantum efficiency of the detector is unity and there are no coupling losses to amplifier and detector, the noise figure of a SOA is provided as:

$$NF = \frac{SNR_{in}}{SNR_{out}} = \frac{1}{G} + \frac{2\rho_{ASE}}{h\nu G} = \frac{1}{G} + \frac{2(G-1)n_{sp}}{G} \tag{4.19}$$

For $G \gg 1, n_{sp} \rightarrow 1$, the low limit of NF of an ideal amplifier has a value of 2 or 3dB (10lg (NF)). The noise figure performance of a packaged SOA can be improved by using high coupling efficiency techniques [134]. Recently the invention of quantum-dot SOA has also shown its advantage in controlling noise figure [135].

4.1.3 Dynamics

The basic function of a SOA is to linearly amplify the input optical signal. As discussed in section 4.1.1, if the input signal intensity increases to a certain point, the SOA gain starts to reduce, and then the device is driven into gain saturation/compression (reduction in gain). The duration of the gain recovery largely depends on the interband dynamics of the SOA, which includes spontaneous emission, stimulated emission and absorption, and nonradioactive recombination mechanisms (dominantly Auger recombination processes). Thus the carrier lifetime introduced in Chapter 2 indicates that the gain recovery time of a SOA is hundreds of picoseconds to nanoseconds. If the input signal has sufficient intensity to saturate the gain, and the data period (pulse width) is shorter than gain recovery time, the SOA may cause intersymbol interference (ISI) or TDM crosstalk as the gain for a given data bit depends on the time interval from the previous data bit which is random [46]. To avoid this, the data period should be chosen to be longer than the gain recovery time, to allow the device sufficient time to recover from the saturation state and provide approximately equal gain for each data bit. On the other hand, if the gain recovery time is large enough compared to the data period, the amplifier will operate in the regime of mean power saturation, thus no ISI will incur. For example, the gain recovery time of the EDFA is in the millisecond range, and the general data rate in WDM system where the EDFAs are widely employed, is in the Gigabit per second region (i.e. the data period is in the picoseconds region). Thus, EDFAs are more suitable for high speed optical amplification than SOAs.

Nevertheless, both EDFAs and SOAs may suffer from interchannel interference (or WDM crosstalk) in a multi-wavelength switched environment [136][137], since the transient gain variation will be induced when wavelengths/channels are adding or dropping [138]. Therefore, gain clamping schemes are proposed to address this problem for both EDFAs [139] and SOAs [140]. In Chapter 6, an adjustable gain clamped SOA (AGC-SOA) which would provide adjustable gain over an extended linear amplification regime without sacrifice of output saturation power [141], will be introduced and studied experimentally and numerically.

The dynamic gain characteristics of the SOA, which is harmful to linear amplification, can be used to realise the all optical wavelength conversion and other optical signal processing applications.

Besides the interband dynamics discussed above, the intraband processes are also important to the gain saturation dynamics, especially when the SOA is used to amplify ultra-short optical pulses (< 10 ps) [142]. A pump-probe measurement [143] employing ultra-short optical pulses and a four wave mixing experiment [144] were used to identify the physical processes governing intraband dynamics, and prove that the main intraband processes are spectral hole burning (SHB), carrier heating (CH) and two photon absorption (TPA). When a strong short pulse is injected into a SOA, the stimulated emission will "burn" a hole in the carrier distribution due to carrier depletion at the transition energies, and make it deviate from the Fermi-Dirac distribution. The gain recovery process can be roughly divided into three stages in different timescales (Figure 4.1): carrier-carrier scattering, carrier-phonon interactions, and electron-hole interactions. The carrier-carrier scattering process helps the disturbed carrier distribution to recover back to the quasi-equilibrium Fermi-Dirac distribution, and normally takes ~100 fs (sub-picosecond timescale) [145]. Carrier-carrier scattering also induces instantaneous coherent processes such as TPA and optical Kerr effects. Amongst all the processes, the stimulated emission is the main process that would heat the carrier distributions, and make its temperature higher than that of the lattice. Then the temperature relaxation of the carrier distribution is achieved by the emission of optical phonons with a characteristic time at up to 2 ps [146]. This relatively long temperature recovery process often refers to CH or carrier-phonon interactions. The last stage of the gain recovery is achieved by carrier injection, which is associated by the electron-hole interactions (interband dynamics discussed above), and usually takes hundreds of picoseconds to nanoseconds (it also depends on the design of the active region [47], advanced QW and QD SOAs could achieve faster recovery time which is several picoseconds [135].).

Compared to the interband dynamics which are normally in the order of hundred of picoseconds, the intraband processes are ultrafast. Thus their contributions to gain saturation are often neglected when the input light is at low data rate (< 10 Gb/s, i.e. pulse width is ~100 ps).

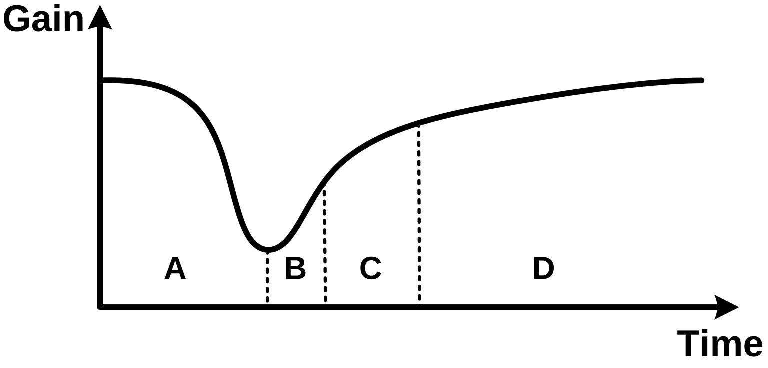

Figure 4.1 Schematic of SOA gain recovery process after saturated by a strong optical pulse. A, B, C, D stands for carrier depletion, carrier-carrier scattering, carrier-phonon interaction and carrier injection process, respectively.

4.1.4 Nonlinearity

Nonlinearity effects can be used to achieve all optical signal processing for ultrafast high speed optical communications. Kerr based optical fibres, materials with a strong second order nonlinear susceptibility $\chi^{(2)}$ (such as AlGaAs) and SOAs are the major nonlinear materials. Especially the powered elements will exhibit higher nonlinearities.

The optical amplification in the SOA relies on the radiative electron-hole recombination processes, which leads to carrier depletion and carrier density distribution variation inside the gain medium. This dynamic carrier density distribution would affect the gain of optical signals propagating in the SOA. Moreover, the refractive index of the active region will also be influenced by the carrier density change. Therefore, the dynamic gain change associated with the refractive index change will bring in a phase change to the amplified optical signals. The Kramer-Krönig relations were used to calculate this effect [147], however it requires long processing time as the material gain coefficient should be integrated over a wide wavelength range [148]. More conveniently, the linewidth enhancement factor [149] or linewidth broadening factor [150] were introduced to characterise this effect. Moreover, the carrier density change will also induce new frequency components and polarization changes to the propagating lights. Besides electron-hole interaction induced strong nonlinearity, others are resulted from Kerr effect and processes like SHB and CH in the SOAs, however they are much weaker.

The main nonlinear effects in SOAs are cross gain modulation (XGM), self and cross phase modulation (SPM and XPM), four wave mixing (FWM) and nonlinear polarization rotation (NPR). These nonlinear effects would be problematic for linear amplification since they may introduce unwanted patterning effects, chirp, frequency components, and polarization rotation etc. Whereas they can be utilized in high speed optical signal processing as described in section 4.2.

4.2 Applications of SOA

4.2.1 Linear Amplification

When the optical power of an input optical signal is not high enough to saturate the SOA, the gain of the device stays nearly constant. This indicates the SOA is operated in the linear region. The SOA can be tailored to meet the specific requirements for the uses as pre-amplifiers, in-line amplifiers, and booster/power amplifiers in optical links. Many techniques have improved the fabrication of SOAs to provide high gain, high output saturation power, low noise, and polarization insensitivity for linear amplification [151]. Also new types of SOAs, such as gain-clamped SOAs and QD-SOAs, have been proposed to achieve better performance.

Linear in-line amplification in the Gigabit-PON is a promising application for SOAs, as traditional EDFAs cannot function over the wavelength band of the upstream traffic in GPON. Furthermore, SOAs have been employed to extend the reach and increase the split ratio of the PON.

4.2.2 Optical Signal Processing

SOAs can also be operated in the nonlinear regime to work as an all optical wavelength converter, 3R regenerator, logic gate, add/drop multiplexer, and an optical delay line. These functions are realized based on four main nonlinear effects in SOAs, which are XGM, XPM, FWM and NPR.

4.2.2.1 Cross Gain Modulation (XGM)

When an optical light (pump light) is injected into the SOA, the optical amplification process would consume the available carrier density in the gain medium. Due to the homogeneous property of SOA gain medium, the gain modulation will take place on the injected light itself (SGM) or any other propagating/probe lights (XGM) inside the SOA. The process is depicted in Figure 4.2, the information carried by the pump light at λ_{Pump} has been transferred to the probe light at λ_{Probe}. As the gain of the SOA is modulated in antiphase to the pump light, the output probe light is modulated with inverted original data. The nonlinear effect can be easily used to achieve all optical wavelength conversion (AOWC) which is expected to become key technique in the future WDM network. Using the wavelength converters would tackle the wavelength congestions at the WDM network nodes, and it will provide flexible network management solutions for the future high capacity complex WDM networks [152].

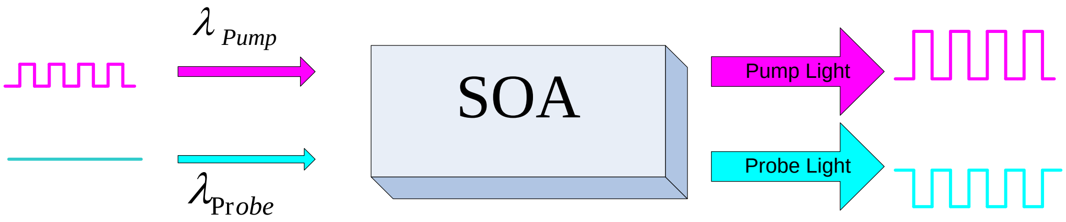

Figure 4.2 Schematic of cross gain modulation (XGM) in the SOA.

The wavelength conversion based on SOA-XGM can be achieved by co-propagation and counter-propagation schemes, i.e. the pump and probe light can be injected into SOA from the same port (co-propagating), or from different ports (counter-propagating). The counter-propagation scheme has an advantage over the co-propagation one as no optical filter is needed to separate the pump and probe light, and the pump and probe light can operate at the same wavelength. However, the counter-propagation scheme suffers from higher ASE noise [153] and narrower modulation bandwidth [154]. And both of two schemes will generate inverted signals in respect to the original pump signal. In Chapter 5, both co-propagating and counter-propagating schemes will be numerically studied.

The bandwidth of SOA-XGM based wavelength converter has been studied extensively both experimentally [155][156] and numerically [48][157]. It shows the frequency response of the wavelength converter exhibits high-pass characteristics, which is beneficial for high data rate operation. And it also indicates that, the bandwidth of the XGM is not restricted by the slow spontaneous carrier lifetime. In fact it depends on the effective carrier lifetime which is affected by the propagation effects. The material parameters of the SOA can be optimized to achieve higher bandwidth, such as increasing the active region length, differential gain, and confinement factor. External measurements such as applying high bias current, high input optical power and cascading SOAs, can also enhance the bandwidth. Wavelength conversion at 100 Gb/s has successfully achieved using a 2 mm long SOA [158], and the speed can be further improved to 170 Gb/s by cascading two SOAs [159]. Recently, the single QD-SOA has demonstrated 160 Gb/s wavelength conversion based on XGM without any patterning effects [160].

There are two limiting factors in the XGM-based wavelength conversion: one is the patterning effect occurred at the high speed data, the other is induced frequency chirp on the output converted signal due to the gain modulation. The first problem can be solved by the proposals discussed above. The output chirped signal can be compensated by using a fiber Bragg grating filter before transmission [161]. However, these instantaneous chirp components on the output signal can be extracted to achieve even higher speed (320 Gb/s) wavelength conversion by placing a filter after the SOA, this will be discussed in next section. Besides wavelength conversion, the XGM effect can be also used to form optical switching gate [162].

4.2.2.2 Cross Phase Modulation (XPM)

According to the Kramer-Krönig relations, the gain modulation introduced by a strong pump light will associate with the refractive index change inside the gain medium. The relation can be approximated by the linewidth enhancement factor (α_H) [150]:

$$\alpha_H = -\frac{4\pi}{\lambda}\frac{\frac{\partial \bar{n}}{\partial N}}{\frac{\partial \Gamma g_m}{\partial N}} \tag{4.20}$$

Where $\bar{n}$ is the modal effective index, N is carrier density, $\mathrm{g_m}$ is the material gain, Γ is the confinement factor. The sign in the expression is chosen to render α_H positive. The typical LEF of SOA can be measured by experiments; the value is range from 2 to 10 [76]. The experimental measurements also indicated that α_H is not a constant factor, it depends on carrier density n and the signal wavelength λ. Since the material gain (g_m) of the SOA is a function of the wavelength, as shown in Figure 2.5. Thus the phase change ($\Delta\phi$) associated with the gain modulation of the input signal at a wavelength λ_0 is given:

$$\begin{aligned}\Delta\phi &= \phi(n_2,\lambda_0) - \phi(n_1,\lambda_0)\\ &= -\frac{\alpha_H(n_1,\lambda_0)}{2}\left(\Gamma g_m(n_2,\lambda_0) - \Gamma g_m(n_1,\lambda_0)\right)L\end{aligned} \tag{4.21}$$

Where n_1 and n_2 are the carrier density before and after perturbation introduced by input signal, respectively.

The phase change ($\Delta\phi$) will inevitably result in frequency variation ($\Delta\nu$) or chirp, it can be expressed as [163]:

$$\Delta\nu = -\frac{1}{2\pi}\frac{\partial\phi}{\partial t} \tag{4.22}$$

Therefore, when a strong optical pulse is injected into SOA, its leading edge saturates the device and reduces the available gain for the trailing edge, the self gain modulation will happen as discussed in the last section. In the meanwhile, the phase change for the leading pulse edge will be different from that of the trailing edge, this leads to self phase modulation (SPM). The SPM results in pulse shape and spectrum shift and distortion. However this effect can also be adopted in the pulse-compression scheme using a dispersive delay line [164].

Similarly, the cross phase modulation (XPM) will take place when two (or more) optical lights are propagating in a saturated SOA. And XPM effect has been widely utilised to achieve wavelength conversion [97], optical logic gate [165], optical signal regeneration [166] and de-multiplexing [167]. These functions can be realized by placing the SOAs in the interferometric setup such as Mach-Zehnder interferometer (MZI), Michelson interferometer (MI), and Sagnac interferometer (SI). Thus the phase change induced by XPM can be converted into intensity by either constructive or destructive interference. The choice of the topologies for realizing XPM depends on the specific applications. However, the MZI configuration is preferable in all optical wavelength conversion and regeneration applications, since it is possible to achieve the functionality on a hybrid integrated platform [97][168] so as to improve the stability of the interferometer and reduce the device size, moreover it could achieve higher modulation bandwidth [169].

The principle of XPM can be explained through its application as a wavelength converter depicted in Figure 4.3. SOAs are placed in both arms of the MZI, and CW light can be split into each arm symmetrically or asymmetrically by a coupler. In the normal operation mode, the signal light is only injected into SOA1; the input intensity will saturate the device, and modulate its refractive index. Thus the optical path length is changed by a half wavelength for the co-propagating CW light in the upper arm of the MZI, and a phase difference will be introduced between the CW lights in the upper and lower arms.

Then the output coupler after the SOAs combines the CW lights where they can interfere constructively or destructively, so as to translate the phase difference caused by the input signal light into intensity modulation of the output light at λ_{CW}.

In the normal operation scheme, the phase difference between two interferometer arms can be affected by the input signal intensity, the operating bias currents and LEF of SOAs. The asymmetric splitters used in some experiments [170] are to ensure an intensity dependent phase difference is obtained between two interferometer arms. Sometimes phase shifters are employed in the interferometer arms for the same purpose.

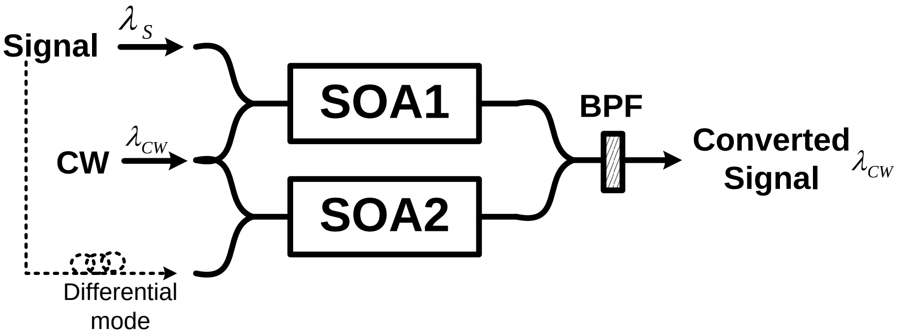

Figure 4.3 Schematic of wavelength conversion based on cross phase modulation (XPM) in the SOA-MZI configuration.

The basic characteristics of the XPM based SOA-MZI wavelength converter can be demonstrated from its optical transfer function as shown in Figure 4.4. The optical transfer function (output converted signal power as a function of input signal power) can be obtained in the experiment [171] where the input signal power increases gradually while the input CW light power and bias currents of both SOAs are set fixed. The optical transfer function is also numerically studied in both time domain [172] and frequency domain [173]. It is obvious from the figure, by increasing the input signal power, the interferometer is shifting from destructive interference state to constructive state. Thus in practice, by adjusting the bias currents of the SOAs, the interferometer could be operated to reproduce either inverted or non-inverted signals in respect to the original input signal at target wavelength. Moreover, the improvement in the extinction ratio of converted signal indicates the SOA-MZI configuration can be adopted to realize signal regeneration [174].

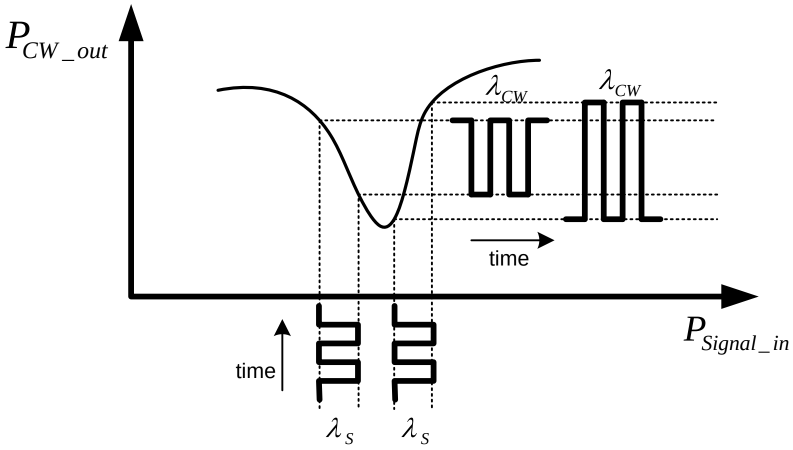

Figure 4.4 Schematic of optical transfer function of SOA-MZI wavelength converter.

The operation speed of XPM based wavelength converters or optical switches, is limited by the slow gain recovery time of the SOA as shown in Figure 4.1. This can be observed from the longer duration of the trailing edges of the output converted signals compared, which may result in ISI at high data rate. To overcome this limitation, the differential mode operation is proposed [169], which introduces another delayed and attenuated replica of the input signal light into the lower arm of the interferometer, so as to create a faster switching window which is shorter than gain recovery time. And the duration of switching window is determined by the optical delay time between the input signals [175]. This can be also achieved in the counter-propagation scheme by spatially displacing the SOAs in both arms [176], however the counter-propagation scheme is not popular since it suffers from lower modulation bandwidth compared to co-propagating one.

The SOA-MZI configuration discussed above can be simplified to include a single SOA, as the polarization-discriminating symmetric Mach-Zehnder (PD-SMZ) or so-called ultrafast nonlinear interferometer (UNI) was proposed [177]. The input light can be split into two orthogonally polarized lights in the PD-SMZ, and they pass through the SOA, then interfere with each other at the output. The 80 Gb/s regenerative wavelength conversion was successfully achieved by using this configuration [178]. A higher speed wavelength conversion can be realized in another variation of the differential MZI configuration, as a delayed interference signal-wavelength converter (DISC) was proposed [179] including a single SOA and a passive asymmetric MZI. 100 Gb/s wavelength conversion was achieved using a fully integrated and packaged SOA delayed-interference configuration [180]. And 168 Gb/s wavelength conversion was obtained using hybrid DISC implementation [165]. Since the delayed interferometers used in these experiments act as filters, a theoretical study was conducted to discover the enhancement in the modulation bandwidth of SOA-based switch using an optical filter [181], the analysis was performed in both time and frequency domain.

As discussed before, due to the nonlinearity of the SOA, instantaneous chirp components will add on the output amplified light. The leading edges of the converted light are red shifted, while the trailing edges are blue shifted. The red-chirped and blue-chirped components can be extracted to obtain non-inverted [182] and inverted [183] wavelength conversion respectively, by using an optical filter. Therefore, wavelength conversion at 160 Gb/s was demonstrated using a single SOA, an optical band filter and a passive delayed interferometer [184]. By using this configuration, the fast blue-chirped frequency components are filtered to obtain inverted wavelength conversion by the optical filter, and the following delayed interferometer is used to change polarity of the converted signal so as to achieve non-inverted wavelength conversion. However the output optical signal-to-noise ratio (OSNR) is reduced significantly [185]. Later even higher speed (at 320 Gb/s) was achieved by adding a FBG into the existing configuration [186]. The same mechanism is also employed to achieve ultrafast signal processing [187][188].

4.2.2.3 Four Wave Mixing (FWM)

Generally, four wave mixing (FWM) refers to nonlinear optical processes with four interacting electromagnetic waves, e.g. with three input waves to generate the fourth wave. As shown in Figure 4.5, two pump lights at angular frequencies ω_1 and ω_2, together with the signal at ω_3, will mix to produce a fourth conjugate signal (or FWM signal) at $\omega_c = \omega_1 + \omega_2 - \omega_3$. When the frequencies of the two pump lights are identical, the process can be referred to as the degenerate FWM. As depicted in Figure 4., a strong pump light at an angular frequency ω_1 and a signal light at angular frequency ω_2 are injected into SOA, both of two lights are at the same polarization. The carrier density and distribution in the gain medium will be modulated by the beating of the input light intensities. Therefore a dynamic population grating [189] is formed, which affects the gain and refractive index of input lights. Thus new frequency components will be created during the interaction between the gain and index gratings and the input lights. The new frequency component at an angular frequency $\omega_c = \omega_1 + (\omega_1 - \omega_2)$ is of most interest, and it is named as conjugate signal (or FWM signal). The $\Delta\omega = \omega_1 - \omega_2$ in the figure denotes frequency detuning between the pump and signal lights. The FWM conversion efficiency is defined as the ratio of the conjugate signal power to the input signal power.

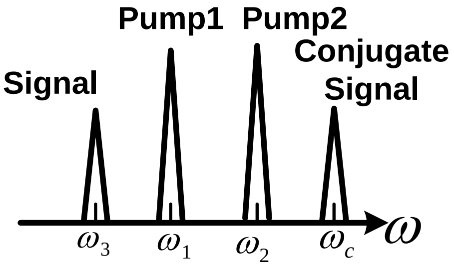

Figure 4.5 Additional signal ($\boldsymbol{\omega_c = \omega_1 + \omega_2 - \omega_3}$) generated through the four wave mixing process. (Output satellite signals are omitted.)

Figure 4.6 Schematic of the degenerate four wave mixing process in the SOA (output satellite signal at a frequency of $\boldsymbol{2\omega_2 - \omega_1}$ and ASE spectrum are omitted).

The population grating formed in the active region of SOA is affected by the both interband and intraband dynamics [190]. The main physical mechanisms include electron-hole recombination, spectral hole burning and carrier heating. The interband dynamics is the dominant process at a small detuning (MHz ~ GHz) between the pump and signal lights. Since the characteristic time of the interband process (equal to effective carrier lifetime τ_{eff}) is in the region of hundreds of picoseconds to nanoseconds, it indicates the carrier density modulation would be very effective within the MHz to GHz detuning range. Therefore high FWM conversion efficiency can be achieved within the range. As the detuning increases, the conversion efficiency rolls off quickly, and the ultrafast intraband dynamics becomes important [191].

The FWM effect in SOAs can be used to realize wavelength conversion as the produced conjugate signal is a copy of input signal. An optical filter centred at ω_c after the SOA could help to obtain the converted light, whereas no external filter operation was also demonstrated [192][193]. Compared to XGM and XPM based wavelength conversion in SOA, the FWM based one has advantages such as simple configuration, multi-channel operation at high speed [194]. And it is transparent to modulation format. However the FWM based scheme is polarization sensitive, the polarization states of the pump and signal should be controlled to be the same before injection, which is not practical in the real scenario. This issue can be addressed using two pump lights with parallel or orthogonal polarization [195] instead of one.

The FWM effect in SOA is also used to achieve mid-span spectral inversion (MSSI) so as to compensate the chromatic dispersion accumulation during long distance transmission in the fibre [196], since the phase conjugation has occurred due to FWM. It is also worth to mention that the SOAs can be employed to realize slow and fast light (SFL) propagation thanks to the coherent population oscillations (CPOs) which is strongly associated with nonlinear effects such as XGM, XPM and FWM [197]. The SFL propagation mechanism can be adopted to construct the tunable optical delay lines and phase shifters for microwave photonics [198]. Moreover, the FWM effect is employed in optical de-multiplexing [199] and sampling [200].

4.2.2.4 Nonlinear Polarization Rotation (NPR)

A lot of work has been carried on with the XGM, XPM and FWM effects and their applications. However, the underlying mechanism of nonlinear polarization rotation still stays obscure. In this part nonlinear polarization rotation phenomena in SOAs will be discussed, and applications in all-optical signal processing based on this nonlinearity will be reviewed.

The polarization sensitivity effect of SOAs consists of two parts: gain and phase dependence on polarization. In general gain dependence on polarization is due to asymmetric structure of active region in SOAs, which results in the difference in confinement factor of Transverse Electric (TE) mode and Transverse Magnetic (TM) mode. Excluding some specialized applications, gain insensitivity to polarization state is a fundamental requirement for fabricating SOAs.. Many approaches such as using tensile strained bulk SOAs [83] or Multi quantum-well (MQW) SOAs with tensile and compressively strained wells [87] could suppress polarization-dependent gain sensitivity. On the other hand, the phase dependence on polarization state is due to birefringence in SOAs, both asymmetric waveguide geometries induced intrinsic birefringence and carried density change induced birefringence will result in refractive indices difference between TE and TM mode. The phase difference between TE and TM mode can be substantial ($> \pi/2$) for a very small index difference (of the order of 2×10^{-4} for a 2-mm long device at 1550 nm) [201]. In the pump-probe scheme, the probe light will experience the variation of gain and state of polarization (SOP) as pump light is also injected into SOAs. This phenomenon is named nonlinear polarization rotation (NPR).

Many experimental studies have been carried out to study the NPR effect. Soto et al. [201] employed a pump-probe co-propagation configuration to explore the birefringence evolution of a SOA with input power and polarization. This demonstrated that the device birefringence would be greatly affected by the input power, and this effect would be further enhanced by using TE or TM polarized pump wave. Manning et al. [202] have measured the nonlinear polarization changes in SOAs; Kennedy et al. [203] investigated the gain and birefringence along the two eigenmodes of the component waveguide with and without injection. Philippe et al. [204] use a free-space pump-probe count-propagation setup to explore the polarization-dependent gain dynamics and the dynamics of the change of the SOP. The experiments were divided into two parts: signal injected along the eigenmodes and linearly polarized at orientations of $45^{\circ}$with respect to the eigenmodes of the device. In the first part, probe and pump beams were injected along the eigenmodes of the device and their SOP stay unchanged throughout the propagation. However, the gain switching is sensitive to the SOP of the input signals. In general the co-polarized probe and pump beams configuration ($TE_{Probe}TE_{Pump}$ or TM_{Probe} TM_{Pump}) experiences large gain compression compared to cross-polarized configuration ($TE_{Probe}TM_{Pump}$ or TM_{Probe} TE_{Pump}). Due to slower interband effects, the TE co-polarized mode is preferred for ultrafast gain switching despite the TM co-polarized mode displays a higher gain compression. The second experiment proved that polarization switching can be optimized by set pump and probe signals linearly polarized at 45° with an output polarizer oriented at 45°.

Several models have been set up for simulating this nonlinear phenomenon. Alvarez et al. [205] introduced confinement factor dependence on the carrier density in long bulk SOA. Zhao et al. [206] investigated the polarization variations of probe light as a function of its own power and the bias current of SOA, but this model cannot applied into pump-probe scheme due to only probe light was involved. Soto et al. [201] studied the phase-shift efficiency in terms of pump and probe light polarization in a pump-probe scheme. Takahashi et al. [207] published results on polarization dependent gain in SOAs in terms of optical switching and optical bistability based on a microscopic model. Dorren et al. [208] thought Takahashi's model was impractical as a design tool for optical switching configuration. Thus they demonstrated a simple rate-equation model for polarization dependent gain saturation in strained bulk SOA, and applied it to all-optical flip-flop memories. Yang et al. [209] extended Dorren's model and described polarization dependent nonlinear gain saturation introduced by sub-picosecond optical pulses. Guo et al. [210] utilized Mueller matrix and Stokes vectors to investigate the SOP of the transmitted light inside a polarization-insensitive SOA with a conventional pump-probe scheme. According to the experimental findings, related theoretical study should be addressed to polarization gain dynamics and dynamics of SOP in future.

Nonlinear Polarization Rotation would cause negative impacts in some applications such as: it reduces the conversion efficiency in the SOA-based four wave mixing wavelength conversion [211], decreases switching contrast ratio of the SOA-based nonlinear loop mirror [212], introduces additional spectral broadening to ultra-short optical pulse in SOAs [213]. However, the performance of applications based on SOA nonlinearity can be improved significantly by proper polarization configuration [202]. Some theoretical studies also explore the impact of NPR on other nonlinear schemes in SOAs [214]. Moreover, SOA based nonlinear polarization rotation can also be applied into all-optical signal processing in telecommunication networks, such as wavelength conversion [215][216][217], demultiplexing [218][219], optical logic gate [201][220][221][222], and optical signal regeneration [206][223].

Application as Wavelength Converter and Optical Signal Regenerator

All-optical wavelength conversion is expected to be a key technology in the future broadband networks. SOA based cross-gain modulation (XGM), cross-phase modulation (XPM) and four-wave mixing (FWM) approaches have been applied into wavelength conversion. Inverted wavelength conversion achieved by cross-gain modulation suffers degradation of the extinction ratio. Interferometric wavelength converters based on cross-phase modulation in combination with XGM could solve the extinction ratio degradation problem and can be realize both inverted and non-inverted conversion, however the cost and reliability may be the issues for this interferometric device. FWM wavelength converters operate independently of modulation format unlike XGM and XPM devices, and can be utilized in high speed conversion without compromising extinction ratio. Whereas FWM scheme efficiency are dependent of signal-pump detuning, and the inherent polarization sensitivity is a concern with this approach. As an example of an all-optical wavelength converter based on NPR, the pump-probe counter-propagating configuration is discussed here. Figure 4.6 shows schematically the set-up of a SOA-NPR wavelength converter. The polarization of probe beam is set to be at an angle (typical 45°) to the TE axis by the Polarization Controller 1 (PC1) before it is coupled into SOA. The Polarization Controller 2 (PC2) before the polarization beam splitter (PBS) is used to control the probe transmission. At the outset the PC2 is aligned to prevent the probe beam passing through the PBS when only the probe beam is present. When a high intensity pump beam is also injected into SOA, the saturated SOA will display additional birefringence which would cause polarization rotation of probe beam. Thus some probe beam will pass through the PBS; the non-inverted wavelength conversion scheme is achieved. Whereas inverted wavelength conversion can be realized by setting the PC2 to let the probe beam pass through the PBS maximally. Wavelength conversion based on NPR can achieve both inverted and non-inverted conversion, high extinction ratio, and operation over a large wavelength range (S- to C/L-band wavelength up-conversion realized by using this scheme [217]).

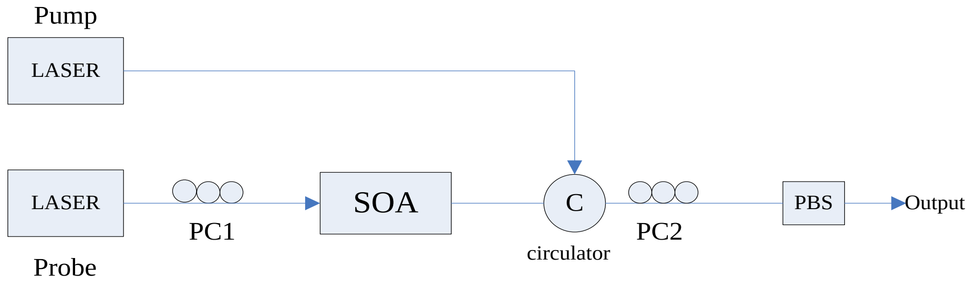

Figure 4.6 Set-up of a SOA-NPR wavelength converter.

All-optical 3R-regeneration consists of signal re-amplification, re-shaping and re-timing. It is used to alleviate the accumulation of transmission impairments so as to increase the maximum transmission distance and cascadability. The pulse regeneration data rate of 80

Gb/s has been achieved by using SOA-XPM [178]. Zhao *et al.* [206] proposed an all-optical 2R-regeneration scheme based on SOA-NPR. It is known that there is no polarization rotation within the linear regime of SOA. Therefore when signal light is propagating in the SOA, polarization controller and polarizer after SOA are set to block the low power signal (logical “0”) and release the high power light (logical “1”) . Under this scheme, the SOA provides re-amplification, re-shaping function. Similar to Wavelength Conversion based on SOA-NPR, 3R-regenration can be achieved by injecting a re-timed pulse train together with signal light into SOA [223]. However the signal speed is limited at 10Gbit/s.

Application as De-multiplexer

The de-multiplexer (DEMUX) is used to drop one or more desired channels of the TDM data signal. DEMUX devices should be stable Bit-Error-Free operation, low control power, and polarization insensitivity. SOA based cross phase modulation and four wave mixing can be utilized in realizing DEMUX. The nonlinear polarization rotation can also been applied. Patrick *et al.* [218] performed that 10 Gbit/s channel can be extracted from a 20Gbit/s data signal using this scheme. By optimizing the operation configuration such as shorten the clock pulse, Stephens *et al.* [219] achieved higher demultiplexing speed. In the method based on SOA-NPR, signal light is injected into SOA along with clock pulses which would cause periodic change of carrier density in SOA. Namely the present of clock pulses results in polarization rotation of the signal light. A polarizer is set after SOA as a discriminator to block the signal pulses don’t experience polarization rotation. Therefore, the demultiplexing is achieved.

Application as optical logic gate

All-optical logic gates which can perform logic operations will also play an important role in future all optical networks. All-optical AND, XOR, and NOT XOR gates have been realized based on SOA-NPR by Soto *et al.* [220][221][222]. Figure 4.7 shows the setup for a SOA-NPR XOR gate. In this scheme, both input lights are set at the same power, polarization and wavelength. A combination of polarisation compensator/controller and polarizer are used to control the signal transmission after the SOA. When both input lights are injected into SOA, compensator and polarizer are tuned to block the signal output. When only one input light is propagating in SOA, the SOP of the output light will change due to input light intensity variation. Thus the output signal cannot be block totally by the polarizer, the output will be logical “1”. When none of light is injected, the output power will be null. Therefore, the all-optical XOR gate is realized.

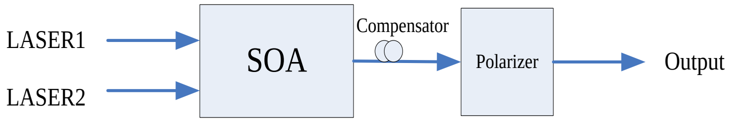

Figure 4.7 Set-up for a SOA-NPR XOR gate.

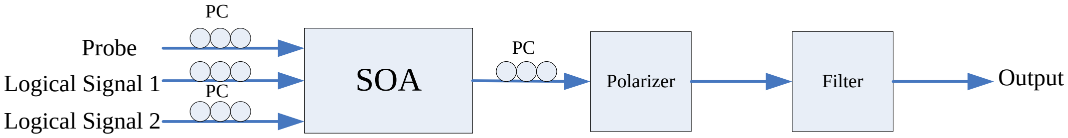

Figure 4.8 Set-up for a SOA-NPR AND gate.

The all-optical AND gate configuration is schematically demonstrated as Figure 4.8. A probe light is employed in this scheme. The filter centered at the probe wavelength will block the input logic signal. Polarization controllers are tuned to block the SOA output signal through the polarizer, when both logical signals are not at high power level (logical “1”). This SOA-NPR based AND gate can work in the gigahertz regime.

The all-optical NOT XOR gate experimental setup is similar to AND gate showed above. By setting the logical signal linearly polarized at an angle between 80° and 90° and probe light at 105°, the NOT XOR gate can be achieved [222].

This section discussed nonlinear polarization rotation based on semiconductor optical amplifiers and applications in all-optical signal processing. Nonlinear polarization rotation has negative impacts on some applications, however experimental results reviewed have predicted that the performance of signal switching based on SOAs would be improved significantly by certain polarization configuration. Moreover nonlinear polarization rotation can be implemented into various applications in all-optical networks like other nonlinear effects in SOAs. SOA-NPR based applications have advantages over other schemes, but the manual polarization control and relative low switching speed would be drawbacks for that. In the theoretical study, the characterization of the dynamics of state of polarization and its effect on other nonlinear schemes such as XGM, XPM and FWM are needed to be further explored.

4.3 Summary

This chapter discussed some basic characteristics and key applications of SOAs. Firstly, through analytical expression deduction, the SOA gain and saturation, noise figure have been discussed. The expressions obtained in the chapter will be used to analyse SOA and AGC-SOA performance in the next two chapters. Secondly, the SOA dynamics is also introduced, especially the intraband dynamics is reviewed. In the end, the applications of SOAs are divided into linear amplification and optical signal processing which is largely taking advantage of SOA's nonlinearities, i.e. cross gain modulation, cross phase modulation, four-wave mixing and nonlinear polarization rotation effects. In each nonlinear effect, the physics origin is shortly discussed, and its applications in optical signal processing are then briefed. It worth noting that, the optical signal processing based on nonlinear polarization rotation is becoming the research focus in recent years, however the review work in this field is rare. This is the major rationale behind this part of the work.

Chapter 5 Modelling of SOAs

5.1 Introduction

Modelling of Semiconductor Optical Amplifiers (SOAs) has attracted considerable attention within the research community for more than two decades. Modelling is a very important tool for designing and developing SOA devices and where use in the communication system. This is because it provides information how the device and system would perform if actually implemented. With modelling, the parameters of the device and system can be changed, tested, and ultimately optimized. It's a cost-effective way for research and development.

Generally, SOA models can be classified in different ways [224]. According to their internal physical properties, SOA models are divided into bulk, quantum well and quantum dot models. In terms of modelling representation space, SOA models can be classified into time domain (TD) and frequency domain (FD) models. Moreover, SOA models can be separated into system level and device level simulations by the complexity and usage of the model. The system level SOA models are concerned about the simulation efficiency, and usually work as a component in the communication system simulation, while device level SOA models puts more attention into simulation accuracy in order to investigate the device level physical characteristics. The present research is carried out under the last criterion.

5.2 Basic Principles and Equations

The SOA models are consisted of a set of equations which describe physical phenomena such as pulse propagation, light-matter interaction in the active region, etc. These equations can be solved either analytically or numerically. Analytical solutions were introduced in Chapter 4. The following discussion will focus on the numerical analysis in both system and device level models. First of all, the equations which are employed in both models will be deduced.

Propagation Equation

The propagation of the electromagnetic field inside the SOA is governed by the wave equation as follows, which can be deduced from Maxwell's equations [3].

$$\nabla \boldsymbol{E} - \frac{\epsilon}{c^2} \frac{\partial^2 \boldsymbol{E}}{\partial t^2} = 0 \tag{5.1}$$

ϵ is the dielectric constant, which is given by $\epsilon = n_b^2 + \chi$. n_b is the background refractive index, the susceptibility χ is a function of the carrier density N:

$$\chi(N) = \frac{\bar{n}}{\omega_0} c(\alpha_\mathrm{H} + i) a_d (N - N_0) \tag{5.2}$$

Where $\bar{n}$ is the effective mode index, ω_0 is the angular frequency of the injected light, α_H is the linewidth enhancement factor (Equation 4.20), a_d and N_0 is gain coefficient and carrier density at transparency point (Equation 4.1).

In order to simplify the analysis, the SOA discussed here is assumed to be an ideal travelling wave amplifier, and its active region supports a single waveguide mode. When linearly polarized light is injected into the SOA, assuming it maintains linear polarisation during propagation, its electric field inside the amplifier can be expressed as [163]:

$$\boldsymbol{E}(x, y, z, t) = \frac{1}{2} \hat{x} \{ F(x, y) A(z, t) \exp[i(k_0 z - \omega_0 t)] + c.c. \} \tag{5.3}$$

Where $\hat{x}$ is the polarization unit vector, $F(x, y)$ is the waveguide-mode distribution. $A(z, t)$ is the slowly-varying envelope associated with the optical pulse. k_0 is the propagation constant which equals to $\bar{n}\omega_0/c$. Substituting (5.3) in (5.1), neglecting the second derivatives of $A(z, t)$ with respect to z and t, and integrating over the transverse dimensions, two equations can be obtained:

$$\frac{\partial^2 F}{\partial x^2} + \frac{\partial^2 F}{\partial y^2} + (n_b^2 - \bar{n}^2) \frac{\omega_0^2}{c^2} F = 0 \tag{5.4}$$

$$\frac{\partial A}{\partial z} + \frac{1}{v_g} \frac{\partial A}{\partial t} = \frac{i \omega_0 \Gamma}{2 \bar{n} c} \chi A - \frac{1}{2} \alpha A \tag{5.5}$$

where $v_g = c/n_g$ is the group velocity and the group index $n_g = \bar{n} + \omega_0 (\partial \bar{n} / \partial \omega)$. The solution of Equation 5.4 provide the transverse distribution $F(x, y)$ and the effective mode index $\bar{n}$. Equation 5.5 governs the evolution of the pulse amplitude along the SOA length, which is essential for both system level and device level SOA models. Please note the group velocity dispersion (GVD) effect is not taken into account in Equation 5.5, as the pulse width discussed here is larger than 1 ps (the current typical data rate in a PON system is 2.5 Gb/s, which suggests its pulse width is on the order of hundreds of picoseconds). For analyzing subpicosecond pulse amplification in the SOA, a term containing $\partial^2 A/\partial t^2$ should be added into the LHS of Equation 5.5 account for GVD. Moreover, other ultrafast effects such as gain dispersion ($\partial g/\partial \omega, \partial^2 g/\partial \omega^2$), intraband dynamics (CH, SHB and TPA) should be considered accordingly [225][226][227][228]. Since this topic is beyond the scope of the thesis, only Equation 5.5 will be employed in the following discussion.

Substituting (5.2) into (5.5), and using the SOA gain expression:

$$g(N) = \Gamma g_m = \Gamma a_d(N - N_0) \tag{5.6}$$

Equation 5.5 can be transformed as:

$$\begin{aligned} &\frac{\partial A(z,t)}{\partial z} + \frac{1}{v_g}\frac{\partial A(z,t)}{\partial t} + \frac{1}{2} i\alpha_{\mathrm{H}} g A(z,t) - \frac{1}{2} g A(z,t) \\ &= -\frac{1}{2}\alpha A(z,t) \end{aligned} \tag{5.7}$$

This can be further simplified by making the transformation [131] (pp364):

$$Z \equiv z \tag{5.8}$$

$$T = t - \frac{z}{v_g} \tag{5.9}$$

Where Z and T refer to coordinates in the moving pulse frame, and the delayed time coordinate T is essentially centered on the pulse's arrival time at each plane Z. Therefore the second term on the LHS of the Equation 5.7 can be removed in the new coordinate system:

$$\frac{\partial A(Z,T)}{\partial Z} = \frac{1}{2}(g - \alpha)A(Z,T) - \frac{1}{2} i\alpha_{\mathrm{H}} g A(Z,T) \tag{5.10}$$

Note the pulse amplitude P and phase information ϕ can be separated as:

$$A(Z,T) = \sqrt{P(Z,T)}\exp\left(i\phi(Z,T)\right) \tag{5.11}$$

By substituting (5.11) into (5.10), the pulse propagation equation can be deduced as:

$$\frac{\partial P}{\partial Z} = (g - \alpha)P \tag{5.12}$$

$$\frac{\partial \phi}{\partial Z} = -\frac{1}{2}\alpha_{\mathrm{H}} g \tag{5.13}$$

There have been many papers on the subject of modeling SOAs throughout the years, which provide various different kinds of propagation equations to simulate the pulse evolution in the active region of the SOA. However, most of papers didn't provide the detailed derivation process. In order to avoid confusion, the underlying consistency of the propagation equations in former publications is explored as follows.

(I) Comparing Equation 5.10 with Equation 27, 28 in [229]

In the Marcuse's paper [229], the traveling-wave amplitudes inside the amplifier obey the following differential equation:

$$\frac{db^{+}(z)}{dz} = \frac{1}{2}(g_s - \alpha)b^{+}(z) - i\beta b^{+}(z) \tag{5.14}$$

Where $b^{+}(z)$ is amplitude coefficient of the wave traveling from left to right in a SOA, the propagation equation for $b^{-}(z)$ representing the backwards wave will not be discussed repeatedly. g_s is the SOA gain expression, same as Equation 5.6. β is the propagation constant as k_0 introduced above. In electromagnetic theory, the propagation constant represents the phase change per unit propagation distance along the path travelled by the wave, i.e. $\beta = k_0 = -\frac{\partial \phi}{\partial z}$. The sign in the definition is chosen to render β positive. By using Equation 5.13, Equation 5.14 can be transformed as:

$$\begin{aligned}\frac{db^{+}(z)}{dz} &= \frac{1}{2}(g_s - \alpha)b^{+}(z) - i\left(-\frac{\partial\phi}{\partial z}\right)b^{+}(z) \\ &= \frac{1}{2}(g_s - \alpha)b^{+}(z) - \frac{1}{2}i\alpha_{\mathrm{H}}g_s b^{+}(z)\end{aligned} \tag{5.15}$$

This proves the propagation equation deduced above is consistent with the one in [229]. The equation proposed in [229] has been widely cited by other researchers as M. J. Adam [230] and M. J. Connelly [231], who laid the foundations of the numerical SOA model.

(II) Comparing Equation 5.12 with Equation 28 in [232]

In another paper from M. J. Connelly [232], the following differential equation was given:

$$\frac{dN_{sig}}{dz} = (\mathit{\Gamma} g_m(v_s, n(z) - \alpha_s))N_{sig} \tag{5.16}$$

Where v_s is signal light frequency, $n(z)$ is carrier density along z, α_s is internal loss. Unlike Equation 5.12, the Equation 5.16 is used to describe N_{sig} , which is the mean signal photon rate within the cavity.

$$N_{sig} = \frac{P_{in}}{hv_{sig}} \tag{5.17}$$

P_{in} is the input signal power and hv_{sig} is the signal photon energy. Substituting (5.17) into (5.16), the equation can be transformed:

$$\frac{dN_{sig}}{dz} = \frac{1}{hv_{sig}}\frac{dP_{in}}{dz} = (\mathit{\Gamma} g_m(v_s, n(z) - \alpha_s))\frac{P_{in}}{hv_{sig}} \tag{5.18}$$

Removing identical components from both sides of Equation 5.18, it is clear that Equation 5.16 is consistent with 5.12. Using the same method, Equation 4.3 in Chapter 4, which describes input signal intensity I, can be deduced.

By comparison, it is found that the basic propagation equation such as (5.10), (5.12) can be tailored to meet different requirements, e.g. including or excluding phase change information in the SOA model. It can be also adapted to demonstrate specific parameters, such as input signal power, mean signal photon rate, or signal power density [233] (refer to Equation 5.21). Depending on the objectives of the model, choosing the right form of the propagation equation can dramatically influence the processing efficiency.

Carrier Density Rate Equation

As introduced in Chapter 4, the carrier density rate equation is used to describe the SOA carrier density variation in the conduction band. The general carrier density rate equation can be expressed as [234]:

$$\frac{\partial N}{\partial t} = R_{pump} - R(N) - R_{st} \tag{5.19}$$

Similar to laser diodes, the external current injection is used to create the population inversion which would produce gain in the SOA. The first term on the RHS of Equation 5.19, R_{pump} represents the rate of addition to carrier density in the active region of a SOA from external pumping (in this case it is bias current). The second term on the RHS of equation is known as recombination rate in the active region, including both radioative and nonradiative recombination, which was introduced as Equation 2.39. R_{st} is the net stimulated emission rate caused by the propagating optical signal and amplified spontaneous emission. The latter two terms decrease the carrier density in the active region. On the LHS of (5.19), $\frac{\partial N}{\partial t}$ represents overall carrier density variation rate. Setting the time derivative equal to zero, the steady-state carrier density rate equation can be obtained. This is widely used in developing analytical steady-state SOA models [230][235]. However, the time derivative term in the rate equation does not necessarily need to be set to zero to build the steady-state model, as the equation can also be solved numerically [231]. In the dynamic SOA model, the time derivative should not be treated as zero (or even approximate to zero), therefore the rate equation can only solved numerically. In common with the propagation equation discussed before, the rate equation has many variations which have been employed in former publications, depending on the complexity of the model. The simplified rate equation is used in the system level SOA models which will be discussed, whereas the rate equation in the device level model is more rounded. The consistency of these two equations will also be given.

5.3 System Level SOA Models

The system level SOA model is usually purposely built as a simulation block in an optical communication system model, in which optical light can be generated using the Laser rate equations [131], and light transmission characteristics in the fibre can be analysed using the nonlinear Schrödinger equation [236]. After optical signals are coupled into the SOA block, the changes of lights are governed by both the propagation equation and carrier density rate equation. As the optical signals travel through the device, the interaction between light and matter takes place, which introduces variation in the carrier density distribution in the active region, and changes in the amplitude, frequency, phase and polarization of the output signal. At the output of the SOA block, these signals will be passed onto the following blocks for further processing.

As introduced in Chapter 4, SOAs are versatile, and can be employed to function as amplifiers, wavelength converters, and switches, etc. In some cases, cascaded SOAs achieve a better performance than single SOAs [237][238]. As the photonic integration techniques improve, more SOA chips can be integrated in a circuit. In the paper [239], the optical packet switching system is formed by 8 SOAs. Therefore, in this scenario, the simplicity of the SOA model is essential for the whole simulation system. The system level SOA model introduced below meets this goal.

Generally, the system level SOA model is a dynamic model, in which the time derivative term of the rate equation is not treated as zero. The basic rate equation 5.19 can be expanded as [233]:

$$\frac{\partial N}{\partial t} = \frac{J}{qV} - R(N) - v_g g_m S - S_{ASE}(N(z,t)) \tag{5.20}$$

where J denotes injection current density, q the electron charge, V is the active region volume. The last two terms on the RHS of the equation 5.20 are the net stimulated emission rate caused by the propagating optical signal and amplified spontaneous emission respectively. S is the signal power density (also known as photon density in some literature),

$$S = \frac{\Gamma P}{\hbar \omega_0 v_g A_{cross}} \tag{5.21}$$

where A_{cross} is the cross section area of active region. Substituting Equation 5.21 into Equation 5.20, the detailed rate equation can be obtained.

$$\frac{\partial N(z,t)}{\partial t} = \frac{J}{qV} - R\big(N(z,t)\big) - \sum_{i} \frac{\Gamma g_{m_i}(N(z,t))}{\hbar\omega_i A_{cross}} \overline{P_i} - S_{ASE}(N(z,t)) \tag{5.22}$$

The subscription i denotes the number of the injected optical lights, as the model could process multiple lights simultaneously. $\overline{P_i}$ is the averaged optical power over a selected distance along the longitudinal path inside the active region. The reason for introducing the average power into the calculation is related to the multi-sectional structure in the SOA model which will be discussed in next section.

When the system level model is used to evaluate the nonlinear effects or applications of SOAs, the saturation of the SOA mainly depends on the input optical power, thus carrier density depletion produced by ASE power can be neglected. In order to simplify the system level model, the last term on the RHS of equation (5.22) is normally omitted, which is the main difference from the device level model.

Based on Equation 5.12, the propagation equations for input optical signals travelling along the SOA can be written as following:

$$\pm \frac{\partial P_i(z,t)}{\partial z} = \{\Gamma g_{m_i}[N(z,t)] - \alpha\} P_i(z,t) \tag{5.23}$$

Where + and – represent a wave propagation in + z and – z direction, $g_{m_i}[N(z,t)]$denotes the material gain coefficient at the wavelength λ_i and the carrier density $\mathrm{N(z,t)}$.

In order to improve the simulation efficiency, the SOA material gain coefficient in the system level model is described by a cubic formula with empirically determined constants [130].

$$g_{m_i}(N) = g_N(N - N_t) - \Upsilon_2(\lambda_i - \lambda_p)^2 + \Upsilon_3(\lambda_i - \lambda_p)^3 \tag{5.24}$$

$$\lambda_p = \lambda_{ref} - k_0(N - N_t) \tag{5.25}$$

g_N is the differential gain, N_t is the transparent carrier density, λ_p is the peak wavelength at carrier density N, Υ_2 is the constant determining the gain bandwidth and Υ_3 is the constant accounting for the asymmetry of the gain curve. λ_{ref} is the peak wavelength at transparency. k_0 is a constant characterizing the gain peak shift.

This material gain expression is relatively more accurate than Equation 5.6, as it takes more factors into account. Although the material gain expression introduced in Chapter 2 (2.32) enjoys a higher accuracy, it also suffers from longer processing time compared to the cubic formula. It should also be noted that the empirical expression of material gain coefficient used in system level model is accurate when the input signal wavelength is not far from the central wavelength. To evaluate the gain coefficient accurately over a wide band of wavelength, a detailed wideband expression will be introduced in the device level model.

In the following, firstly, the system level model will be deployed into analysing wavelength conversion in the SOA. Depending on the propagation directions of the pump and probe light inside the SOA, the system level model is classified into co-propagation and counter-propagation models. Secondly, the system level model will be used to evaluate the performance of the SOA, the comparisons between simulation and experimental results will be given. Finally, the direct modulation response of a SOA will be investigated using modified system level model.

5.3.1 Co-propagation SOA Model

The SOA system level model equations introduced in previous section can be solved using Matlab®. The following section will present the results of this model demonstrating its effectiveness by applying the model to all optical wavelength conversion (AOWC) which was discussed in Chapter 4.

All optical wavelength conversion is a technique used to convert an optical signal from one wavelength to another wavelength. SOAs can realize the wavelength conversion through nonlinear effects such as cross gain modulation (XGM), cross phase modulation (XPM), four wave mixing (FWM) and nonlinear polarization rotation (NPR). Amongst all of these methods, wavelength conversion based on XGM is the easiest to understand. The signal light (also known as pump light) and the probe light (normally a CW beam at the desired target wavelength) are injected into a SOA. When the signal light is at a high level (namely signal "1"), the SOA will be driven into saturation, then the probe light will receive less gain compared to when the signal light is at a low level (signal "0"). In this way, an inverted image of the signal light is transferred on to the probe light. The effect is schematically displayed in Figure 5.1.

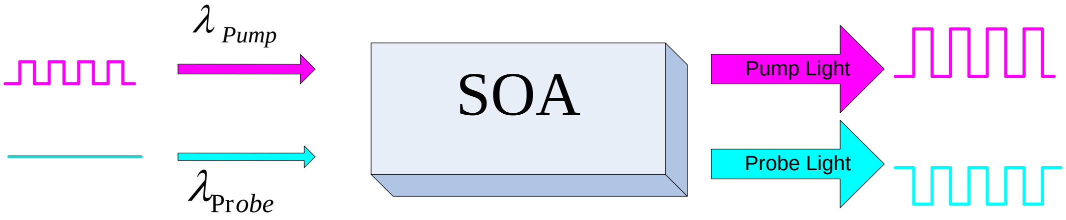

Figure 5.1 Schematic of cross gain modulation (XGM) in the SOA (Co-propagation).

The co-propagation model of a SOA is preferred in the system level simulation, as the model follows an input-output approach and the computation time is relatively short. In the model, the pump and the probe light are injected into the SOA at the same port. Therefore, the longitudinal carrier density, photon density and refractive index of the SOA change simultaneously as the input signals travel along the SOA. In order to simulate the internal changes accurately, the SOA active region is divided into n parts, as can be seen from Figure 5.2.

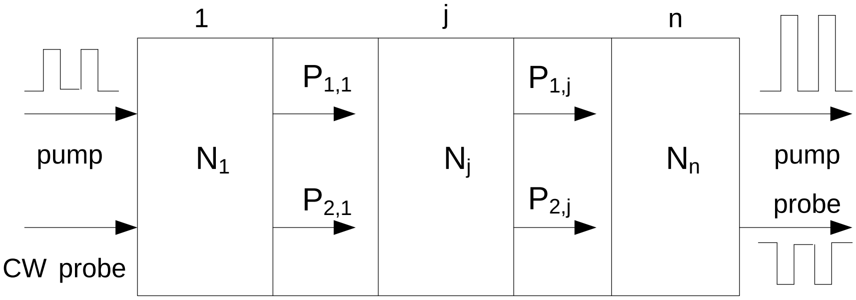

Figure 5.2 Multi-section co-propagation model of SOA.

As the active region is divided into n parts, if the section number is big enough, the carrier density, photon density and refractive index within each section can be treated uniformly, which means there is no change within the section. However, all the conditions are different from one section to another. The accuracy of simulation results can be improved to some extent by increasing the number of divided sections, however the computation time will rise accordingly. As shown in Figure 5.2, the carrier density in each section is represented by N_j (j=1, 2… n). The averaged optical power $\overline{P_{i,j}}$ in each section is calculated by:

$$\overline{P_{i,j}} = \frac{1}{\Delta L}\int_0^{\Delta L} \overline{P_{i,j-1}}\, exp\{[\Gamma g_{m_i}(\overline{N_j}) - \alpha]z\}\, dz = \frac{G_j - 1}{\ln(G_j)}\overline{P_{i,j-1}} \tag{5.26}$$

Where i denotes different optical input signals, e.g. $i = 1$ denotes pump light, 2 is probe light. j is the section number. ΔL is the length of each divided section. $\overline{N_j}$ is averaged carrier density in the section j. G_j is the net optical gain factor in the section j, expressed as:

$$G_j = exp\{[\Gamma g_{m_i}(N_j) - \alpha]\Delta L\} \tag{5.27}$$

Using G_j, the propagation Equation 5.23 can be solved as:

$$P_{i,j} = G_j P_{i,j-1} = exp\{[\Gamma g_{m_i}(N_j) - \alpha]\Delta L\} P_{i,j-1} \tag{5.28}$$

In the following, the mechanism of the co-propagation model is explained. First of all, the initial carrier density for each section is given. The optical power of the pump and probe light at the input port is described as $P_{1,0}(t)$, $P_{2,0}(t)$ respectively, and they are treated as the initial averaged input optical power. When they are injected into the first section of the active region, the averaged optical power in the section can be calculated by substituting $P_{1,0}(t)$ and $P_{2,0}(t)$ into Equation 5.26, which results in $\overline{P_{1,1}}$, $\overline{P_{2,1}}$. Then these values can be substituted into the carrier density rate equation (Equation 5.22), and it can be solved using the fourth-order Runge-Kutta method, thus the carrier density in the first section can be updated. By using the updated carrier density, the real-time material gain for the first section can be obtained, and the output power of the pump and probe light at the boundary of the section 1 can be calculated using Equation 5.28. The output power of section 2 is calculated by treating the output power of section 1 as the input power of the section 2 and iterating the calculation process in the last section. Finally, the output power of pump and probe light can be obtained.

In order to evaluate the amplification process of an optical pulse train rather than a continuous wave, pseudorandom bit sequence (PRBS) non-return-to-zero (NRZ) data of $2^7 - 1$ word length was used as the input pump signal. A chirp-free super Gaussian pulse model was introduced to simulate the realistic pulse shapes in the pulse train. In the model, the amplitude of the pulse is given by [163]:

$$A = \sqrt{P} \exp\left[-\frac{1}{2}\left(\frac{t}{T_0}\right)^{2m}\right] \tag{5.29}$$

where P here denotes peak power of the pulse, m controls the shape of the super Gaussian pulse. For large m, the pulse becomes square shaped with steeper leading and trailing edges, in this simulation, $m = 4$. T_0 is the width parameter of the pulse, which is given as,

$$T_0 = \frac{T_B \mathrm{C}}{2(2ln2)^{\frac{1}{2m}}} \tag{5.30}$$

T_B is the period of a pulse, C is the duty cycle. By using the SOA parameters displayed in Table 2 Table 2 (see Appendix), the wavelength conversion process can be demonstrated as shown in Figure 5.3.

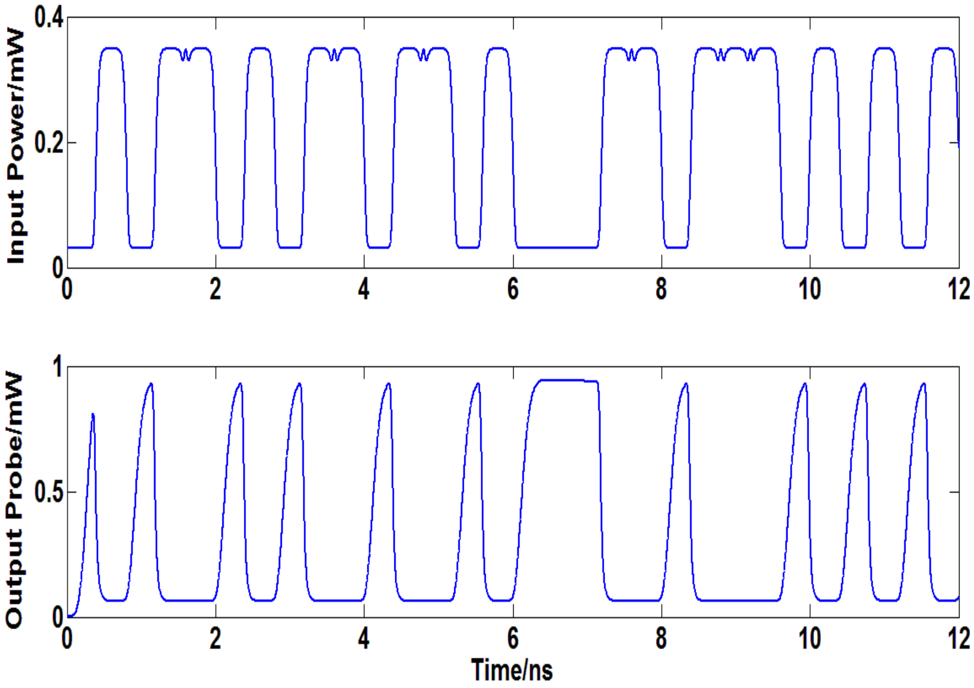

Figure 5.3 Data pattern of a 2.5 Gb/s original input pump light (upper) and amplified output probe light (lower). Inputs: $P_{pump} = -45 \sim -5$ *dBm,* $\boldsymbol{\lambda_{pump} = 1550\ nm}$*,* $P_{CW} = -30$ *dBm,* $\boldsymbol{\lambda_{CW} = 1535\ nm}$*.*

The data carried by the input pump light (upper) has been successfully transferred on the amplified output probe light (lower), although data is inverted due to the underlying mechanism introduced in Chapter 4. It is also shown in the lower figure, the converted pulses become sharp and narrow, especially the rise time of the pulse becomes longer than the fall time. This is because the wavelength conversion is a product of SOA saturation. As demonstrated in Figure 4.1, the carrier depletion process is much faster than the recovery in the active region. Taking the first pulse in the output probe for example, as the co-propagating pump pulse is firstly at low power level, the SOA is in the process of recovery (or reserving the carriers), the probe pulse is gradually amplified. When the leading edge of first pump pulse comes, it consumes available carriers quickly, therefore the gain which the probe pulse could obtain drops instantly, results in a sharp trailing edge on the output probe pulse.

It can be also observed from Figure 5.3, that the extinction ratio of the output probe light is less stable than the original input signal, this is due to the SOA gain dynamics characteristics. When the data rate of input signal increases, this will become even more severe.

The co-propagation model can be also used to analyze the phase change and induced chirp during the wavelength conversion, if Equation 5.13 is employed in the model.

5.3.2 Counter-propagation SOA Model

In many applications, including wavelength conversion, it may not be sufficient to model the SOA with a simple co-propagating model. A more comprehensive model which considers both forward and backward propagation can be advantageous or even essential. Unlike the co-propagation model, the output optical power of a counter-propagating SOA cannot be solved using a single marching algorithm. The counter-propagation model SOA is schematically displayed in Figure 5.4.

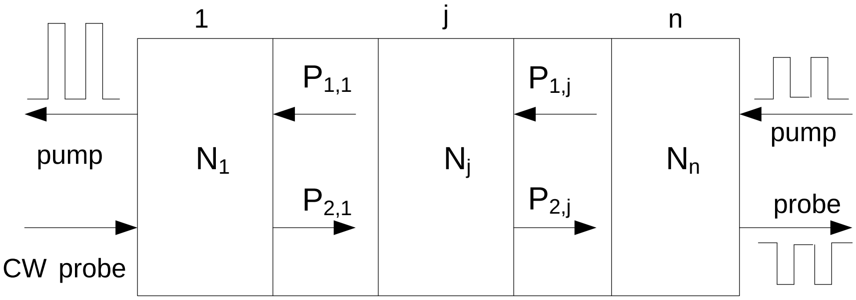

Figure 5.4 Multi-section counter-propagation model of SOA

Similar to the co-propagation model, the active region is divided into many small sections. Thus the carrier density, photon density and refractive index within each section can be treated uniformly. In order to simulate the dynamic changes of the optical pulse and carrier density in the active region, the initial carrier density of each section is given. Thus the output optical power of each section can be obtained by solving the nonlinear propagation equation group using a modified transfer matrix method (TMM) [240].

$$f(P_{1,0}, N_1, P_{1,1}) = 0; \cdots ; f(P_{1,j-1}, N_j, P_{1,j}) = 0; \cdots f(P_{1,n-1}, N_n, P_{1,n}) = 0; \qquad (5.31)$$

$$f\left(P_{2,0}, N_1, P_{2,1}\right) = 0; \cdots; f\left(P_{2,j-1}, N_j, P_{2,j}\right) = 0; \cdots f\left(P_{2,n-1}, N_n, P_{2,n}\right) = 0; \tag{5.32}$$

$f(x) = 0$ denotes the pulse propagation equation as Equation 5.23, $P_{1,n}$, $P_{2,0}$ is the initial optical power of pump and probe light, respectively, which are given. Together with initial carrier density in each section (N_1 to N_n), using TMM, Equations 5.31 and 5.32 can be solved, and the output power of the pump and probe light in each section can be obtained. Hence, the average optical power in each section can be calculated using Equation 5.26. When the average power of the pump and probe light are known, the carrier density of each section can be updated by solving the carrier rate equation (Equation 5.22) using the fourth order Runge-Kutta method. By iterating the process above, the counter-propagation SOA model is established, and the final output power for the pump and probe light can be obtained. The algorithm of counter-propagation model is depicted in Figure 5.5. The techniques of solving the propagation equation group and obtaining averaged power in each section can be also applied to analysing the co-propagation scheme. And the device level SOA model which will be introduced below is also equipped with this method.

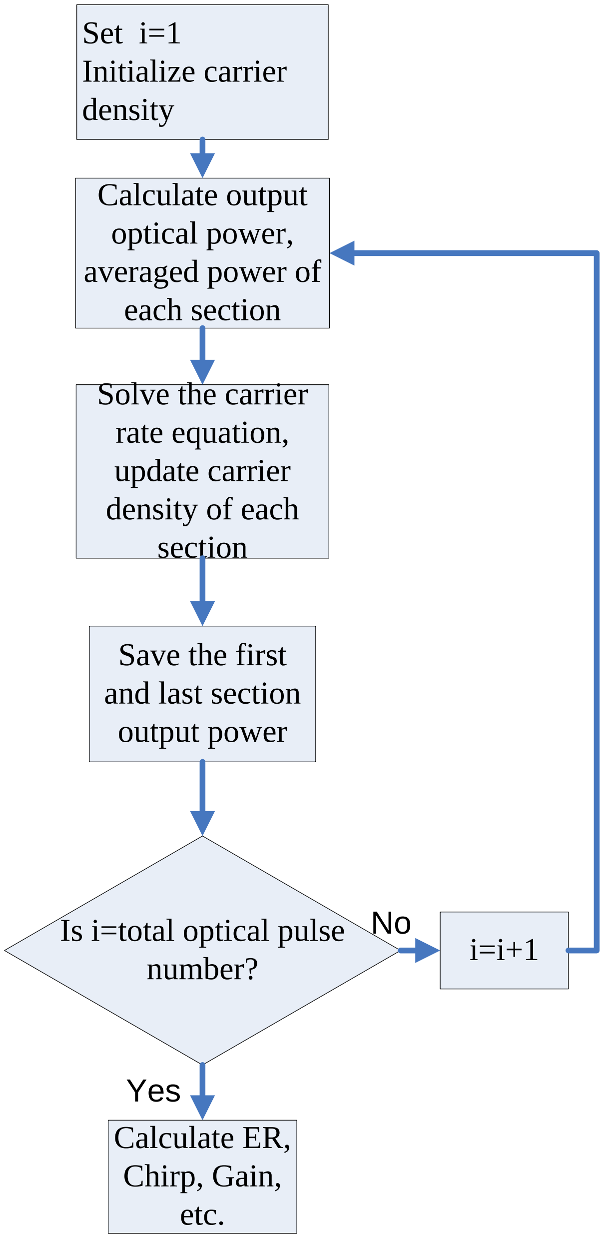

Figure 5.5 Flowchart of counter-propagation SOA model

Using the same SOA parameters and pulse train setup as in the co-propagation model, Figure 5.6 and Figure 5.7 represent the difference of output probe light using two models at the input data rate of 2.5 Gb/s and 5 Gb/s. As shown in the figures, wavelength conversion is achieved clearly using both co-propagation and counter-propagation models. Due to the mechanism of the XGM, the data on the output probe light is inverted.

The counter-propagation scheme shows an apparently better performance than co-propagation, as the output power level in counter-propagation is higher than co-propagation. Slower rise time and quicker fall time of the output probe pulse are also observed in the counter-propagation scheme, since the SOA physical parameters such as carrier lifetime used in two models are identical. When the input data rate increases, both co-propagation and counter-propagation schemes experience output signal degeneration, as the pulse duration is becoming comparable to the SOA gain recovery time. As suggested by the studies on modulation bandwidth of XGM, this issue can be mitigated by optimising the design of the SOA device, e.g. increasing the length of active region [48]. As discussed in Chapter 4, in practice the counter-propagating wavelength conversion is preferred because there’s no need to place filters to separate the output pump and probe light.

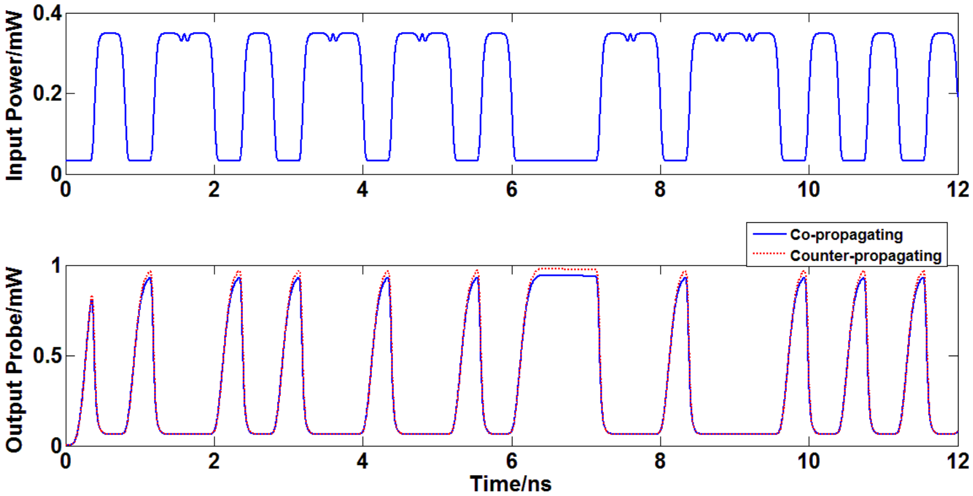

Figure 5.6 Data pattern of 2.5 Gb/s input pump signal (upper) and output probe light (lower) in both co-propagation and counter-propagation models. Blue solid line: co-propagation; red dotted line: counter-propagating. Inputs: P_{pump} *= – 45~ – 5 dBm,* $\boldsymbol{\lambda_{pump} = 1550\ nm}$*,* P_{CW} *= – 30 dBm,* $\boldsymbol{\lambda_{CW} = 1535\ nm}$*.*

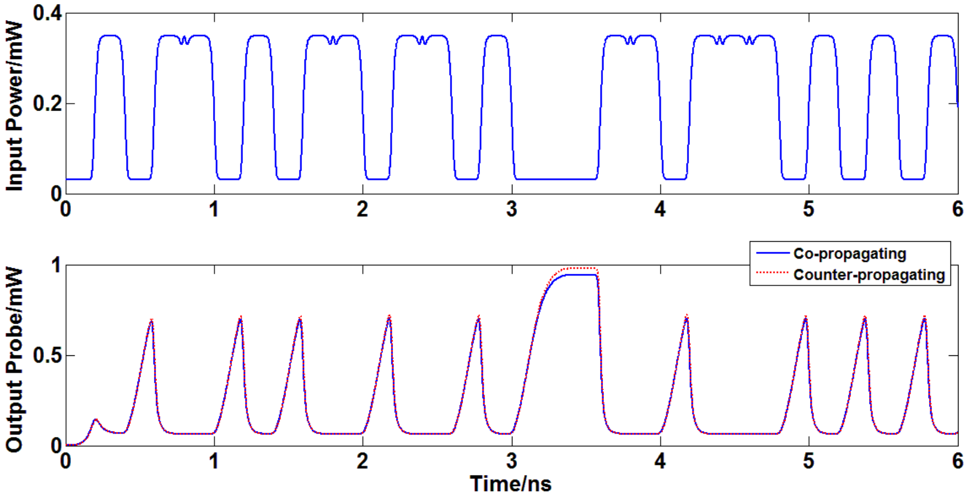

Figure 5.7 Data pattern of 5 Gb/s input pump signal (upper) and output probe light (lower) in both co-propagation and counter-propagation models. Blue solid line: co-propagation; red dotted line: counter-propagating. Inputs: P_{pump} *= – 45~ – 5 dBm,* $\boldsymbol{\lambda_{pump} = 1550\ nm}$, P_{CW} *= – 30 dBm,* $\boldsymbol{\lambda_{CW} = 1535\ nm}$.

Figure 5.8 and Figure 5.9 represent the difference of output probe light using two models when increasing the input data amplitude. The peak power of the input data was increased from – 5 dBm in Figure 5.6 and Figure 5.7 to 0 dBm in Figure 5.8, and further increased to 5 dBm in Figure 5.9. As a result, the amplitude of output probe light has been significantly reduced. And the difference of output probe light between co- and count-propagation schemes is becoming negligible. As the amplitude of input data increases, the output probe pulses become square. This can be understood as, increasing input signal power would shorten the effective carrier lifetime of the device, which was discussed in Chapter 4. Therefore, the rise time of the output pulse will be shortened, which results in a steeper leading edge. This makes the output pulse square. This explanation can be checked by comparing Figure 5.7 with Figure 5.10. As the input peak data power is increased from – 5 dBm to 5 dBm, and the data rate is kept at 5 Gb/s, the rise time of the output probe pulse in Figure 5.10 is obviously shorter than that in the Figure 5.7.

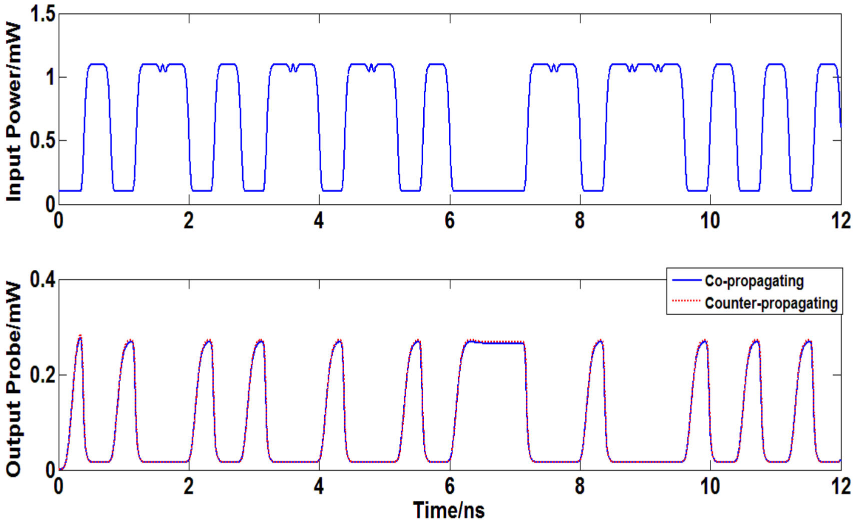

Figure 5.8 Data pattern of 2.5 Gb/s input pump signal (upper) and output probe light (lower) in both co-propagation and counter-propagation models. Blue solid line: co-propagation; red dotted line: counter-propagating. Inputs: P_{pump} *= – 40~ 0 dBm,* $\boldsymbol{\lambda_{pump} = 1550\ nm}$*,* P_{CW} *= – 30 dBm,* $\boldsymbol{\lambda_{CW} = 1535\ nm}$*.*

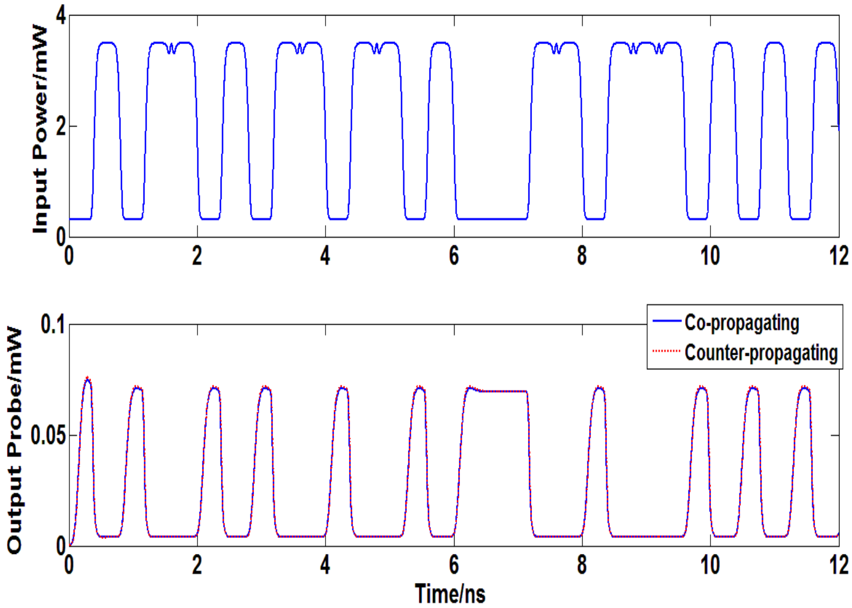

Figure 5.9 Data pattern of 2.5 Gb/s input pump signal (upper) and output probe light (lower) in both co-propagation and counter-propagation models. Blue solid line: co-propagation; red dotted line: counter-propagating. Inputs: P_{pump} *= – 35~ 5 dBm,* $\boldsymbol{\lambda_{pump} = 1550\ nm}$*,* P_{CW} *= – 30 dBm,* $\boldsymbol{\lambda_{CW} = 1535\ nm}$*.*

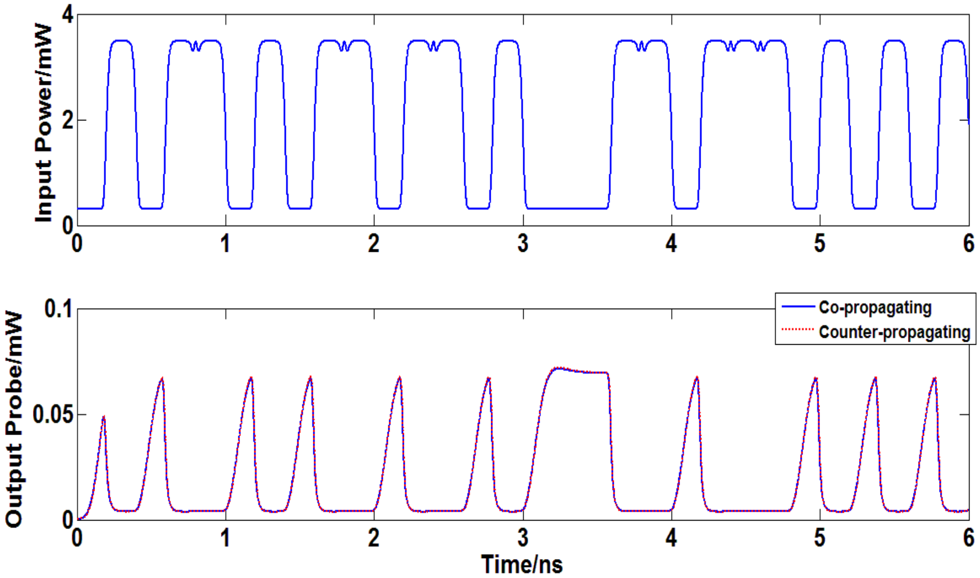

Figure 5.10 Data pattern of 5 Gb/s input pump signal (upper) and output probe light (lower) in both co-propagation and counter-propagation models. Blue solid line: co-propagation; red dotted line: counter-propagating. Inputs: $P_{pump} = -35 \sim 5$ *dBm,* $\boldsymbol{\lambda_{pump} = 1550\ nm}$*,* $P_{CW} = -30$ *dBm,* $\boldsymbol{\lambda_{CW} = 1535\ nm}$*.*

5.3.3 Experimental Validation

The co-propagation and counter-propagation models can be used to investigate characteristics of SOAs by turning off the input probe light. Then only signal beam is travelling through the SOA and analyzed. In the following example, the SOA parameters have been modified to be consistent with the design parameters for a commercially available SOA manufactured by Kamelian [241]. The modelled and experimental characterisation of these devices is shown below to bench mark the performance of the theoretical framework. In the first instance, the gain of the SOA is derived as a function of optical input power. This is shown below in Figure 5.11. Here we can see the gain compression that takes place as the input power to the amplifier increases above -20 dBm. The model and the experimental characterisation reflect this trend in good agreement. The absolute gain of the SOA differs by a few dB from the modelled SOA however, the overall characteristics are broadly similar.

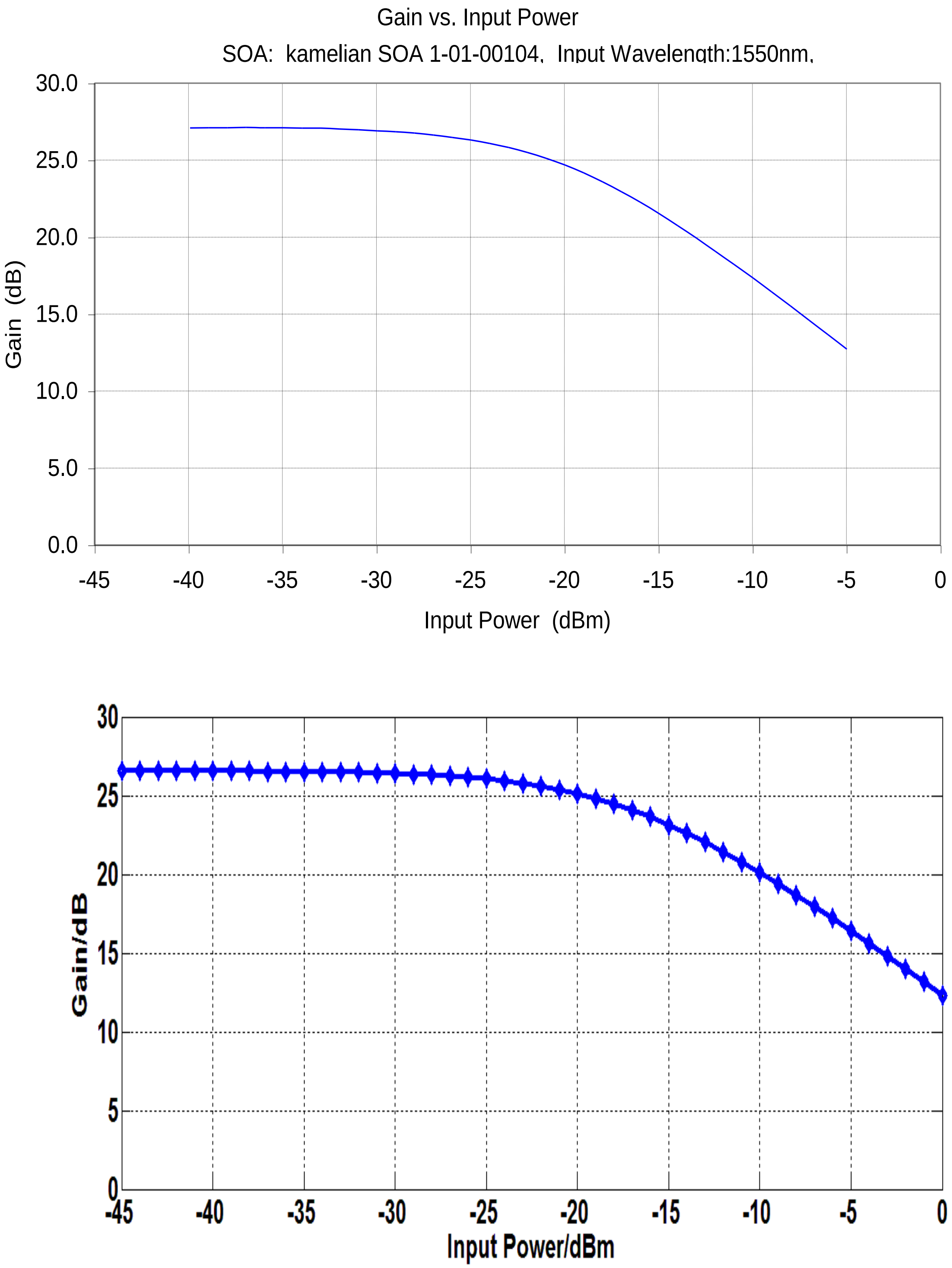

Figure 5.11 SOA gain versus input signal power depicted by experiment (upper) and simulation (lower) results.

Following on from the above, a data pattern was injected into the SOA at a range of input signal levels. The eye diagrams of the data pattern at the SOA output were generated and these were contrasted against eye diagrams obtained experimentally under similar conditions, in order to assess whether or not the dynamic operation of the SOA was being faithfully represented by the model. The following diagrams show cases where the signal input to the SOA was small (- 25 dBm) ranging through to the case where a high level signal was input to the SOA.

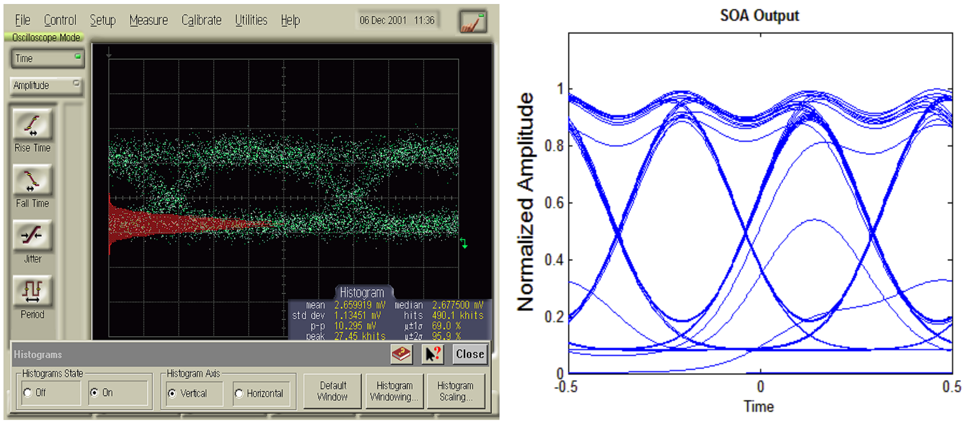

```
    mean  2.659919 mV    median  2.677500 mV
 std dev  1.13451 mV       hits  490.1 khits
     p-p  10.295 mV        μ±1σ  69.0 %
    peak  27.45 khits      μ±2σ  95.9 %
```

Figure 5.12 Eye diagrams from experiment (left) and simulation (right) when input power is -25dBm

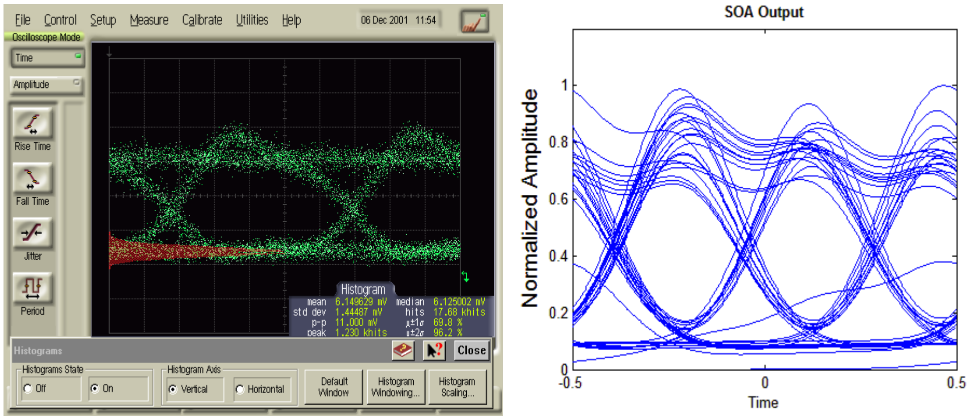

```
    mean  6.149629 mV    median  6.125002 mV
 std dev  1.44487 mV       hits  17.68 khits
     p-p  11.000 mV        μ±1σ  69.8 %
    peak  1.230 khits      μ±2σ  96.2 %
```

Figure 5.13 Eye diagrams from experiment (left) and simulation (right) when input power is -20dBm

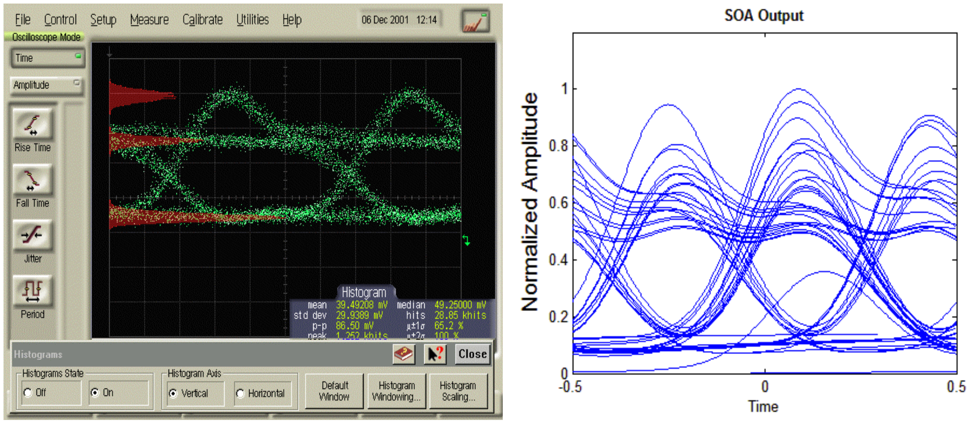

```
Histogram
    mean  39.49208 mV   median  49.25000 mV
 std dev  29.9389 mV      hits  28.85 khits
     p-p  86.50 mV        μ±1σ  65.2 %
    peak  1.252 khits     μ±2σ  100 %
```

Figure 5.14 Eye diagrams from experiment (left) and simulation (right) when input power is -15dBm

It is clear from a visual inspection of the above eye diagrams that the model is demonstrating similar dynamic behaviour to that observed experimentally. At low input signal levels (- 25 dBm) the gain of the SOA is not sufficient to drive the SOA in to saturation and therefore a relatively clean and open eye diagram is observed. As the signal levels are increased, over shoots on the rising edge of the bit are observed to cause a splitting of the signal level representing the transmission of a 1. This is clearly visible in the experimental measurements to the extent that the probability density function, describing the variation of signal amplitude in the case of a 1, is seen to split in to two pdfs. A similar characteristic is observed in the modelled SOA case. While this is not a rigorous evaluation of the dynamic operation of the SOA model, it gives confidence that the model is generally reflecting what is observed in reality.

5.3.4 Small Signal Modulation of SOA

The studies on the small signal modulation of a SOA can be divided into two categories: optical and electrical modulation. The analysis on the optical small signal modulation has been employed to study the modulation bandwidth of XGM in the SOA [48]. As a modulated (signal) and a continuous wave (CW) light are injected into SOA, through the process of optical amplification, the modulation on the signal light can be transferred onto the other signal. Therefore, the transfer/conversion efficiency as a function of the modulation frequency of input signal light can be studied under different conditions. By optimizing the design of the SOA, higher modulation bandwidth can be achieved [158].

Alternatively, the electrical modulation of SOAs is realised by directly modulating the bias current. Some SOA based optical switches and external modulators use this technique. Direct intensity modulation achieved by RSOAs is becoming more and more important in passive optical networks, as it is a cost effective way to build an optical source near users' premises. Moreover, this technique is also used by the adjustable gain-clamped SOA, which will be introduced in next chapter. Therefore, it is sensible to explore the direct bias modulation characteristic of a SOA. The study is carried out by using a similar method to that was used in analysing small signal modulation in a laser.

Most predictions of direct modulation response behaviour of a laser are derived from a small signal analysis: normally, the laser diode is driven by a 'small' sinusoidal current at frequency Ω, superimposed on a DC bias current:

$$J = J_0 + jexp(i\Omega t) \tag{5.33}$$

The equation is also applicable for the SOA. After a modulated bias is applied on the device, the photon and carrier density variables, S and N are assumed to similarly consist of a 'steady state' part, and a 'small' time varying part:

$$S = S_0 + sexp(i\Omega t) \tag{5.34}$$

$$N = N_0 + nexp(i\Omega t) \tag{5.35}$$

These functions are substituted into the pulse propagation Equation 4.3 and the carrier rate equation 5.20. In order to simplify the calculations, the ASE term is not taken into account in the rate equation and the recombination rate is deduced from Equation 2.36. The material gain for the SOA is taken to be directly proportional to the carrier density as

Equation 4.1. By ignoring the products of the small terms, then the steady state part and the time varying part of propagation equation can be separated as:

$$\frac{dS_0}{dz} = [\Gamma a_d(N_0 - N_t) - \alpha]S_0 \tag{5.36}$$

$$\frac{ds}{dz} = \Gamma a_d n S_0 + [\Gamma a_d(N_0 - N_t) - \alpha]s \tag{5.37}$$

Similarly, by ignoring the products of the small terms, the steady state part and time varying part of rate equation can be separated as:

$$\frac{dN_0}{dt} = \frac{J_0}{qV} - \frac{N_0}{\tau} - v_g a_d(N_0 - N_t)S_0 = 0 \tag{5.38}$$

$$-i\Omega n = \frac{j}{qV} - \frac{n}{\tau} - v_g a_d(N_0 s + nS_0 - N_t s) \tag{5.39}$$

The Equation 5.38, 5.39 can be simplified and inserted into Equation 5.37. Equation 5.37 can be solved using the expression in Equation 5.28, provided by the initial photon density of the input CW light. Based on these, Equation 5.39 can be solved for the small signal amplitude as a function of frequency $\Omega/2\pi$. The parameters used in the simulation are given in Table 2 (see Appendix). The results are demonstrated below.

As seen in the Figure 5.15 and Figure 5.16, increasing the length of the active region or unsaturated material gain coefficient (Equation 4.7) would improve the modulation response of the device. It also can be seen in Figure 5.15, the frequency response curve lifts up before it rolls down in the long SOA. And there is a drop of DC response for higher unsaturated gain in the Figure 5.16. These phenomena have been noticed but currently there is no satisfactory explanation.

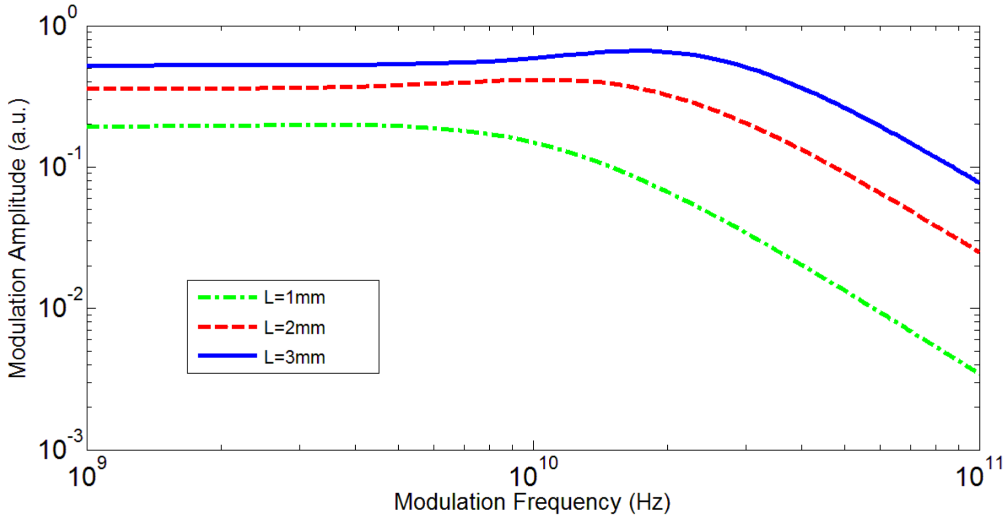

Figure 5.15 Modulation amplitude (s) as a function of modulation frequency $(\boldsymbol{\Omega/2\pi})$ *for different SOA length (L).*

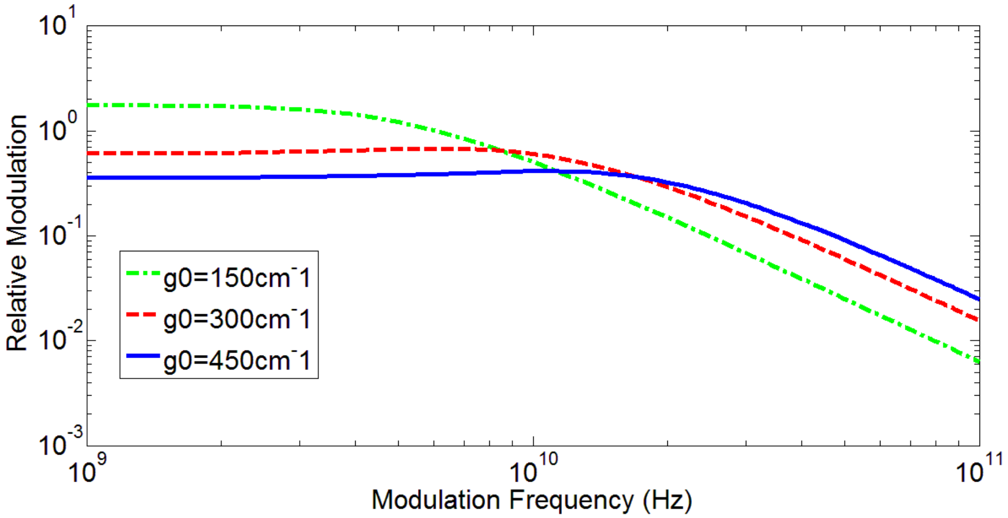

Figure 5.16 Relative modulation (s/S) as a function of modulation frequency $(\boldsymbol{\Omega/2\pi})$ *for different unsaturated signal material gain coefficient* $(\boldsymbol{g_0})$*.*

5.4 Device Level SOA Model

In order to study the detailed characteristics of SOAs, the device level SOA model is designed to take more physical factors into account. Compared to the system level one, the device level model is numerically studied in steady-state. The material gain expression for the device level model is also treated numerically. This is quite different from the analytical approximations as introduced in the system level model, which are based on the empirical curve fitting technique. Also, the ASE is no longer ignored in the model. A simulated wideband ASE spectrum of SOA can be obtained using the device level model, which laid solid foundation for numerically studying the characteristic of the AGC-SOA in Chapter 6.

In this section, an improved material gain expression will be introduced. Then the detailed device level model will be introduced. The propagation equation for ASE in the SOA, and an efficiency improved steady-state numerical algorithm are highlighted. Based on this detailed wideband model, steady-state gain characteristics of the SOA is studied, and the output saturation power P_{sat} is discussed. The output ASE spectrum is also simulated.

5.4.1 An Improved Material Gain Expression for Bulk SOA

The material gain of the semiconductor lasers and amplifiers can be obtained experimentally from analysing the amplified spontaneous emissions (ASE) or true spontaneous emissions (TSE) of the devices. The first method was originally proposed by Hakki and Paoli [69]. They recorded the maxima and minima of the output ASE spectrum caused by the F-P resonance to calculate the depth of modulation, then the material gain can be obtained via the relation [68] between the gain and the depth of modulation. The accuracy of the Hakki-Paoli technique was improved by Cassidy’s mode-sum method [234]. On the other hand, C. H. Henry [242] suggests the spontaneous emissions from the side of the laser (transversely to the laser cavity) can be employed to calculate the material gain spectrum based on the general relations between the rates of spontaneous emission, spontaneous emission, and optical absorption. Since the spontaneous emission from the side of a laser will experience very limited optical gain or loss along its optical path, it is also called true spontaneous emission (TSE) [243]. Besides techniques using ASE and TSE, the direct transmission measurement is often employed to obtain the gain spectrum of a device with weak F-P resonance.

The expression for the material gain of semiconductor lasers and amplifiers has been studied by many research groups. Generally, the theoretical gain expressions can be divided into two main groups: analytic and detailed numerical models. The analytic approximations of the gain expression are normally based on the empirical curve fitting techniques. In the beginning, the analytic expression was modeled linearly relating with the carrier density in the gain medium (see Equation 3.1), which has been demonstrated by the gain spectrum obtained from experiments discussed above. However, this expression is only valid around the gain peak. As more operating wavelengths are required to be taken into account in the model, gain expressions having a Lorentzian lineshape [16], using an inverse quadratic function [129], or employing a cubic formula [130] have been proposed. Especially, a polynomial model for the material gain, which is the sum of a quadratic and cubic function, is capable of providing improved accuracy over a large carrier density and wavelength range [244]. The analytic gain expressions are widely employed in the system level SOA models, as they are efficient in calculation. However the accuracy of the model is largely dependent on the curve-fitting parameters which can be obtained by analyzing the experimental gain spectrum measurements.

On the other hand, detailed physical models for material gain have also been studied extensively. Instead of using curve fitting technique, the detailed numerical models focus on the physical origins of the optical amplification in the gain medium. Thus most of the models are required to perform numerical calculations using the quantum mechanics. The expressions for gain and spontaneous emission can be obtained by integrating the transition probabilities over the available electron and hole states in the semiconductor. Kane’s four-band model [40] is used to model the band structure of the III-V direct gap semiconductor. The transition probabilities between the conduction band and valence band can be calculated by two approaches, i.e. using the time-dependent perturbation theory [45] [36] or the density-matrix theory [245][246]. The detailed expression for material gain can be also obtained without using quantum mechanics [41] [231], as introduced in the Chapter 2. However, some assumptions were made during the expression derivation, and the intraband relaxation time was not taken into account.

As introduced in [247], the material gain coefficient for bulk or quantum well material can be defined from Fermi’s Golden Rule, assuming the k-selection rule applies. The derivation process required quantum mechanics treatment will not be discussed here as it’s beyond the scope of this thesis. It is given as:

$$g_m(E) = \left(\frac{\pi e^2 \hbar}{\varepsilon_0 n_1 c m_0^2 E}\right) |M|^2 \rho_{red}(E) \times (f_c - f_v) \tag{5.40}$$

Where E is the photon energy, ε_0 is the permittivity of free space, m_0 is the electron rest mass, n_1 is the refractive index of active region. $|M|^2$ is the transition matrix element, given by [36],

$$|M|^2 = \frac{m_0 E_p}{6} \times 2 \tag{5.41}$$

E_p is the optical matrix parameter, the number 2 on the RHS of the equation denotes two orthogonal polarization states. For $In_{1-x}Ga_xAs_yP_{1-y}$ compounds, it can be obtained using interpolation scheme introduced in Chapter 2 and optical matrix parameters of binary compounds $InAs$, InP, $GaAs$, GaP [36].

$\rho_{red}(E)$ in Equation 5. 40 is the reduced density of states for a bulk or quantum well material when k-selection rule applies, which is given [247]

$$\rho_{red}(E) = \left(\frac{1}{2\pi^2\hbar^3}\right) \times \left(\frac{2m_c m_v}{m_c + m_v}\right)^{\frac{3}{2}} \times (E - E_g)^{\frac{1}{2}} \tag{5.42}$$

f_c, f_v is Fermi distribution function, and the calculation of the quasi Fermi levels are based on assuming equal injection of holes and electrons for charge neutrality [248].

One of the limitations of the material gain expression 5.40 is ignoring the intraband relaxation time of the electrons, which would result in broadening and also reducing the peak values of the gain and emission spectra [249] . In [251], the author employed density matrix theory with the phenomenologically introduced intraband relaxation time, and modified the Lorentzian lineshape to obtain the line broadening function $L(\hbar\omega - E_{cv})$.

$$L(\hbar\omega - E_{cv}) = \frac{1}{\pi} \frac{\hbar/\tau_{in}}{(\hbar\omega - E_{cv})^2 + (\hbar/\tau_{in})^2} \tag{5.43}$$

where τ_{in} is the intraband relaxation time, which is considered as the reciprocal intraband scattering probability averaged between electrons and holes [251]. Thus the intraband relaxation effect can be taken into account in the material gain calculation by integrating the line broadening function $L(\hbar\omega - E_{cv})$ into material gain expression:

$$G(\hbar\omega) = \int_{E_g'}^{\infty} g(E_{cv}) \times L(\hbar\omega - E_{cv}) dE_{cv} \tag{5.44}$$

However, according to [34][249], the use of the Lorentzian lineshape function overestimates the effects of broadening as it has slowly decaying tails. This will result in some absorption at frequencies below the bandgap. Alternatively, a sech lineshape function would provide enhanced accuracy compared to Lorentzian one in estimating the intraband relaxation effect. As shown in Figure 5.17, the sech function decays faster than the Lorentzian, which would give a better estimation in the gain model.

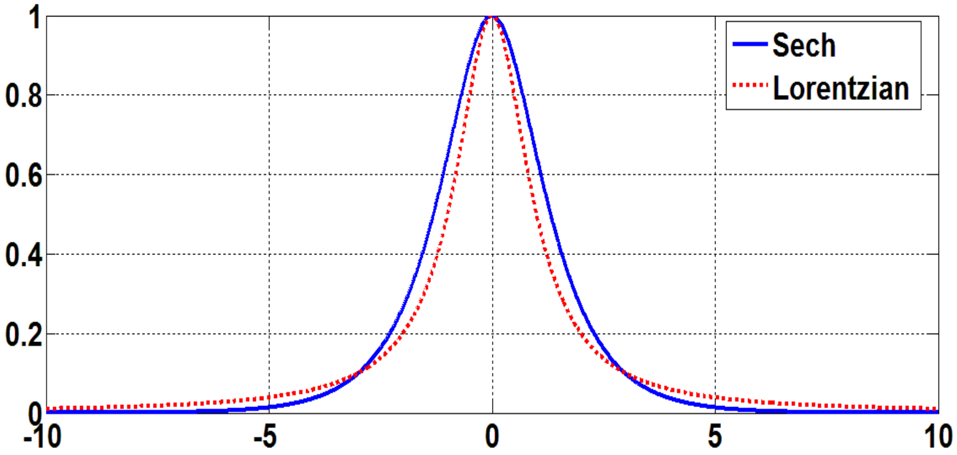

Figure 5.17 Comparison between a sech(x) and basic Lorentzian function ($\frac{1}{1+x^2}$ *) .*

Thus, the expression in Equation 5.40 is further improved as,

$$g_m(E) = \left(\frac{\pi e^2 \hbar}{\varepsilon_0 n c m_0^2 E}\right) |M|^2 \int_{E_g}^{\infty} \rho_{red}\left(E_{cv} - E_g\right) \times (f_c - f_v) \times L(E_{cv}) dE_{cv} \tag{5.45}$$

Where $L(E_{cv})$ is sech lineshape function, given as

$$L(E_{cv}) = \frac{\tau_r}{\hbar\pi} sech\left[\frac{\tau_r}{\hbar}(E_{cv} - E)\right] \tag{5.46}$$

τ_r is the intraband relaxation time, which equals to $1 \times 10^{-13} s$. E_{cv} is the transition energy from conduction band to valence band, expressed as

$$E_{cv} = E_g + E_c + E_v = E_g + \frac{\hbar^2 k^2}{2m_c} + \frac{\hbar^2 k^2}{2m_v} \tag{5.47}$$

By using the parameters given by Table 1, for a given carrier density $n = 1.2 \times 10^{24}\ \mathrm{m}^{-3}$, the material gain coefficient for a SOA can be calculated using Equation 5. 45. The material gain coefficient obtained by using both Equation 2.32 and 5.45 is compared in Figure 5.18.

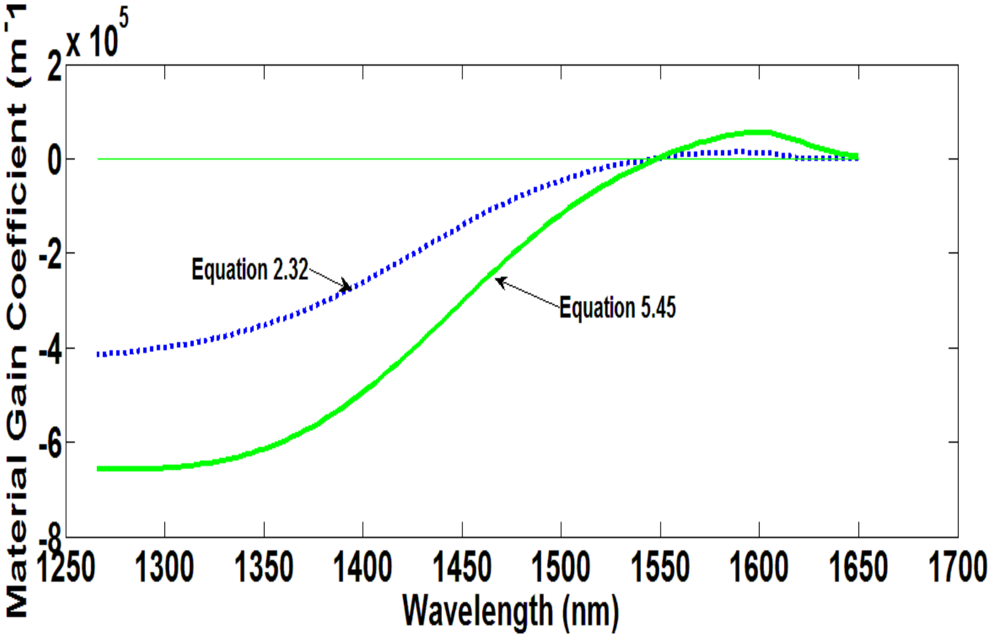

Figure 5.18 Material gain coefficient for a SOA, dotted line: calculated by Equation 2.32, solid line: calculated by Equation 5.45.

By employing a similar approach, the proposed expression for spontaneous emission rate $(m^{-3}s^{-1}J^{-1})$ of bulk SOAs can be obtained by convolving the existing spontaneous emission rate [247] with the sech linewidth function:

$$r_{sp}(E) = \left(\frac{ne^2E}{\pi\varepsilon_0 c^3 m_0^2 \hbar^2}\right)|M|^2 \int_{E_g}^{\infty} \rho_{red}\left(E_{cv} - E_g\right) \times f_c \times (1 - f_v) \times L(E_{cv}) dE_{cv} \tag{5.48}$$

5.4.2 Device Level Model

Besides the wideband material gain coefficient introduced above, the device level SOA model includes many aspects of physical factors, e.g. reflection and refraction on both end facets, the ASE travelling along with signal light. Hence a complex carrier density rate equation is employed in the model. The multi-section technique used in system level model is included as well.

Propagation Equation for Signal Light

The propagation equation in device level SOA model is consistent with the one in system level model, except that it uses the improved material gain coefficient proposed in last section. It is described as:

$$\frac{dA^{\pm}(z)}{dz} = (\Gamma g_m - \alpha)A^{\pm}(z) \tag{5.49}$$

Where $A^{+}(z)$, $A^{-}(z)$ is the signal power density of forward and backward travelling wave in the active region section respectively. The backward wave is required to account for the existence of reflection on the output facet, Γ is the confinement factor, α is the internal loss coefficient. The solution of the propagation equation is the same as the one used in the counter-propagation model- the transfer matrix method (TMM).

Propagation Equation for Amplified Spontaneous Emission

In the device level model, the effect of amplified spontaneous emission along the SOA axis should be taken into account. The propagation of the spontaneous emission field is presented as:

$$\frac{dS_k^{\pm}(z)}{dz} = (\Gamma g_m - \alpha)S_k^{\pm}(z) + R_{sp} \tag{5.50}$$

$S_k^{\pm}(z)$ is the forward or backward amplified spontaneously emitted photon density per unit frequency spacing centred at frequency v_k. As can be seen in the Figure 2.6, the spontaneous emission rate continuously spreads over a wide frequency band. Due to the residual reflections of facets in the SOA, the spontaneously emitted noise will display the longitudinal cavity modes. In order to simplify the simulation, the model assumes the spontaneous emission only exists at discrete frequencies which are integer multiples of cavity resonances. If there are m discrete frequencies and n sections in the model, the $S(v,z)$ represent a $m \times n$ matrix which stores a general profile of spontaneous emission photon density rate along the amplifier axis z.

$$\begin{bmatrix} S(v_1,z_1) & \cdots & S(v_1,z_n) \\ \vdots & \ddots & \vdots \\ S(v_m,z_1) & \cdots & S(v_m,z_n) \end{bmatrix} \tag{5.51}$$

R_{sp} is the ASE noise coupled into S_k^+ or S_k^- , and it is expressed as:

$$R_{sp} = \frac{\beta}{v_g} r_{sp} h\Delta v \tag{5.52}$$

β is the spontaneous emission coupling factor [252], r_{sp} is the spontaneous emission rate which was introduced in the last section, Δv is frequency spacing between resonant frequency and non-resonant frequency as depicted in Figure 2.12:

$$\Delta v = \frac{C_0}{4L} = \frac{C}{4n_{eq}L} \tag{5.53}$$

Equation 5.50 can be transformed as below:

$$\begin{aligned} &S^{\pm}(v_k,z_{j\pm1}) \\ &= exp\,[\big(\Gamma g_m(v_k,N_j) - \alpha(N_j)\big)\Delta z]S^{\pm}(v_k,z_j) \\ &+ \frac{exp\left[\Big(\Gamma g_m\big(v_k,N_j\big) - \alpha\big(N_j\big)\Big)\Delta z\right] - 1}{\Gamma g_m(v_k,N_j) - \alpha(N_j)} R_{sp}(v_k,N_j) \end{aligned} \tag{5.54}$$

using the boundary conditions which take into account facet reflectivity R_1, R_2:

$$S_k^+(0) = R_1 S_k^-(0),\ S_k^-(L) = R_2 S_k^+(L) \tag{5.55}$$

Then Equation 5.54 can be solved numerically. The results can be further processed to simulate the output ASE spectrum using the technique described in [231].

Carrier Density Rate Equation

According to Equation 5.20, the carrier density rate equation is expanded as Equation 5.56. $R\big(N(z,t)\big)$ is the total carrier recombination rate introduced in Equation 2.39. The third and fourth term on the RHS of the equation represent radiative recombination of carriers due to the amplified signal and amplified spontaneous emission (ASE). $G(z)$ is the net optical gain factor described in Equation (5.27). The number "2" in the last term on the RHS of the equation denotes two orthogonal polarizations (TE and TM).

$$\begin{aligned} \frac{\partial N(z,t)}{\partial t} &= \frac{J}{qV} - R\big(N(z,t)\big) \\ -v_g \cdot g_m\big(v_0, N(z,t)\big) &\cdot \frac{G(z)-1}{\ln\,(G(z))} \cdot [A^+(z) + A^-(z)] \\ -\sum_{k=1}^{m} 2 \cdot v_g \cdot g_m\big(v_k, N(z,t)\big) &\cdot [S_k^+(z) + S_k^-(z)] \end{aligned} \tag{5.56}$$

Algorithm

By using a multi-section structure approximation and the boundary conditions, the differential equations 5.49 and 5.50 can be solved. The results can be substituted into rate equation (5.56). The rate equation in the device level model is normally treated in the steady-state, which means, the term $\frac{\partial N(z,t)}{\partial t}$ is equal or approaching to zero. In the Connelly's steady-state model [231], the term $\frac{\partial N(z,t)}{\partial t}$ is set to equal to $Q(z)$. Then the algorithm adjusts the carrier density in order to make the value of $Q(z)$ approach to zero throughout the amplifier. However, this technique usually takes a long time to obtain convergence in the processing and can only be used in steady-state model analysis.

An alternative, efficient method to solve the rate equation(similar to Connelly's model) assumes that, the term $\frac{\partial N(z,t)}{\partial t}$ is set to equal to $Q(z,t)$,

$$\frac{\partial N(z,t)}{\partial t} = Q(z,t) \tag{5.57}$$

Rather than simply comparing the value of $Q(z,t)$ with zero, the equation is solved as follows,

$$N(z,t+\Delta t) = N(z,t) + Q(z,t) \times \Delta t \tag{5.58}$$

Δt is the transit time for the light travelling through each section in the active region. The program starts with an initial guess for the carrier density in each section, (in the present case this was set as $1.2 \times 10^{24}\ \mathrm{m}^{-3}$). By solving Equation 5.56, $Q(z,t)$ can be calculated in each section, hence $N(z,t+\Delta t)$ can be obtained. Then the program compares the carrier density difference $(N(z,t+\Delta t) - N(z,t))$ with the required condition which was set to be less than $10^{-4} \times N(z,t+\Delta t)$ in each section. If the requirement cannot be achieved, the program will solve the Equation 5.49, 5.50 and 5.56 again with the updated carrier density and will not terminate until the requirement is met. The improved steady-state algorithm shows faster convergence compared to Connelly's model.

By using the device parameters presented in Table 1, the steady-state model is used to study the characteristics of a SOA.

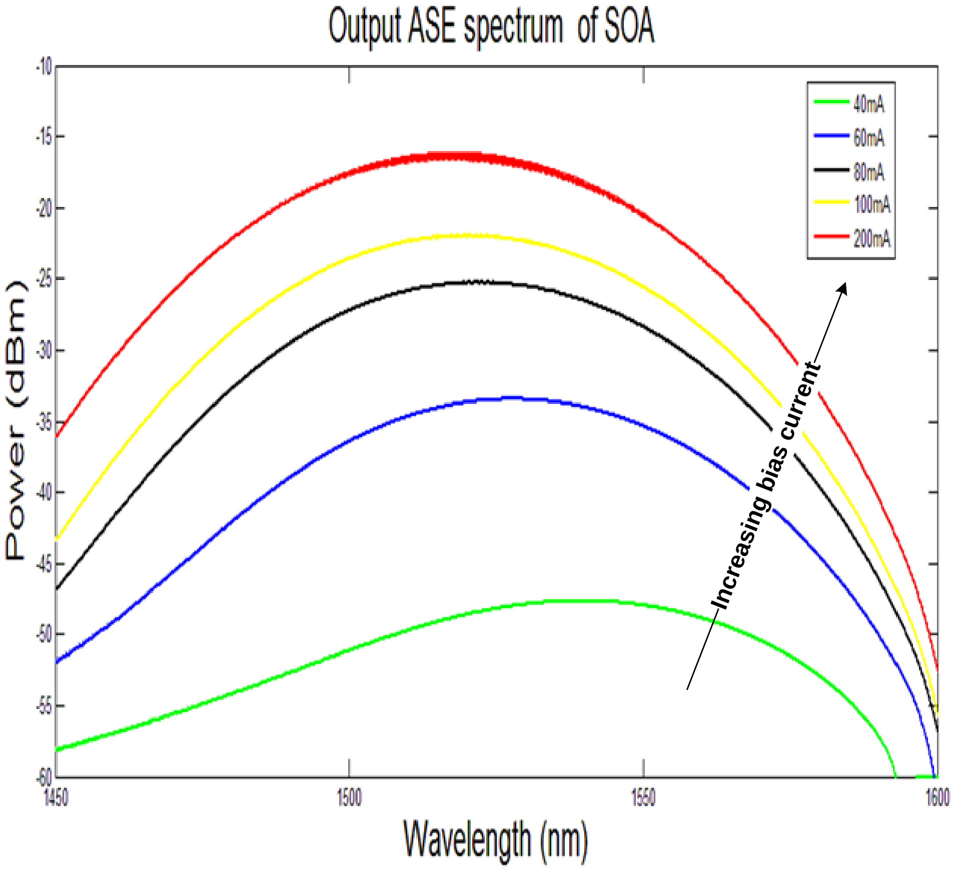

Figure 5.19 Output ASE spectrum of a SOA under different bias currents

As shown in Figure 5.19, the output ASE spectrum of a SOA at different driving currents is obtained when no input optical signal is introduced into the model. Since wideband material gain coefficient is employed in the model, the device level model is capable of evaluating the SOA characteristics over a wide wavelength range. As the bias current rises from 40 mA to 200 mA, the output ASE power increases significantly, and the peak wavelength of the spectrum moves towards short wavelength because of the band filling effect. It is also noticeable that the gain ripple becomes more obvious under high bias current.

The fibre to fibre gain performance can also be evaluated using the device level model. As an optical signal (- 45 dBm) is introduced into the SOA, by solving the propagation equation for signal light, the output optical power can be obtained and the fibre to fibre gain calculated. By gradually increasing the input power of optical light, the gain saturation characteristics of a SOA is demonstrated in

Figure ***5.20***.

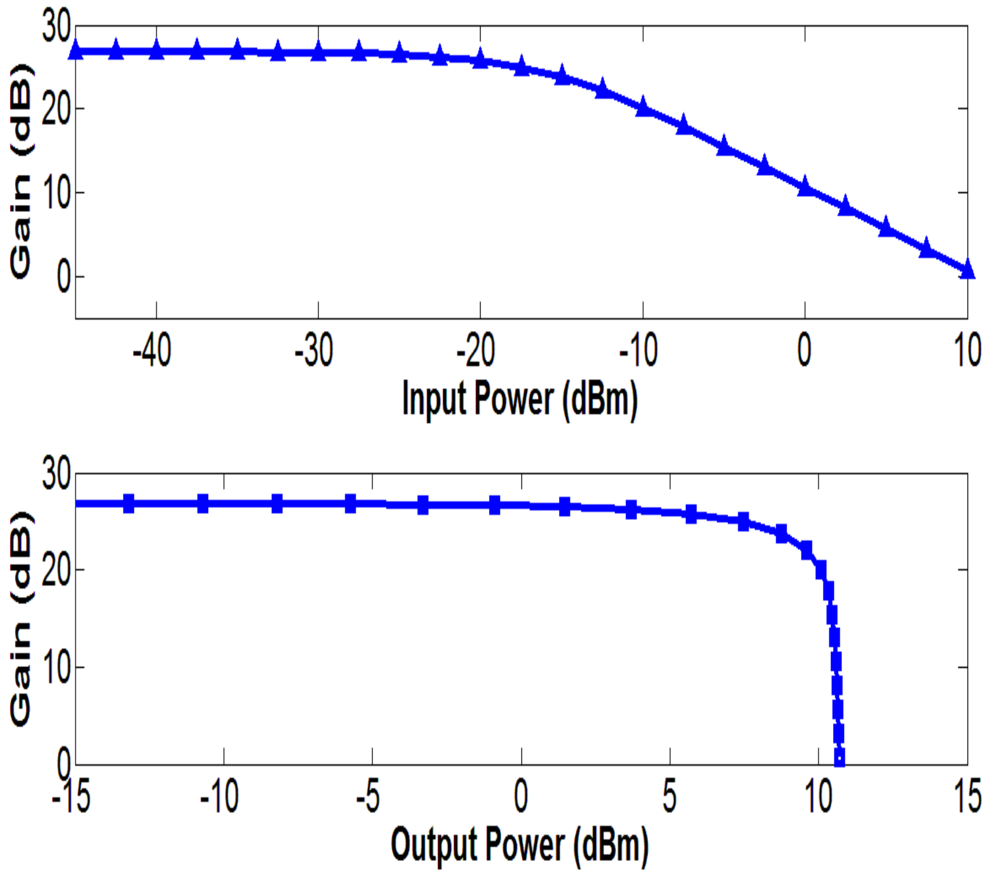

Figure 5.20 Gain saturation characteristics of a SOA, upper: Gain versus input power, lower: Gain versus output power.

As can be seen in Figure 5.20, before the input optical power reaches to - 25 dBm, the gain stays relatively constant. Then the gain drops dramatically as the input optical power continues to increase. This can also be observed from the figure depicting gain as a function of output power. The gain saturation happens when the input optical power is so high that the available carriers in the active region have been exhausted.

The SOA gain can be improved by increasing the bias current, as seen in Figure 5.21. By tuning the bias current from 80 mA to 150 mA, the gain has increased from 21 dB to 26.5 dB, since more carriers have been supplied to the active region. However, implementing

SOA gain control via adjusting the bias current would also significantly affect the output saturation power (P_{sat}) of the SOA. For example, by changing the bias current from 150 mA to 80 mA, the P_{sat} has reduced 5.6 dBm (from 8.7 dBm to 3.1 dBm). This implies that, for a standard SOA, it is not a good way to achieve gain control by directly changing the bias current. However, an adjustable gain-clamped SOA (AGC-SOA) which will be introduced in next chapter would address this issue. It could provide a wide dynamic gain range without compromising its output saturated power.

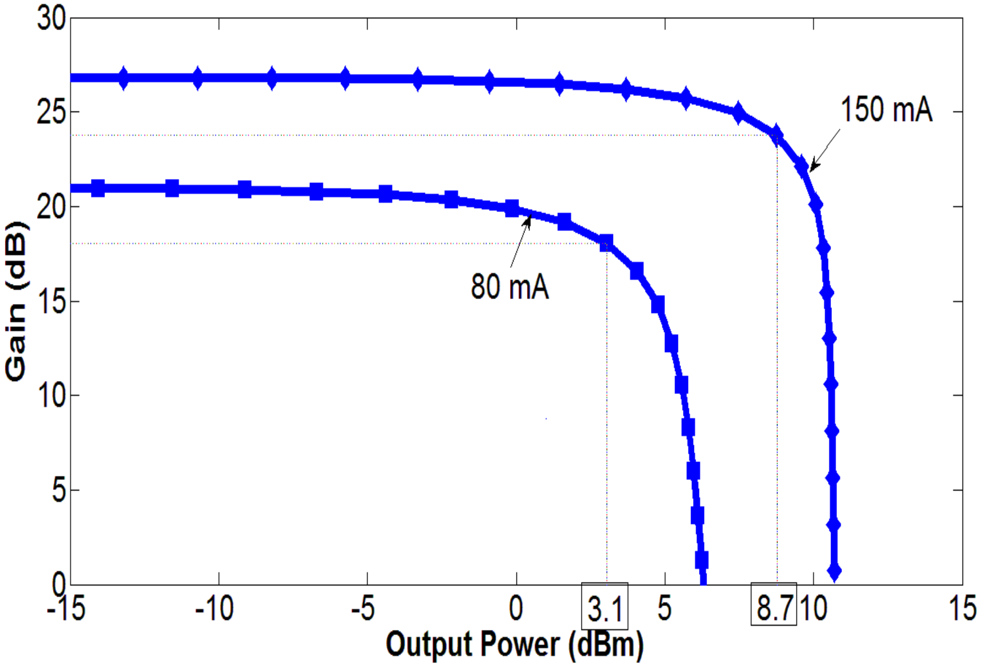

Figure 5.21 SOA Gain as a function of output power under two bias currents.

5.5 Summary

This chapter has introduced and discussed two kinds of numerical models for studying the characteristics of SOAs, namely system level and device level SOA models. In the beginning, the classification of SOA theoretical models has been discussed. And two basic equations, the propagation equation and carrier density rate equation, which are employed in both system and device level models, have been deduced. Especially, the propagation equation used in this thesis has been compared with the ones in other publications, the underlying consistency has been proved. Based on these, the system level model has been introduced and applied into studying the all optical wavelength conversion using a SOA. Depending on travelling directions of pump and probe lights, the system model has been classified into co-propagation and counter-propagation models. The simulated wavelength conversion achieved by cross gain modulation (XGM) in the SOA has been performed in both co-propagation and counter-propagation models. The co-propagation system model has also been employed to numerically study the gain compression effect of the SOA. It is clear that the model is demonstrating similar dynamic behaviour to that observed experimentally, which proves the model is capable of studying the characteristics of SOAs. Then the direct modulation response of a SOA is investigated using a modified system level model. The numerical results show that increasing the length of active region or unsaturated material gain coefficient would improve the modulation response of the device.

The remainder of the chapter discussed the device level SOA model. It starts with the review of material gain coefficient for a semiconductor optical device. An improved material gain expression is introduced, which is based on the wideband material gain expression defined from the Fermi’s Golden rule. It also takes the intraband relaxation effect into consideration. Then the detailed device level model is introduced. The propagation equation for ASE in the SOA, and an efficiency improved steady-state numerical algorithm are highlighted. Based on this detailed wideband model, steady-state gain characteristics of SOA is studied, and the output saturation power P_{sat} is discussed. The output ASE spectrum under different bias currents is also simulated.

Chapter 6 Characteristics of AGC-SOA

6.1 Introduction

The growing penetration of home DSL connections demonstrates clear demand for high bandwidth services. Realistic predictions estimate annual traffic growth from 34% to 50% [253][254]. Analysis shows that to sustain this level of growth economically requires cost reduction in the price per unit of bandwidth that has hitherto been unachievable by technological developments alone. The solution is therefore to reduce the amount of equipment (interfaces between nodes) in the network. These drivers have stimulated interest in access solutions based upon Passive Optical Networks (PONs) with high (>512) splitting ratios [255]. Central, in particular for extended reach PONs which may cover distances of 100 km or more [99][253], is the need for low cost optical amplifier technologies: Semiconductor Optical Amplifiers (SOAs) have a clear role to play in this context. The wavelength plan for future 10 Gbit/s (XG-PON) [94] uses wavelengths from 1260 nm up to 1620 nm and alternative optical amplifier technologies do not function efficiently across this band.

Upstream traffic in a PON (from the Optical Network Unit, ONU to the Optical Line Terminal, OLT) is normally time division multiplexed (TDM) with a wide variation in path loss arising from differences in transmission distances and splitting losses. The bursty nature of this traffic combined with a wide dynamic range of signal strength (-15 dBm to -28 dBm – the difference between a very close ONU with a small split ratio and a distant ONU with a high split ratio), places severe demands on the burst mode receiver at the OLT. In particular, the design of trans-impedance and limiting amplifiers and Avalanche Photo Diodes (APDs) is complicated by the need to cater for this wide dynamic range. As the upstream data rate increases, and longer reach PONs are deployed, this issue will become even more critical.

Adjusting the gain of an optical amplifier positioned at the OLT (Figure 6.1), in order to regulate path losses and the signal strength at a packet level substantially alleviates many of the above issues in long reach PONs. Signal strengths will be presented at the OLT at an optimized power level thus reducing the receiver dynamic range requirement and thus overall complexity. To be of value, the timescale of the gain adjustment should take place at least within the guard band of the packet/frame transmission. For 10 Gbit/s PON systems this implies that the amplifier be able to regulate its gain, without loss of Psat, within a 26 ns timescale, (64 bits at 2.5 Gbit/s on the upstream direction) [256]. Potentially, the dynamic control of the optical amplifier can be implemented through the standard GPON protocol which provides knowledge of distance to a transmitting node. Alternatively, a rapid control circuit based on high speed measurements of signal strength may be appropriate.

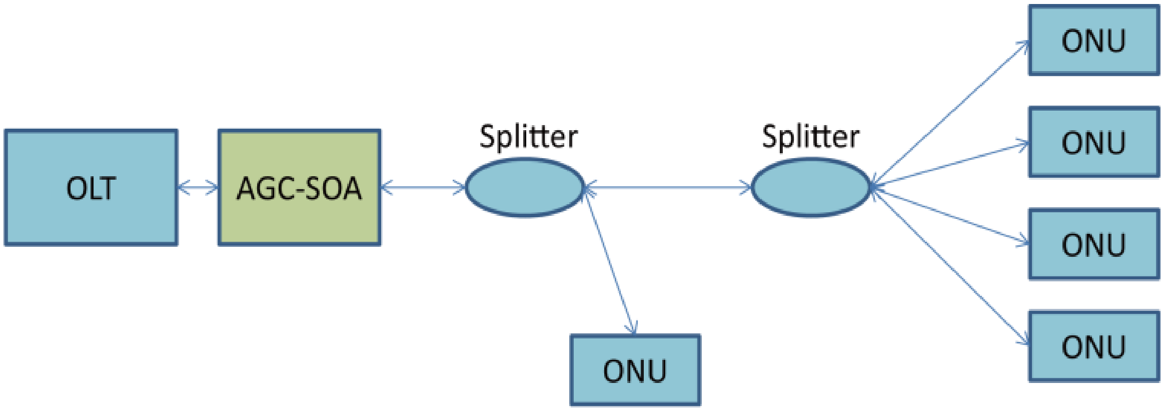

Figure 6.1 Schematic of PON with AGC-SOA pre-amplifier.

Erbium Doped Fibre Amplifiers (EDFAs) operate reliably at high data rates in a multi-wavelength environment, because of its high output saturation powers and slow gain dynamics. However, these same dynamics cause undesirable gain transients when operated within a packet switched or bursty environment [257]. Furthermore, being fibre based, EDFAs have no path to solutions that demand a high degree of integration. Conversely, SOAs have a small form factor and offer the potential for direct integration with other functions on a common InP platform [141][258] and more importantly their temporal dynamics are better suited for use in switched environments. While SOAs have been demonstrated as effective amplifier solutions in multi-wavelength long distance transmission applications [237][258], their operation in this regime requires careful management of signal power levels, so as to maintain operation within their linear region. This additional degree of management is not desirable, especially in PONs where bursty signals can operate over a wide dynamic range. Gain clamping has been shown to linearise SOA performance over a wider range of input powers, which in turn significantly reduces crosstalk between data bits (TDM crosstalk) at high transmission rates [237]. However in these cases, gain clamping fixes the gain and as a consequence does not provide a solution to dynamic gain adjustment. Consequently the current, indirect solution is to combine a linear amplifier with a variable optical attenuator at the input which severely degrades the overall system noise figure. This technique has also been applied to cascaded Praseodymium Doped Optical Fibre Amplifiers (PDFAs) specifically for PON applications. However, the modulation timescales were limited to 100s of nanoseconds [260].

The chapter demonstrates a semiconductor optical amplifier topology which has the unique capability to provide variable gain and maintain linear operation through gain clamping over a wide (40 dB) dynamic range, without compromising the saturable output power of the device [141]. A key advantage of this approach is that there are no mechanical tuning elements and hence the gain can be adjusted via direct electrical control at ns timescales. While the operation of this device has been presented previously for the static gain case [141], its behaviour under dynamic gain modulation conditions is not well understood. Here theoretical modelling, supported by experimental analysis is used to validate that the geometry can provide gain adjustment and stabilisation within a nanosecond timeframe.

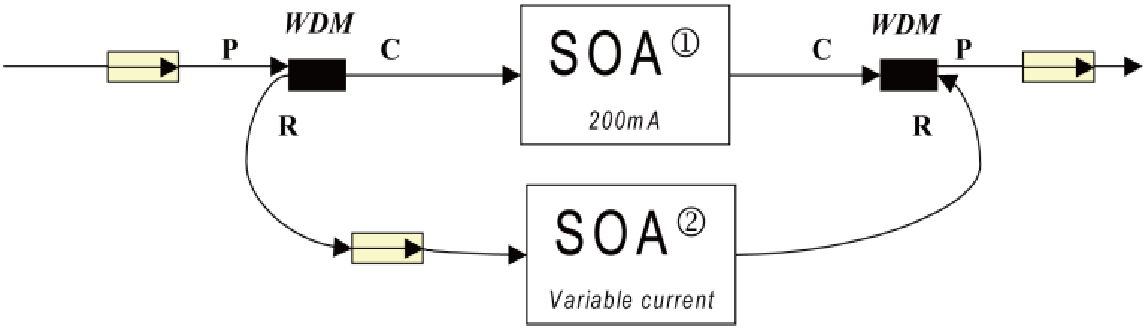

Figure 6.2 Counter propagating ring laser Adjustable Gain Clamped SOA (AGC-SOA) implementation. The P, R, C port of the WDM coupler denotes pass, reflect, C band.

Figure 6.2 illustrates conceptually the design of the Adjustable Gain Clamped SOA (AGC-SOA). The architecture comprises two active (gain) regions defining a data path through the signal SOA (SOA1) and a laser cavity containing SOA1 and a control SOA (SOA2). SOA1 amplifies light in the signal path. The lasing mode derives gain from both SOA1 and SOA2. The composite gain provided by both SOAs regulates the condition for the onset of lasing. This in turn defines the carrier concentration (gain) of the signal SOA. Hence by controlling the drive to SOA2, the gain imparted by SOA1 can be adjusted.

SOA1 is continually operated at full current and therefore the AGC-SOA allows signals to be amplified by SOA1 at a clamped gain which is varied by SOA2. This maximises the saturation output power thereby maintaining an extended linear regime [141].

6.2 DC Characterisation of AGC-SOA

The key advantage that the AGC-SOA offers over other optical amplifiers is that it enables the gain to be adjusted directly through the drive current to the clamping SOA without dramatic loss of P_{sat}. Hence linear operation is maintained over a wider range of input signals. In standard SOAs it is possible to adjust the gain by altering the drive current however, as is demonstrated in the experimental measurement shown in Figure 6.3, this leads to a dramatic loss in P_{sat}.

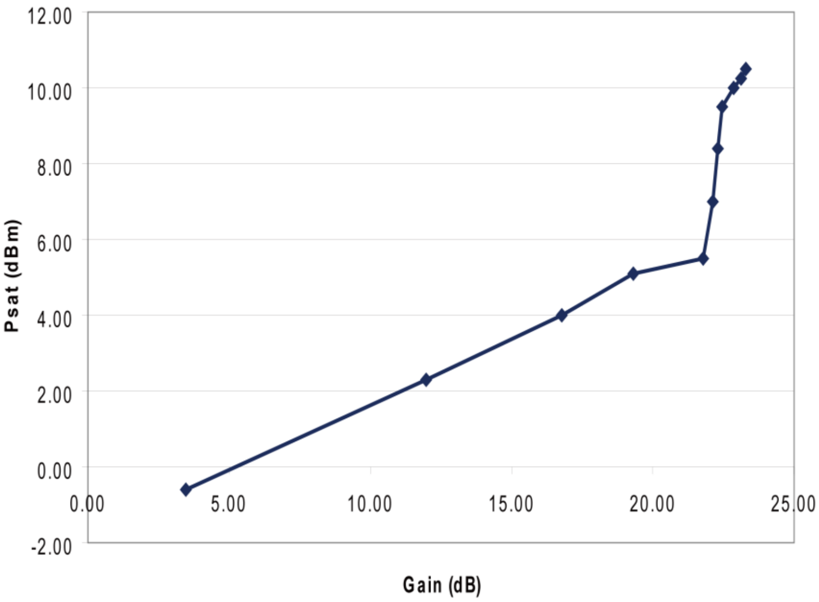

Figure 6.3 P_{sat} variation as a function of SOA gain.

At high gains, where the SOA is highly inverted, the P_{sat} value is at its highest. However, in this region, adjusting the small signal gain through the bias current has a dramatic effect on the P_{sat} value. In the example depicted in Figure 6.3, at high gains P_{sat} changes with gain at a rate of ~3 dBm/dB- i.e. for every dB that the gain is reduced, the P_{sat} value drops by 3 dBm. This characteristic is related to the self saturation behaviour of the SOA.

If the SOA has a long active region, the carrier density will vary along the length of SOA cavity. The ASE generated in the centre of the device will tend to deplete the carrier inversion at either end of the device. The small signal gain may remain high since it is integrated along the cavity length. However the P_{sat} may fall because of loss of carriers. As the drive current is further reduced, the drop in P_{sat} with gain is weaker at ~0.4 dBm/dB. However, by the time that this point has been reached the P_{sat} value is already significantly compromised (5 dBm compared to the high gain value of 10 dBm). The AGC-SOA enables gain modulation to be achieved without this dramatic loss of P_{sat} value.

Figure 6.4 depicts the gain of an AGC-SOA as a function of output power for a set of different clamping currents ranging from 0 mA to 200 mA. The P_{sat} values are constant over the range of clamping currents despite significant gain reduction (>20 dB).

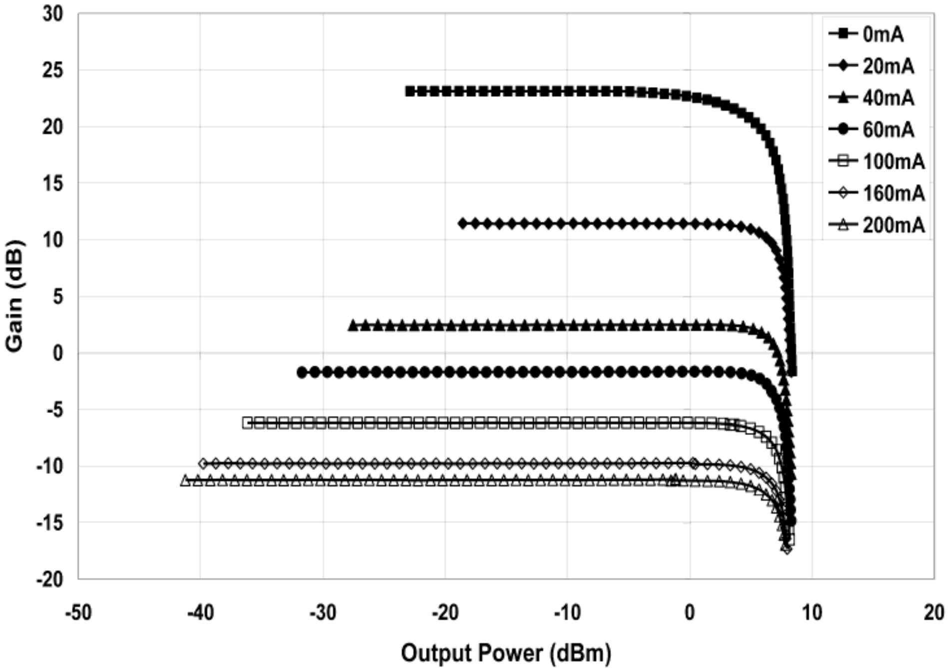

Figure 6.4 AGC-SOA gain as a function of output power at different clamping currents.

6.3 Numerical Model for AGC-SOA

6.3.1 GC-SOA Models Comparison

Several numerical models have been developed to investigate the characteristics of both conventional SOAs and gain-clamped SOAs using either an external or internal lasing mode.

In [261], a detailed numerical model was built to study the characteristics of the linear optical amplifier (LOA) [262] which employs an internal vertical laser field to achieve gain clamping. Compared to the device level SOA model introduced in Chapter 5, the LOA model includes an extra spatially averaged rate equation for the vertical laser field, accordingly the laser field induced carrier recombination in the active region is taken into account in the carrier density rate equation. By solving the propagation equations for injected signal and ASE along the signal travelling path, and the rate equation for vertical laser, the carrier distribution can be obtained from the carrier density rate equation. Therefore, the output signal power can be estimated. Since the gain clamping in the LOA largely depends on internal lasing rather than ASE power, the model is not applicable for the AGC-SOA.

In [263], the wideband steady-state SOA model [231] was used to investigate the characteristics of a fiber Bragg grating (FBG) based GC-SOA [264]. In their studies, the FBG is placed at the output of the SOA. Thus the output ASE at the peak reflection wavelength of the FBG will be reflected back into the SOA, so as to achieve gain clamping. Since only the selected ASE wavelength, rather than the whole wideband ASE account for the gain clamping, and the power of reflected ASE is not adjustable, the model is not suitable for AGC-SOA.

As we can see, the current existing GC-SOA numerical models cannot handle the proposed new device. And the underlying mechanism of gain clamping achieved by adjusting wideband amplified spontaneous emission (ASE) power still remains largely unknown. Therefore, a new numerical model built to study the AGC-SOA will be introduced in section 6.3.2.

6.3.2 Model for AGC-SOA

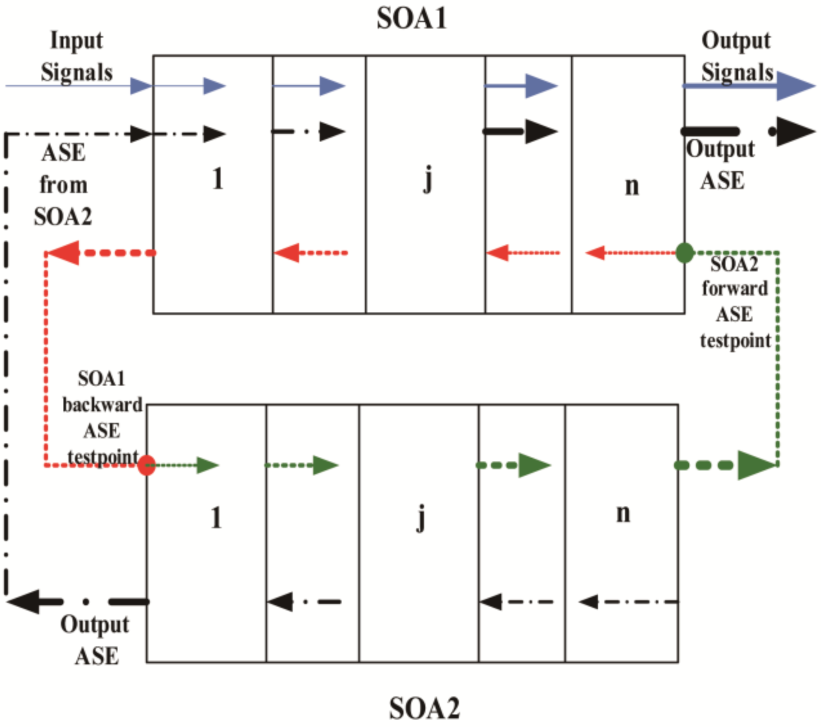

Figure 6.5 Schematic of the simulation model for an AGC-SOA.

As shown in Figure 6.5, the ASE circulating within the AGC-SOA travels in clockwise and counter-clockwise directions, however, the isolator in the ring cavity ensures that ASE travelling in the clockwise direction is not amplified. Thus, the counter-clockwise ASE generated by both SOAs accounts for gain clamping.

The two SOAs are simulated as independent modules using the device level SOA model introduced in Chapter 5. The model uses two different sets of material parameters summarised in Table 3 (see Appendix). (typical bulk SOA parameters from [36][141]). The active region length of SOA1 and SOA2 is 600 μm and 1000 μm, respectively. The confinement factor is 0.15 for both SOAs. The facet reflectivity is 5×10^{-5} and 1×10^{-5} for SOA1 and SOA2 respectively, and the coupling loss is 3 dB and 2 dB for SOA1 and SOA2 respectively. The WDM coupler pass band insertion loss is 0.5 dB. The parameters used in the model are set to match the real ones in the experimental setting. In the model, both SOAs generate ASE in the forward and backward directions in the active regions. In each SOA, the ASE profile extends over 1300 nm~1650 nm and is partitioned into discrete frequency bands.

The numerical model for the whole system of Figure 6.5 is achieved using iterative circulations. In the first iteration, the ASE in both directions of SOA2 is calculated assuming no ASE power is coupled in. Then the ASE generated by SOA2 travels in both clockwise and counter-clockwise order towards SOA1. Under this boundary condition, the ASE originated from SOA2 together with the one generated by SOA1 is amplified by SOA1 as it travels through, however only the backward ASE inside SOA1 is input to SOA2. For any successive iterations, the ASE from SOA1 couples into SOA2 before SOA2 generates ASE. When ASE travels inside the ring cavity, the facet reflectivity and coupling loss of both SOAs, the insertion loss for the isolator and WDM couples are taken into account. The round trip time is ~1.67 ns viz. the fibre length is about 0.5 m. Therefore, fibre loss and dispersion are neglected. The iterative procedure is terminated when the maximum difference of the ASE powers at each discrete frequency band between successive iterations is less than the desired tolerance. The numerical model is implemented using Matlab. In the present case an amplifier centred around 1550 nm was studied. Although it is accepted that in a deployed PON, the operation would be at 1300 nm, evaluation at 1550 nm was a compromise based on access to components for experimental characterization. Furthermore, since the object of the work was to investigate the steady-state and dynamic behavior the extrapolation to 1300 nm is assumed to be valid.

6.3.3 Characterisation

By using the numerical model described above, the evolution of travelling ASE power and spectrum within the ring cavity, important for gain clamping, is then characterised. The gain, Noise Figure (NF), maximum output power at gain saturation (P_{sat}) of an AGC-SOA under different clamping currents are also studied. Based on this model, the timescale for adjusting and stabilising the gain, crucial for dynamic packet equalisation, is evaluated in next dynamic performance section.

6.3.3.1 ASE Power, Spectrum Evolution

The characteristics of AGC-SOA were studied from the initial state when no input signal is introduced. The ASE power after every counter-clockwise ASE round trip is recorded. In Figure 6.6, the counter-clockwise output ASE powers from SOA2 and SOA1 are displayed after each loop transit. It should be noted that there is a substantial difference in the amplitudes of the co-propagating and counter propagating ASE strengths. This is due to the fact that the ASE in the forward direction has in effect only a single transit of the SOA as a result of the isolator in the ring cavity. On the other hand, the counter propagating ASE is amplified according to the combination of clamping and signal SOA gains.

The ASE power increases rapidly within the first 3 loops and then stabilises. Since the cavity round trip time is ~1.7 ns, stabilising the travelling ASE power in the loop takes between 1.7-5.1 ns (several round trips). The ASE spectrum within the clamping mode was examined after every circulation. Figure 6.7 shows the SOA2 output ASE spectrum at different loop transits. In the first loop, the output ASE power from SOA2 is relatively low, and the whole spectrum is divided into two parts falling outside the C-band due to presence of the WDM coupler in the ring cavity.

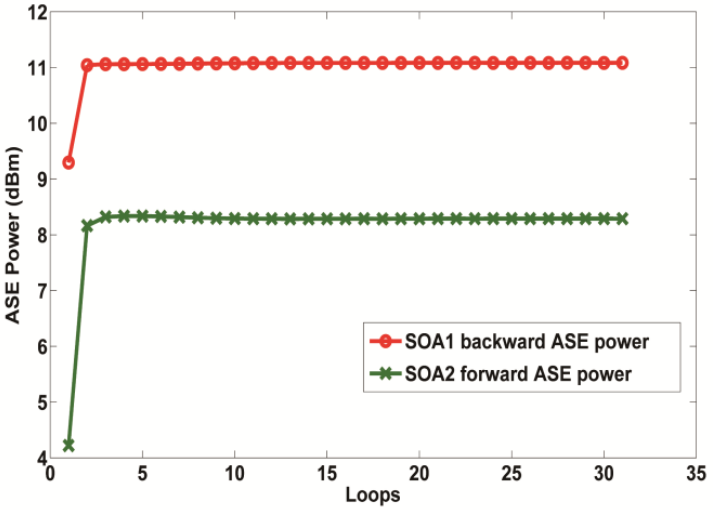

Figure 6.6 Counter-clockwise ASE power after N loops, Cross: SOA2 output ASE power; Circle: SOA1 output ASE power.

Initially, the ASE power within the S-band is greater than that within the L-band. However, as the lasing mode becomes established, the output ASE power develops as predicted in Figure 6.7. With the ASE power within S-band decreases significantly, the spectrum becoming sharp and narrow.

As ASE circulation progress, ASE emission in the S-band is further restrained becoming negligible and ASE within the L-band accounts for gain clamping. The results agree well with experimental observation. However, there is no satisfactory explanation with regard to this phenomenon.

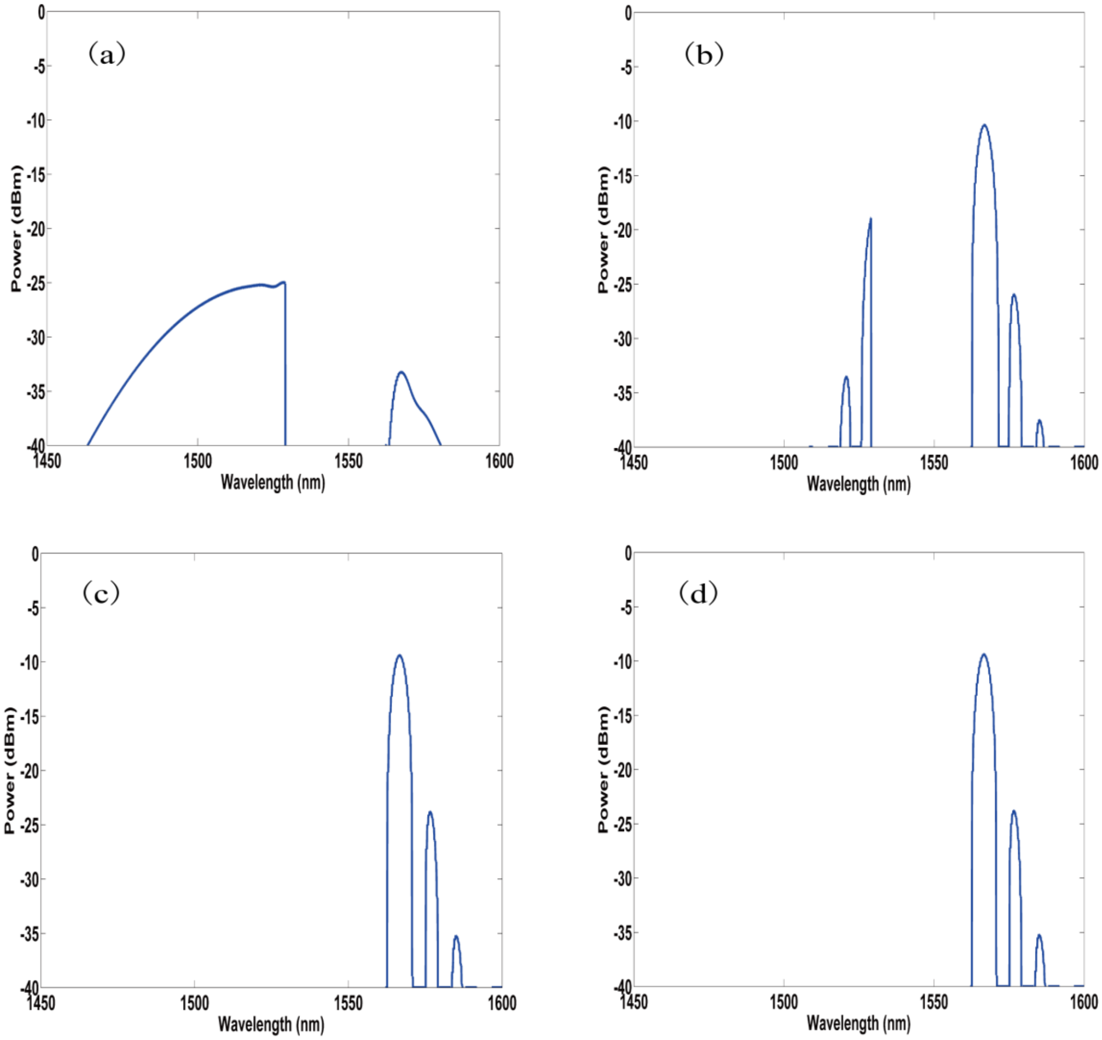

Figure 6.7 SOA2 ASE spectrum (counter-clockwise). (a) Loop number = 1; (b) Loop number = 10; (c) Loop number = 20; (d) Loop number = 100.

Figure 6.8 demonstrated SOA1 forward output ASE spectrum after the WDM coupler at different loop transits. In the first loop, the forward output ASE power from SOA1 is relatively high, and only the ASE spectrum within the C-band was displayed due to presence of the WDM coupler at the output port. As the loop increases, the forward output ASE power from SOA1 decreases. Because the counter-propagating ASE power in the ring cavity increased significantly in the first several loops as shown in Figure 6.6, the carrier density in the SOA1 will be dominantly consumed by the lasing mode. Once the lasing mode stabilised, the output ASE spectrum from SOA1 remains unchanged, which can seen from Figure 6.8 (b) (c) (d).

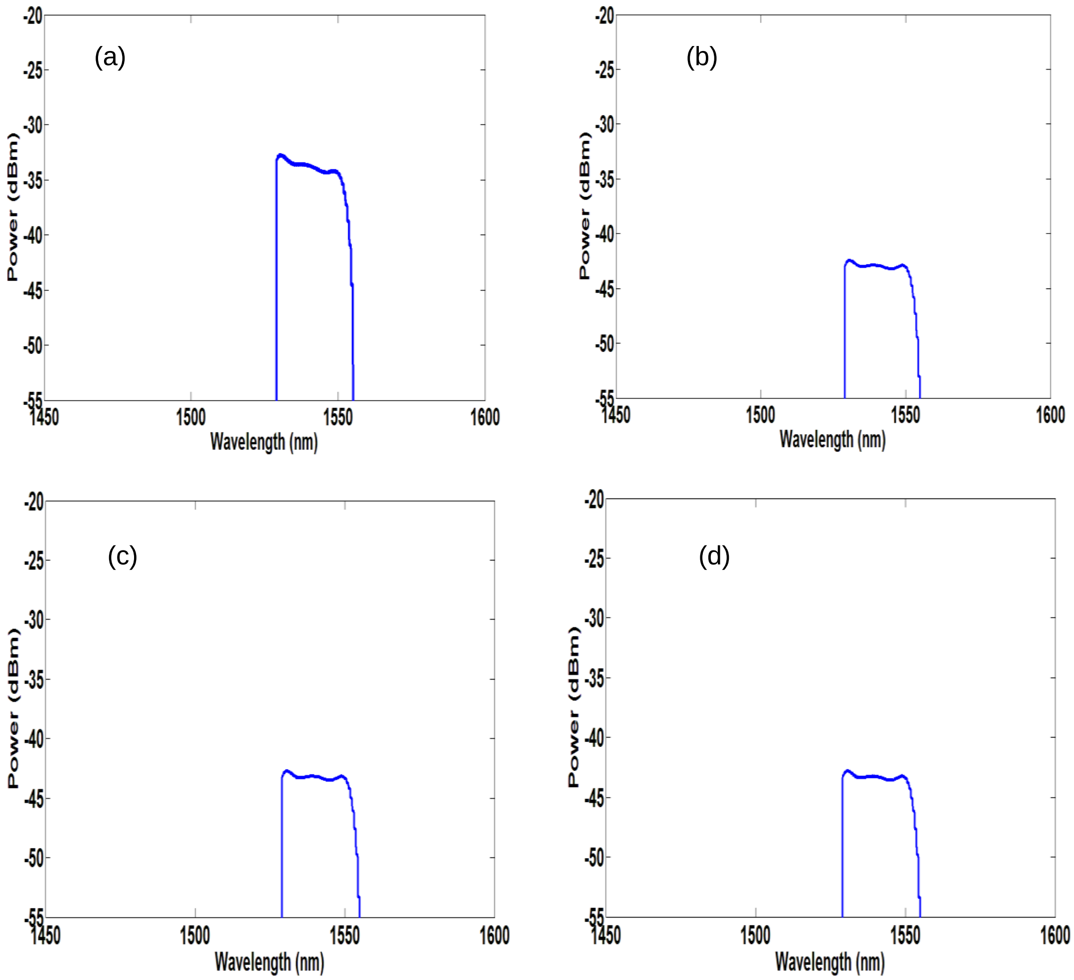

Figure 6.8 SOA1 forward output ASE spectrum after WDM coupler. (a) Loop number = 1; (b) Loop number = 10; (c) Loop number = 20; (d) Loop number = 100.

6.3.3.2 Gain Vs Output Power

Having established the steady state conditions of model operation, an input optical signal was introduced after the ASE inside the AGC-SOA cavity stabilizes. The gain of a 1550 nm CW light as a function of travelling ASE loop numbers is depicted in Figure 6.9. An optical signal power of -20 dBm was injected into SOA1. The drive current of SOA1 was set at 200 mA, and SOA2 at 65 mA. The simulation demonstrates that the signal gain settles within the first ASE loop transit and then remains unchanged; thus after AGC-SOA stabilizes from the initial state (shown in the evolution depicted in Figure 6.7), it takes < 2 ns (within one loop time) for the gain to settle.

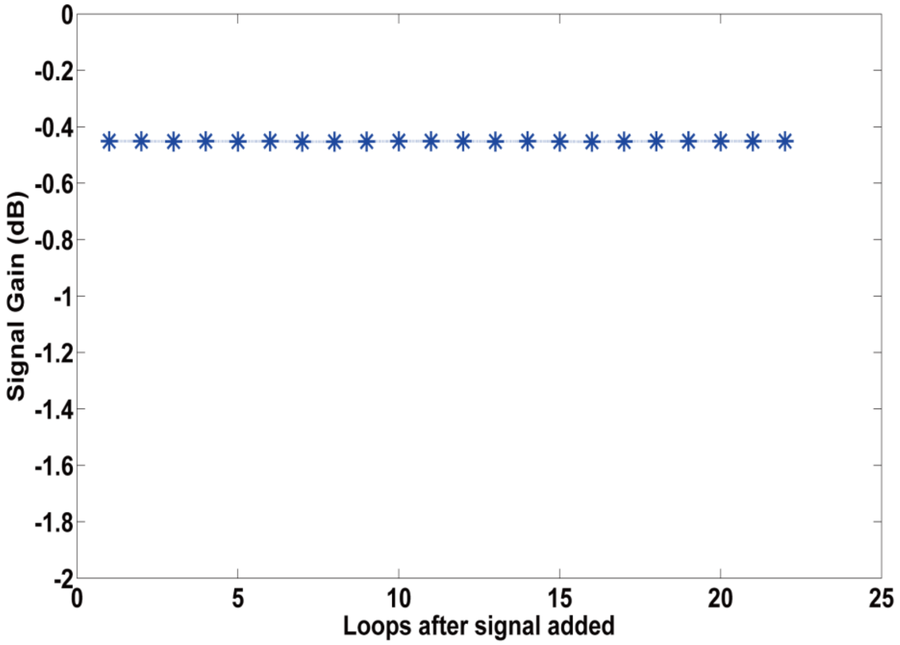

Figure 6.9 CW light (1550 nm, -20 dBm) gain as a function of circulating ASE loops after AGC-SOA stabilisation.

The variation of the gain with clamping SOA drive current was modelled over a range of clamping currents to corroborate that the model faithfully reproduced the experimental behaviour of the AGC-SOA. The model outputs (Figure 6.10) indicate broadly that the model is predicting the trends. According to the simulation result, the P_{sat} value stayed constant at 10.21 dBm when the clamping current increases from 0 mA to 40 mA, while the gain reduced significantly from 25.68 dB to 4.12 dB. Then the P_{sat} and gain dropped by 0.3 dB and 3 dB respectively when the clamping current reached 60 mA. And both values have been further reduced to 9.04 dBm and – 1.55 dB as the clamping current increased to 80 mA. However, the simulated values of P_{sat} and gain differ slightly from the experimental measurements, in which the P_{sat} value remains constant at 7.8 dBm when the clamping current increases from 0 mA to 80 mA. This difference most likely derives from small differences between the physical parameters used in the model and the real device.

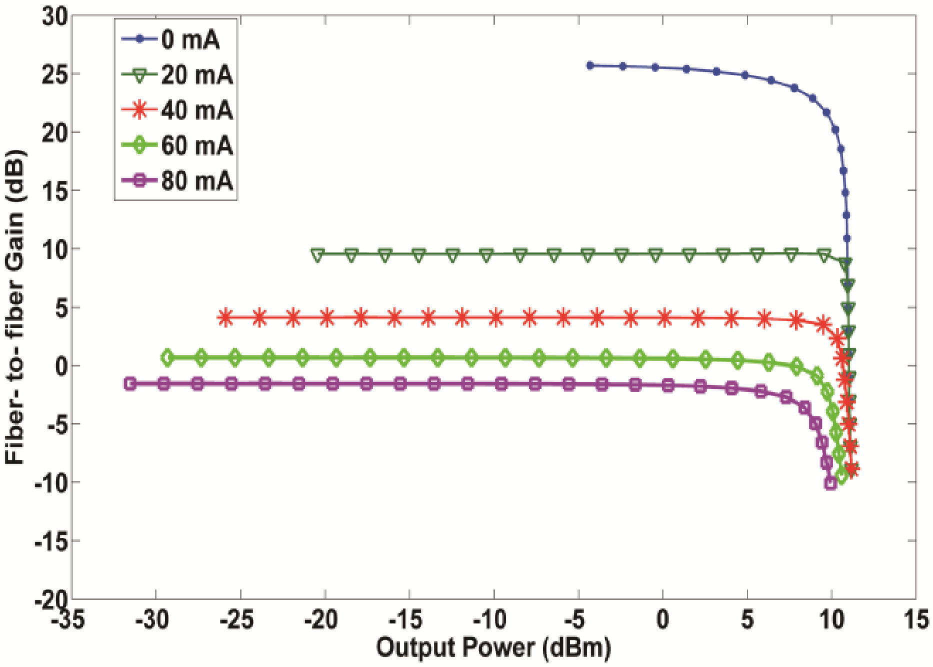

Figure 6.10 AGC-SOA gain as a function of output power at different clamping currents (modelling result).

6.3.3.3 Gain, Saturation & Noise Figure

The DC parametric operation of the AGC-SOA can be estimated using the above model. A CW light source (1550 nm) was introduced into the AGC-SOA once steady state operation was established. The input signal power was then increased steadily from -35 dBm to 20 dBm and the normal performance metrics of gain, maximum output power at gain saturation (P_{sat}) and noise figure (NF) were recorded for a given clamping current condition; the clamping current is changed from 0 mA to 200 mA. The simulation results are presented as a function of clamping current in Figure 6.11.

Figure 6.11 can be divided into two regions: where the clamping current is less than 60 mA, the gain is above zero; and the current is larger than 60 mA, the device has a negative gain. In the first part, when the clamping current is increased from 0 to 60 mA, the gain is significantly reduced by 24.78 dB, from 25.68 dB to 0.9 dB, while the noise figure is increased from 9.1 dB to 11.6 dB, and the P_{sat} value is slightly reduced from 10.21 dBm to 9.91 dBm. This part of graph show clearly that as the drive current to the clamping SOA is increased, the gain is dramatically reduced with the noise figure slightly increasing and the P_{sat} value relatively unchanged. This is in good agreement with reported experimental characterizations [141] with the following exception. Gain clamping begins at a clamping bias current of greater than 0 mA. Experimentally it was observed that this value should be nearer 10 mA before there was sufficient gain within the clamping SOA to overcome loop losses and allow the lasing mode to stabilize. This difference is due in part to an overestimation of ASE noise within the model [231] but may also reflect an additional loss within the experimental setup that was not accounted for. In the other part of the graph, where the clamping current is increased from 60 mA to 200 mA. The gain is decreased from 0.9 dB to – 7.4 dB, the noise figure is increased by 1.61 dB from 11.6 dB to 13.21 dB. And the P_{sat} value is dramatically reduced by 4.38 dB from 9.91 dBm to 5.53 dBm. As can be seen the model predicts a big drop of the P_{sat} value at high clamping levels (> 60 mA) but this was not observed experimentally.

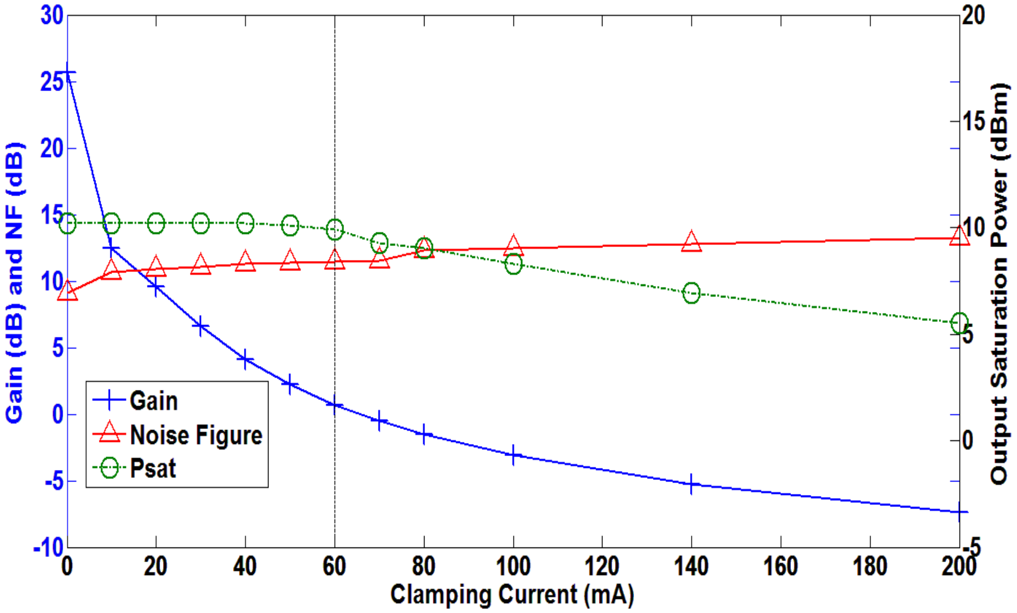

Figure 6.11 Modeled steady state AGC-SOA performance.

In summary the model agrees well with the experimental characterisation in that it predicts all of the trends that were observed. There are slight difference between experiment and model but nonetheless the model has been shown to provide a realistic description of the SOA behaviour and is a valuable tool which can be used to describe system level performance.

6.4 Dynamic Gain Modulation Performance of AGC-SOA

6.4.1 Simulation Performance

The previous section has demonstrated that the DC parametric behaviour of the AGC-SOA can be relatively accurately modelled using a counter propagating model that takes in to account the ASE. This provides a useful tool which enables designs of AGC-SOA to be studied and optimised. In many instances however, we are interested not only in the DC characteristics of the device but in how it will operate when subject to dynamic changes. This theoretical model can also be used to better understand the dynamic behaviour of the AGC-SOA which up until now is relatively ill-understood.

In order to do this, the model was run under the following conditions. Firstly stable operation of the AGC-SOA was ensured by running the simulation with only ASE for the first 30 loop iterations and at a SOA2 (clamping SOA) bias of 20 mA. This allows the dc characteristics to stabilise to a point where we are comfortable that they represent a real device.

At this point a 0 dBm input signal was introduced. This was amplified by the AGC-SOA by around 10 dB consistent with the dc operation above. The clamping SOA bias current was then increased every 10 iterations of the model loop, from 20 mA to 200 mA, in steps of 20 mA and the gain change observed (Figure 6.12).

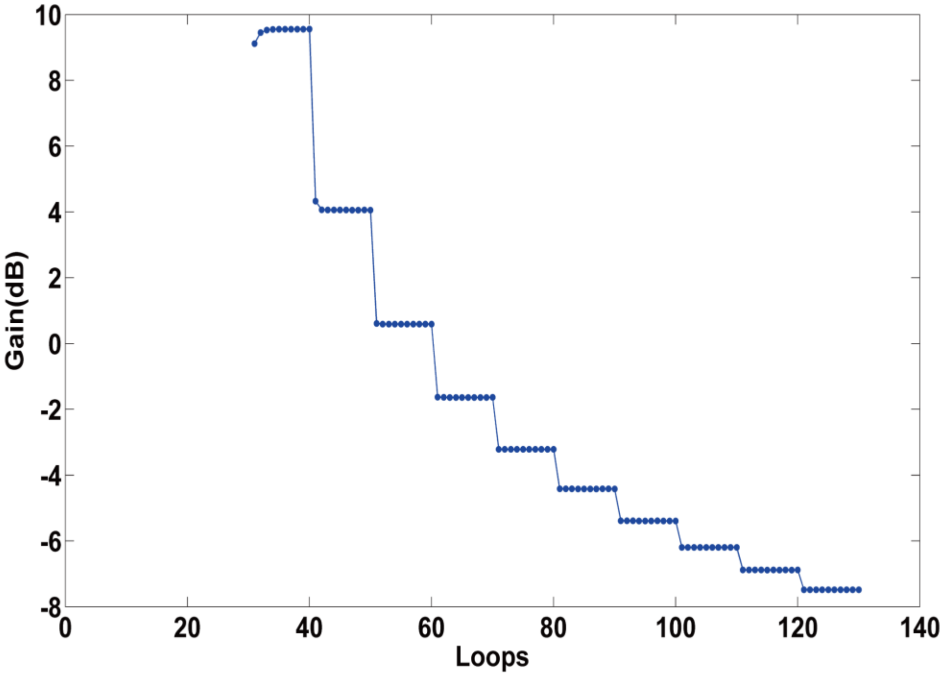

Figure 6.12 Dynamic gain variation as a function of clamping current.

It is clear from these simulations that not only is the gain regulated according to the changes in clamping bias, it is also adjusted and stabilized within 1 or 2 loops of the model iteration. This implies therefore that the gain can be adjusted within one or two transit times of the clamping mode, i.e. with nanosecond timescales which agree with experimental results [265].

6.4.2 Experimental Verification

A key application for such a device lies within PONs, where it is desirable to regulate the strength of a packet arriving at a burst mode receiver. In a dynamic packet equalisation scenario, the AGC-SOA must be able to adjust and stabilise its gain within the period of the guard band of the PON transmission viz. 32 bit periods which represents ~26 ns. For 10 Gbit/s PON systems (64 bits at 2.5 Gbit/s on the upstream direction) this equates to 26 ns [256]. The model therefore predicts that this is feasible.

Central to attaining high speed gain modulation is the capability to directly modulate the gain of the clamping SOA through the drive current. Traditional butterfly packages that are used to house SOAs are generally not optimized for high speed modulation. Although it is possible to do this, the commercially available devices in the main have neither the high speed electronic feed throughs that would be required nor the appropriate tracking on the tile leading to the SOA.

On the other hand, Reflective SOAs (RSOAs), packaged in a TO can, have been designed to both amplify and modulate signals at data rates in excess of 1 Gbit/s [266]. This is due to the fact that they are designed to be used as high speed transmitters in wavelength seeded WDM PON applications. The topology of the AGC-SOA was therefore modified to include an RSOA as shown in Figure 6.13. This arrangement is topologically equivalent to the geometry shown in Figure 6.2. Signals to be amplified are input through the P (pass) port on the WDM coupler. C-band signals are passed through to the SOA. At the output of the SOA, the amplified C-band signal is passed through the WDM coupler on the output. Out of band signals, ASE from the S-band and L-band signals, are amplified by the RSOA and used to form a counter propagating clamping mode.

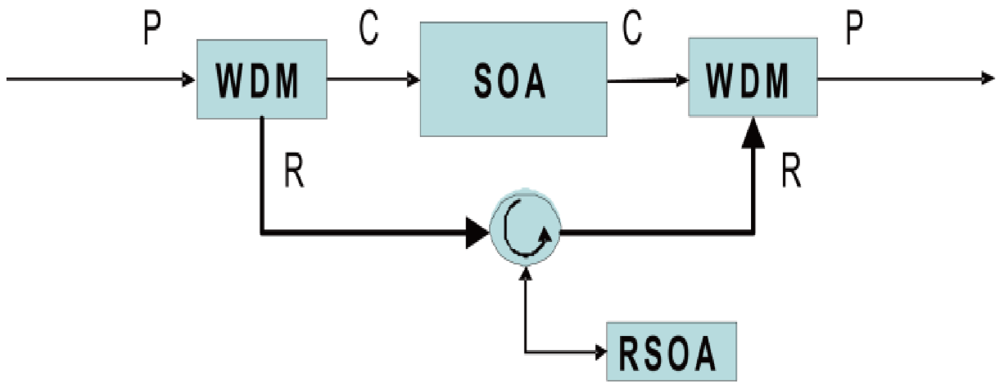

Figure 6.13 RSOA regulated AGC-SOA.

In order to assess the modulation capability of the AGC-SOA, the RSOA was driven with a data stream between two gain extremes i.e. high gain and low gain. In the RSOA high gain state, the gain of the AGC-SOA is highly clamped, i.e. it has very low gain. Conversely, when the RSOA is turned to a low gain state, the gain of the AGC-SOA is high. The transition time between the two states represents the minimum time required to adjust and settle the gain of the AGC-SOA. Figure 6.14 shows the variation in ASE signal emitted by the in-line signal SOA in response to directly modulating the RSOA gain. The transition between a high and a low state is in response to the $\overline{data}$ signal. This shows clearly that this transition time is < 2 ns.

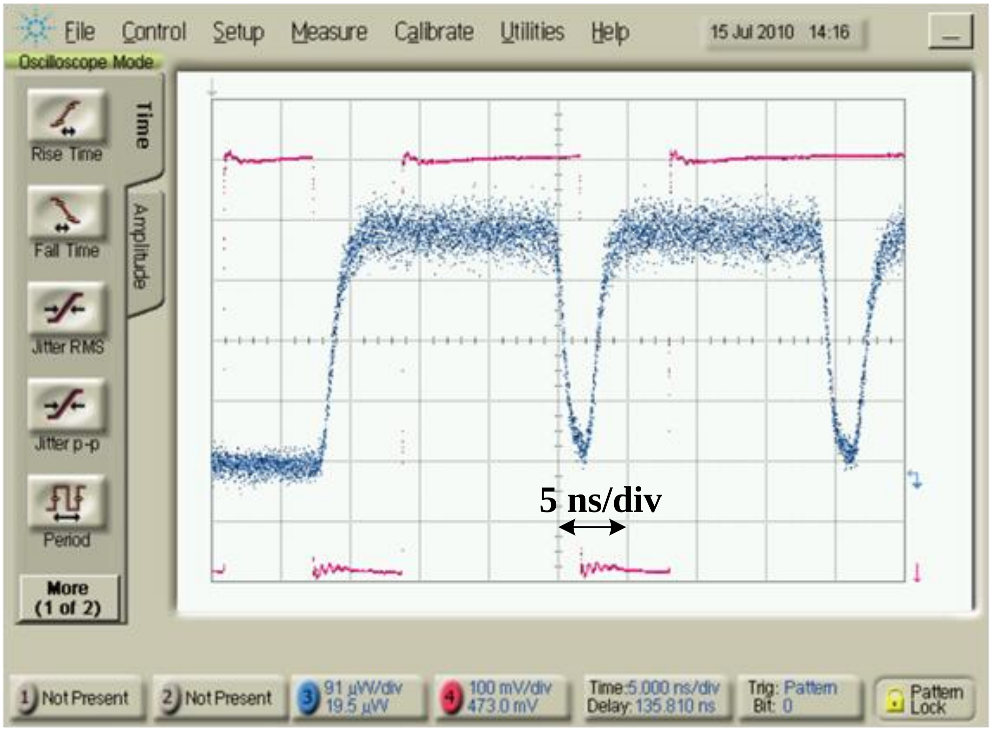

Figure 6.14 Directly modulated SOA ASE (blue), driving signal (red).

The experiment was repeated with a steady state signal of 0 dBm presented at the input to the AGC-SOA, Figure 6.15 shows that the amplitude of the seed signal has been directly modified through changing the gain of the AGC-SOA. Again it is clear that the transitions between gain states are < 2 ns (2 ns per division timescale). The experimental characterization and the modeling are therefore in broad agreement and indicate that the gain of the AGC-SOA can be adjusted and stabilized within the 26 ns timescale that would be required for packet equalisation in PONs.

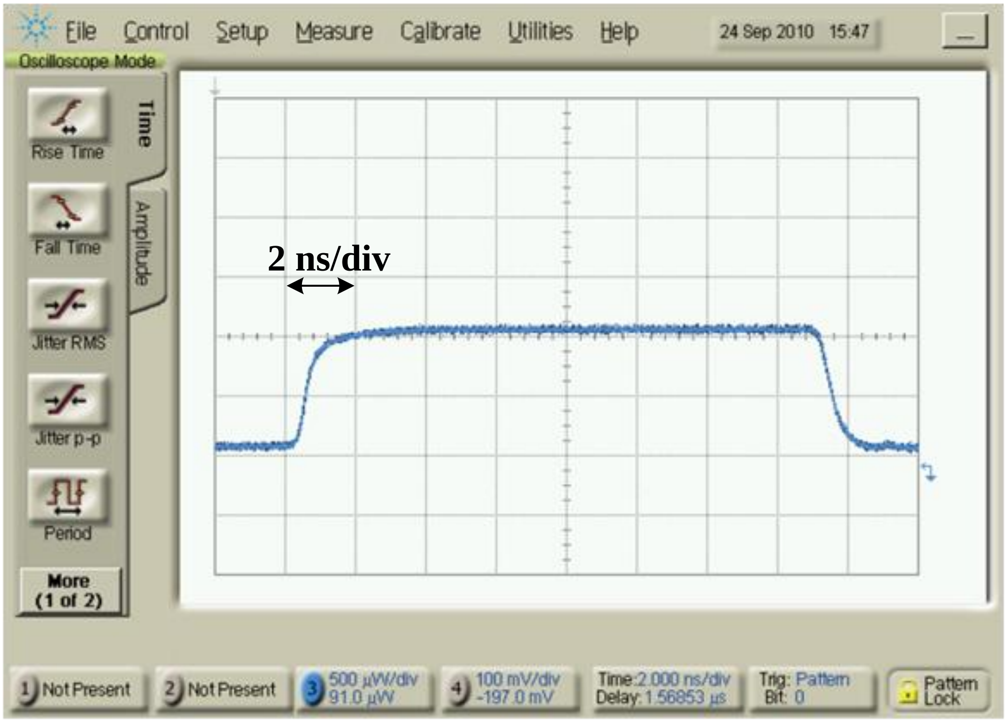

Figure 6.15 Directly modulated seed signal.

High speed gain modulation of the AGC-SOA on a data signal was demonstrated using the experimental arrangement shown in Figure 6.16. Data from an Agilent N4903A J-BERT Bit Error Rate (BER) test set was used to modulate a CWDM transmitter module (Finisar FDB 1027) at a data rate of 1.25 Gbit/s. The signal amplitude was then regulated using a combination of an Erbium Doped Fibre Amplifier (EDFA) and a variable optical attenuator (VOA). The output of the VOA was then input to the AGC-SOA. The gain of the AGC-SOA was regulated by applying a square wave to the RSOA via an ETS3869 laser driver, which provides control over the bias current (I_{bias}) and the data modulation power. The output from the AGC-SOA was detected using a pin photoreceiver and displayed on an Agilent Digital Communications Analyzer (DCA). All instruments were synchronised from a common clock source so that modulation and data signals could be observed at the same time.

An unfiltered eye diagram of the recovered data signal is shown below in Figure 6.17. Indicating that the output from the SOA was presented with a signal level that is sufficiently high to produce a degree of patterning. The gain of the AGC-SOA is then rapidly reduced to the point where the onward transmitted signal is much reduced but is substantially cleaner. The transition from the high gain state to the low gain state takes place over two bit periods i.e. just over 2 ns. The ER ratio of the eye diagram at high gain looks poorer than it actually is. This is because the high level of ASE contributes a significant DC term at the detector.

According to Figure 6.11, when increasing the clamping current, the device is changing from high gain to low gain. And the NF is increasing according but at a smaller gradient compared to the gain curve. According to the definition of the NF depicted in Equation 4.15, the SNR_{out} should be deteriorate during the transition from high gain to low gain. However, this contradicts the experimental result in Figure 6.17. Currently, there is no satisfactory explanation regarding this.

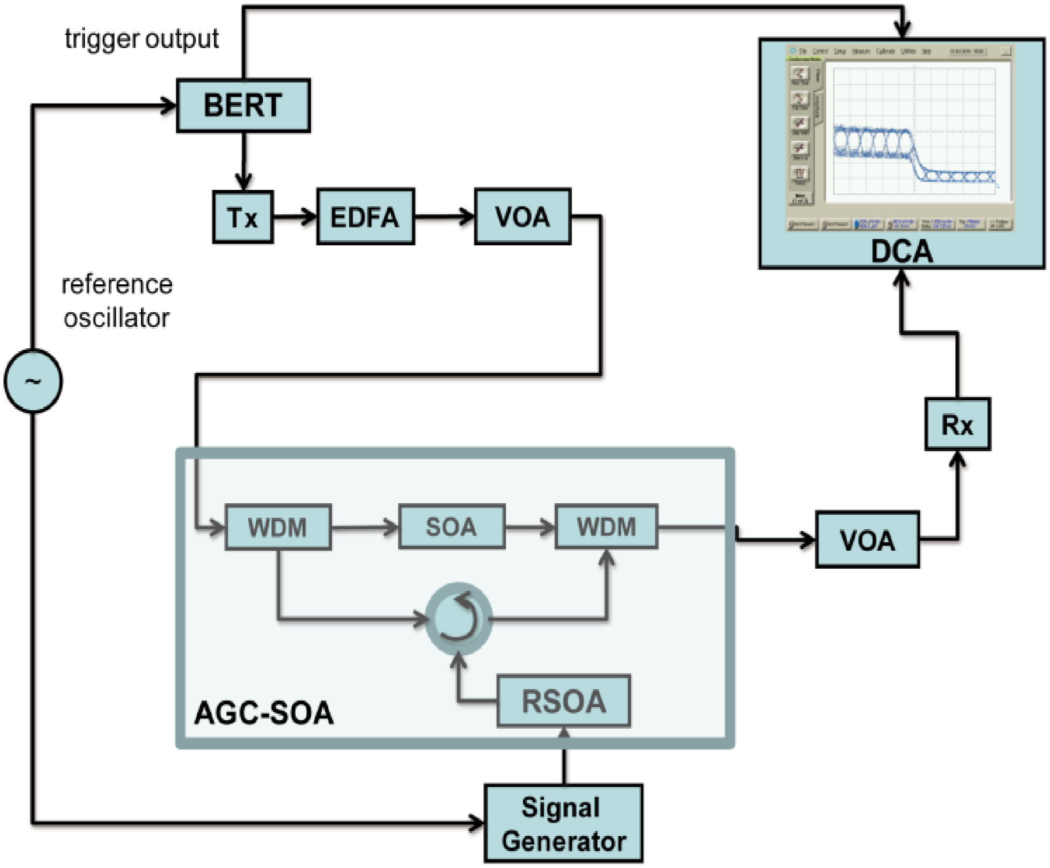

Figure 6.16 Gain equalisation experiment.

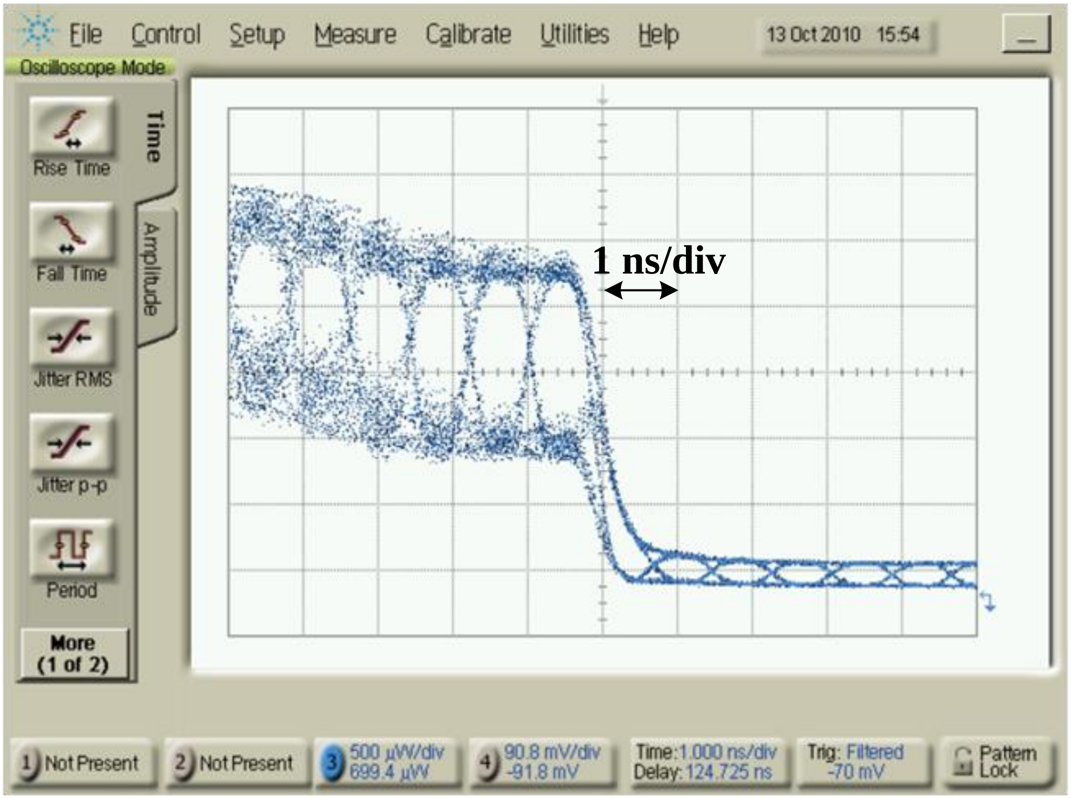

Figure 6.17 Eye diagram of a gain modulated data signal.

6.5 Summary

This chapter has presented a theoretical analysis of an AGC-SOA. Both the steady state operation and the case where the gain of the AGC-SOA is dynamically modulated are addressed. The DC parametric behaviour is shown to agree well with experimental measurements. An adaptation of the models has shown that in principle, the gain of the AGC-SOA can be regulated dynamically to respond within the guard band of packet based PON transmissions. Gain settling times within the order of 2 ns are predicted. This analysis was shown to agree well with experimental evaluation of the AGC-SOA behaviour which demonstrated gain modulation and settling within two bit periods of a 1.25 Gbit/s data signal.

A key motivation for this study was to better understand the dynamic behaviour of the AGC-SOA with a view to establishing a means for dynamically modulating the gain of the AGC-SOA in response to changes in packet amplitude. For this to be effective, the gain should be adjusted and stabilised within a timespan of less than 20 ns. Both the theoretical analysis and the experimental investigation indicate that it is possible.

Chapter 7 Conclusions and Future Work

This thesis has presented a detailed numerical study into the characteristics of Semiconductor Optical Amplifiers (SOAs), and their application within Passive Optical Networks (PONs). In particular, the thesis focuses attention on the modelling and experimental evaluation of an adjustable gain-clamped semiconductor optical amplifier (AGC-SOA), designed to maximize the output saturated power while enabling gain adjustment to regulate power differences between packets without loss of linearity. This theoretical analysis, together with experimental measurements has shown that, the gain of the AGC-SOA can be regulated dynamically to respond within the guard band of packet based PON transmissions.

The key feature of the optical amplification process in semiconductor optical devices is the interaction of electromagnetic radiation with semiconductor lasing materials in which population inversion is achieved. Thus the introduction of a SOA starts with the explanations of *p-n* junction and heterojunction. The classic four band model is employed to study the micro structure of SOA: energy band gap, quasi-Fermi level, material gain, spontaneous emission rate and carrier recombination rate, etc. The structure of SOA device is introduced with the gain-guided and index-guided heterostructure. An analysis of the impact of facet reflectivity showed that the suppression of the SOA gain ripple can be achieved by reducing the facet reflectivity for a given single pass gain. The use of antireflection coatings, angled facets, and window facet techniques used in reducing facet reflectivity have been reviewed. According to the review of the antireflection coating, the reflectivity of antireflection coating can be numerically expressed as a function of coating thickness and refractive index. This numerical prediction gives a guideline for the manufacturing process. The single and multilayer antireflection coating were also compared. In terms of angled facet technique, the analytical results showed that, the effective mode reflectivity decreases as increasing the facet angle and mode size. However, increasing the facet angle may induce far-field asymmetry which degrades the coupling efficiency between SOA and fibre, and also the guided mode size is limited, therefore, the optimal facet angles are usually between 7° and 10°. The effective reflectivity can be also reduced by increasing the window region length and decreasing the Gaussian mode size according to the analytical results. The last part of the chapter discussed the approaches to make the SOA polarization insensitive, such as using square cross section as active region and employing strained materials in the active region.

The basic optical communications system consists of optical transmitter, optical fibre, optical receiver and periodically placed regenerators or optical amplifiers. The loss, dispersion, and nonlinearities of the fibre are reviewed in Chapter 3. The PIN and APD diodes located in optical receivers are also compared. With regard to optical amplifiers, optical fibre amplifiers which could be classified into doped fibre amplifiers and Raman amplifiers are compared with semiconductor optical amplifiers in terms of optical amplification process and performance. After demonstrating a simple optical netork model, passive optical networks were introduced to tackle the bandwidth bottleneck in the first/last mile. PONs can be classified into TDM-PON and WDM-PONs. These were described and discussed separately. In the downstream traffic of TDM-PON, the time-division multiplexed signals are broadcasted to each ONU. For the upstream traffic, the time division multiple access mechanism is used in the OLT to synchronize all ONUs in order to avoid packet collision and improve the efficiency of upstream channel usage. In a standard TDM-PON, the downstream and upstream signals are carried by the same fibre but over two wavelengths so as to differentiate from each other. As transmission speed and PON reach increasing, and the dynamic range of signals arriving at the receiver becomes greater, the design of the burst mode receiver in the OLT is becoming more and more complicated. The AGC-SOA offers a potential solution to alleviate this issue. The dynamic gain modulation performance of AGC-SOA demonstrates its potential to regulate optical power difference between packets, and hence reduce the burden on Burst Mode Receiver design. In the long term, the WDM-PON is a promising alternative to TDM-PON however the deployment of the WDM-PON faces many technical challenges, especially the realization of the colorless ONU operation. The approaches such as central seeding and self seeding ONU are discussed and the cost effective hybrid WDM/TDM PON introduced. The use of SOA in PON is reviewed in the last past of the chapter. Implementing SOAs in PONs would extend the optical link budget to achieve a longer reach and more splits, which leads to CAPEX and OPEX saving. Moreover the reflective SOAs in the WDM-PON are usually used to generate, amplify or modulate the upstream signal light.

The basic characteristics and key applications of SOAs are discussed in Chapter 4. Firstly, through analytical expression deduction, the SOA gain and saturation, noise figure have been discussed. These expressions obtained in the chapter are essential for analyzing SOA and AGC-SOA performance in the following chapters. Secondly, the SOA dynamics is classified into the interband and intraband dynamics. The interband dynamics largely affect the duration of the gain recovery of a SOA. And the intraband processes become important when the SOA is amplifying the ultra-short optical pulses, it includes spectral hole burning (SHB), carrier heating (CH) and two photon absorption (TPA) processes. In the end, the applications of SOAs are divided into linear amplification and optical signal processing which is mainly taking advantage of SOA's nonlinearities, i.e. cross gain modulation (XGM), cross phase modulation (XPM), four-wave mixing (FWM) and nonlinear polarization rotation (NPR) effects. The XGM based wavelength conversion in the SOA can be achieved by both co-propagation and counter-propagation schemes, which are studied numerically in Chapter 5. The bandwidth of the XGM based converter can be enhanced by optimizing material parameters such as increasing the length of active region, increasing the differential gain and confinement factor, also by some external measurements e.g. high bias current, high input power and cascading SOAs. The XPM based applications are realized by placing the SOAs in the interferometric setup such as Mach-Zehnder interferometer (MZI), Michelson interferometer (MI), and Sagnac interferometer (SI). The principle of XPM is explained through its application as a wavelength converter in which MZI configuration is employed. Some variations of the MZI configuration such as polarization-descriminating symmetric Mach-Zehnder (PD-SMZ), delayed interferometer etc. have been discussed. Then the physics origin of FWM and its applications are introduced. In the end, the NPR effect and its applications in all-optical signal processing such as wavelength converter and optical signal regenerator, de-multiplexer, and optical logic gate have been reviewed.

Chapter 5 introduced and discussed two kinds of numerical models for studying the characteristics of SOAs, namely system level and device level SOA models. The classification of SOA theoretical models has been discussed and two basic equations, the propagation equation and carrier density rate equation, which are employed in both system and device level models, have been deduced. In particular, the propagation equation used in this thesis has been compared with the ones in other publications, the underlying consistency has been established. Based on these, the system level model has been introduced and applied into studying the all optical wavelength conversion using a SOA. Depending on travelling directions of pump and probe lights, the system model has been classified into co-propagation and counter-propagation models. The simulated wavelength conversion achieved by cross gain modulation (XGM) in the SOA has been performed in both co-propagation and counter-propagation models. The co-propagation system model has also been employed to numerically study the gain compression effect of the SOA. It is clear that the model is demonstrating similar dynamic behaviour to that observed experimentally, which proves the model is capable of studying the characteristics of SOAs. Then the direct modulation response of a SOA is investigated using modified system level model. The numerical results show that increasing the length of active region or unsaturated material gain coefficient would improve the modulation response of the device. The remainder of the chapter discussed the device level SOA model. It starts with the review of material gain coefficient for a semiconductor optical device. An improved material gain expression was introduced, This was based on the wideband material gain expression defined from the Fermi's Golden rule. It also takes the intraband relaxation effect into consideration. Further a detailed device level model is introduced taking into account the propagation of ASE in the SOA, and an efficiency improved steady-state numerical algorithm are highlighted. Based on this detailed wideband model, the output ASE spectrum under different bias currents is simulated. As the bias current increasing, the output ASE power increases significantly, and the peak wavelength of the spectrum moves towards short wavelength because of the band filling effect. It is also noticeable that the gain ripple becomes more obvious under high bias current which is consistent with the simulation result from Chapter 2. The device level model also studied the steady-state gain characteristics of SOA. It is shown that directly changing the bias current of a standard SOA is not a good way to achieve gain control since the output saturation power (P_{sat}) changes significantly.

Chapter 6 reports on an adjustable gain-clamped semiconductor optical amplifier (AGC-SOA) designed to maximize the output saturated power while adjusting gain to regulate power differences between packets without loss of linearity. The characteristics of the AGC-SOA are studied both numerically and experimentally. First of all, the existing numerical models for GC-SOAs are reviewed, and it is clear that these models are not suitable for the proposed device. Thus, a new numerical model has been proposed for the AGC-SOA which is based on the device level SOA model introduced in Chapter 5. Based on the simulation results obtained using the model, the power of internal counter-clockwise ASE increases rapidly within the first 3 loops of roundtrips and then stabilises. Since the cavity round trip time is ~1.7 ns, this implies stabilising the travelling ASE power in the loop takes between 1.7-5.1 ns (several round trips). By reviewing the SOA2 output ASE spectrum at different loop transits, it can be seen that the ASE in the S-band is weakened after every roundtrip and finally became negligible. However the ASE within the L-band is amplified after every roundtrip and the spectrum becoming sharp and narrow, which accounts for gain clamping. The variation of the gain with clamping SOA drive current is modelled over a range of clamping currents to corroborate that the model faithfully reproduced the experimental behaviour of the AGC-SOA. The maximum output power at gain saturation (P_{sat}) and noise figure (NF) performances are also modelled, which broadly agree with the experimental results. Then the dynamic behaviour of the AGC-SOA is simulated which implies the gain can be adjusted within one or two transit times of the clamping mode, i.e. with nanosecond timescales. The following experimental verifications have proved the gain modulation and settling within two bit periods of a 1.25 Gbit/s data signal. Therefore, it is clear that the gain of AGC-SOA would be dynamically modulated in response to changes in packet amplitude in PONs.

Future Work:

1. The detailed dynamic numerical model of the AGC-SOA can be established to study in-depth dynamic performance of the device, e.g. frequency response, so as to optimize the device to support high speed gain modulation.
2. The experimental work would carry out the BER measurements on dynamically regulated packets using AGC-SOA. This is not trivial and was considered out of scope of the present thesis.
3. The model that have been developed for standard and gain clamped SOAs can be applied to reflective SOAs to give a greater appreciation of their operation, particularly under modulation.

References

[1] G. Keiser, *Optical Fiber Communications.* 4th Ed, McGraw-Hill, 2010.

[2] E. Risberg, "A history of the Finnish telegraph administration, 1855-1955," General Direction of Posts and Telecommunications, Helsinki, 1955.

[3] J. C. Maxwell, "On physical lines of force," *The London, Edinburgh, and Dublin Philos. Mag. J. Sci.*, pp.161, 1861, and J. C. Maxwell, *A Treatise on Electricity and Magnetism*, Oxford, U.K. : Clarendon, 1873.

[4] D. Hondros and P. Debye, "Elektromagnetische wellen an dielektrischen draehten," *Ann. Phys.,* vol. 32, pp. 465-476, 1910.

[5] M. I. Schwartz, "Optical fibre transmission – from conception to prominence in 20 years," *IEEE Commun. Mag.,*vol. 22, no. 5, pp. 38-48, May 1984.

[6] M. Planck, "On an improvement of wien's equation for the spectrum," *Verh. Deut. Phys. Ges.,* vol. 2, pp. 202-204, 1900.

[7] M. Planck, "On the theory of the energy distribution law of the normal spectrum," *Verh. Deut. Phys. Ges.,* vol. 2, pp. 237-245, 1900.

[8] A. Einstein, "On the quantum theory of radiation," *Phys. Z.* vol. 18, pp. 121-128, 1917.

[9] T. H. Maiman," Stimulated Optical Radiation in Ruby", *Nature,* vol. 187, no. 4736, pp493-494, 1960

[10] R. N. Hall, G. E. Fenner, J. D. Kingsley, T. J. Soltys, and R. O. Carlson, "Coherent light emission from GaAs junctions," *Phys. Rev. Lett.,* vol. 9, no. 9, pp. 366-368, 1962.

[11] I. Hayashi, M. B. Panish, P. W. Foy and S. Sumski, "Junction lasers which operate continuously at room temperature," *Appl. Phys. Lett.,* vol. 17, no. 3, pp109-111, 1970.

[12] K. C. Kao and G. A. Hockham, "Dielectric-fibre surface waveguides for optical frequencies," *Proc. Inst. Elec. Eng.,* vol. 113, pp. 1151-1158, Jul 1966.

[13] F. P. Kapron, D. B. Keck, and R. D. Maurer, "Radiation losses in glass optical waveguides," *Appl. Phys. Lett.,* vol. 17, pp. 423-425, Nov 1970.

[14] R. J. Sanferrare, "Terrestrial lightwave systems" *AT&T Tech. J.,* vol. 66, no. 1, pp95-107, 1987.

[15] C. Fan, and L. Clark, "Impact of new lightwave technologies on terrestrial longhaul network evolution," *Opt. Photon. News.*,vol. 6, no. 2, pp. 26, Feb. 1995.

[16] G. P. Agrawal, Fiber-Optic Communication Systems, 4th Ed, New Jersey, Wiley, 2010.

[17] T. Miya, Y. Terunuma, T. Hosaka and T. Miyashita, "Ultimate low loss single mode fibre at 1.55µm," *Electron Lett.,* vol. 15, no. 4, pp. 106-108, 1979.

[18] K. Nakagawa, *Trans. IECE Jpn. Pt.* J78B, 713, 1995.

[19] R. J. Mears, L. Reekie, I. M. Jauncey and D. M. Payne,"Low noise Erbium Doped Fibre Amplifier operating at 1.54µm," *Electron Lett.*, vol. 23, no.19, pp.1026-1028, 1987.

[20] W. J. Tomlinson, "Wavelength multiplexing in multimode optical fibres," *Appl. Opt.*, vol. 16, no. 8, pp. 2180- 2194, Aug, 1977.

[21] N. S. Bergano, J. Aspell, C. R. Davidson, P. R. Trischitta, B. M. Nyman and F. W. Kerfoot, "Bit error rate measurements of 14000 km 5 Gbit/s fibre-amplifier transmission system using circulating loop," *Electron Lett.*, vol. 27, no. 21, pp. 1889-1890, Oct, 1991.

[22] K. Fukuchi, T. Kasamatsu, M. Morie, R. Ohhira, T. Ito, K. Sekiya, D. Ogasahara, and T. Ono, "10.92-Tb/s (273×40-Gb/s) triple-band/ultra-dense WDM optical-repeatered transmission experiment," *Proc. Optical Fiber Commun. Conf.,* Paper PD24, Mar, 2001.

[23] B. Mikkelsen, G. Raybon, B. Zhou, R. J. Essiambre, P. G. Bernasconi, K. Dreyer, L. W. Stulz, and S. N. Knudsen, "High spectral efficiency (0.53 bit/s/Hz) WDM transmission of 160 Gb/s per wavelength over 400 km of fibre," *Proc. Optical Fiber Commun. Conf.*, Paper ThF2, Mar, 2001.

[24] G. C. Gupta, , L. L. Wang, O. Mizuhara, R. E. Tench, N. N. Dang, P. Tabaddor, and A. Judy, "3.2-Tb/s (40 ch x 80 Gb/s) transmission with spectral efficiency of 0.8 b/s/Hz over 21 x 100 km of dispersion-managed high local dispersion fiber using all-Raman amplified spans," *IEEE Photon.Technol. Lett.*, vol. 15, no. 7, pp. 996-998, Jul, 2003.

[25] X. Zhou, L. E. Nelson, R. Isaac, P. D. Magill, B. Zhu, D. W. Peckham, P. Borel, and K. Carlson, "4000km transmission of 50GHz spaced, 10×494.85-Gb/s hybrid 32-64QAM using cascaded equalization and training-assisted phase recovery," *Proc. Optical Fiber Commun. Conf.,* Paper PDP5C, Mar, 2012.

[26] E. Lach, and W. Idler, "Modulation formats for 100G and beyond," *Opt Fiber Technol.,* vol. 17, pp. 377-386, 2011.

[27] M. Camera, B-E. Olsson, and G. Bruno, “Beyond 100Gbit/s: System implications towards 400G and 1T,” *Proc. ECOC*, paper Th10G1, pp. 1-15, Sep, 2010.

[28] X. Zhou, L. E. Nelson, P. Magill, R. Isaac, B. Zhu, D. W. Peckham, P. Borel, and K. Carlson, “PDM-Nyquist-32QAM for 450-Gb/s per-channel WDM transmission on the 50 GHz ITU-T grid ,” *J. Lightw Technol.,* vol. 30, no. 4, pp. 553-559, Feb, 2012.

[29] R. Essiambre and A. Mecozzi, "Capacity limits in single mode fiber and scaling for spatial multiplexing," in *Proc. Optical Fiber Commun. Conf.,* paper OW3D.1, Mar. 2012.

[30] T. Hayashi, T. Sasaki, and E. Sasaoka, "Multi-core fibers for high capacity transmission," in *Proc. Optical Fiber Commun. Conf.,* paper OTu1D.4, Mar. 2012.

[31] S. Randel, A. Sierra, S. Mumtaz, A. Tulino, R. Ryf, P. Winzer, C. Schmidt, and R. Essiambre, "Adaptive MIMO signal processing for mode-division multiplexing," in *Proc. Optical Fiber Commun. Conf.,* paper OW3D.5, Mar. 2012.

[32] H. Ghafouri-Shiraz, *The Principles of Semiconductor Laser Diodes and Amplifiers,* Imperial College Press, 2004.

[33] A. Yariv, *Quantum Electronics*, New York, Wiley, 1989.

[34] W. W. Chow and S. W. Koch, *Semiconductor Laser- Fundamentals*, New York, Springer-Verlag, 1999.

[35] L. Vegard, “Die Konstitution der Mischkristalle und die Raumfüllung der Atome,” *Phys. Z.* vol. 5, no. 1, pp. 17-26, 1921.

[36] S. L. Chuang, *Physics of Optoelectronic Devices*. New York: Wiley Interscience, 1995.

[37] G. Giesecke, in *Semiconductors and Semimetals*, Vol. 2, R. K. Willardson and A. C. Beer, eds., Academic, New York, 1966, pp. 63; H. Kressel and J. K. Butler, *Semiconductor Lasers and Heterojunction LED’s*, Academic, New York, 1977.

[38] S. Adachi, *Physical Properties of Ⅲ-Ⅳ semiconductor compounds,* New York: Wiley, 1992.

[39] T. P. Pearsall, *GaInAsP Alloy Semiconductors,* Wiley, Chichester, UK, 1982, pp. 295.

[40] E. O. Kane, “Band structure of indium antimonide”, *J. Phys. Chem. Solids.,* vol. 1, no. 4, pp. 249-261, 1957.

[41] A. Yariv, *Photonics: Optical Electronics in Modern Communications,* 6th Ed, Oxford University Press, 2007.

[42] N. G. Nilsson, "Empirical approximations for the Fermi energy in a semiconductor with parabolic bands", *Appl. Phys. Lett.,* Vol. 33, pp. 653-654, 1978.

[43] S. L. Chuang, J. O'Gorman, and A. F. J. Levi, "Amplified spontaneous emission and carrier pinning in laser diodes," *IEEE J. Quantum Electron.,* vol. 29, no. 6, pp. 1631-1639, Jun, 1993.

[44] M. Kot, and K. Zdansky, "Measurement of radiative and nonradiative recombination rate in InGaAsP-InP LED's ," *IEEE J. Quantum Electron.,* vol. 28, no. 8, pp. 1746-1750, Aug, 1992.

[45] G. P. Agrawal and N. K. Dutta, *Long-Wavelength Semiconductor Lasers,* Van Nostrand Reinhold, 1986.

[46] G. Eisenstein, P. B. Hansen, J. M. Wiesenfeld, R. S. Tucker, and G. Raybon, "Amplification of high repetition rate picoseconds pulses using an InGaAsP traveling wave optical amplifier, " *Appl. Phys. Lett.,*vol. 53, no. 16, pp. 1539-1541, Oct, 1988.

[47] G. Eisenstein, R. S. Tucker, J. M. Wiesenfeld, P. B. Hansen, G. Raybon, B. C. Johnson, T. J. Bridges, F. G. Storz, and C. A. Burrus, "Gain recovery time of travelling-wave semiconductor optical amplifiers," *Appl. Phys. Lett.,*vol. 54, no. 5, pp. 454-456, Jan, 1989.

[48] D. A. O. Davies, "Small-signal analysis of wavelength conversion in semiconductor laser amplifiers via gain saturation," *IEEE J. Quantum Electron.,* vol. 7, no. 6, pp. 617-619, Jun, 1995.

[49] R. J. Manning and D. A. O. Davies, "Three-wavelength device for all-optical signal processing," *Opt. Lett.,* vol. 19, no. 12, pp. 889-891, Jun, 1994.

[50] J. L. Pleumeekers, M. Kauer, K. Dreyer, C. Burrus, A. G. Dentai, S. Shunk, J. Leuthold, and C. H. Joyner, "Acceleration of gain recovery in semiconductor optical amplifiers by optical injection near transparency wavelength," *IEEE Photon.Technol. Lett.,* vol. 14, no. 1, pp. 12–14, Jan. 2002.

[51] J. J. Hsieh, J. A. Rossi and J. P. Donnelly, "Room-temperature cw operation of GaInAsP/InP double-heterostructure diode lasers emitting at 1.1 µm" *Appl. Phys. Lett.,* vol. 28, no. 12, pp. 709-712, 1976.

[52] P. S. Zory, Jr, *Quantum Well Lasers,* Academic Press, London, UK, 1993.

[53] T. Mukai and Y. Yamamoto, “Gain, frequency bandwidth, and saturation output power of AlGaAs DH laser amplifiers,” *IEEE J. Quantum Electron.*, vol. 17, no. 6, pp. 1028-1034, 1981.

[54] T. Saitoh and T. Mukai, "1.5 µm GaInAsP traveling-wave semiconductor laser amplifier," *IEEE J. Quantum Electron.*, vol. 23, no. 6, pp. 1010-1020, 1987.

[55] D. Huang, D. Liu, S. Yu, M. Zhou, X. Liu, and J. Huang, “Packaged double-pass travelling-wave semiconductor laser amplifiers,” *Electron. Lett.*, vol. 27, no. 7, pp. 571–572, Mar. 1991.

[56] K. Y. Cho, Y. Takushima, and Y. C. Chung, “10-Gb/s operation of RSOA for WDM PON,” *IEEE Photon.Technol. Lett.*, vol. 20, no. 18, pp. 1533-1535, Sep, 2008.

[57] K. Y. Cho, and Y. C. Chung, “10-Gb/s operation of RSOA for WDM PON using return-to-zero modulation format,” *Proc. Optical Fiber Commun. Conf.*, Paper OTh1F, Mar, 2012.

[58] C. Michie, A. E. Kelly, L. Liu, I. Andonovic, and W.-D. Zhong, “Semiconductor optical amplifiers in future passive optical networks,” *Proc. International Conference on Information, Communications and Signal Processing (ICICS 2009)*, Dec, 2009.

[59] M. D. Feuer, J. M. Wiesenfeld, J. S. Perino, C. A. Burrus, G. Raybon, S. C. Shunk, and N. K. Dutta, “Single-port laser-amplifier modulators for local access,” *IEEE Photon.Technol. Lett.*, vol. 8, no. 9, pp. 1175-1177, Sep, 1996.

[60] C. E. Zah, C. Caneau, F. K. Shokoohi, S. G. Menocal, F. Favire, L. A. Reith, and T. P. Lee, “1.3 µm GaInAsP near-traveling-wave laser amplifiers made by combination of angled facets and antireflection coatings,” *Electron. Lett.*, vol. 24, no. 20, pp. 1275–1276, Sept. 1988.

[61] I. Cha, M. Kitamura, H. Honmou, and I. Mito, “1.5 µm band travelling-wave semiconductor optical amplifiers with window facet structure,” *Electron. Lett.*, vol. 25, no. 18, pp. 1241–1242, Aug. 1989.

[62] S. A. Merritt, D. S. Fox, I.-F. Wu, and M. Dagenais, “Measurement of the facet modal reflectivity spectrum in high quality semiconductor traveling wave amplifiers,” *J. Lightwave Technol.*, vol. 13, no. 3, pp. 430–433, Mar. 1995.

[63] J. Lee, T. Tanaka, S. Sasaki, S. Uchiyama, M. Tsuchiya, and T. Kamiya, "Novel design procedure of broad-band multilayer antireflection coatings for optical and optoelectronic devices," *J. Lightwave Technol.*, vol. 16, no. 5, pp. 884-891, May. 1998.

[64] T. Saitoh, T. Mukai, and O. Mikami, “Theoretical analysis and fabrication of antireflection coatings on laser diode facets,” *J. Lightwave Technol.,* vol. LT-3, no. 2, pp. 288-293, Apr. 1985.

[65] L. Atternas, and L. Thylen, “Single-layer antireflection coating of semiconductor lasers: polarization properties and the influence of the laser structure,” *J. Lightwave Technol.,* vol. 7, no. 2, pp. 426-430, Feb. 1989.

[66] D. J. Gallant, M. L. Tilton, D. J. Bossert, J. D. Barrie, and G. C. Dente, "Optimized single-layer antireflection coatings for semiconductor lasers," *IEEE Photon.Technol. Lett.,* vol. 9, no. 3, pp. 300-302, March, 1997.

[67] I-F. Wu, I. Riant, J-M. Verdiell, and M. Dagenais, “Real-time *in situ* monitoring of antireflection coatings for semiconductor laser amplifiers by ellipsometry,” *IEEE Photon.Technol. Lett.,* vol. 4, no. 9, pp. 991-993, Sep, 1992.

[68] B. W. Hakki, and T. L. Paoli, "cw degradation at 300 ^{o}K of GaAs double-heterostructure junction lasers. II. Electronic gain," *J. Appl. Phys.*, vol. 44, no. 9, pp. 4113-4119, May, 1973.

[69] B. W. Hakki and T. L. Paoli, “Gain spectra in GaAs double-heterostructure injection lasers,” *J. Appl. Phys.*, vol. 46, pp. 1299–1306, Mar. 1975.

[70] B. Luo, L. Wu, J. Chen, and Y. Lu, “Determination of wavelength dependence of the reflectivity at AR coated diode facets,” *IEEE Photon.Technol. Lett.,* vol. 5, pp. 1279–1281, Nov. 1993.

[71] J. Lee and T. Kamiya, "Improved characterization of multilayer antireflection coatings for broad-band semiconductor optical amplifiers," *J. Lightwave Technol.*, vol. 18, no. 12, pp. 2158-2166, Dec. 2000.

[72] C. Vassallo, "Polarisation-independent antireflection coatings for semiconductor optical amplifiers," *Electron. Lett.,* vol. 24, no. 1, pp. 61-62, Jan. 1988.

[73] D. Marcuse, "Reflection loss of laser mode from tilted end mirror," *J. Lightwave Technol.*, vol. 7, no. 2, pp. 336-339, Feb. 1989.

[74] C. E. Zah, R. Bhat, S. G. Menocal, N. Andreadakis, F. Favire, and C. Caneau, "1.5 µm GaInAsP angled-facet flared-waveguide traveling-wave laser amplifiers," *IEEE Photon.Technol. Lett.,* vol. 2, no. 1, pp. 46-47, Jan. 1990.

[75] W. B. Joyce and B. C. Deloach, “Alignment of Gaussian beams,” *Appl. Opt.,* vol. 23, pp. 4182-4196, 1984.

[76] T. Kelly, "Optimisation of Semiconductor Optical Amplifiers for Optical Networks," Ph.D thesis, University of Strathclyde, 1999.

[77] N. A. Olsson, R. F. Kazarinov, W. A. Nordland, C. H. Henry, M. G. Oberg, H. G. White, P. A. Garbinski, and A. Savage, "Polarisation-independent optical amplifier with buried facets," *Electron. Lett.*, vol. 25, no. 16, pp. 1048-1049, Aug. 1989.

[78] K. Utaka, S. Akiba, K. Sakai and Y. Matsushima, "Effect of mirror facets on the lasing characteristics of distributed feedback InGaAsP/InP laser diodes at 1.55μm range," *IEEE J. Quantum Electron.*, vol. 20, No. 3, pp. 236-244, Mar, 1984.

[79] C. Michie, A. E. Kelly, J. McGeough, I. Armstrong, I. Andonovic, and C. Tombling, “Polarization-insensitive SOAs using strained bulk active regions,” *J. Lightwave Technol.*, vol. 24, no. 11, pp. 3920-3927, Nov. 2006.

[80] P. Doussiere, P. Garabedian, C. Graver, D. Bonnevie, T. Fillion, E. Derouin, M. Monnot, J. G. Provost, D. Leclerc, and M. Klenk, “1.55 μm polarisation independent semiconductor optical amplifier with 25 dB fiber to fiber gain,” *IEEE Photon. Technol. Lett.*, vol. 6, no. 2, pp. 170–172, 1994.

[81] P. Doussiere, “Polarisation independent 1550 nm semiconductor optical amplifier packaged module with 29 dB fibre to fibre gain,” in *Proc. Opt. Amplifiers and Their Appl.*, pp. 119. Paper FA4, Davos, Switzerland, 1995.

[82] A. Miller, K. R. Welford and B. Daino, *Nonlinear Optical Materials and Devices for Applications in Information Technology,* Series E, vol. 289, Kluwer Academic Publishers, 1993.

[83] J.-Y. Emery, T. Ducellier, M. Bachmann, P. Doussiere, F. Pommereau, R. Ngo, F. Gaborit, L. Goldstein, G. Laube, and J. Barrau, “High performance 1.55 μm polarisation insensitive semiconductor optical amplifier based on low-tensile-strained bulk GaInAsP,” *Electron. Lett.*, vol. 33, pp. 1083–1084, 1997.

[84] K. Morito, M. Ekawa, T. Watanabe, T. Fujii, and Y. Kotaki, “Polarization insensitive type semiconductor optical amplifiers based on tensile-strained-bulk active layers,” *Tech. Rep. IEICE.* OPE99-95, 1999.

[85] A. Ougazzaden, D. Sigogne, A. Mircea, E.V.K. Rao, A. Ramdane, L. Silvestre, "Atmospheric pressure MOVPE growth of high performance polarisation insensitive strain compensated MQW InGaAsP/InGaAs optical amplifier," *Electron. Lett.*, vol. 31, no.15, pp. 1242-1244, Jul, 1995.

[86] L. F. Tiemeijer, P. J. A Thijs, T. vanDongen, J. J. M. Binsma, E. J. Jansen, "Polarization resolved, complete characterization of 1310 nm fiber pigtailed multiple-quantum-well optical amplifiers," *IEEE Photon. Technol. Lett.*, vol. 14, no.6, pp. 1524-1533, Jun, 1996.

[87] M. A. Newkirk, B. I. Miller, U. Koren, M. G. Young, M. Chien, R. M. Jopson, and C. A. Burrus, “1.5 μm multiquantum-well semiconductor optical amplifer with tensile and compressively strained wells for polarization-independent gain,” *IEEE Photon. Technol. Lett.*, vol. 4, no.4, pp. 406-408, Apr, 1993.

[88] J-Y. Emery, P. Doussiere, L. Goldstein, F. Pommereau, C. Fortin, R. Ngo, N. Tscherptner, J-L. Lafragette, P. Aubert and F. Brillouet, “New, process tolerant, high performance 1.55 μm polarization insensitive semiconductor optical amplifier based on low tensile bulk GaInAsP,” *Proc. ECOC*, paper WeD.2.3, pp. 165-168, Sep, 1996.

[89] G. A. Thomas, B. I. Shraiman, P. F. Glodis, and M. J. Stephen, “Towards the clarity limit in optical fibre,” *Nature*, vol. 404, Mar, 2000.

[90] D. B. Keck, “Fundamentals of optical waveguide fibers,” *IEEE Commun Mag.*, vol. 23, no. 5, pp. 17-22, May, 1985.

[91] ITU-T G.653, *Characteristics of a dispersion-shifted, single-mode optical fibre and cable*, Jul, 2010.

[92] S. D. Personick, “Applications for quantum amplifiers in simple digital optical communication systems,” *Bell Syst. Tech. J.*, vol. 52, pp. 117-133, 1973.

[93] L. Spiekman, D. Piehler, P. Iannone, K. Reichmann, and H. Lee, “Semiconductor optical amplifiers for FTTx,” in *Proc. ICTON*, pp. 48–50, 2007.

[94] F. J. Effenberger, “The XG-PON system: Cost effective 10 Gb/s access,” *J. Lightwave Technol.*, vol. 29, no. 4, pp. 403–409, Feb. 2011.

[95] A. Rostami, H. B. A. Nejad, R. M. Qartavol, and H. R. Saghai, “Tb/s optical logic gates based on quantum-dot semiconductor optical amplifiers,” *IEEE J. Quantum Electron.*, vol. 46, no. 3, pp. 354–360, 2010.

[96] L. Banchi, M. Presi, A. D’Errico, G. Contestabile, and E. Ciaramella, “All-optical wavelength 10 and 40 Gbit/s RZ-to-NRZ format and wavelength conversion using semiconductor optical amplifiers,” *J. Lightwave Technol.*, vol. 28, no. 1, pp. 32–38, 2010.

[97] I. Armstrong, I. Andonovic, A. E. Kelly, S. Bonthron, J. Bebbington, C. Michie, C. Tombling, S. Fasham, and W. Johnstone, “Hybridization platform assembly and demonstration of all-optical wavelength conversion at 10 Gb/s,” *J. Lightwave Technol.*, vol. 23, no. 5, pp. 1852–1859, May. 2005.

[98] http://www.huawei.com/ilink/en/about-huawei/newsroom/press-release/HW_062712?KeyTemps=DSL%20prototype

[99] R. P. Davey, D. B. Grossman, M. Rasztovits-Wiech, D. B. Payne, D. Nesset, A. E. Kelly, A. Rafel, S. Appathurai, and Sheng-Hui. Yang, “Long-reach passive optical networks,” *J. Lightwave Technol.*, vol. 27, no. 3, pp. 273-290, Feb, 2009.

[100] P. J. Winzer and R. –J. Essiambre, “Advanced optical modulation formats,” *Proc. IEEE*, vol. 94, no. 5, pp. 952-985, May, 2006.

[101] J. M. Simmons, Optical Network Design and Planning, Springer, New York, USA, 2008.

[102] C. F. Lam, Passive Optical Networks: Principles and Practice, Elsevier, San Diego, CA, USA, 2007.

[103] Cisco Systems, Cisco Visual Networking Index: Forecast and Methodology, 2010–2015 Jun. 2011 [Online]. Available: http://www.cisco.com/en/US/solutions/collateral/ns341/ns525/ns537/ns705/ns827/white_paper_c11-481360.pdf

[104] T. Kuroda, “Current status on super HDTV development in Japan,” *IEEE Int’l. Symp. Broadband Multimedia Sys. Broadcasting*, Mar, 2010.

[105] S. S. Wagner, H. L. Lemberg, “Technology and system issues for a WDM-based fiber loop architecture,” *J. Lightwave Technol.*, vol. 7, no. 11, pp. 1759–1768, Nov. 1989.

[106] http://www.idate.org

[107] OVUM: http://ovum.com/events/ftthodnotn-china-conference-2012-foocc/

[108] M. Nakamura, S. Nishihara, T. Ito, T. Kurosaki, M. Nogawa, and Y. Ohtomo, “Burst-mode optical receiver ICs for broadband access networks,” *IEEE Bipolar/BiCMOS Circuits and Technology Meeting*, pp. 21-28, 2010.

[109] K.-Y. Liou, U. Koren, E.C. Burrows, J.L. Zyskind, K. Dreyer, ‘‘A WDM access system architecture based on spectral slicing of an amplified LED and delay-line multiplexing and encoding of eight wavelength channels for 64 subscribers,’’ *IEEE Photon. Technol. Lett.*, vol. 9, no. 4, pp. 517–519, Apr, 1997.

[110] B. Zhang, C. Lin, L. Huo, Z. Wang, and Chun-Kit. Chan, “A simple high-speed WDM PON utilizing a centralized supercontinuum broadband light source for colorless ONUs,” *Proc. Optical Fiber Commun. Conf.*, Paper OTuC6, Mar, 2006.

[111] D. J. Shin, Y. C. Keh, J. W. Kwon, E. H. Lee, J. K. Lee, M. K. Park, J. W. Park, Y. K. Oh, S. W. Kim, I. K. Yun, H. C. Shin, D. Heo, J. S. Lee, H. S. Shin, H. S. Kim, S. B. Park, D. K. Jung, S. Hwang, Y. J. Oh, D. H. Jang, and C. S. Shim, “Low-cost WDM-PON with colorless bidirectional transceivers,” *J. Lightwave Technol.*, vol. 24, no. 1, pp. 158–165, Jan. 2006.

[112] W. Lee, M. Y. Park, S. H. Cho, J. Lee, C. Kim, G. Jeoing, and B. W. Kim, “Bidirectional WDM-PON based on gain-saturated reflective semiconductor optical amplifiers,” *IEEE Photon.Technol. Lett.*, vol. 17, no. 11, pp. 2460-2462, Nov, 2005.

[113] S.-M. Lee, K.-M. Choi, S.-G. Mun, J.-H. Moon, and C.-H. Lee, “Dense WDM-PON based on wavelength locked Fabry-Perot lasers,” *Proc. Optical Fiber Commun. Conf.*, Paper JWA55, Mar, 2005.

[114] P. Healey, P. Townsend, C. Ford, L. Johnston, P. Townley, I. Lealman, L. Rivers, S. Perrin, and R. Moore, “Spectral slicing WDM-PON using wavelength-seeded reflective SOAs,” *Electron Lett.*, vol. 37, no.19, pp. 1181-1182, 2001.

[115] B. Kim and Byoung-Whi. Kim, “WDM-PON development and deployment as a present optical access solution,” *Proc. Optical Fiber Commun. Conf.*, Paper OThP5, Mar, 2009.

[116] S. Hann, T-Y. Kim and C.-S. Park, “Direct-modulated upstream signal transmission using a self-injection locked F-P LD for WDM-PON,” *Proc. ECOC.*, Paper We 3.3.3, vol. 3, pp. 451-452, Sep, 2005.

[117] H.-C. Kwon, Y.-Y. Won, and S.-K. Han, “A self-seeded reflective SOA-based optical network unit for optical beat interference robust WDM/SCM-PON link,” *IEEE Photon.Technol. Lett.*, vol. 18, no. 17, pp. 1852-1854, Sep, 2006.

[118] E. Wong, K.-L. Lee and T. Anderson, “Low-cost WDM passive optical network with directly-modulated self-seeding reflective SOA,” *Electron Lett.*, vol. 42, no.5, Mar, 2006.

[119] J.-J. Yoo, H.-H. Yun, T.-Y. Kim, K.-B. Lee, M.-Y. Park, B.-W. Kim, and B.-T. Kim, ‘‘A WDM-Ethernet hybrid passive optical network architecture,’’ *Proc. International Conference on Advanced Communication Technology (ICACT 2006)*, vol. 3, pp. 1754-1757, Feb., 2006.

[120] D. J. Shin, D. K. Jung, H. S. Shin, J. W. Kwon, S. Hwang, Y. Oh, and C. Shim, ‘‘Hybrid WDM/TDM PON with wavelength-selection-free transmitters,’’ *J. Lightwave. Technol.*, vol.23, no.1, Jan, 2005.

[121] D. Nesset, D. Payne, R. Davey and T. Gilfedder, “Demonstration of enhanced reach and split of a GPON system using semiconductor optical amplifiers,” *Proc. ECOC.*, Sep, 2006.

[122] R. P. Davey, D. B. Grossman, M. Rasztovits-Wiech, D. B. Payne, D. Nesset, A. E. Kelly, A. Rafel, S. Appathurai, and S.-H. Yang, “Longreach passive optical networks,” *J. Lightwave Technol.*, vol. 27, no. 3, pp. 273–291, Feb. 2009.

[123] S. Y. Kim, S. B. Jun, Y. Takushima, E. S. Son, and Y. C. Chung, “Enhanced performance of RSOA-based WDM PON by using Manchester coding,” *J. Opt. Netw.,* vol. 6, no. 6, pp. 624-630, Jun, 2007.

[124] Y. J. Lee, K. Y. Cho, A. Murakami, A. Agata, Y. Takushima, and Y. C. Chung, “Reflection tolerance of RSOA-based WDM PON,” *Proc. Optical Fiber Commun. Conf.,* Paper OTuH5, Mar, 2008.

[125] T. Maekawa, M. Okayasu, K. Wakita, “Bidirectional transmission experiment employing a single light source and waveguide-type modulator,” *Proc. 8th Int. Workshop Optical/Hybrid Access Networks (OAN),* Atlanta, GA, 1997. Session IV.

[126] M. Feuer, M. Thomas, and L. Lunardi, “Backreflection and loss in single-fiber loopback networks,” *IEEE Photon. Technol. Lett.*, vol. 12, no. 8, pp. 1106–1108, Aug. 2000.

[127] M. Fujiwara, J.-i. Kani, H. Suzuki, and K. Iwatsuki, “Impact of backreflection on upstream transmission in WDM single-fiber loopback access networks,” *J. Lightwave Technol.*, vol. 24, no. 2, pp. 740–746, Feb, 2006.

[128] Y. Takushima, K. Y. Cho, and Y. C. Chung, “Design issue in RSOA-based WDM PON,” *Proc. International Photonics Global Conference (IPGC),* Dec, 2008.

[129] I. D. Henning, M. J. Adams, and J. V. Collins, “Performance prediction from a new optical amplifier model,” *IEEE J. Quantum Electron.*, vol. QE-21, no. 6, pp. 609-613, Jun, 1995.

[130] A. E. Willner, and W. Shieh, “Optimal spectral and power parameters for all-optical wavelength shifting: single stage, fanout, and cascadability,” *J. Lightwave Technol.,* vol. 13, no. 5, pp.771-781, May, 1995.

[131] A. E. Siegman, *Lasers*. University Science Books, USA, 1986.

[132] C. Michie, A. E. Kelly, J. McGeough, S. Karagiannopoulos, and I. Andonovic, “Optically amplified passive optical networks: a power budget analysis,” *J. Opt. Netw.,* vol. 8, no. 4, pp. 370-382, Apr, 2009.

[133] J. C. Simon, P. Doussiere, L. Pophillat and B. Fernier, “Gain and noise characteristics of a 1.5 µm near-travelling wave semiconductor laser amplifier,” *Electron. Lett.,* vol. 25, no. 7, pp. 434-436, Mar, 1989.

[134] A. E. Kelly, C. Michie, I. Armstrong, I. Andonovic, C. Tombling, J. McGeough, and B. C. Thomsen, “High-performance semiconductor optical amplifier modules at 1300 nm,” *IEEE Photon. Technol. Lett.*, vol. 18, no. 24, pp. 2674–2676, Dec, 2006.

[135] T. Akiyama, M. Ekawa, M. Sugawara, K. Kawaguchi, H. Sudo, A. Kuramata, H. Ebe, and Y. Arakawa, "An ultrawide-band semiconductor optical amplifier having an extremely high penalty-free output power of 23 dBm achieved with quantum dots," *IEEE Photon. Technol. Lett.,* vol. 17, no. 8, pp. 1614–1616, Aug, 2005.

[136] A. K. Srivastava, Y. Sun, J. L. Zyskind, and J. W. Sulhoff, "EDFA transient response to channel loss in WDM transmission system," *IEEE Photon. Technol. Lett.,* vol. 9, no. 3, pp. 386–388, Mar, 1997.

[137] T. Durhuus, B. Mikkelsen, and K. E. Stubkjaer, "Detailed dynamic model for semiconductor optical amplifiers and their crosstalk and intermodulation distortion," *J. Lightwave Technol.,* vol. 10, no. 8, pp.1056-1065, Aug, 1992**.**

[138] C. R. Giles, E. Desurvire, and J. R. Simpson, "Transient gain and cross talk in erbium-doped fiber amplifiers," *Opt. Lett.,* vol. 14, no. 16, pp. 880-882, 1989.

[139] J. Bryce, G. Yoffe, Y. Zhao, and R. Minasian, "Tunable, gain-clamped EDFA incorporating chirped fibre Bragg grating," *Electron. Lett.,* vol. 34, no. 17, pp. 1680-1681, Aug, 1998.

[140] D. A. Francis, S. P. DiJaili, and J. D. Walker, "A single chip linear optical amplifier," in *Proc. Opt. Fiber Commun. Conf.,* pp. PD13-1–PD13-3, Mar, 2001.

[141] C. Michie, A. E. Kelly, I. Armstrong, I. Andonovic and C. Tombling, "An adjustable gain-clamped semiconductor optical amplifier (AGC-SOA)," *J. Lightwave Technol.,* vol. 25, no. 6, pp. 1466-1473, Jun. 2007.

[142] Y. Lai, K. L. Hall, E. P. Ippen, and G. Eisenstein, "Short pulse gain saturation in InGaAsP diode laser amplifiers," *IEEE Photon. Technol. Lett.,* vol. 2, no. 10, pp. 711–713, Oct, 1990.

[143] J. Mark, and J. Mørk, "Subpicosecond gain dynamics in InGaAsP optical amplifiers: experiment and theory," *Appl. Phys. Lett.,* vol. 61, no. 19, pp. 2281-2283, Nov, 1992.

[144] A. Uskov, J. Mørk, J. Mark, M. C. Tatham, and G. Sherlock, "Terahertz four-wave mixing in semiconductor optical amplifers: experiment and theory," *Appl. Phys. Lett.,* vol. 65, no. 8, pp. 944-946, Aug, 1994.

[145] J. Mørk, M. L. Nielsen, and T. W. Berg, "The dynamics of semiconductor optical amplifiers: modeling and applications," *Opt. Photon. News.,* vol. 14, no. 7, pp. 42-48, Jul, 2003.

[146] A. Uskov, J. Mørk, and J. Mark, “Wave mixing in semiconductor laser amplifiers due to carrier heating and spectral-hole burning,” *IEEE J. Quantum Electron.*, vol. 30, no. 8, pp. 1769-1781, Aug, 1994.

[147] L. Kador, “Kramers-Krönig relations in nonlinear optics,” *Appl. Phys. Lett.*, vol. 66, no. 22, pp. 2938-2939, May, 1995.

[148] L. Occhi, L. Schares, and G. Guekos, “Phase modeling based on the α-factor in bulk semiconductor optical amplifiers,” *IEEE J. Select. Topics Quantum Electron.*, vol. 9, no. 3, pp. 788-797, Jun. 2003.

[149] C. H. Henry, “Theory of the linewidth of semiconductor lasers,” *IEEE J. Quantum Electron.*, vol. 18, no. 2, pp. 259-264, Feb. 1982.

[150] M. Osinski and J. Buus, “Linewidth broadening factor in semiconductor lasers-an overview,” *IEEE J. Quantum Electron.*, vol. 23, no. 1, pp. 9-28, Jan. 1987.

[151] C. Tombling, C. Michie, I. Andonovic and A. E. Kelly, “Recent advances in semiconductor optical amplifiers,” in *Proc. IEEE 16th LEOS.*, 2003.

[152] S. J. B. Yoo, “Wavelength conversion technologies for WDM network applications,” *J. Lightwave Technol.*, vol. 14, no. 6, pp.955-966, Jun, 1996**.**

[153] K. Obermann, S. Kindt, D. Breuer, K. Petermann, C. Schmidt, S. Diez, and H. G. Weber, “Noise characteristics of semiconductor-optical amplifiers used for wavelength conversion via cross-gain and cross-phase modulation,” *IEEE Photon. Technol. Lett.*, vol. 9, no. 3, pp. 312–314, Mar, 1997.

[154] K. Obermann, S. Kindt, D. Breuer, and K. Petermann, “Performance analysis of wavelength converters based on cross-gain modulation in semiconductor-optical amplifiers,” *J. Lightwave Technol.*, vol. 16, no. 1, pp.78-85, Jan, 1998**.**

[155] D. D. Marcenac, A. E. Kelly, D. Nesset and D. A. O. Davies, “Bandwidth enhancement of wavelength conversion via cross-gain modulation by semiconductor optical amplifier cascade,” *Electron. Lett.*, vol. 31, no. 17, pp. 1442-1443, Aug, 1995.

[156] C. Joergensen, S. L. Danielsen, K. E. Stubkjaer, M. Schilling, K. Daub, P. Doussiere, F. Pommerau, P. B. Hansen, H. N. Poulsen, A. Kloch, M. Vaa, B. Mikkelsen, E. Lach, G. Laube, W. Idler, and K. Wunstel, “All-optical wavelength conversion at bit rates above 10 Gb/s using semiconductor optical amplifiers,” *IEEE J.Select. Topics. Quantum Electron.*, vol.3, no. 5, pp. 1168-1180, Oct, 1997.

[157] M. L. Nielsen, D. J. Blumenthal, and J. Mørk, “A transfer function approach to the small-signal response of saturated semiconductor optical amplifiers,” *J. Lightwave Technol.*, vol. 18, no. 12, pp. 2151-2157, Dec. 2000.

[158] A. D. Ellis, A. E. Kelly, D. Nesset, D. Pitcher, D. G. Moodie and R. Kashyap, "Error free 100 Gbit/s wavelength conversion using grating assisted cross-gain modulation in 2 mm long semiconductor amplifier," *Electron. Lett.,* vol. 34, no. 20, pp. 1958-1959, Oct, 1998.

[159] R. J. Manning, X. Yang, R. P. Webb, R. Giller, F. C. G. Gunning, and A. D. Ellis, "The 'Turbo-Switch' – a novel technique to increase the high-speed response of SOAs for wavelength conversion," *Proc. OFC,* paper OWS8, 2005.

[160] G. Contestabile, A. Maruta, S. Sekiguchi, K. Morito, M. Sugawara and K. Kitayama, "160 Gb/s cross gain modulation in quantum dot SOA at 1550 nm," *Proc. ECOC,* no. 1.4, pp. 1-2, Sep, 2009.

[161] H. Y. Yu, D. Mahgerefteh, P. S. Cho, and J. Goldhar, "Improved transmission of chirped signals from semiconductor optical devices by pulse reshaping using a fiber Bragg grating filter," *J. Lightwave Technol.,* vol. 17, no. 5, pp.898-903, May, 1999**.**

[162] A. Ehrhardt, M. Eiselt, G. Groβkopf, L. Küller, R. Ludwig, W. Pieper, R. Schnabel, and H. G. Weber, "Semiconductor laser amplifer as optical switching gate," *J. Lightwave Technol.*, vol. 11, no. 8, pp.1287-1295, Aug, 1993**.**

[163] G. P. Agrawal, and N. A. Olsson, "Self-phase modulation and spectral broadening of optical pulses in semiconductor laser amplifiers," *IEEE J. Quantum Electron.,* vol. 25, no. 11, pp. 2297-2306, Nov. 1989.

[164] G. P. Agrawal, and N. A. Olsson, "Amplification and compression of weak picoseconds optical pulses by using semiconductor-laser amplifiers," *Opt. Lett.,* vol. 14, no. 10, pp. 500-502, May, 1989.

[165] S. Nakamura, Y. Ueno, and K. Tajima, "168-Gb/s all-optical wavelength conversion with a symmetric-Mach-Zehnder-Type switch," *IEEE Photon. Technol. Lett.*, vol. 2, no. 10, pp. 711–713, Oct, 1990.

[166] Z. Zhu, M. Funabashi, Z. Pan, L. Paraschis, D. L. Harris, and S. J. B. Yoo, "High-performance optical 3R regeneration for scalable fiber transmission system applications," *J. Lightwave Technol.,* vol. 25, no. 2, pp.504-511, Feb, 2007**.**

[167] X. Song, F. C. Yu, H. Song, M. Sugiyama, and Y. Nakano, "All-optical OTDM DEMUX with monolithic SOA-MZI switch by regrowth-free selective area MOVPE," in *Proc. Conf. Lasers and Electro-Opt.,* pp. 424-425, paper CTuJ4-4, Aug, 2005.

[168] Y. Miyazaki, T. Miyahara, K. Takagi, K. Matsumoto, S. Nishikawa, T. Hatta, T. Aoyagi, and K. Motoshima, "Polarization-insensitive SOA-MZI monolithic all-

optical wavelength converter for full C-band 40Gbps-NRZ operation," *Proc. ECOC*, paper Th3.4.2., Sep, 2006.

[169] K. Tajima, "All-optical switch with switch-off time unrestricted by carrier lifetime," *Jpn. J. Appl. Phys.*, vol. 32, no. 12A, pp. L1746-L1749, Dec. 1993.

[170] T. Durhuus, B. Mikkelsen, C. Joergensen, S. L. Danielsen, and K. E. Stubkjaer, "All-optical wavelength conversion by semiconductor optical amplifiers," *J. Lightwave Technol.*, vol. 14, no. 6, pp.942-954, Jun, 2006.

[171] M. Schilling, K. Daub, W. Idler, D. Baums, U. Koerner, E. Lach, G. Laube and K. Wünstel, "Wavelength converter based on integrated all-active three-port Mach-Zehnder interferometer," *Electron. Lett.*, vol. 30, no. 25, pp. 2128-2130, Dec, 1994.

[172] A. M. de Melo, S. Randel, and K. Petermann, "Mach-Zehnder interferometer-based high-speed OTDM add-drop multiplexing," *J. Lightwave Technol.*, vol. 25, no. 4, pp.1017-1026, Apr, 2007.

[173] M. Spyropoulou, N. Pleros, and A. Miliou, "SOA-MZI-based nonlinear optical signal processing: a frequency domain transfer function for wavelength conversion, clock recovery, and packet envelope detection," *IEEE J. Quantum Electron.*, vol. 47, no. 1, pp. 40-49, Jan, 2011.

[174] G. T. Kanellos, D. Petrantonakis, D. Tsiokos, P. Bakopoulos, P. Zakynthinos, N. Pleros, D. Apostolopoulos, G. Maxwell, A. Poustie, and H. Avramopoulos, "All-optical 3R burst-mode reception at 40Gb/s using four integrated MZI switches," *J. Lightwave Technol.*, vol. 25, no. 1, pp.184-192, Jan, 2007.

[175] B. Mikkelsen, K. S. Jepsen, M. Vaa, H. N. Poulsen, K. E. Stubkjaer, R. Hess, M. Duelk, W. Vogt, E. Gamper, E. Gini, P. A. Besse, H. Melchior, S. Bouchoule and F. Devaux, "All-optical wavelength converter scheme for high speed RZ signal formats," *Electron. Lett.*, vol. 33, no. 25, pp. 2137-2139, Dec, 1997.

[176] K. I. Kang, T. G. Chang, I. Glesk, P. R. Prucnal, and R. K. Boncek, "Demonstration of ultrafast, all-optical, low control energy, single wavelength, polarization independent, cascadable, and integratable switch," *Appl. Phys. Lett.*, vol. 67, no. 5, pp. 605-607, Jul, 1995.

[177] K. Tajima, S. Nakamura, and Y. Sugimoto, "Ultrafast polarization-descriminating Mach-Zehnder all-optical switch," *Appl. Phys. Lett.*, vol. 67, no. 25, pp. 3709-3711, Dec, 1995.

[178] A. E. Kelly, I. D. Phillips, R. J. Manning, A. D. Ellis, D. Nesset, D. G. Moodie and R. Kashyap, "80Gbit/s all-optical regenerative wavelength conversion using

semiconductor optical amplifier based interferometer," *Electron. Lett.,* vol. 35, no. 17, pp. 1477-1478, Aug, 1999.

[179] Y. Ueno, S. Nakamura, K. Tajima, and S. Kitamura, "3.8-THz wavelength conversion of picosecond pulses using a semiconductor delayed-interference signal-wavelength conversion (DISC)," *IEEE Photon. Technol. Lett.,* vol. 10, no. 3, pp. 346–348, Mar, 1998.

[180] J. Leuthold, C. H. Joyner, B. Mikkelsen, G. Raybon, J. L. Pleumeekers, B. I. Miller, K. Dreyer and C. A. Burrus, "100 Gbit/s all-optical wavelength conversion with integrated SOA delayed-interference configuration," *Electron. Lett.,* vol. 36, no. 13, pp. 1129-1130, Jun, 2000.

[181] M. L. Nielsen and J. Mørk, "Increasing the modulation bandwidth of semiconductor-optical-amplifer-based switches by using optical filtering," *J. Opt. Soc. Amer. B.,* vol. 21, no. 9, pp. 1606-1619, Sep, 2004.

[182] H. Chayett, S. Ben Ezra, N. Shachar, S. Tzadok, S. Tsadka, and J. Leuthold, "Regenerative all-optical wavelength converter based on semiconductor optical amplifier and sharp frequency response filter," *Proc. Optical Fiber Commun. Conf.,* paper ThS2, Feb, 2004.

[183] M. L. Nielsen, B. Lavigne, and B. Dagens, "Polarity-preserving SOA-based wavelength conversion at 40 Gbit/s using bandpass filtering," *Electron. Lett.,* vol. 39, no. 18, pp. 1334-1335, Sep, 2003.

[184] Y. Liu, E. Tangdiongga, Z. Li, S. Zhang, H. de Waardt, G. D. Khoe, and H. J. S. Dorren, "Error-free all-optical wavelength conversion at 160 Gb/s using a semiconductor optical amplifier and an optical bandpass filter," *J. Lightwave Technol.,* vol. 24, no. 1, pp.230-235, Jan, 2006**.**

[185] M. L. Nielsen, and J. Mørk, "Impact of optical filtering on linear and nonlinear patterning effects in SOA-based all-optical switches," in *Proc. Optical Amplifiers and their Applications (OAA),* paper SuB6, Aug, 2005.

[186] Y. Liu, E. Tangdiongga, Z. Li, H. de Waardt, A. M. J. Koonen, G. D. Khoe, X. Shu, I. Bennion, and H. J. S. Dorren, "Error-free 320-Gb/s all optical wavelength conversion using a single semiconductor optical amplifer," *J. Lightwave Technol.,* vol. 25, no. 1, pp.103-108, Jan, 2007**.**

[187] S. Nakamura, and K. Tajima, "Ultrafast all-optical gate switch based on frequency shift accompanied by semiconductor band-filling effect," *Appl. Phys. Lett.,* vol. 70, no. 26, pp. 3498-3500, Jun, 1997.

[188] J. Dong, X. Zhang, S. Fu, J. Xu, P. Shum, and D. Huang, “Ultrafast all-optical signal processing based on single semiconductor optical amplifers,” *IEEE J.Select. Topics. Quantum Electron.*, vol. 14, no. 3, pp. 770-778, Jun, 2008.

[189] G. P. Agrawal, “Population pulsations and nondegenerate four-wave mixing in semiconductor lasers and amplifiers,” *J. Opt. Soc. Am. B.*, vol. 5, no. 1, pp. 147-159, Jan, 1988.

[190] S. Diez, C. Schmidt, R. Ludwig, H. G. Weber, K. Obermann, S. Kindt, I. Koltchanov, and K. Petermann, “Four-wave mixing in semiconductor optical amplifiers for frequency conversion and fast optical switching,” *IEEE J.Select. Topics. Quantum Electron.*, vol. 3, no. 5, pp. 1131-1145, Oct, 1997.

[191] A. Uskov, J. Mørk, and J. Mark, “Wave mixing in semiconductor laser amplifiers due to carrier heating and spectral-hole burning,” *IEEE J. Quantum Electron.*, vol. 30, no. 8, pp. 1769-1781, Aug, 1994.

[192] D. X. Zhu, D. Tishinin, K. Uppal, S. Dubovitsky, J. Burger, W. H. Steier and D. P. Dapkus, “Filter-free four-wave mixing wavelength conversion in semiconductor optical amplifiers,” *Electron. Lett.*, vol. 34, no.1, pp. 87-88, Jan, 1998.

[193] J. Leuthold, F. Girardin, P. A. Besse, E. Gamper, G. Guekos, and H. Melchior, “Polarization independent optical phase conjugation with pump-signal filtering in a monolithically intergrated Mach-Zehnder interferometer semiconductor optical amplifier configuration,” *IEEE Phot. Technol. Lett.*, vol. 10, no. 11, pp. 1569–1571, Nov, 1998.

[194] A. E. Kelly, A. D. Ellis, D. Nesset, R. Kashyap, and D. G. Moodie, “100 Gbit/s wavelength conversion using FWM in an MQW semiconductor optical amplifier,” *Electron. Lett.*, vol. 34, no.20, pp. 1955-1956, Oct, 1998.

[195] J. P. R. Lacey, M. A. Summerfield and S. J. Madden, “Tunability of polarization-insensitive wavelength converters based on four-wave mixing in semiconductor optical amplifiers,” *J. Lightwave Technol.*, vol. 16, no. 12, pp.2419-2427, Dec, 1998**.**

[196] D. D. Marcenac, D. Nesset, A. E. Kelly, M. Brierley, A. D. Ellis, D. G. Moodie, and C. W. Ford, “40 Gbit/s transmission over 406 km of NDSF using mid-span spectral inversion by four-wave-mixing in a 2 mm long semiconductor optical amplifier,” *Electron. Lett.*, vol. 33, no.10, pp. 879-880, May, 1997.

[197] C. J. Chang-Hasnain, and S. L. Chuang, “Slow and fast light in semiconductor quantum-well and quantum-dot devices,” *J. Lightwave Technol.,* vol. 24, no. 12, pp.4642-4654, Dec, 2006**.**

[198] S. Ö. Düill, R. F. O’Dowd and G. Eisenstein, “On the role of high-order coherent population oscillations in slow and fast light propagation using semiconductor optical amplifiers,” *IEEE J. Select. Topics. Quantum Electron.,* vol. 15, no. 3, pp. 578-584, May/Jun, 2009.

[199] T. Morioka, H. Takara, S. Kawanishi, K. Uchiyama, and M. Saruwatari, “Polarisation-independent all-optical demultiplexing up to 200 Gbit/s using four-wave mixing in a semiconductor laser amplifier,” *Electron. Lett.,* vol. 32, no. 9, pp. 840-841, Apr, 1996.

[200] M. Jinno, J. B. Schlager, and D. L. Franzen, “Optical sampling using nondegenerate four-wave mixing in a semiconductor laser amplifier,” *Electron. Lett.,* vol. 30, no. 18, pp. 1489-1491, Sep, 1994.

[201] H. Soto, D. Erasme, and G. Guekos, “Cross-polarization modulation in semiconductor optical amplifiers,” *IEEE Phot. Technol. Lett.,* vol. 11, no. 8, pp. 970–972, Aug, 1999.

[202] R. J. Manning, A. Antonopoulos, R. Le Roux and A. E. Kelly, “Experimental measurement of nonlinear polarisation rotation in semiconductor optical amplifiers,” *Electron. Lett.,* vol. 37, no. 4, pp. 229-231, Feb, 2001.

[203] B. F. Kennedy, S. Philippe, P. Landais, A. L. Bradley and H. Soto, “Experimental investigation of polarisation rotation in semiconductor optical amplifiers,” *IEE Proc.-Optoelectron.,* vol. 151, no. 2, pp. 114-118, Apr. 2004.

[204] S. Philippe, A. L. Bradley, B. Kennedy, F. Surre, and P. Landais, “Experimental investigation of polarization effects in semiconductor optical amplifiers and implications for all-optical switching,” *J. Lightwave Technol.,* vol. 26, no. 16, pp.2977-2985, Aug, 2008**.**

[205] E. Alvarez, H. Soto, J. Torres, “Investigation of the carrier density dependence on the confinement factor in a bulk semiconductor optical amplifier with a ridge waveguide,” *Optics. Comm.,* vol. 222, pp. 161-167, 2003.

[206] M. Zhao, J. D. Merlier, G. Morthier, and R. G. Baets, “Dynamic birefringence of the linear optical amplifier and application in optical regeneration,” *IEEE J. Select. Topics. Quantum Electron.,* vol. 8, no. 6, pp. 1399-1404, Nov/Dec, 2002.

[207] Y. Takahashi, A. Neogi, and H. Kawaguchi, “Polarization-dependent nonlinear gain in semiconductor lasers,” *IEEE J. Quantum Electron.,* vol. 34, no. 9, pp. 1660-1672, Sep, 1998.

[208] H. J. S. Dorren, D. Lenstra, Y. Liu, M. T. Hill, and G-D. Khoe, “Nonlinear polarization rotation in semiconductor optical amplifiers: theory and application to all-optical flip-flop memories,” *IEEE J. Quantum Electron.,* vol. 39, no. 1, pp. 141-148, Jan, 2003.

[209] X. Yang, D. Lenstra, G. D. Khoe, H. J. S. Dorren, “Nonlinear polarization rotation induced by ultrashort optical pulses in a semiconductor optical amplifier,” *Optics. Comm.,* vol. 223, pp. 169-179, 2003.

[210] L. Q. Guo and M. J. Connelly, “A Mueller-Matrix formalism for modelling polarization azimuth and ellipticity angle in semiconductor optical amplifiers in a pump-probe scheme,” *J. Lightwave Technol.,* vol. 25, no. 1, pp.410-420, Jan, 2007**.**

[211] S. Diez, C. Schmidt, R. Ludwig, H. G. Weber, P. Doussiere, and T. Ducellier, “Effect of birefringence in a bulk semiconductor optical amplifier on four-wave mixing,” *IEEE Photon. Technol. Lett.*, vol. 10, no. 2, pp. 212–214, Feb, 1998.

[212] R. J. Manning, A. E. Kelly, A. J. Poustie and K. J. Blow, “Wavelength dependence of switching contrast ratio of semiconductor optical amplifier-based nonlinear loop mirror,” *Electron. Lett.,* vol. 34, no. 9, pp. 916-918, Apr, 1998.

[213] H. Lirong, H. Dexiu, S. Junqiang, and L. Deming, “Spectral broadening of ultrashort optical pulse due to birefringence in semiconductor optical amplifiers,” *Optics. Comm.,* vol. 223, pp. 295-300, 2003.

[214] M. C. Acosta, and H. Soto, “Evaluation of the cross-polarization modulation impact on the conversion efficiency of a four wave mixing process developed in a bulk-SOA,” *Optics. Comm.*, vol. 269, pp. 215-222, 2007.

[215] M. F. C. Stephens, M. Asghari, R. V. Penty and I. H. White, “Demonstration of ultrafast all-optical wavelength conversion utilizing birefringence in semiconductor optical amplifiers,” *IEEE Photon. Technol. Lett.*, vol. 9, no. 4, pp. 449–451, Apr. 1997.

[216] Y. Liu, M. T. Hill, E. Tangdiongga, H. de Waardt, N. Calabretta, G. D. Khoe, and H. J. S. Dorren, “Wavelength conversion using nonlinear polarization rotation in a single semiconductor optical amplifier,” *IEEE Photon. Technol. Lett.*, vol. 15, no. 1, pp. 90–92, Jan. 2003.

[217] W. W. Tang, and C. Shu, "Optical pumping of a semiconductor optical amplifier for wide-band noninverting wavelength conversion," *IEEE Photon. Technol. Lett.,* vol. 17, no. 9, pp. 1905–1907, Sep. 2005.

[218] D. M. Patrick, A. D. Ellis, D. A. O. Davies, M. C. Tatham, and G. Sherlock, "Demultiplexing using polarisation rotation in a semiconductor laser amplifier," *Electron. Lett.,* vol. 30, no. 4, pp. 341-342, Feb, 1994.

[219] M. F. C. Stephens, A. E. Kelly, D. Nesset, A. Wonfor, and R. V. Penty, "Demonstration of time division demultiplexing from 40Gb/s to 10Gb/s via polarisation switching in a semiconductor optical amplifier," *Proc. Lasers and Electro-Optics Europe.,* paper. CFG8, 1998.

[220] H. Soto, D. Erasme, and G. Guekos, "5-Gb/s XOR optical gate based on cross-polarization modulation in semiconductor optical amplifiers," *IEEE Photon. Technol. Lett.,* vol. 13, no. 4, pp. 335–337, Apr. 2001.

[221] H. Soto, C. A. Diaz, J. Topomondzo, D. Erasme, L. Schares, and G. Guekos, "All-optical AND gate implementation using cross-polarization modulation in a semiconductor optical amplifiers," *IEEE Photon. Technol. Lett.,* vol. 14, no. 4, pp. 498–500, Apr. 2002.

[222] H. Soto, E. Alvarez, C. A. Diaz, J. Topomondzo, D. Erasme, L. Schares, L. Occhi, G. Guekos, and M. Castro, "Design of an all-optical NOT XOR gate based on cross-polarization modulation in a semiconductor optical amplifier," *Optics. Comm.,* vol. 237, pp. 121-131, 2004.

[223] G. Gavioli, and P. Bayvel, "Novel 3R regenerator based on polarization switching in a semiconductor optical amplifier-assisted fiber Sagnac interferometer," *IEEE Photon. Technol. Lett.,* vol. 15, no. 9, pp. 1261–1263, Sep. 2003.

[224] S. J. Bianco, *Computer Physics Research Trends.* New York: Nova Science, 2007.

[225] A. Dienes, J. P. Heritage, M. Y. Hong, and Y. H. Chang, "Time- and spectral-domain evolution of subpicosecond pulses in semiconductor optical amplifiers," *Opt. Lett.,* vol. 17, no. 22, pp. 1602-1604, Nov, 1992.

[226] M. Y. Hong, Y. H. Chang, A. Dienes, J. P. Heritage, and P. J. Delfyett, "Subpicosecond pulse amplification in semiconductor laser amplifiers: theory and experiment," *IEEE J. Quantum Electron.,* vol. 30, no. 4, pp. 1122-1131, Apr, 1994.

[227] S. Bischoff, A. Buxens, H. N. Poulsen, A. T. Clausen, and J. Mørk, “Bidirectional four-wave mixing in semiconductor optical amplifiers: theory and experiment,” *J. Lightwave Technol.,* vol. 17, no. 9, pp. 1617-1625, Sep, 1999**.**

[228] M. Razaghi, V. Ahmadi, and M. J. Connelly, “Comprehensive finite-difference time-dependent beam propagation model of counterpropagating picoseconds pulses in a semiconductor optical amplifiers,” *J. Lightwave Technol.,* vol. 27, no. 15, pp. 3162-3174, Aug, 2009**.**

[229] D. Marcuse, “Computer model of an injection laser amplifier,” *IEEE J. Quantum Electron.,* vol. 19, no. 1, pp. 63-73, Jan, 1983.

[230] M. J. Adams, J. V. Collins, and I. D. Henning, “Analysis of semiconductor laser optical amplifiers,” *IEE Proceedings,* vol. 132, no. 1, pp. 58-63, Feb. 1985.

[231] M. J. Connelly, “Wideband semiconductor optical amplifier steady-state numerical model,” *IEEE J. Quantum Electron.,* vol. 37, no. 3, pp. 439-447, Mar. 2001.

[232] M. J. Connelly, and R. F. O’Dowd, “Travelling-wave semiconductor laser amplifier detector noise characteristics,” *IEE Proc. Optoelectron.,* vol. 142, no. 1, Feb. 1995.

[233] R. Gutiérrez-Castrejón, and M. Duelk, “Uni-directional time-domain bulk SOA simulator considering carrier depletion by amplified spontaneous emission,” *IEEE J. Quantum Electron.,* vol. 42, no. 6, pp. 581-588, Jun. 2006.

[234] D. T. Cassidy, “Comparison of rate-equation and Fabry-Perot approaches to modeling a diode laser,” *Appl. Opt.,* vol. 22, no. 21, pp. 3321-3326, Nov. 1983.

[235] C. Y. J. Chu, and H. Ghafouri-Shiraz, “Analysis of gain and saturation characteristics of a semiconductor laser optical amplifier using transfer matrices,” *J. Lightwave Technol.,* vol. 12, no. 8, pp. 1378-1386, Aug. 1994.

[236] G. P. Agrawal, *Nonlinear Fiber Optics,* 3rd Ed, Academic press, 2001.

[237] L. H. Spiekman, J. M. Wiesenfeld, A. H. Gnauck, L. D. Garrett, G. N. van den Hoven, T. van Dongen, M. J. H. Sander-Jochem, and J. J. M. Binsma, “Transmission of 8 DWDM channels at 20 Gb/s over 160 km of standard fiber using a cascade of semiconductor optical amplifiers,” *IEEE Phot. Technol. Lett.,* vol. 12, no. 6, pp. 717–719, Jun. 2000.

[238] M. Matsuura, N. Kishi, and T. Miki, “Ultrawideband wavelength conversion using cascaded SOA-based wavelength converters,” *J. Lightwave Technol.,* vol. 25, no. 1, pp. 38-45, Jan. 2007.

[239] S. Tanaka, S-H. Jeong, S. Yamazaki, A. Uetake, S. Tomabechi, M. Ekawa, and K. Morito, "Monolithically integrated 8:1 SOA gate switch with large extinction ratio and wide input power dynamic range," *IEEE J. Quantum Electron.*, vol. 45, no. 9, pp. 1155-1162, Sep. 2009.

[240] M. G. Davis and R. F. O'Dowd, "A transfer matrix method based large-signal dynamic model for multielectrode DFB lasers," *IEEE J. Quantum Electron.*, vol. 30, no. 11, pp. 2458-2466, Nov. 1994.

[241] http://www.kamelian.com/

[242] C. H. Henry, R. A. Logan, and F. R. Merritt, "Measurement of gain and absorption spectra in AlGaAs buried heterostructure lasers," *J. Appl. Phys.*, vol. 51, no. 6, pp. 3042-3051, Jun. 1980.

[243] M. Dutta, and M. A. Stroscio, *Advances in Semiconductor Lasers and Applications to Optoelectronics*, World Scientific, Singapore, 2000.

[244] J. Leuthold, M. Mayer, J. Eckner, G. Guekos, and H. Melchior, "Material gain of bulk 1.55 μm InGaAsP/InP semiconductor optical amplifers approximated by a polynomial model," *J. Appl. Phys.*, vol. 87, no. 1, pp. 618-620, Jan. 2000.

[245] M. Asada, A. Kameyama, and Y. Suematsu, "Gain and intervalence band absorption in quantum-well lasers," *IEEE J. Quantum Electron.*, vol. QE-20, no. 7, pp. 745-753, Jul. 1984.

[246] M. Asada, and Y. Suematsu, "Denstiy-matrix theory of semiconductor lasers with relaxation broadening model-gain and gain-suppression in semiconductor lasers," *IEEE J. Quantum Electron.*, vol. QE-21, no. 5, pp. 434-442, May. 1985.

[247] R. H. Yan, S. W. Corzine, L. A. Coldren, and I. Suemune, "Corrections to the expression for gain in GaAs," *IEEE J. Quantum Electron.*, vol. 26, no. 2, pp. 213-216, Feb. 1990.

[248] G. Jones, and E. P. O'Reilly, "Improved performance of long-wavelength strained bulk-like semiconductor lasers," *IEEE J. Quantum Electron.*, vol. 29, no. 5, pp. 1344-1354, May. 1993.

[249] P. S. Zory, Jr. *Quantum Well Lasers*, Academic Press, 1993.

[250] M. J. Connelly, "Wide-band steady-state numerical model and parameter extraction of a tensile-strained bulk semiconductor optical amplifier," *IEEE J. Quantum Electron.*, vol. 43, no. 1, pp. 47-56, Jan. 2007.

[251] M. Asada, A. R. Adams, K. E. Stubkjaer, Y. Suematsu, Y. Itaya, and S. Arai, "The temperature dependence of the threshold current of GaInAsP/InP DH lasers," *IEEE J. Quantum Electron.*, vol. QE-17, no. 5, pp. 611-619, May. 1981.

[252] K. Petermann, “Calculated spontaneous emission factor for double-heterostructure injection lasers with gain-induced waveguiding,” *IEEE J. Quantum Electron.*, vol. QE-15, no. 7, pp. 566-570, Jul. 1979.

[253] R. P. Davey and D. B. Payne, “The future of optical transmission in access and metro networks – an operator’s view,” in *Proc. ECOC,* 2005, Vol. 5, pp. 53-56.

[254] Cisco Systems, “Cisco visual networking index: forecast and methodology, 2010-2015,” Jun. 2011. [Online]. Available: http://www.cisco.com/en/US/solutions/collateral/ns341/ns525/ns537/ns705/ns827/white_paper_c11-481360.pdf

[255] S. Chatzi and I. Tomkos, “Techno-economic study of high-splitting ratio PONs and comparison with conventional FTTH-PONs/FTTH-P2P/FTTB and FTTC deployments,” presented at the Optical Fiber Commun., Los Angeles, CA, 2011, Paper JWA15.

[256] ITU-T Recommendation G.987.2, “10-Gigabit-capable passive optical networks (XG-PON): physical media dependent (PMD) layer specification,” Jan. 2010.

[257] A. K. Srivastava, Y. Sun, J. L. Zyskind, and J. W. Sulhoff, “EDFA transient response to channel loss in WDM transmission system,” *IEEE Photon. Technol. Lett.,* vol. 9, no. 3, pp. 386-388, Mar. 1997.

[258] K. Wakao, H. Soda, and Y. Kotaki, “Semiconductor optical active devices for photonic networks," *FUJITSU Sci. Tech. J.,* vol. 35, no. 1, pp. 100-106, Jul, 1999.

[259] G. Onishchukov, V. Lokhnygin, A. Shipulin, and P. Riedel, “10 Gbit/s transmission over 1500 km with semiconductor optical amplifiers,” *Electron. Lett.,* vol. 34, no. 16, pp. 1597-1598, Aug. 1998.

[260] M. Fujiwara, K. Suzuki, K. Hara, T. Imai, K. Taguchi, H. Ishii, N. Yoshimoto, and H. Hadama, “Burst-mode compound optical amplifier with automatic level control circuit that offers enhanced setting flexibility in a 10 Gb/s-Class PON,” in *Proc. ECOC*, 2010, pp. 1-3.

[261] C-Y. Jin, Y-Z. Huang, L-J, Yu, and S-L. Deng, “Detailed model and investigation of gain saturation and carrier spatial hole burning for a semiconductor optical amplifier with gain clamping by a vertical laser field,” *IEEE J. Quantum Electron.,* vol. 40, no. 5, pp. 513-518, May. 2004.

[262] D. A. Francis, S. P. DiJaili, and J. D. Walker, “A single-chip linear optical amplifier,” in *Proc. OFC,* 2001, paper PD13-1.

[263] X-H. Jia, “Theoretical investigation of gain-clamped semiconductor optical amplifiers using the amplified spontaneous emission compensating effect,” *J. Opt.*

Soc. Am. B, vol 23, no. 12, pp. 2503-2510, Dec. 2006.

[264] J. T. Ahn, J. M. Lee, and K. H. Kim, "Gain-clamped semiconductor optical amplifier based on compensating light generated from amplified spontaneous emission," *Eletron. Lett.*, vol. 39, no. 15, pp. 1140-1141, Jul. 2003.

[265] L. Liu, C. Michie, A. E. Kelly, and I. Andonovic, "Packet equalisation in PONs using adjustable gain-clamped semiconductor optical amplifiers (AGC-SOA)," *in Proc. Photonics Global Conference,* Singapore, Dec. 2010.

[266] D. C. Kim, B. S. Choi, H. S. Kim, K. S. Kim, O. K. Kwon, and D. K. Oh "2.5 Gbps operation of RSOA for low cost WDM-PON sources," in *Proc. ECOC,* 2009, pp. 1-2.

Appendix

Table 1 The SOA parameters used in the simulation.

Symbol	Parameter	Value
L_c	Central active region length	400 μm
L_t	Tapered active region length	200 μm
d	Active region thickness	0.4 μm
W	Active region width	0.4 μm
y	Molar fraction of Arsenide	0.892
Γ	Confinement factor	0.15
R_1	Input facet reflectivity	5×10^{-5}
R_2	Output facet reflectivity	5×10^{-5}
η_{in}	Input coupling loss	3 dB
η_{out}	Output coupling loss	3 dB
K_0	Carrier independent absorption loss coefficient	6200 m^{-1}
K_1	Carrier dependent absorption loss coefficient	7.5×10^{-21} m^2
n_r	Active region refractive index	3.22
A_{rad}	Linear radiative recombination coefficient	1.0×10^{7} s^{-1}
A_{tr}	Linear nonradiative recombination coefficient for traps and surface effect	3.6×10^{8} s^{-1}
B_{rad}	Bimolecular radiative recombination coefficient	5.6×10^{-16} m^3/s
C_{aug}	Auger recombination coefficient	3×10^{-41} m^6/s

Table 2 Parameters used in the system level model.

Symbol	Parameter	Value
L	Active region length	1000 μm
d	Active region thickness	0.1 μm
W	Active region width	1.2 μm
N_t	Transparent carrier density	0.9×10^{24} m^{-3}
Γ	Confinement factor	0.15
g_N	Differential gain	2.5×10^{-20} m^2
λ_{ref}	Peak wavelength at transparency	1605 nm
γ_2	Constant determining the gain bandwidth	7.4×10^{18}
γ_3	Constant accounting for the asymmetry of the gain curve	3.155×10^{25}
k_0	Constant characterizing the gain peak shift	3.0×10^{-32}
α	Internal loss	2×10^3 m^{-1}
n_r	Active region refractive index	3.5
C_1	Surface and defect recombination coefficient	1×10^8 s^{-1}
C_2	Radiative recombination coefficient	2.5×10^{-17} m^3/s
C_3	Auger recombination coefficient	9.4×10^{-41} m^6/s
T_B	Period of a pulse	2^7
C	Duty cycle	1

Table 3 Device parameters used in the AGC-SOA simulation.

Symbol	Parameters	SOA1	SOA2
L_c	Central active region length	400 μm	840 μm
L_t	Tapered active region length	200 μm	160 μm
d	Active region thickness	0.4 μm	0.1 μm
W	Active region width	0.4 μm	1.1 μm
y	Molar fraction of Arsenide	0.892	0.816
Γ	Confinement factor	0.15	0.15
R_1	Input facet reflectivity	5×10^{-5}	1×10^{-5}
R_2	Output facet reflectivity	5×10^{-5}	1×10^{-5}
η_{in}	Input coupling loss	3 dB	2 dB
η_{out}	Output coupling loss	3 dB	2 dB
K_0	Carrier independent absorption loss coefficient	6200 m^{-1}	3000 m^{-1}
K_1	Carrier dependent absorption loss coefficient	7.5×10^{-21} m^2	6.83×10^{-21} m^2
n_r	Active region refractive index	3.22	3.56
C_1	Recombination coefficients	3.7×10^{8} s^{-1}	
C_2		5.6×10^{-16} m^3/s	
C_3		3×10^{-41} m^6/s	
α	WDM coupler pass band insertion loss	0.5 dB	